Dissertation zur Erlangung des Doktorgrades
der Fakultät für Chemie und Pharmazie
der Ludwig-Maximilians-Universität München

In vitro and *in vivo* analysis of voltage- and cyclic nucleotide-gated cation channels

René Dominik Rötzer

aus

Rottweil, Deutschland

2021

Erklärung

Diese Dissertation wurde im Sinne von § 7 der Promotionsordnung vom 28. November 2011 von Herrn Prof. Dr. Christian Wahl-Schott betreut.

Eidesstattliche Versicherung

Diese Dissertation wurde eigenständig und ohne unerlaubte Hilfe erarbeitet.

München, den 04. Oktober 2021

_____

(René Dominik Rötzer)

Dissertation eingereicht am: 04. Oktober 2021

1. Gutachter: Prof. Dr. Christian Wahl-Schott
2. Gutachter: Prof. Dr. Martin Biel

Mündliche Prüfung am: 18. November 2021

Meinen Eltern

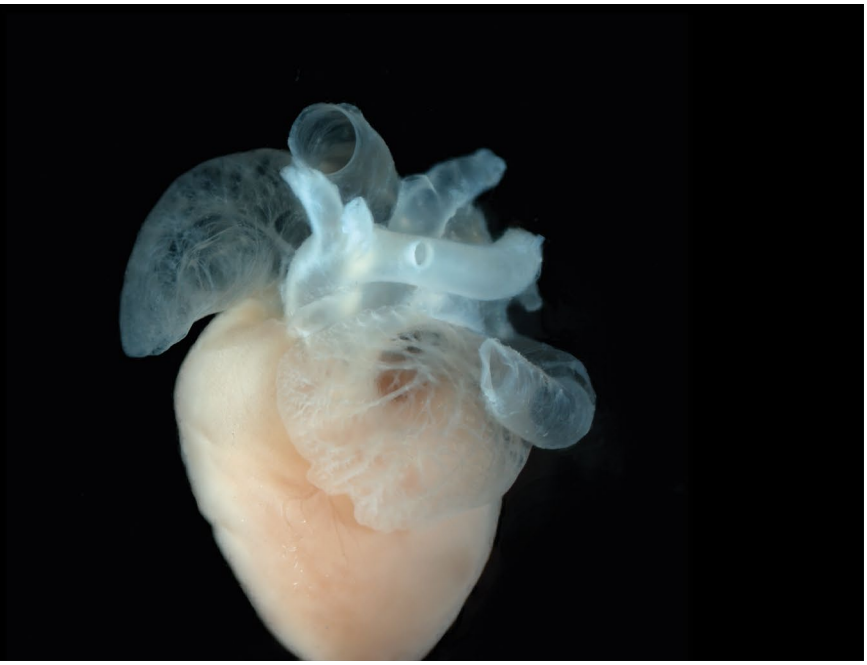

Table of contents

1 Abbreviations

AM	atrial myocyte
ANS	autonomic nervous system
BRS	baroreflex sensitivity
cAMP	cyclic adenosine monophosphate
CCS	cardiac conduction system
CDR	cAMP-dependent regulation
cGMP	cyclic guanosine monophosphate
CNBD	cyclic nucleotide-binding domain
CNBHD	cyclic nucleotide-binding homology domain
CNG	cyclic nucleotide-gated
CNS	central nervous system
Cryo-EM	cryo-electron microscopy
dLGN	dorsolateral geniculate nucleus
GIRK	G protein-coupled inwardly rectifying potassium channel
HCN	hyperpolarization-activated cyclic nucleotide-gated
HCND	HCN domain
HR	heart rate
ICNS	intrinsic cardiac nervous system
IS	inner segment
KCNH	voltage-gated potassium channel, subfamily H
MAP	mean arterial pressure
MGN	medial geniculate nucleus
mRNA	messenger ribonucleic acid

NREM	non-rapid eye movement
OS	outer segment
OSN	olfactory sensory neuron
PD	pore domain
PKA	protein kinase A
rAAV	recombinant adeno-associated virus
Rho $^{+/-}$	rhodopsin-deficient
SAN	sinoatrial node
sgRNA	single guide ribonucleic acid
TMD	transmembrane domain
$V_{0.5}$	half-maximal activation voltage
VB	ventrobasal
VGIC	voltage-gated ion channel
VM	ventricular myocyte
VSD	voltage sensing domain
WT	wild-type

2 List of manuscripts

This thesis is based on the following publications, which are referred to in the text by their roman numbering (I-IV):

I. Sybille Böhm*, Victoria Splith*, Lisa Maria Riedmayr, **René Dominik Rötzer**, Gilles Gasparoni, Karl J. V. Nordström, Johanna Elisabeth Wagner, Klara Sonnie Hinrichsmeyer, Jörn Walter, Christian Wahl-Schott, Stefanie Fenske, Martin Biel, Stylianos Michalakis, Elvir Becirovic

A gene therapy for inherited blindness using dCas9-VPR–mediated transcriptional activation
2020, **Science Advances**, 6(34): eaba5614
* equal contribution

II. Verena Hammelmann, Marc Sebastian Stieglitz, Henrik Hülle, Karim Le Meur, Jennifer Kass, Manuela Brümmer, Christian Gruner, **René Dominik Rötzer**, Stefanie Fenske, Jana Hartmann, Benedikt Zott, Anita Lüthi, Saskia Spahn, Markus Moser, Dirk Isbrandt, Andreas Ludwig, Arthur Konnerth, Christian Wahl-Schott, Martin Biel

Abolishing cAMP sensitivity in HCN2 pacemaker channels induces generalized seizures
2019, **JCI Insight**, 4(9): e126418

III. Stefanie Fenske, Konstantin Hennis*, **René D. Rötzer***, Verena F. Brox*, Elvir Becirovic, Andreas Scharr, Christian Gruner, Tilman Ziegler, Verena Mehlfeld, Jaclyn Brennan, Igor R. Efimov, Audrys G. Pauža, Markus Moser, Carsten T. Wotjak, Christian Kupatt, Rasmus Gönner, Rai Zhang, Henggui Zhang, Xiangang Zong, Martin Biel, Christian Wahl-Schott

cAMP-dependent regulation of HCN4 controls the tonic entrainment process in sinoatrial node pacemaker cells
2020, **Nature Communications**, 11, 5555
* equal contribution

IV. **René D. Rötzer**, Verena F. Brox, Konstantin Hennis, Stefan B. Thalhammer, Martin Biel, Christian Wahl-Schott, Stefanie Fenske

Implantation of Combined Telemetric ECG and Blood Pressure Transmitters to Determine Spontaneous Baroreflex Sensitivity in Conscious Mice
2021, **Journal of Visualized Experiments**, (168): e62101

3 Summary

The present thesis deals with voltage-gated ion channels (VGIC) that are additionally controlled by binding of cyclic nucleotides to a cyclic nucleotide-binding domain (CNBD). The two channel families investigated are cyclic nucleotide-gated (CNG) and hyperpolarization-activated cyclic nucleotide-gated (HCN) channels. Thereby, the following questions were addressed using electrophysiological methods: (1) Can specific CNG currents be measured in cells lacking endogenous CNG channel expression after the gene encoding for CNGA1 is switched on using a novel gene activation method? (2) Does cyclic adenosine monophosphate (cAMP) increase the maximum conductance of HCN channels? (3) What is the physiological role of cAMP-dependent regulation (CDR) of HCN4 in sinoatrial pacemaking and (4) how does hysteresis of HCN4 contribute to it?

In **manuscript I**, a gene editing approach involving catalytically inactive Cas9 (dCas9) was used to activate genes. The method takes advantage of the existence of gene isoforms in the genome. These genes encode for protein isoforms with almost identical function. Importantly, the expression of protein isoforms is cell specific. For example, a given cell only expresses one isoform, while the genes for the other isoforms are silenced. Consequently, loss of function mutation of the gene encoding the expressed isoform becomes functionally and clinically apparent and leads to disease. However, selectively switching on the genes of the silenced but homologous isoforms provides a means to substitute for the mutated gene and to cure the disease. Since many inherited retinal diseases are caused by mutations of genes that have functional equivalents, the aim in this study was to activate the healthy counterpart in affected cells.

To validate the approach *in vitro*, an immortalized cell line generated from murine cones (661W cell line), cells that normally lack CNGA1 expression, was used to test transcriptional activation of the *Cnga1* gene. Following transactivation, inside-out patch clamp experiments with these cells detected cyclic guanosine monophosphate (cGMP)-sensitive outwardly rectifying currents that were blocked by divalent cations – typical properties of currents through CNGA1 channels. These findings confirmed that the transactivation approach was successful. In another experiment conducted by participating researchers, the gene encoding the cone-specific M-opsin was transactivated *in vivo* in a rhodopsin-deficient mouse model (Rho $^{+/-}$) of retinitis

pigmentosa. This experiment revealed improved retinal function and attenuation of disease progression.
In this project, the transactivation induced expression of CNG channels was used as prove of principle to validate the method. Together, the successful transactivation of CNGA1 *in vitro* and M-opsin *in vivo* in mice suggested that this approach might also bear a very high potential for *in vivo* treatment of human degenerative diseases of the retina and beyond.

The remaining questions (2-4) were addressed by studying the functional properties of the channel isoforms HCN2 and HCN4.

The activity of HCN2 and HCN4 channels is markedly regulated by cytosolic cAMP levels. Binding of cAMP to the CNDB of HCN channels accelerates activation kinetics, decelerates deactivation kinetics, and shifts the half-maximal activation voltage ($V_{0.5}$) toward more depolarized potentials, effects referred to by the term CDR. The autonomic nervous system (ANS) determines intracellular cAMP levels and hence is a modulator of CDR. However, the functional relevance of CDR of HCN channels remained unclear.

To analyze this important issue we investigated the significance of cAMP modulation of HCN2 in thalamocortical neurons in a mouse model, lacking this feature, i.e., expressing cAMP insensitive HCN2EA channels. In this context, in **manuscript II**, the question of whether cAMP affects the maximum conduction of the channel was addressed with a planar patch-clamp experiment. Internal perfusion of flp-In-293 cells stably expressing HCN2 or HCN2EA channels revealed a similar current density in the presence or absence of the cyclic nucleotide once the channels are opened completely for both channel variants. This result indicated that cAMP has no effect on the maximum channel conductance and implied that cAMP increases the HCN current solely by elevating the number of open channels. Complementary to this important result, other members of the Wahl-Schott and Biel group have shown that the mutant HCN2 channel lacks a depolarizing shift of $V_{0.5}$ upon binding of cAMP and exhibits slower activation kinetics. Together, these altered features impaired the firing properties of thalamocortical neurons. In HCN2EA mice, this led to deficits in visual learning, generalized seizures of thalamic origin, and altered non-rapid eye movement (NREM) sleep properties.

Therefore, this work answered a long-standing question about cAMP-induced effects on HCN channel conductance. Furthermore, the publication suggests the HCN2 channel as molecular target to regulate firing in thalamocortical neurons, thereby expanding the range of proposed anti-epileptic drug strategies.

In **manuscript III** the physiological relevance of CDR of HCN4 in the sinoatrial node (SAN) was investigated. Mice expressing cAMP insensitive HCN4 channels (termed HCN4FEA channels) suffered from a severe cardiac phenotype clinically consistent with sick sinus syndrome. The molecular mechanism underlying this phenotype was investigated at the single cell level and the level of the sinoatrial network. Patch-clamp experiments obtained by me and complementary by other members of the group have shown that biophysical properties of the mutant channel lie between those of the wild-type (WT) channel without and with cAMP. Consequently, SAN cells in which binding of cAMP to HCN4 is abolished displayed pronounced pauses in firing, giving rise to bradycardia in isolated hearts and further arrhythmia such as isorhythmic AV dissociation and junctional escape rhythm *in vivo*. My investigations on the hysteresis behavior of HCN4 have shown that it contributes to switches between firing and non-firing in SAN cells by shifting the $V_{0.5}$ of HCN4. Determination of the spontaneous baroreceptor reflex using telemetric blood pressure and ECG recordings, a method that is the subject of **manuscript IV**, in mice expressing the cAMP-insensitive HCN4 channel revealed overshooting responses to parasympathetically induced heart rate (HR) changes (result obtained by another investigator of the study). Vagus nerve stimulation on isolated hearts that I performed confirmed increased responses to activity of the ANS. Compensatory mechanisms that might account for the phenotype were excluded with shared electrophysiological experiments and independent immunohistological/histological staining. Altogether, in this study the role of CDR of HCN4 in SAN cells was linked to the regulation of pauses and firing in individual cells and to sustain rhythmic activity of the heart during destabilizing activity of the ANS. Understanding the mechanisms involved in maintaining a stable HR may be valuable for developing future drug therapy.

Zusammenfassung

Die vorliegende Arbeit befasst sich mit spannungsgesteuerten Ionenkanälen (VGIC), die zusätzlich durch die Bindung von zyklischen Nukleotiden an eine zyklische Nukleotidbindungsdomäne (CNBD) gesteuert werden. Die beiden untersuchten Kanalfamilien sind zyklische Nukleotid-gesteuerte (CNG) und Hyperpolarisations-aktivierte zyklische Nukleotid-gesteuerte (HCN) Kanäle. Dabei wurden die folgenden Fragen mit elektrophysiologischen Methoden untersucht: (1) Können spezifische CNG-Ströme in Zellen ohne endogene CNG-Kanalexpression gemessen werden, nachdem das Gen, das für CNGA1 kodiert, mit einer neuartigen Genaktivierungsmethode eingeschaltet wurde? (2) Erhöht zyklisches Adenosinmonophosphat (cAMP) die maximale Leitfähigkeit von HCN-Kanälen? (3) Welche physiologische Rolle spielt die cAMP-abhängige Regulation (CDR) von HCN4 bei der sinuatrialen Schrittmacherfunktion und (4) wie trägt das Hysterese-Verhalten von HCN4 dazu bei?

In **Manuskript I** wurde ein Gen-Editierungs-Ansatz mit katalytisch inaktivem Cas9 (dCas9) zur Aktivierung von Genen verwendet. Die Methode macht sich die Existenz von Gen-Isoformen im Genom zunutze. Diese Gene kodieren für Protein-Isoformen mit nahezu identischer Funktion. Wichtig ist, dass die Expression von Protein-Isoformen zellspezifisch ist. Eine bestimmte Zelle exprimiert beispielsweise nur eine Isoform, während die Gene für die anderen Isoformen still sind. Folglich wird eine Loss-of-function-Mutation des Gens, das für die exprimierte Isoform kodiert, funktionell und klinisch sichtbar und führt zu Krankheiten. Das selektive Einschalten der Gene stiller, aber homologer Isoformen bietet jedoch die Möglichkeit, das mutierte Gen zu ersetzen und die Krankheit zu heilen. Da viele erbliche Netzhauterkrankungen durch Mutationen von Genen verursacht werden, die funktionelle Äquivalente haben, bestand das Ziel dieser Studie darin, das gesunde Gegenstück in den betroffenen Zellen zu aktivieren. Zur Validierung des Ansatzes *in vitro* wurde eine immortalisierte Zelllinie aus Mäusezapfen (661W-Zelllinie), Zellen, die normalerweise keine CNGA1-Expression aufweisen, verwendet, um die transkriptionelle Aktivierung des *Cnga1*-Gens zu testen. Nach der Transaktivierung wurden in Inside-Out-Patch-Clamp-Experimenten mit diesen Zellen für zyklisches Guanosinmonophosphat (cGMP) empfindliche, nach außen gleichrichtende Ströme nachgewiesen, die durch zweiwertige Kationen blockiert wurden – typische Eigenschaften von Strömen durch CNGA1-Kanäle. Diese Ergebnisse bestätigten, dass der Transaktivierungsansatz erfolgreich war. In einem

weiteren von beteiligten Forschern durchgeführten Experiment wurde das Gen, das für das zapfenspezifische M-Opsin kodiert, in einem Rhodopsin-defizienten Mausmodell (Rho $^{+/-}$) für Retinitis pigmentosa *in vivo* transaktiviert. Dieses Experiment zeigte eine verbesserte Netzhautfunktion und eine Abschwächung des Fortschreitens der Krankheit.
In diesem Projekt wurde die durch Transaktivierung induzierte Expression von CNG-Kanälen als Grundsatzbeweis für die Validierung der Methode verwendet. Die erfolgreiche Transaktivierung von CNGA1 *in vitro* und von M-Opsin *in vivo* bei Mäusen deutet darauf hin, dass dieser Ansatz auch für die *In-vivo*-Behandlung von degenerativen Erkrankungen der Netzhaut beim Menschen und darüber hinaus ein sehr hohes Potenzial besitzt.

Die verbleibenden Fragen (2-4) wurden durch die Untersuchung der funktionellen Eigenschaften der Kanalisoformen HCN2 und HCN4 beantwortet.

Die Aktivität von HCN2- und HCN4-Kanälen wird deutlich durch den zytosolischen cAMP-Spiegel reguliert. Die Bindung von cAMP an die CNDB von HCN-Kanälen beschleunigt die Aktivierungskinetik, verlangsamt die Deaktivierungskinetik und verschiebt die halbmaximale Aktivierungsspannung ($V_{0.5}$) in Richtung depolarisierterer Potenziale, Effekte, die mit dem Begriff CDR bezeichnet werden. Das autonome Nervensystem (ANS) bestimmt den intrazellulären cAMP-Spiegel und ist somit ein Modulator der CDR. Die funktionelle Bedeutung der CDR von HCN-Kanälen blieb jedoch unklar.

Um diese wichtige Frage zu analysieren, untersuchten wir die Bedeutung der cAMP-Modulation von HCN2 in thalamokortikalen Neuronen in einem Mausmodell, dem diese Eigenschaft fehlt, d.h. in dem cAMP-unempfindliche HCN2EA-Kanäle exprimiert werden. In diesem Zusammenhang wurde in **Manuskript II** die Frage, ob cAMP die maximale Leitfähigkeit des Kanals beeinflusst, mit einem planaren Patch-Clamp-Experiment untersucht. Die interne Perfusion von flp-In-293-Zellen, die HCN2- oder HCN2EA-Kanäle stabil exprimieren, ergab für beide Kanalvarianten eine ähnliche Stromdichte in Gegenwart oder Abwesenheit des zyklischen Nukleotids, sobald die Kanäle vollständig geöffnet sind. Dieses Ergebnis deutet darauf hin, dass cAMP keine Auswirkung auf die maximale Kanalleitfähigkeit hat und impliziert, dass cAMP den HCN-Strom ausschließlich durch die Steigerung der Anzahl der geöffneten Kanäle erhöht. Ergänzend zu diesem wichtigen Ergebnis haben andere Mitglieder der Gruppe

von Wahl-Schott und Biel gezeigt, dass der mutierte HCN2-Kanal keine depolarisierende Verschiebung von $V_{0.5}$ nach Bindung von cAMP aufweist und eine langsamere Aktivierungskinetik zeigt. Zusammengenommen beeinträchtigen diese veränderten Merkmale die Feuereigenschaften thalamokortikaler Neurone. Bei HCN2EA-Mäusen führte dies zu Defiziten beim visuellen Lernen, zu generalisierten Anfällen thalamischen Ursprungs und zu veränderten Eigenschaften des non-rapid eye movement-(NREM)-Schlafs.
Diese Arbeit beantwortete somit eine seit langem bestehende Frage über die cAMP-induzierten Auswirkungen auf die HCN-Kanalleitfähigkeit. Darüber hinaus deutet die Publikation auf den HCN2-Kanal als molekulares Ziel zur Regulierung des Feuerns in thalamokortikalen Neuronen hin und erweitert damit das Spektrum der vorgeschlagenen Antiepileptika-Strategien.

In **Manuskript III** wurde die physiologische Bedeutung der CDR von HCN4 im sinuatrialen Knoten (SAN) untersucht. Mäuse, die cAMP-unempfindliche HCN4-Kanäle (so genannte HCN4FEA-Kanäle) exprimierten, litten an einem schweren kardialen Phänotyp, der klinisch mit dem Sick-Sinus-Syndrom übereinstimmt. Der molekulare Mechanismus, der diesem Phänotyp zugrunde liegt, wurde auf der Ebene einzelner Zellen und auf der Ebene des sinuatrialen Netzwerks untersucht. Patch-Clamp-Experimente, die ich selbst durchgeführt habe und die von anderen Mitgliedern der Gruppe ergänzt wurden, haben gezeigt, dass die biophysikalischen Eigenschaften des mutierten Kanals zwischen denen des Wildtyp (WT)-Kanals ohne und mit cAMP liegen. Folglich zeigten SAN-Zellen, in denen die Bindung von cAMP an HCN4 aufgehoben ist, ausgeprägte Pausen beim Feuern, die in isolierten Herzen zu Bradykardie und *in vivo* zu weiteren Arrhythmien wie isorhythmischer AV-Dissoziation und junktionalem Ersatz-Rhythmus führten. Meine Untersuchungen des Hysterese-Verhaltens von HCN4 haben gezeigt, dass es zum Wechsel zwischen Feuern und Nichtfeuern in SAN-Zellen beiträgt, indem es $V_{0.5}$ von HCN4 verschiebt. Die Bestimmung des spontanen Barorezeptorreflexes mittels telemetrischer Blutdruck- und EKG-Aufzeichnungen, eine Methode, die Gegenstand von **Manuskript IV** ist, in Mäusen, die den cAMP-unempfindlichen HCN4-Kanal exprimieren, ergab überschießende Reaktionen auf parasympathisch induzierte Herzfrequenz-(HR)-Änderungen (Ergebnis eines anderen Forschers der Studie). Die von mir durchgeführte Stimulation des Vagusnervs an isolierten Herzen bestätigte erhöhte Reaktionen auf die Aktivität des ANS. Kompensatorische Mechanismen, die den

Phänotyp erklären könnten, wurden durch gemeinsame elektrophysiologische Experimente und eigenständige immunhistologische/histologische Färbungen ausgeschlossen. Insgesamt wurde in dieser Studie die Rolle der CDR von HCN4 in SAN-Zellen mit der Regulierung der Pausen und des Feuerns in einzelnen Zellen und mit der Aufrechterhaltung der rhythmischen Aktivität des Herzens bei destabilisierender Aktivität des ANS in Verbindung gebracht.

Das Verständnis der Mechanismen, die an der Aufrechterhaltung einer stabilen Herzfrequenz beteiligt sind, könnte für die Entwicklung künftiger medikamentöser Therapien von Nutzen sein.

4 Introduction

In 1952 the groups of Hodgkin, Huxley and Katz, discovered that voltage-dependent sodium and potassium currents underlie the action potential of the squid giant axon [1-5]. This discovery represents a milestone in the field of ion channel research and was awarded the Nobel Prize in Physiology or Medicine in 1963. Although the idea that channels form pores that allow ions to permeate biological membranes can be tracked back to the 1950s [6], their existence was not proven until 20 years later with single channel patch-clamp recordings [7]. This achievement of Neher and Sakmann was also honoured with the Nobel Prize in Physiology or Medicine in 1991. Another breakthrough in ion channel research was achieved in 1998 when the first 3D X-ray structure of an ion channel, namely the prokaryotic potassium channel KcsA [8], was resolved by the group of MacKinnon. This provided fundamental insights into the mechanisms of ion selectivity and ion conduction not only of this channel but of the entire family of voltage-gated ion channels (VGICs). Due to the significance of these pioneering findings MacKinnon was awarded the Nobel Prize in the category of chemistry. To date, VGICs have been studied extensively. These channels form a large protein superfamily currently comprising more than 140 members [9], of which three subfamilies carry the motif for direct binding of cyclic nucleotides such as cyclic adenosine monophosphate (cAMP) or cyclic guanosine monophosphate (cGMP) (Figure 1).

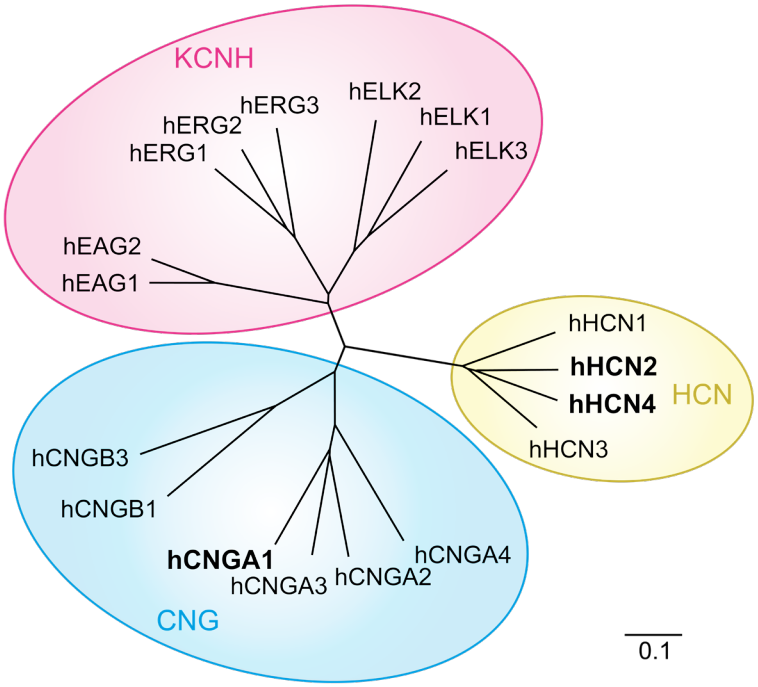

Figure 1 | Phylogenetic tree of cyclic nucleotide-binding domain (CNBD) containing voltage-gated cation channels. The protein sequences underlying this phylogenetic tree were taken from NCBI database, aligned with clustal omega multiple sequence alignment tool and visualized with dendroscope software [10]. The members of the three CNBD containing subfamilies of VGICs (CNG, HCN and KCNH) are closely related. The channel isoforms that are the subject of this dissertation and the publications on which this dissertation is based are highlighted in bold.

The cyclic nucleotide-binding domain (CNBD) containing subfamilies are the voltage-gated potassium channel, subfamily H (KCNH), cyclic nucleotide-gated (CNG) and hyperpolarization-activated cyclic nucleotide-gated (HCN) channel families. Binding of cyclic nucleotides to their CNBD induces conformational changes that facilitate channel opening. However, in KCNH channels this binding site is named cyclic nucleotide-binding homology domain (CNBHD). Their channel structure includes an intrinsic ligand formed by a conserved additional β-strand in the CNBHD of the channel protein. The aromatic amino acid residues tyrosine or phenylalanine as well as leucine within this β-strand occupy important binding sites to which cAMP normally attaches [11]. This sterically precludes ligand binding and supposedly restricts cAMP-dependent regulation (CDR) of KCNH channels to cAMP-dependent protein kinase A (PKA) mediated effects, which reduce current amplitudes and accelerate deactivation kinetics of these channels, i.e., are inhibitory [12-16]. Although being structurally closely related, the biophysical properties and physiological roles of CNBD containing VGICs differ markedly.

In the present dissertation, I have investigated the function of CNG and HCN channels. In the following I will describe the different expression patterns as well as structural and functional properties of these channels that lead to their different physiological roles.

4.1 Expression pattern of CNG and HCN channels

To date, six vertebrate isoforms of CNG channels (CNGA1-4, CNGB1 and CNGB3) and four mammalian isoforms of HCN channels (HCN1-4) are known [17,18]. There are two splice variants for the CNGB1 isoform, the longer CNGB1a and the shorter CNGB1b variant [19,20]. CNG and HCN channels are expressed primarily in the sensory system, central nervous system (CNS), and heart.

4.1.1 Expression in the sensory system and CNS

CNG channels are expressed in the visual and olfactory system (Figure 2A). Within the visual system, they are expressed in the specialized sensory neurons of the retina (photoreceptors), which are rods and cones. In rods CNGA1 and CNGB1a subunits are expressed, whereas in cones the isoforms CNGA3 and CNGB3 are found [21,22]. In these cells, hetero-tetrameric CNG channels localized at the discs of rods and the lamellae of cones in the outer segments (OS) conduct an inward current that is reduced by a signalling cascade induced by incoming photons. Therefore, they translate the perception of light into a change in the electrical signal [23].

At the roof of the nasal cavity, CNG channels are expressed in the sensory neurons of the olfactory epithelium (Figure 2A). The olfactory CNG channels, localized at the cilia of olfactory sensory neurons (OSN), consist of the subunits CNGA2, CNGA4 and CNGB1b [24,25]. Binding of odorant molecules to their ciliary receptor triggers a G-protein-mediated signalling cascade that opens CNG channels, causing an inward flow of cations and thereby depolarization of the cells. The signal is then transmitted to the CNS [26]. Thus, CNG channels also play an important role in odour perception.

Furthermore, CNG channel variants have been identified in inner and outer hair cells of the cochlea and in taste buds. However, their functional importance in these tissues is not well understood yet [27-31]. In addition to sensory tissues, the presence of CNG channels has been detected in cells of, e.g., the kidney, testis, and brain [32,33].

All four HCN isoforms are expressed in cells of the olfactory bulb [34] and the retina [35]. HCN channels in the olfactory bulb are essential to glomerular formation [36,37]. In retinal photoreceptors, HCN1-3 are expressed and localized in the inner segments (IS), somata, axons, and pedicles [35,38]. HCN1 has been found to contribute to the light response of rods and cones [38-40]. Photosensitive retinal ganglion cells have been shown to have an HCN-mediated phototransduction pathway involving HCN4 channels [41]. Additionally, HCN1 channels have been shown to play a role for the sense of balance and acoustic perception, due to expression in hair cells and spiral ganglion neurons in the cochlea [42,43]. Furthermore, a contribution of HCN1 and HCN4 in the perception of sour taste in taste buds has been discovered [44,45]. In general, however, the role of HCN channels in sensory perception is rather modest or poorly studied.

Within the CNS, HCN1-4 are expressed [46]. HCN2, for example, is expressed almost ubiquitously in the brain and has high expression levels in the thalamus (Figure 2B), which includes the dorsolateral geniculate nucleus (dLGN). This structure represents the main thalamic relay station, where visual input from the primary visual pathway is forwarded to the visual cortex [47]. The ventrobasal (VB) complex is the main relay nucleus of the thalamus for somatosensory and gustatory stimuli, coexpressing HCN2 and HCN4 [47,48]. Comparable HCN expression is reported from the major thalamic auditory-responsive part, the medial geniculate nucleus (MGN) [49,50].

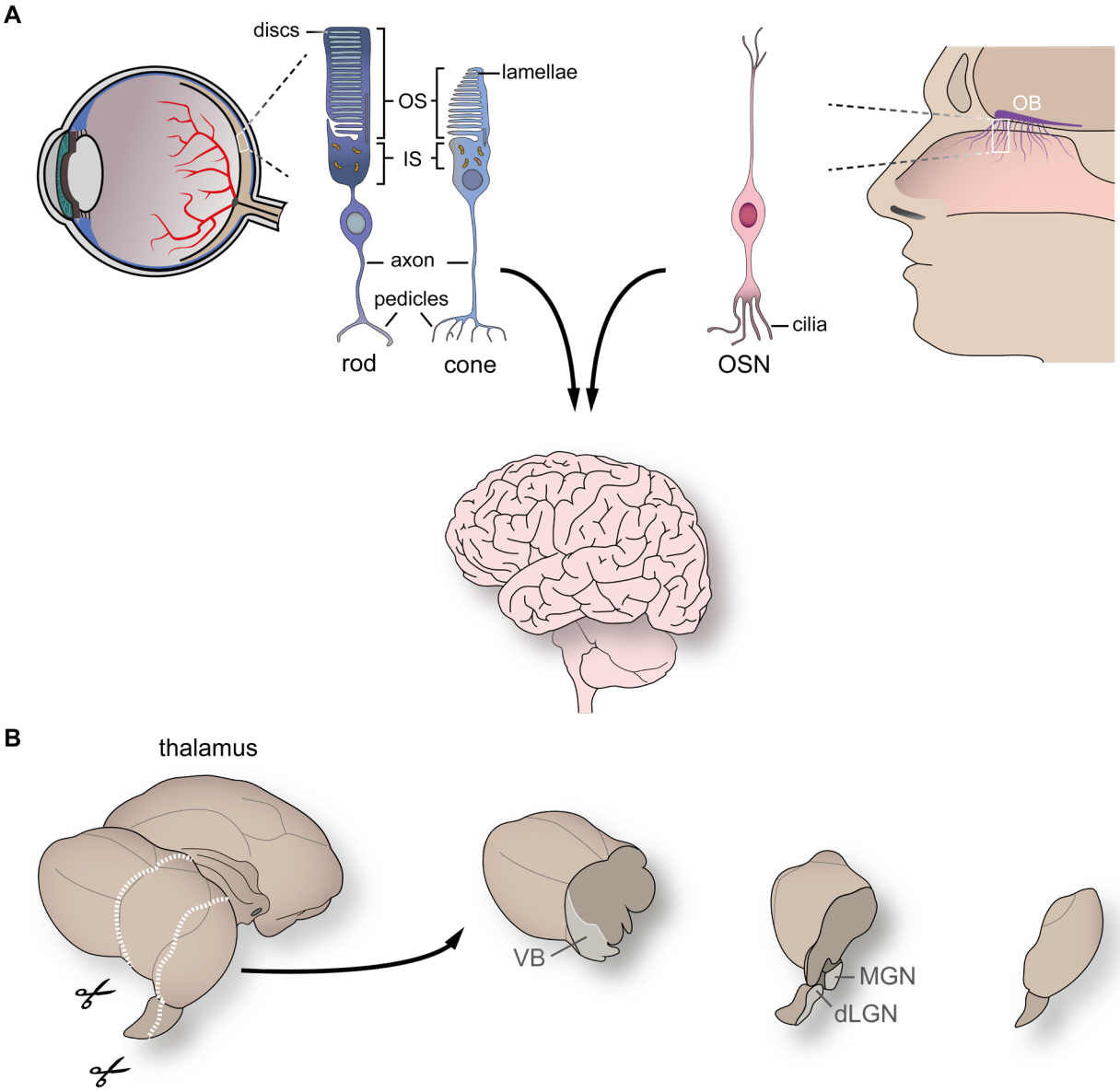

Figure 2 | Sensory and CNS structures in which CNG and HCN channels play an important role. **(A)** Rods and cones are retinal photoreceptors. CNG channels are localized in their outer segments (OS). More precisely, they are located at the discs of rods and the lamellae of cones [23]. HCN channels are localized in the inner segments (IS), somata, axons, and pedicles [35,38]. Another tissue involved in sensory perception is the olfactory epithelium at the roof of the nasal cavity. It contains the cilia of the olfactory sensory neurons (OSN), which have CNG channels in their membrane. The OSN axons connect to the olfactory bulb (OB), a neuronal structure whereupon the primary olfactory pathway begins. Electrical signals generated in photoreceptors and OSNs are transmitted to the CNS (black arrows) and processed in various brain regions that require HCN channels for proper function, e.g. thalamus, hippocampus and hypothalamus [46,51]. **(B)** The thalamus contains relay nuclei that are involved in visual, somatosensory, gustatory, and auditory information processing. Coronal sections (dashed white lines) reveal the dorsolateral geniculate nucleus (dLGN), ventrobasal (VB) complex, and medial geniculate nucleus (MGN).

4.1.2 Expression in the heart

HCN channels are highly expressed in the cells of the cardiac conduction system (CCS) within the heart. Because of their unique ability to fire action potentials spontaneously, cells of the CCS are also referred to as pacemaker cells. Since HCN channels conduct a depolarizing current that contributes to the ability of these cells to trigger spontaneous action potentials, they are also termed pacemaker channels. The CCS is organized hierarchically (Figure 3). The sinoatrial node (SAN) is the initiator of the electrical impulse needed for excitation and contraction of the myocardium and is the primary instance of the CCS. The SAN can be further subdivided into a head, body, and tail region. In all mammals studied to date, HCN4 is the predominant isoform and is expressed throughout the SAN. In human SAN, also HCN1 and HCN2 are present without restriction of the individual isoforms to specific areas within the SAN [52]. In mouse SAN, HCN4 is expressed throughout the SAN whereas HCN1 is restricted to the head region [53,54] and HCN2 is only present in very low amounts in the periphery of the SAN [55]. Functional studies in mice have shown that HCN4 mediates the major fraction of the sinoatrial pacemaker current, approximately 70%, and that HCN1 accounts for the remaining 30% of the current [54,56]. HCN2 channels play a rather minor role in the primary pacemaker activity of mouse SAN cells.

The electrical excitation generated in pacemaker cells exits the SAN, spreads rapidly across the atria, and reaches the atrioventricular node (AVN), a bottleneck that builds the only electrically conductive connection between the atria and the ventricles [57]. From there, the signal travels to the bundle of His, and via the right and left bundle branches to the Purkinje fibers, the most subordinate functional units of the CCS. Lower portions of the CCS characteristically also show expression of HCN channels, notably HCN1 and HCN4 [55,58]. The only isoform absent in the CCS is HCN3.

The working myocardium of the atria and ventricles is not capable of generating spontaneous action potentials, yet the presence of low amounts of pacemaker channels have been reported. In atrial tissue surrounding the SAN and in ventricle HCN2 and HCN4 were detected in mouse, dog and human [52,59,60]. In mice, HCN3 is also found in the working myocardium of the atria and ventricles serving as a source for a depolarizing background current [61].

For CNG channels, only low expression of CNGA3 was reported in rabbit atrium and ventricle, however no further investigations were done so far [62].

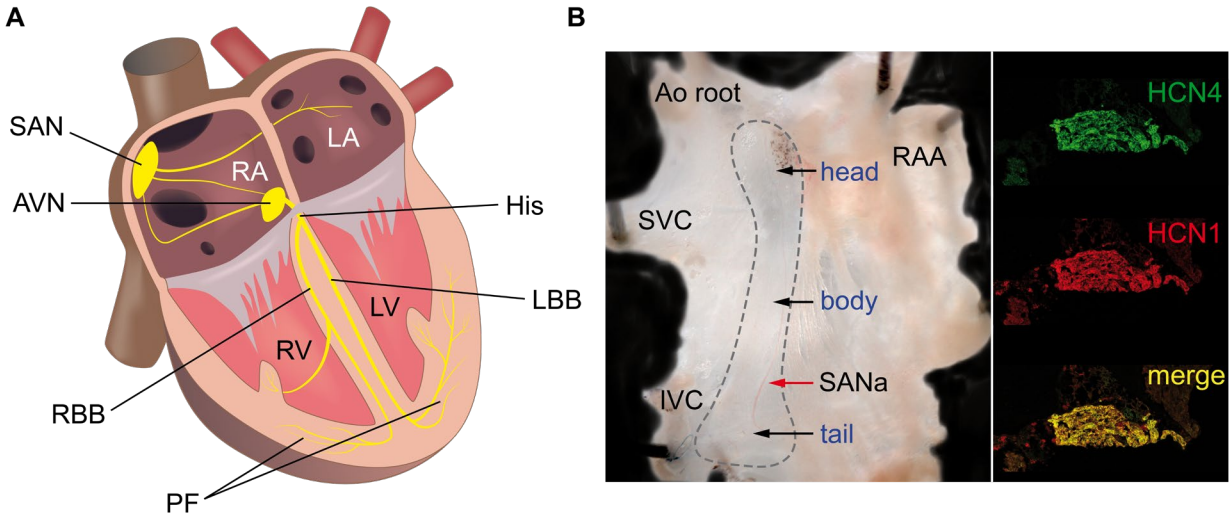

Figure 3 | HCN channel expression in cardiac tissue. (A) Schematic coronal section of a heart showing the CCS (yellow). The primary excitation site is located in the sinoatrial node (SAN). The atrioventricular node (AVN) is the secondary instance of the CCS and the only electrically conductive connection between the atria and the ventricles. Connected to the AVN, the His bundle (His) splits into a left and right bundle branch (LBB; RBB), which divide to form the left and right Purkinje fiber (PF) network. **(B)** Murine right atrial tissue preparation containing the SAN region (left panel, area indicated by gray dashed line). The SAN can be divided into head, body, and tail areas. Cross sections of the head region (right panel) show expression of HCN4 (green) and HCN1 (red) isoforms. The merged image (yellow) indicates that both isoforms are expressed in the same region. Additional abbreviations: Ao root; aortic root; IVC, inferior vena cava; LA, left atrium; LV, left ventricle; RA, right atrium; RAA, right atrial appendage; RV, right ventricle; SANa, sinoatrial nodal artery; SVC superior vena cava. Figure A adapted from [57].

4.2 Structural comparison of CNG and HCN channels

X-ray crystallography was the pioneering technique for resolving 3D atomic structures of proteins, but it is increasingly being replaced by cryo-electron microscopy (cryo-EM). On average, cryo-EM currently reveals structures with a resolution of less than 5 ångströms [63].

Macroscopic architecture is the same for CNG and HCN channels: Four subunits assemble as a tetramer around a central pore. The complex is incorporated into the membrane, generating functional ion-conducting elements [26,64] (Figure 4).

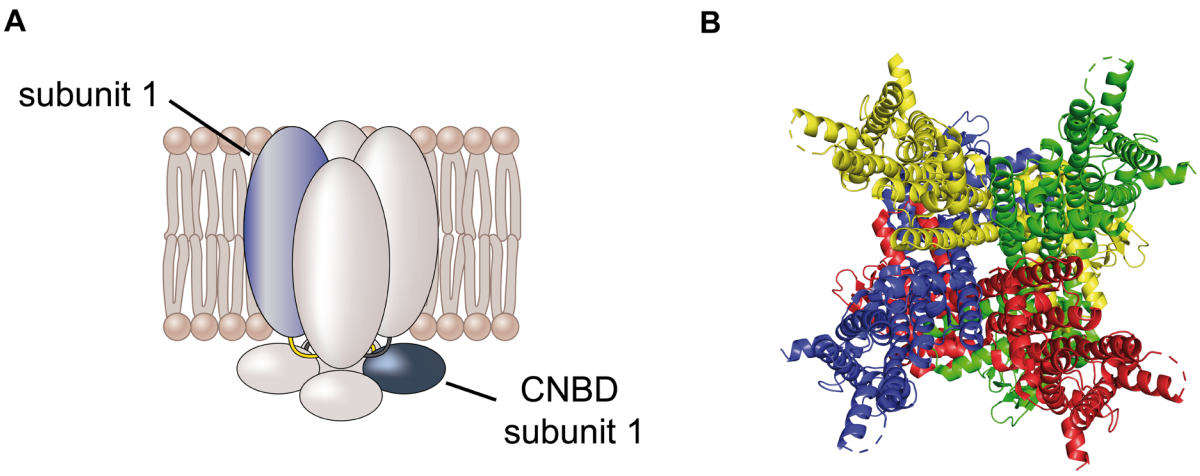

Figure 4 | Tetrameric channel structure of CNG and HCN channels. (A) Schematic representation of a tetrameric, cyclic nucleotide-binding domain (CNBD) containing channel. Four channel subunits build a tetrameric complex with a central pore. The complex is incorporated into the membrane, allowing the permeation of ions. The CNBD of subunit 1 is located in the cytosol, opposite to its membrane-bound counterpart. **(B)** The top view of a modelled structure based on the human HCN1 channel cryo-EM structure (PDN #5U6P) reveals the ion conductive pathway in the middle of the complex.

The A1-3 subunits of the CNG family are capable of forming functional homo-tetrameric channels in heterologous expression systems. The CNGA4 and the B subunits are unable to do so, and therefore these subunits are thought to be modulatory [65]. In native tissues, CNG channels form hetero-tetrameric complexes with a subunit composition characteristic of different cell populations [21,22,24,25]. All HCN isoforms can assemble as functional homomeric channels, but in cells expressing more than one HCN isoform, heteromerization also occurs [66].

Elucidating the cryo-EM structure of the human HCN1 channel in the unbound and bound state of cAMP had wide-reaching impact on the field, as for the first time cAMP induced conformational changes could be clearly identified [67]. Currently, no mammalian CNG 3D atomic structure is available. However, the structure of the eukaryotic CNG channel TAX-4 from *C. elegans* has been resolved in the cGMP-bound state and only recently complemented with a cGMP-unbound structure [68,69]. In the following section, the structure details of the CNG channels refer to the structure of TAX-4.

The principle structure of a single CNG or HCN subunit is similar to other VGICs (Figure 5). The channel core region is the transmembrane domain (TMD), which is formed by six alpha-helical transmembrane segments (S1-S6). S1-S4 build the voltage

sensing domain (VSD) whereof S4 constitutes the voltage sensor containing multiple positively charged amino acids, i.e., arginine and lysine. In VGICs, changes in membrane potential cause the sensor segment to undergo transmembrane movement due to electrostatic forces, which triggers conformational changes that open or close the channel pore [70]. HCN channel opening is induced by hyperpolarization and not depolarization, which is unique among VGICs. Despite having a similar structure, CNG channels respond barely to voltage changes. The S4-S5 linker connects the VSD to the pore domain (PD), which comprises segments S5 and S6. The loop between the two pore segments is called pore-loop. It contains the selectivity filter, a characteristic sequence of amino acids that determines the ions able to pass the pore. The VSD and PD of a CNG or HCN channel subunit are in close proximity to each other due to a short S4-S5 linker, thus interactions between these domains occur within the respective subunit (Figure 5C). This is referred to as a non-domain swapped architecture and distinguishes them from many other VGICs with swapped-domain interactions, e.g., K_v1-7, Na_v and Ca_v channels (Figure 5D). A swapped-domain architecture is enabled by a long α-helical S4-S5 linker that creates space occupied by the PD of an adjacent subunit in a tetrameric setup, causing the VSD to interact with the "swapped" PD [68,71-73]. The N- and C-termini of the subunits are exposed to the cytosol.

Another structural feature shared by CNG and HCN channels is the presence of a CNBD in the C-terminus, which is connected to the end of S6 via the C-linker. The C-linker consists of six α-helices (A'-F'). The CNBD is attached to it and begins with one α-helix (A), continues with eight β-strands forming an antiparallel β-roll, and ends with two further α-helices (B and C).

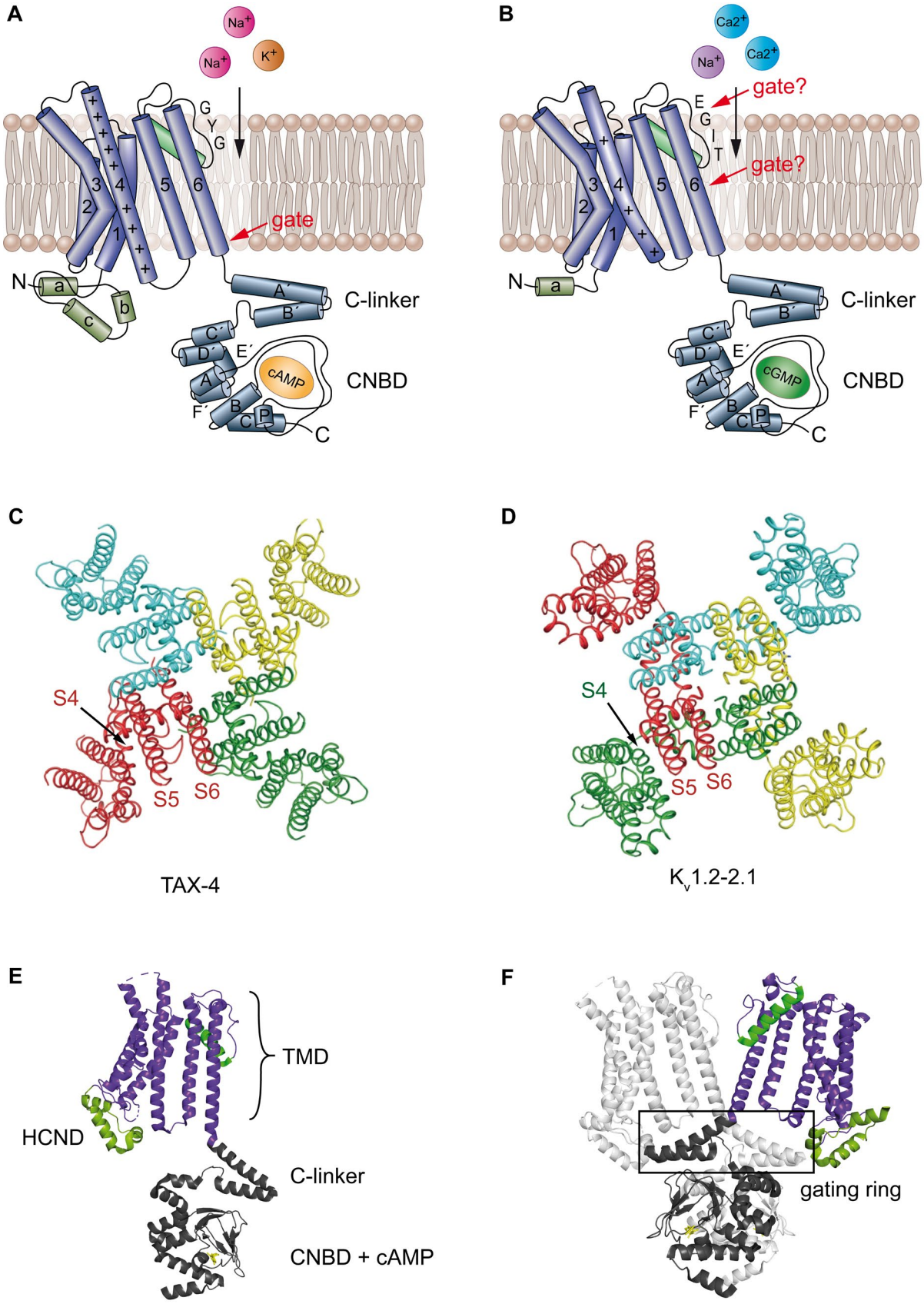

Figure 5 | CNG and HCN channel subunit structure. (A) Schematic representation depicting a simplified structure of a single HCN subunit. The N-terminal part contains the HCN domain (HCND, helices a, b and c) connected to the transmembrane domain (TMD) containing six segments (S1-S6).

(Figure 5 continued) Segments S1-S4 form the VSD with the long S4 representing the actual voltage sensor. Positively charged amino acids (arginine and lysine) regularly distributed within the S4 enable it to sense changes in the transmembrane voltage, which in turn translate into movements of the VSD. The S4-S5-linker couples the VSD to the PD (S5 and S6) that contains the pore loop and the selectivity filter between S5 and S6. The selectivity filter of HCN channels carries the characteristic GYG-motif known from potassium-selective channels. Nevertheless, the channels conduct Na^+ and K^+ due to a different conformation. At the C-terminal end of S6 the gate is located which closes the pore in the depolarized state and opens upon hyperpolarization. The C-linker is attached to the TMD and connects the binding region for cAMP (CNBD) with the S6. The main differences between HCN and CNG channels can be summarized as follows and depicted in **(B)**: CNG channels do not host the HCND in their N-terminus, they have a shorter S4 segment with less, rather accumulating positive charges and their selectivity filter carries the sequence TIGE allowing the flow of mainly Ca^{2+} and Na^+ ions under physiological conditions. Furthermore, the inner gate present in HCN channels is missing. **(C)** In the non-domain swapped subunit architecture of TAX-4 channels (and also HCN channels) the S4 contacts the PD of the very same subunit. **(D)** The domain-swapped arrangement of, e.g., K_V1-7 subunits is enabled by a longer S4-S5 linker. S4 interacts with the PD of an adjacent subunit. **(E)** The simplified structure of (A) modelled from the published cryo-EM structure of HCN1 in complex with cAMP (PDB #5U6P). The arrangement with other subunits **(F)** shows the gating ring formed by the A' and B' helices of the C-linkers, which undergoes important movements during gating (for clarity two subunits are hidden). Figure A adapted from [57]. Figures C and D adapted from [68].

The CNBDs of both channel families show sequence homology to the CNBDs of the catabolite activator protein (CAP) of Escherichia coli and the cAMP- and cGMP-dependent protein kinases (PKA and PKG, respectively), thus binding sites for cyclic nucleotides are highly conserved within cyclic nucleotide binding proteins [67,74-82]. cAMP binds in the *anti*-configuration, whereas cGMP binds in the *syn*-configuration to the CNBD (Figure 6) [76,83]. The phosphate, purine ring and phosphoribose of the cyclic nucleotides are involved in interactions with the β-roll, P-helix and C-helix of the channel [26]. An arginine (R559 in bovine CNGA1, R591 in murine HCN2, and R669 in murine HCN4) and threonine (T560, T592, and T670 respectively) between the β-strands 2 and 3 of the CNBD are crucial binding residues that interact with cAMP or cGMP [83,84]. Mutation of the arginine to glutamine or glutamate and/or mutation of the threonine to alanine completely disrupts channel modulation by cyclic nucleotides [53,85,86].

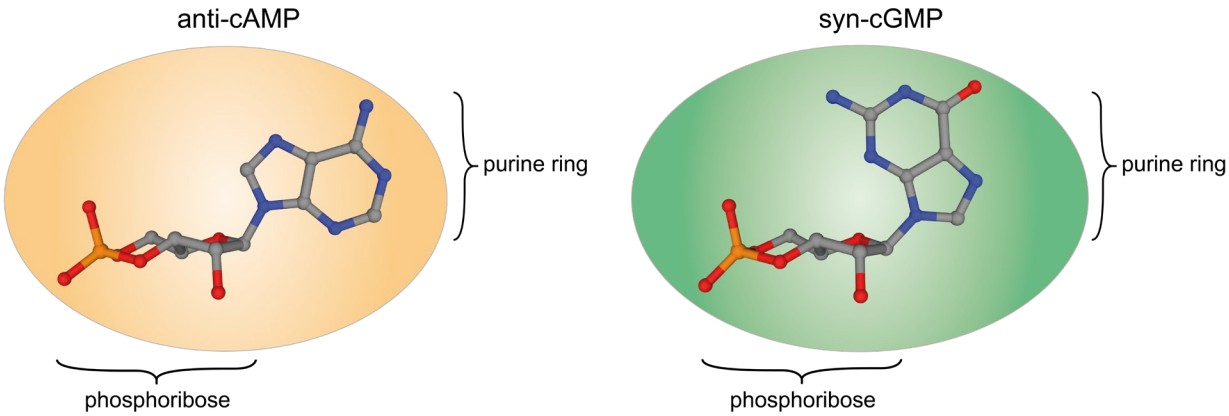

Figure 6 | Differences in binding conformations of cAMP and cGMP to the CNBD. Binding to the CNBD occurs in the *anti*-configuration for cAMP and *syn*-configuration for cGMP. The phosphate, purine ring and phosphoribose of the cyclic nucleotides interact with the β-roll, P-helix and C-helix of the CNBD. Gray: carbon; red: oxygen; blue: nitrogen; orange: phosphate.

In addition to the many structural similarities, there are also differences between the two channel families that are of particular interest in the question of why HCN channels are controlled in a voltage-dependent manner, whereas CNG channels are considered to be rather voltage-independent [87,88]. The N-terminus of HCN channels hosts a conserved structure termed the HCN domain (HCND) that precedes the S1 segment (Figure 5A and E). It consists of three α-helices squeezed between the VSD and the C-terminal part and is absent in CNG channels [67]. A recent study highlights that the HCND couples cyclic nucleotide- and voltage-dependent gating by conserved, direct interactions with the VSD and the C-linkers, which together create an electro-mechanical continuum [89].

Moreover, the voltage sensor of HCN channels has nine regularly distributed, positively charged amino acids [67], whereas in CNG channels the S4 seems to be segmented, with charges accumulating towards the C-terminal end of the sensor (Figure 5A and B) [68]. This could explain why it is not able to sense the transmembrane potential throughout the membrane and thus is poorly voltage gated [68]. Furthermore, the length of the HCN S4 is longer compared to other VGICs, potentially contributing to the reversed polarity of HCNs. Due to its length, it can contact the C-linker already in the depolarized conformation and thus stabilize the closed gate, whereas the shorter voltage sensors of other VGICs require an inward movement towards the cytosol induced by hyperpolarization for this contact [67,90].

Apart from the structural distinctions explaining the voltage sensitivity or insensitivity of HCN and CNG channels respectively, another major difference is found in the selectivity filters (Figure 5A and B). Both channels are non-selective cation channels, with HCN channels having the highest permeability for monovalent ions [46] and CNG channels for divalent ions [87]. The selectivity filter of HCN channels contains the GYG motif known from potassium selective ion channels. However, orientation of the tyrosine is significantly different rendering it also to be permeable for Na^+ [67]. Carbonyl oxygen atoms of the main chain, which would form two ion binding sites to coordinate K^+ ions, are no longer facing the ion conducting pathway, resulting in a selectivity filter in HCN channels that preserves only two of four binding sites [67,91]. The conserved amino acid sequence forming the selectivity filter in CNG channels is TIGE with the glutamic acid (E) as the narrowest constriction of the whole ion conducting path in the open state of TAX-4 [68]. Thus, the filter region is also thought to be the gate of CNG channels. Accessibility experiments confirmed this assumption. Intracellularly applied Cd^{2+} or Ag^+ could interact with the external end of a cysteine-containing CNG selectivity filter only in the open channel state, whereas the internal part of the filter was also accessible in the closed channel state [92]. However, recently it was shown that this constriction is almost unaffected by cGMP binding/unbinding in TAX-4 and two other amino acids below the selectivity filter build a gate in the cGMP unbound state that is relieved upon binding (Figure 5B) [69]. Whether structural differences between vertebrate CNG and TAX-4 channels account for this discrepancy remains to be resolved. Other VGICs, including HCN channels, are believed to have their gate at the cytosolic end of S6 (Figure 5A). Structural analysis and cysteine modification experiments are in agreement that this inner gate is missing in CNG channels [67,69,92].

Gating of ion channels generally is achieved by relaxation of the pore due to altered conformations and interactions following voltage changes or ligand binding. The bundle of the S6 segments is densely packed in the closed state and stabilized by the gating ring, formed by the A' and B' helices of the four subunits (Figure 5F). In CNG channels, upon cyclic nucleotide binding, the CNBD contracts, C-terminal structures undergo an upward movement towards the membrane paralleled by a rotation of the gating ring and finally the lower end of the S6 segment connected to the A' helix expands significantly, opening the gate of the pore [69]. A similar mechanism is observed in cAMP induced conformational changes in HCN1, however, the rotation of the A' helix and concomitant displacement of the S6 is much smaller, favoring pore opening

but not sufficient on its own [67,69]. In contrast, voltage gating is more relevant in HCN channels compared to CNG channels due to the reasons mentioned above (transmembrane potential sensing S4 and the electro-mechanical continuum built by the HCND, VSD and the C-linkers). Furthermore, close contacts between S4, S5 and S6 were reported in HCN channels, and it was hypothesized that these interactions directly translate changes in the electrical field onto the pore, stabilizing a closed pore in the depolarized state and vice versa enabling an open pore with hyperpolarization. The S5-S6 helices were shown to be densely packed and stabilized by lateral S4-S5 contacts. Additional lateral pressure on the cytosolic end of the S4 helix by the HCND possibly pushes it together with the whole bundle of S4-S6 towards the pore, which ultimately stabilizes the channel in the closed state when depolarized. The cytosolic displacement of S4 upon hyperpolarization releases this compression [67]. S4-S5 interactions were also shown to play a role in the reversed gating in HCN channels [93].

4.3 Biophysical properties of CNG and HCN channels

Due to the presence of a CNBD both ion channels share sensitivity to cyclic nucleotides of which cAMP and cGMP have most physiological relevance. Ligand binding is required and sufficient for CNG channels, but not HCN channels, to open.

The native ligand of the olfactory CNG channel is cAMP [94]. There are a few specialized OSNs that express a cone type CNG channel and are gated by cGMP [87]. Retinal photoreceptors express a channel that is gated by cGMP *in vivo* [23]. However, CNG variants are ~35-fold more sensitive to cGMP than to cAMP [85]. The relative permeability sequence for monovalent alkali cations for retinal CNG channels has been reported to be $Li^+ \geq Na^+ \geq K^+ \geq Rb^+ \geq Cs^+$. The relative permeability for the divalent cations Ca^{2+} and Mg^{2+} appears to be higher than for the monovalent ions [87]. Upon activation, the current flowing through CNG channels is mainly carried by Ca^{2+} but also Na^+ under physiological conditions. The current develops very rapid, is rather voltage-independent and does not desensitize, thus directly translates the cyclic nucleotide concentration into an electrical signal (Figure 7).

A remarkable property is the voltage-dependent blockage of the monovalent cation influx through CNG channels by divalent cations. Divalent ions have a significantly longer dwell time inside the pore, thus slow down permeation of the faster monovalent ions [87,95,96]. Especially, a conserved glutamate residue in the pore loop of CNGA1-

CNGA3 providing a negative charge determines the high Ca^{2+} affinity, but within these isoforms the general S5-pore loop-S6 structure contributes to differences in this property [87,97,98]. Furthermore, the subtle outward rectification, reflected in stronger outward currents than inward currents at the same respective voltages under symmetrical ion conditions, is a known feature of CNG channel-mediated currents measured in rods and cells heterologously expressing CNGA subunits [99]. However, this depends on the ions used for the symmetrical solution [100]. Single channel flickering, block by L-*cis*-diltiazem and Ca^{2+}/Calmodulin-dependent ligand desensitization are further identifiers of a CNG conducted current [87].

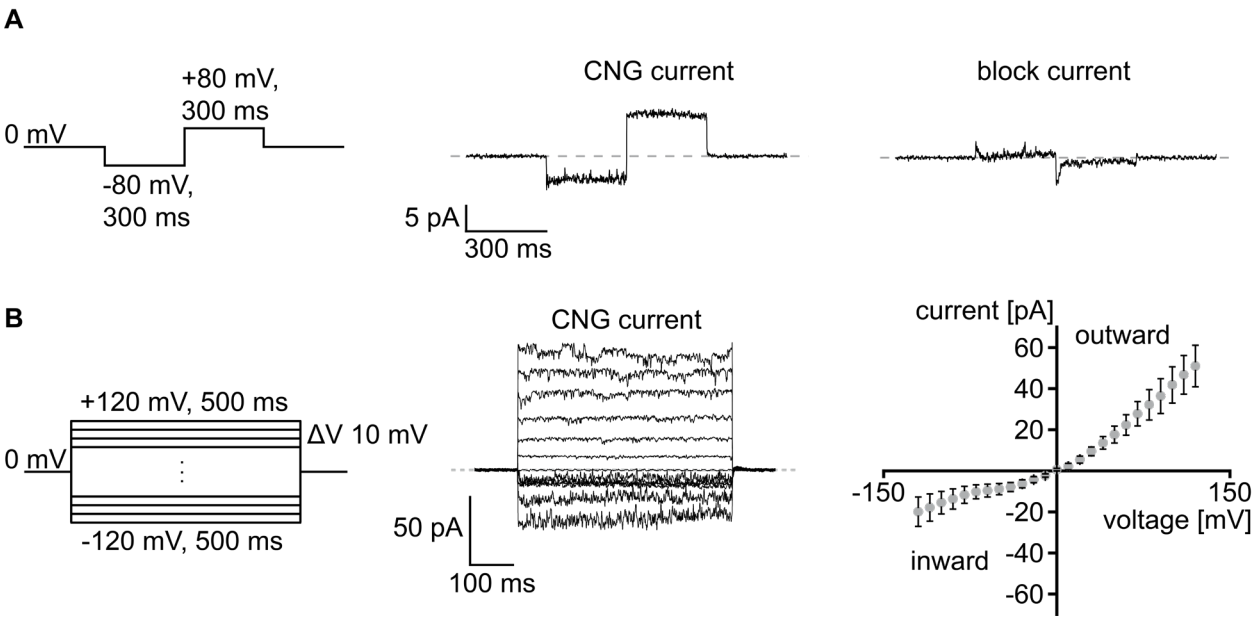

Figure 7 | Patch-clamp measurements of excised patches from 661W-cells with transactivated CNGA1 channel expression. (A, left) Voltage protocol used to measure cGMP-induced CNG channel currents. **(A, middle)** Upon cGMP application CNG channels open and conduct inward and outward currents at negative and positive membrane potentials, respectively. **(A, right)** The currents are blocked by application of divalent cations (Ca^{2+}/Mg^{2+}). The zero current is indicated by a gray dashed line. **(B)** In measurements with solutions containing symmetrical concentrations of Na^+ outward rectification becomes apparent. Figure adapted from [101].

HCN channels are dually gated. Hyperpolarization is a prerequisite for opening, whereas cyclic nucleotide binding stabilizes the open pore. The current flowing through HCN channels is termed I_f (f for “funny”) in the heart and I_h (h for “hyperpolarization”) in neurons, more rarely the term I_q (q for “queer”) is used. The channels are permeable for Na^+ and K^+ ions, with a four times higher permeability for K^+ compared to Na^+ [46,64]. However, under physiological conditions the inwardly directed current is driven by sodium ions as the driving force is greater due to significantly higher extracellular Na^+

concentrations (~143 mM Na^+ versus ~4 mM K^+) [102]. Under basal conditions the channels open at potentials below -50 mV allowing a cation influx that slowly reaches its maximum according to the applied voltage (steady-state) and does not desensitize (Figure 8). The activation kinetics of HCN channels are in the range of several milliseconds to seconds depending on the isoform and applied voltage, thus are ~100-1000 times slower compared to fast activating VGICs, e.g., Ca_V or Na_V channels [103,104]. For the activation kinetics, the following ratio can be given for the time constant τ of HCN isoforms: HCN1<<HCN2<HCN3<<HCN4 (fast to slow activation) [105]. The response to cAMP binding includes a reduced time to reach the steady-state current, prolonged deactivation kinetics and a shift of voltage-dependent activation to more depolarized potentials (Figure 8B-D). The shifts of the half-maximal activation voltage ($V_{0.5}$) directly reflect the cAMP sensitivity and are reported to be 10-25 mV for HCN2/HCN4 [64], 2-9 mV for HCN1 [84,89,106] and are absent in HCN3 [105]. It needs to be noted that the large shifts for HCN1 are due to comparison of channels where cAMP binding was genetically abolished with the cAMP sensitive wild-type (WT) variant. This results in greater shifts as the shift induced by basal cAMP is included. Calculation of the relative current increase induced by cAMP by dividing the values for normalized currents in the presence and absence of cAMP (Figure 8E) demonstrates that the relative current is not increased by CDR at voltages where HCN channels are fully activated (-140 to -130 mV). Towards physiological membrane potentials (-50 to -70 mV), however, it can be increased continuously up to a saturating maximum of about 3.5-fold. Within this saturating range, the current increase does not change significantly and is rather constant, indicating that it is independent of the membrane voltage.

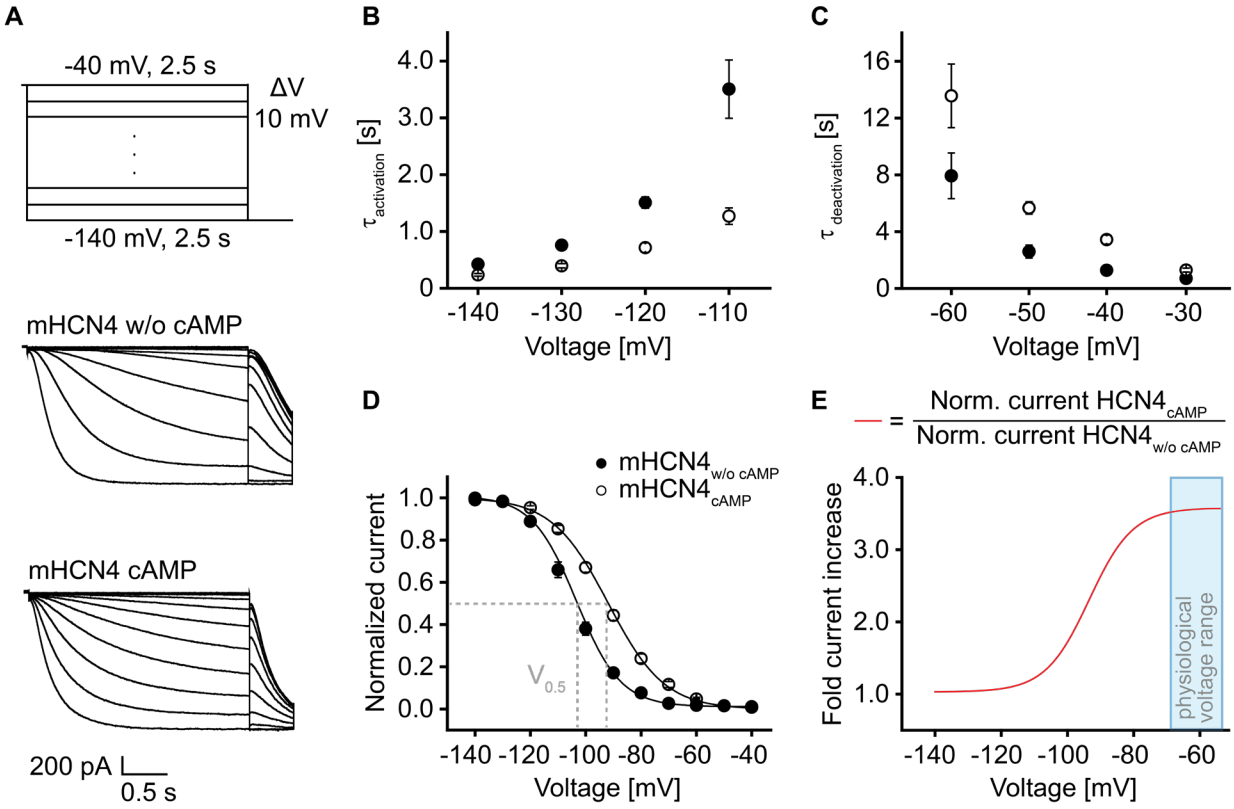

Figure 8 | Voltage-clamp measurements in HEK293 cells stably expressing mHCN4 in absence and presence of cAMP. (A, top) Voltage-clamp protocol used to evoke HCN-mediated currents. **(A, middle)** Measurements in absence of cAMP. Hyperpolarizing voltage steps induce slowly activating inward currents. **(A, bottom)** Measurements in presence of cAMP. Channel opening is accelerated by cAMP application. **(B, C)** Determination of activation (B) and deactivation (C) time constants. cAMP accelerates activation kinetics and decelerates deactivation kinetics over a broad range of test voltages. **(D)** Activation curves determined from measurements as shown in (A). cAMP induces a pronounced right-shift of the activation curve and shifts the half-maximal activation voltage ($V_{0.5}$, dashed gray line) from -104.91 mV to -92.61 mV (ΔV = 12.3 mV). **(E)** The relative current increase is calculated by dividing the values of the activation curve in presence of cAMP by the values of the activation curve in absence of cAMP. Note that the net current increase is most pronounced in the physiological voltage range.

Investigation of the absolute current increase induced by binding of cAMP to fully activated HCN channels can provide insight into whether the maximum conductance of the channels is increased by cAMP. Conventional patch-clamp experiments address this by measuring and comparing whole-cell currents of different cells using glass pipettes filled with cAMP-free or cAMP-enriched intracellular solution. Direct comparison of the same cells under both conditions is not possible because the intracellular solution in the glass pipettes used cannot be exchanged during the experiment. The planar patch-clamp technique offers a special configuration that allows the intracellular space of the same cell to be perfused in the whole-cell mode in a running experiment with different solutions, e.g., a cAMP-free solution and a solution

enriched with cAMP. The results obtained with this technique allow more precise conclusions to be drawn about the changes in maximum channel conductance compared to the conventional approach. When macroscopic currents are measured in whole-cell mode using the planar patch-clamp technique in cell lines expressing either HCN2 or HCN4, the current density does not increase further after intracellular perfusion with cAMP-containing solution at voltages more negative than -140 mV than in the absence of cAMP (Figure 9). This indicates that cAMP does not increase the conductance of the channels when all channels are open in steady-state and that the increase in current amplitude at more depolarized potentials is caused solely by the change in voltage dependence (right shift of the activation curve). Furthermore, it indicates that the single channel conductance of the opened channel is not affected by the cyclic nucleotide.

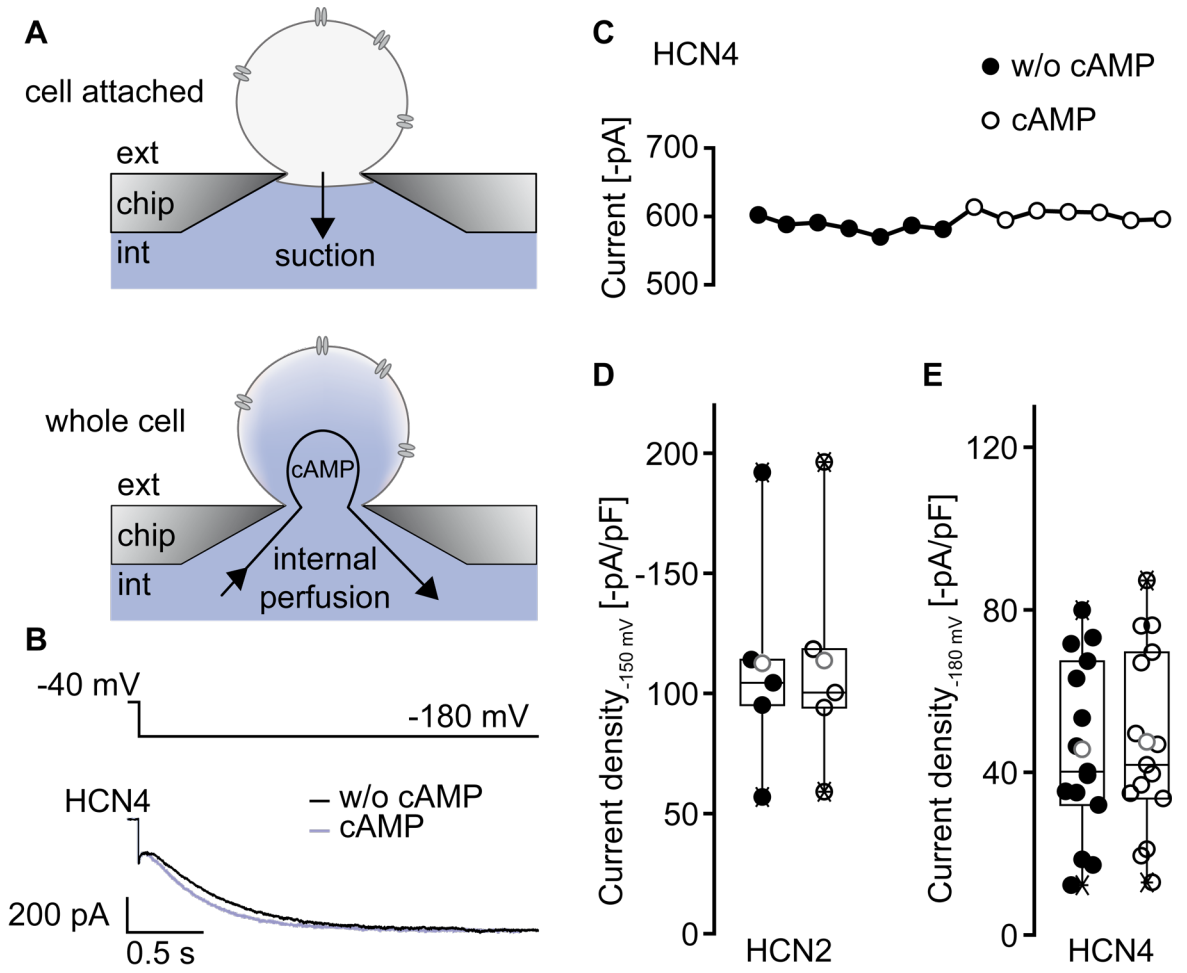

Figure 9 | The planar patch-clamp technique enables intracellular perfusion of HEK293 cells stably expressing mHCN2 or mHCN4 with solutions without or with cAMP. (A) Cells are immobilized (cell attached mode) on a glass chip and whole-cell patch clamp mode is established by applying negative pressure (suction). In this mode, current recordings can be performed within the same cell with cAMP-free and cAMP-supplemented solution by internal perfusion. **(B)** Channels are fully activated by extremely hyperpolarized voltages. cAMP perfusion (purple trace) affects channel kinetics

(Figure 9 continued) but not the steady-state current amplitude. **(C)** Time-course of HCN channel amplitude upon repetitive channel activation at -180 mV during perfusion with cAMP-free solution (filled circles) and subsequent perfusion with cAMP-supplemented solution (empty circles). The current amplitude remained constant. **(D-E)** Current densities determined from voltage steps to -150 mV (D) and -180 mV (E) for mHCN2 and mHCN4, respectively. Boxplots show the median line, perc 25/75, and min/max value; gray open symbols represent the mean value.

The voltage-dependent gating of the HCN4 channel is also “history”-dependent. This is described as hysteresis and occurs in the isoforms HCN1 and HCN2, too [53,107-110]. Hysteresis is based on the existence of several states that modulate the channel properties and can be switched between. For VGICs, including HCN channels, this can be described well by a model with two modes, each with an open and closed state of the channel, i.e. a model with four states (Figure 10A) [108]. Both modes impact channel kinetics and voltage dependency. The focus in this thesis is on the voltage dependency. HCN channels in the closed channel state preferentially adopt mode I with the activation curve set in direction of hyperpolarized potentials. If the open state of the channel is increasingly adopted due to voltage changes (hyperpolarization), a mode switch occurs. In mode II, the channels are preferentially in the open state, which could be explained by a stabilization of the channel pore due to conformational changes caused by the opening [108]. The activation curve is shifted towards depolarized potentials compared to mode I.

Hysteresis behavior can be investigated by applying different holding potentials. Depending on the holding potential applied the half-maximal activation potential of HCN4 shifts (Figure 10B). Compared to -65 mV ($V_{0.5}$ = -90.65 ± 3.98 mV), depolarized holding potentials of -55 mV yield more negative $V_{0.5}$ values (-100.13 ± 1.87 mV) as under this condition HCN4 prefers the closed state and thus adopts mode I. Hyperpolarized holding potentials of -75 mV result in less negative $V_{0.5}$ values (-77.63 ± 3.06 mV) as a switch to mode II is induced, because the open state is preferred. The depolarizing shift of the activation curve due to cAMP binding mimics or enhances the effect of hyperpolarized holding potentials as it also stabilizes the open pore.

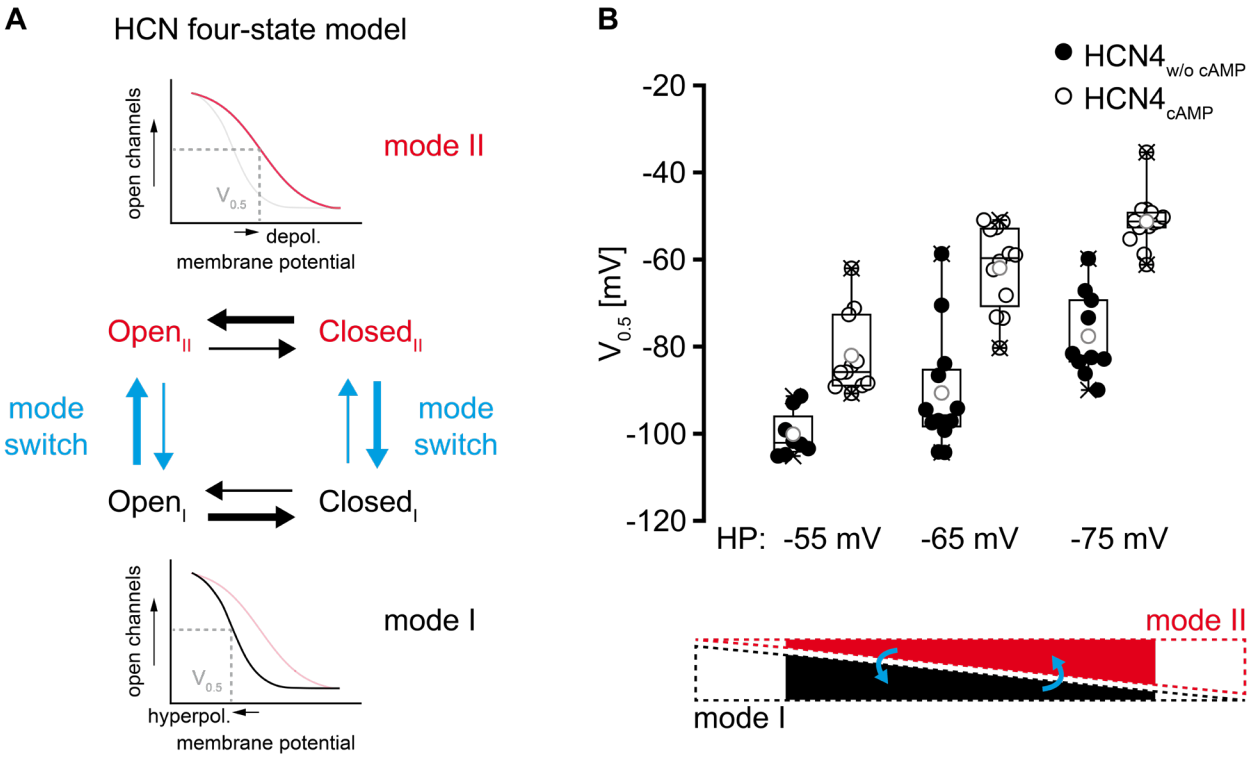

Figure 10 | Hysteresis behavior of HCN4. (A) The hysteresis of HCN channels can be described by a four-state model with two modes. In mode I, the closed state is favored and the activation curve is set to more hyperpolarized potentials. If voltage changes occur that promote the open state, a switch to mode II occurs. In this mode, the open state is preferred, and the activation curve is shifted towards depolarized potentials. When voltage changes occur that favor the closed state, mode switch to mode I is triggered. **(B)** From a depolarized holding potential (-55 mV) to hyperpolarized holding potentials (-65 mV and -75 mV) the half maximal activation voltage of HCN4 shifts to more depolarized values, because mode II (red triangle) is increasingly adopted by channels in mode I (black triangle) by a mode switch (blue arrow). This history-dependent shift is enhanced by cAMP binding. More complete mode switches occur at even more depolarized or hyperpolarized voltages than tested (dashed lines of the triangles). Boxplots show the median line, perc 25/75, and min/max value; gray open symbols represent the mean value. Figure A is adapted from [108] and B from [53].

Besides the mentioned characteristics, the HCN current is blocked efficiently with millimolar extracellular Cs^+ concentrations and micromolar concentrations of the clinically approved I_f-blocker ivabradine, which acts from the intracellular side [46,111-113].

4.4 Cardiac pacemaking and its regulation by the autonomic nervous system

The mechanical contraction of cardiac cells follows electrical excitation that is *per se* independent of the nervous system because the heart is auto-excitatory. The excitation is initiated in the SAN, an elongated network of specialized cardiomyocytes located subepicardially in the right atrium. It extends from the anterior root of the superior vena cava to the posterior end of the right atrium, next to the inferior vena cava (Figure

11A and B). An anatomical landmark that indicates the course of the SAN is the sulcus terminalis, a furrow separating the right atrium from the right atrial appendage. The dimensions of the murine SAN are approximately 1000 µm in lengths and 150 µm in width, whereas in human length reaches 15 mm and width 7 mm [114-116].

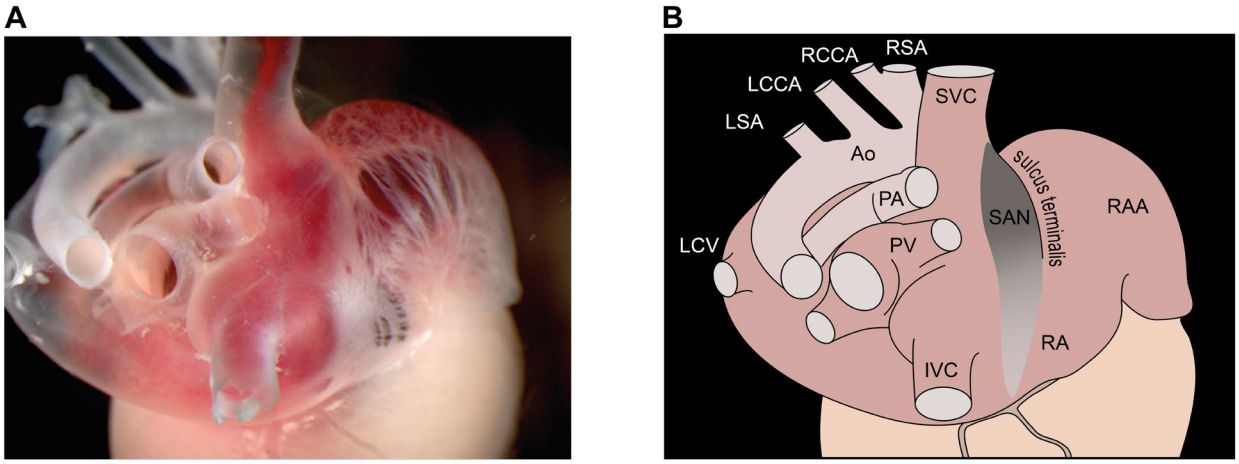

Figure 11 | Anatomical localization of the sinoatrial node. (A) A gelatine-filled murine heart exposes the sinoatrial node (SAN) region on its dorsal side. **(B)** The schematic illustration of the heart depicted in (A) indicates the position and dimensions of the SAN (gray). Additional abbreviations: Ao, Aorta; IVC, inferior vena cava; LCCA, left common carotid artery; LCV, left cranial vein; LSA; left subclavian artery; PA, pulmonary arteries; PV, pulmonary veins; RAA, right atrial appendage; RCCA, right common carotid artery; RSA, right subclavian artery; SVC, superior vena cava. Adapted from [57].

A major characteristic of pacemaker cells is the slow diastolic depolarization (SDD) at the end of a previous action potential (Figure 12A). SAN cells show slow and spontaneous depolarization after reaching the maximum diastolic potential (MDP) of ~-60 mV due to the I_f current flowing through open HCN channels. Positive charges entering the SAN cells increase the intracellular potential and facilitate the opening of other VGICs, e.g., T- and L-type calcium channels. At the end of the SDD the threshold potential is reached where firing of an action potential is elicited with the major contribution of currents flowing through L-type calcium channels and the intracellular calcium release events triggered by it [117].

The cycle length of the action potentials can be modulated by the autonomic nervous system (ANS) (Figure 12A and B). It controls the intrinsic cardiac nervous system (ICNS), which is composed of interconnected ganglia embedded in epicardial fat tissue, building ganglionated plexus [118]. Within these ganglionated plexus cholinergic neurons receive efferent synaptic projections from medullary neurons located primarily in the nucleus ambiguous and the adrenergic neurons receive efferent inputs from

neurons located in intrathoracic ganglia [119]. SAN activity is mainly controlled by the right vagus nerve and the stellate ganglion via the right atrial ganglionated plexus, with greater influence from vagal control [120]. The vagus nerve is part of the parasympathetic nervous system. Activity of the vagus nerve causes the release of the neurotransmitter acetylcholine from efferent synaptic terminals. This in turn activates G_i protein-coupled receptors of SAN cells, inhibiting adenylyl cyclase activity and reducing cytosolic cAMP. Additionally, G protein-coupled inwardly rectifying potassium channels (GIRK1 and GIRK4) are activated that conduct an outward current which leads to hyperpolarization [117]. The opposite effect occurs with activation of the sympathetic nervous system, e.g., the stellate ganglion. Here, G_s protein-coupled receptors are activated via noradrenaline release and, as a result, cAMP synthesis through adenylyl cyclases is increased. A low cAMP concentration reduces the rate of depolarization (i.e., flattening of the SDD) and ultimately slows down the beating frequency. Elevated cAMP levels increase depolarizing currents and thus lead to a steeper SDD, concomitant with an accelerated beating frequency.

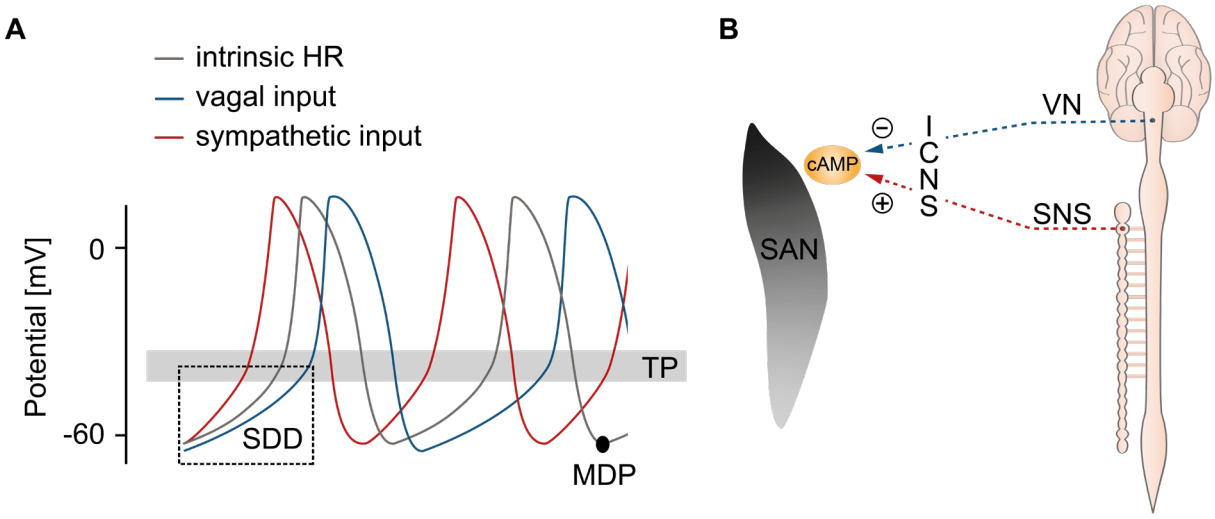

Figure 12 | Control of sinoatrial node action potential frequency via the ANS. (A) Schematic sinoatrial node (SAN) action potentials. At the maximum diastolic potential (MDP), HCN channels initiate the slow diastolic depolarization (SDD, dashed square) that precedes a pacemaker action potential before the threshold potential (TP) is reached. The intrinsic firing frequency (gray trace) is slowed down by vagal input (blue trace) due to a flatter SDD and accelerated by sympathetic input (red trace) owing to the steeper SDD. **(B)** The ANS controls the SAN activity via the intrinsic cardiac nervous system (ICNS), which innervates the SAN. Activity of the vagus nerve (VN) lowers cAMP levels in the SAN cells, whereas the sympathetic nervous system (SNS) elevates cAMP concentration during activity. Adapted from [57].

To enable spreading of the excitation from the SAN, cardiomyocytes are electrically coupled. Intercellular connections between adjacent cells are built by gap junctions (Figure 13A). These consist of two overlapping connexin hexamers (one hexamer is termed a connexon), one from each cell, which are incorporated into the plasma membrane. The alignment creates functional channels that allow the passage of small molecules, e.g., cAMP, and ions [121,122]. In the central murine SAN, the connexin isoforms Cx45, Cx30.2, associated with a slow conduction velocity, and little Cx40 are expressed, whereas in the SAN periphery and the working myocardium the fast-conducting isoforms Cx40 and Cx43 are typical [123,124]. However, electrical insulation of the SAN from the surrounding atrial myocardium by connective tissue and the SAN artery limits the exit pathways for the excitation [125,126]. Due to electrical coupling the fastest pacemaker determines the contraction rate of all residual cardiomyocytes, as it triggers a charge front that spreads and accelerates depolarization in slower pacemaker cells, e.g., AVN cells and induces depolarization in atrial or ventricular myocytes (AM and VM, respectively) (Figure 13B and C). In regular pacemaking, this cluster of cells is located in the upper body or head region of the SAN, where expression of HCN1 and HCN4 overlap in murine tissue [127].

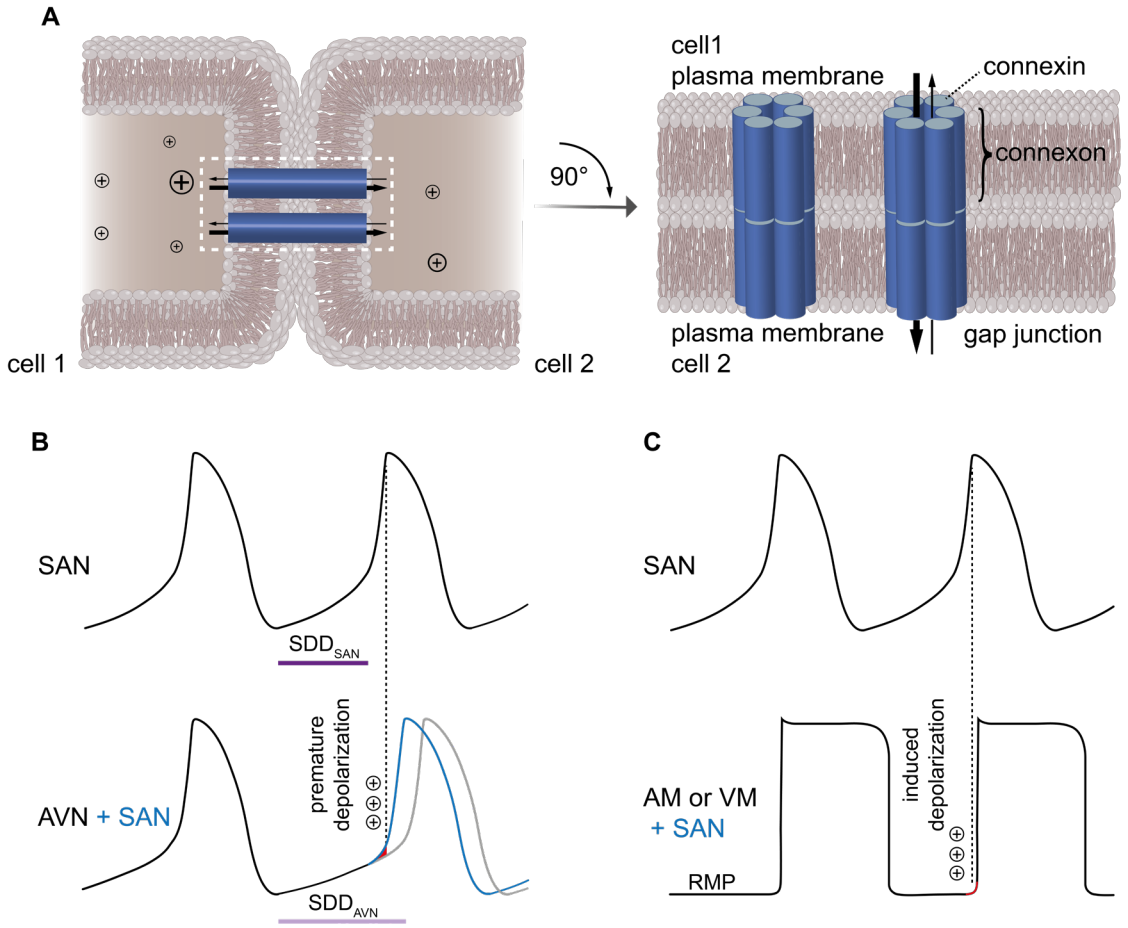

Figure 13 | Intercellular connections enable spreading of the excitation. (A, left) More positive charges are present in the cytosol of depolarized cell 1 than in hyperpolarized cell 2. Due to the resulting potential difference, positive charges are drawn towards cell 2. Gap junctions (blue cylinders) allow the passage of ions and therefore electrically couple the intracellular spaces. **(A, right)** Magnification of the inset (dashed white line, left panel) reveals the structure of gap junctions: connexin monomers assemble as hexamers to form connexons incorporated in the plasma membrane. Gap junctions are built by overlapping connexons of adjacent cells. **(B)** Sinoatrial node (SAN) cells have a steeper slow diastolic depolarization (SDD) and therefore elicit an earlier action potential than the slower depolarizing pacemaker cells of the atrioventricular node (AVN). Thus, the SAN induced propagating excitation triggers premature depolarization in the AVN cells due to gap junctions generating a common rhythm. **(C)** Atrial myocytes (AM) and ventricular myocytes (VM) usually exhibit a stable resting membrane potential (RMP), which is elevated by positive charges from neighboring depolarized cells influxing via gap junctions. These induced depolarizations, originating from the sinus node, elicit action potentials in AMs and VMs at the frequency of SAN cells.

4.5 Role of the baroreceptor reflex in heart rate control

A stable mean arterial pressure (MAP) is essential to maintain appropriate blood supply to organs via the vascular system [128]. In humans, MAP fluctuates in the range of ~80-105 mmHg during the day and night under normal conditions [129]. Chronically elevated values are associated with a significantly increased cardiovascular risk [129]. MAP values below 60 mmHg can cause a deficient supply of cerebral tissue

accompanied by loss of consciousness, thus are life-threatening [130]. To keep the MAP within a relatively narrow physiological range and to buffer short-term blood pressure perturbations induced by physiological or environmental triggers, homeostatic control circuits are crucial [131]. The MAP is calculated as the product of the cardiac output and total peripheral vascular resistance. Hence, a change in either the cardiac output or peripheral vascular resistance will affect the MAP. Since the cardiac output is proportional to the HR, the HR represents a possible parameter for MAP modulation.

The baroreceptor reflex builds a feedback loop that regulates the HR in response to the arterial blood pressure, utilizing the ANS regulation of the heart (Figure 14). This is enabled by baroreceptors, which are specialized mechanosensory neurons with afferent nerve terminals located in the vascular walls of the aortic arch and carotid sinuses, sensing stretch [132]. The information they perceive is relayed to the CNS and communicated to the branches of the ANS to finally adjust the HR. Recently the mechanosensitive Piezo and Tentonin 3 channels were suggested to be the sensing molecular components in these neurons that enable cation influx upon mechanical stress [133-136]. An increase in blood pressure exerts stretch on the arterial wall, opens the channels, and enhances action potential firing in baroreceptors, transmitting the information to the brain stem via the aortic depressor nerve or the carotid sinus nerves respectively [131]. This induces an efferent reflex response as follows: sympathetic tone is decreased, paralleled by an activation of the vagus nerve. Signalling to the ICNS and neurotransmitter release translates nervous inputs into a reduction in HR, cardiac output, and vascular resistance [133,136-138]. By contrast, if blood pressure drops the mechanosensitive channels are inactive and thus the sympathetic nervous system is activated and vagal efferents are diminished, causing an increase in the previously mentioned parameters.

Experimental data from animal models with denervated or genetically impaired baroreceptors revealed an increased blood pressure variability and an acutely increased MAP with elevated HR, however the long-term changes of blood pressure remain controversial [139,140]. In sustained hypertension the reflex itself might play a secondary role and rather reduced distensibility of arterial walls is a primary factor [141].

The baroreflex sensitivity (BRS) is the ratio of the HR response to the triggering blood pressure change expressed in ms/mm Hg and is therefore calculated with the formula:

$$\frac{\Delta RR}{\Delta BP} = BRS$$

Clinical studies show a reduced BRS in patients suffering from hypertension, chronic heart failure and post myocardial infarction or stroke states accompanied by a higher cardiac mortality [142-145]. Therefore, assessment of the BRS can be used as a prognostic marker. Determination of the spontaneous BRS with the sequence method is currently gold standard, as it excludes any physical or pharmacological interferences that might affect the result.

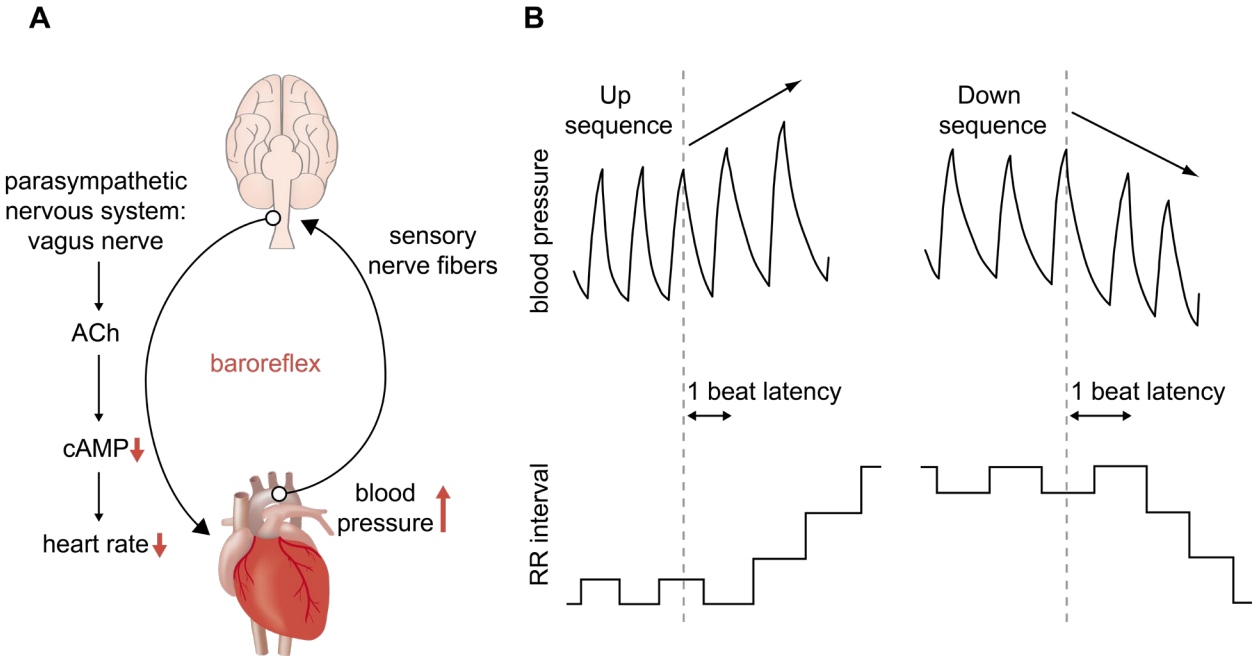

Figure 14 | Regulation of the HR in response to blood pressure via the baroreflex. (A) Baroreceptors located in the aortic arch and carotid sinus sense the arterial blood pressure. An increase of blood pressure is signalled to and transduced by the CNS, resulting in a reduction in sympathetic tone and an increase in parasympathetic activity. Consequently, nerves innervating the SAN release acetylcholine from their terminals, triggering a decrease in cAMP in the pacemaker cells and thus a slowing of the HR. An acute rise in blood pressure causes the contrary effect, by activating sympathetic and deactivating parasympathetic branches. These reflex adaptions of the HR are referred to by the baroreflex. **(B)** Schematic illustration of simultaneous blood pressure traces and RR intervals depicting an up (left panel) and down sequence (right panel). An up sequence is defined as a rise in blood pressure with a subsequent fall in HR, which means an increase in the RR interval. The reverse relationship applies to down sequences. Usually, this mechanism involves a latency time, e.g., the duration of one beat. Figure taken from [131].

4.6 Role of HCN4, its CDR and hysteresis behavior for SAN function

As a highly expressed isoform throughout the SAN, HCN4 contributes significantly to the pacemaker current I_f. The characteristics of the channel make it an ideal target for

HR regulation by the ANS. First, it is opened by hyperpolarization and conducts a depolarizing cation influx (I_f) throughout the time course of the SDD, i.e., it is essential in generating the electrical signal that precedes an action potential. Second, the activity of HCN4 is directly regulated by the binding of cAMP to the CNBD and is therefore tightly controlled by the ANS [117]. Classical concepts highlight the contribution of I_f to the SDD phase, controlled by the ANS, to accelerate or slow HR, i.e., the chronotropic effect [146]. This theory is becoming more and more challenged as many studies indicate that the chronotropic effect is independent of HCN4 and its CDR [53]. The occurrence of an elevated number of pausing, non-firing SAN cells, when isolated or within the sinoatrial network, together with reduced basal HRs in the absence of HCN4 or its CDR, have given rise to a novel concept [53]. Individual SAN cells spontaneously adopt a transient non-firing mode within the network, characterized by a hyperpolarized membrane potential and absence of action potentials (Figure 15). Gap junctions couple the intracellular spaces of adjacent depolarized firing and hyperpolarized non-firing cells, enabling a mutual, tonic interaction through direct exchange of charges. The firing cell serves as a source for positive charges, whereas the non-firing cell acts as a sink that drains these charges, resulting in a common voltage equilibrium of the involved cells shifted towards more hyperpolarized potentials compared to firing cells only. This prolongs the time required for depolarization and thus slows down the beating frequency of the sinoatrial network. Therefore, the ratio of simultaneously firing and non-firing cells affects the HR and slows it down with increasing number of silent cells. The CDR of HCN4 controls the switch of the non-firing to firing mode, or vice versa, by increasing or decreasing the I_f via shifts of the activation curve. Thus, it determines the ratio of the two cell populations at a time which sets the HR.

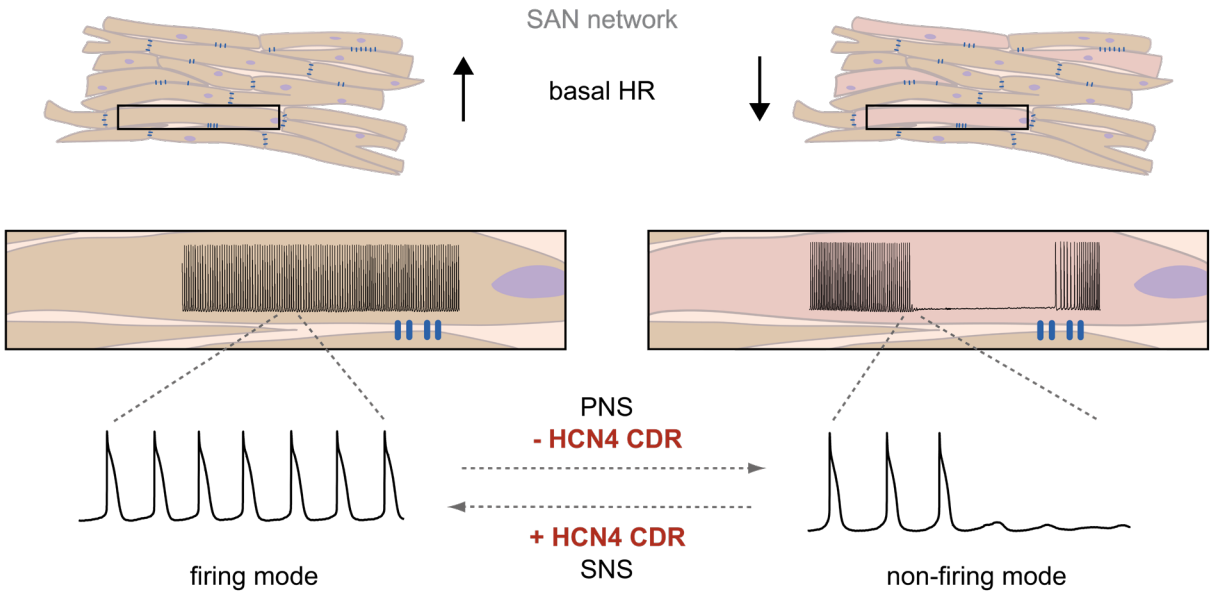

Figure 15 | Non-firing cells in the sinoatrial node control the basal HR. (Top) A low number of non-firing sinoatrial node (SAN) cells (purple colored cells) implies a high basal heart rate (HR), whereas many non-firing SAN cells cause a reduced basal HR. **(Middle, bottom)** Within the network, each cell can be in either mode, with neighbouring cells interacting via gap junctions (blue rounded bars). Firing cells show regular action potentials (left), while in the non-firing mode cells are quiescent and characterized by a hyperpolarized membrane potential (right). Activation of the parasympathetic nervous system (PNS) favors the non-firing mode by reducing CDR of HCN4. Activity of the sympathetic nervous system (SNS) causes more cells to be in the firing mode by increasing CDR of HCN4. Adapted from [57].

Besides the contribution of CDR, hysteresis of HCN4 needs to be included in this theory. The duration of a murine SAN action potential is ~100 ms, whereas the kinetics of the HCN4 channel are in the second range. Hence, it is not the voltages of individual action potentials that drive the channels, but rather the mean membrane potential in the temporal range of the kinetics. This potential determines whether the open or closed state of the channel is preferred and thus sets the position of the activation curve. In the firing mode the mean membrane potential corresponds to a relatively depolarized holding potential of ~-55 mV (Figure 16A, upper panel), therefore the HCN4 channel prefers the closed state, adopts mode I of the previously described four-state model with the activation curve shifted to hyperpolarized potentials (Figure 16B, black curve). Under this condition, the percentage of opened HCN4 channels, and thus its conducted depolarizing current, is very small within the physiological voltage range (Figure 16B, blue box). The equilibrium of flowing currents is shifted to hyperpolarization, inducing the non-firing mode in SAN cells (Figure 16B, arrow from firing to non-firing). In the non-firing mode, however, the mean membrane potential is

relatively hyperpolarized with ~-75 mV (Figure 16A, lower panel), as action potentials are absent. The HCN4 channel favors the open state under this condition and switches slowly to mode II. The activation curve is shifted to depolarized potentials (Figure 16B, red curve), where opening of HCN4 channels dramatically increases within physiological potentials. The large conducted HCN4 current progressively depolarizes the cell and induces firing again (Figure 16B, arrow from non-firing to firing).

Together, CDR and hysteresis of HCN4 control the firing and non-firing mode in SAN cells, and thus contribute to the HR in this manner.

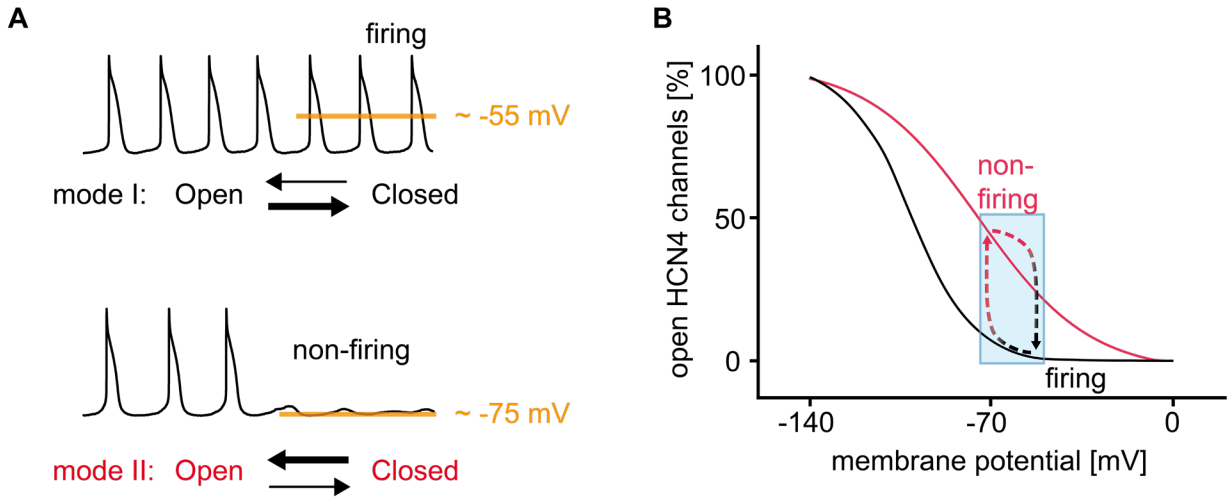

Figure 16 | The firing and non-firing mode determine the position of the activation curve. For description see text. Figure B taken from [53].

5 Aim of the thesis

The objective of the present thesis was to determine electrophysiological properties of the closely related, cyclic nucleotide-gated VGICs CNGA1, HCN2 and HCN4 to validate a transactivation approach used for gene therapy of inherited blindness (CNGA1) and to further investigate the role of CDR in a physiological context (HCN2 and HCN4).

Specifically, the following questions were addressed:

(1) Can characteristic CNG currents be measured upon transactivation of the *Cnga1* gene using a novel dCas9-VPR approach?

(2) Does cAMP increase the conductance of HCN2 channels after complete voltage-dependent opening?

(3) What is the physiological role of CDR of HCN4 in sinoatrial pacemaking?

(4) How does hysteresis of HCN4 contribute to sinoatrial pacemaking?

6 Short summary of manuscripts

6.1 A gene therapy for inherited blindness using dCas9-VPR–mediated transcriptional activation

Sybille Böhm*, Victoria Splith*, Lisa Maria Riedmayr, **René Dominik Rötzer**, Gilles Gasparoni, Karl J. V. Nordström, Johanna Elisabeth Wagner, Klara Sonnie Hinrichsmeyer, Jörn Walter, Christian Wahl-Schott, Stefanie Fenske, Martin Biel, Stylianos Michalakis, Elvir Becirovic

2020, **Science Advances**, 6(34): eaba5614

* *equal contribution*

Rod and cones are retinal photoreceptors that convert light into electrical signals, a process known as phototransduction. The signaling pathway for phototransduction involves visual pigments (opsins) and CNG channels. For opsins and CNG channels, respectively, several genes encode functional analog protein variants. Expression of the functional equivalent genes is photoreceptor-specific and typically only one gene variant is active while the other homologs are silenced. In rods, the visual pigment rhodopsin and the CNG channel subunit CNGA1 are expressed, whereas in cones M-opsin and CNGA3 exert the respective roles. If mutations affect the gene encoding the expressed protein variant, its function can be disrupted completely and thus a defect in phototransduction can arise. In the retina, this can lead to inherited retinal degenerations, such as retinitis pigmentosa or achromatopsia. Substitution of diseased rod-specific genes by activation of silenced cone-specific homologs or vice versa is an attractive novel strategy for treatment.

In this study, an approach using catalytically inactive Cas9 (dCas9) fused to the transcriptional activator domain VPR (dCas9-VPR) together with single guide ribonucleic acids (sgRNAs) targeting the promotor region of a target gene was established and used to transactivate functionally equivalent analogs of diseased genes in mice displaying retinal dystrophy.

In vitro transactivation of genes encoding CNGA1, or M-opsin was tested in cell lines lacking expression of these proteins. The presence of CNGA1 protein after transactivation was confirmed with immunocytochemical staining. Furthermore, patch-

clamp experiments have shown the presence of an outwardly rectified cGMP-induced current that is blocked by divalent cations, suggesting the presence of functional CNG channels in the plasma membrane. Subsequently, transactivation of the *Opn1mw* gene (M-opsin protein) in murine rods was investigated *in vivo* with subretinal recombinant adeno-associated virus (rAAV) delivery. Efficient upregulation of messenger ribonucleic acid (mRNA) and protein levels was confirmed in WT animals.

The therapeutic potential of this approach was then tested using heterozygous rhodopsin-deficient mice (Rho $^{+/-}$), an established mouse model for retinitis pigmentosa. The rod photoreceptors of these mice show reduced expression of rhodopsin, leading to a phenotype characterized by a slow course retinal degeneration. The induced expression of the functionally equivalent cone photopigment M-opsin in rods of treated Rho$^{+/-}$ mice was able to rescue the phenotype. One year post-injection, the treatment resulted in preserved retinal morphology and function in treated versus untreated eyes. Adverse effects resulting from the therapy were excluded by immunohistochemistry.

Taken together, these results highlight the power of this approach and encourage for further clinical applications.

Declaration of Contribution: The patch-clamp measurements of this publication and concomitant analysis were conducted by me.

The extensive characterization of the conducted currents substantiated the presence of fully functional tetrameric CNG channels upon transactivation. This important finding validated the method and furthermore suggest *Cnga1* transactivation as a substitutive treatment option for inherited retinal dystrophies caused by a defective *Cnga3* gene.

6.2 Abolishing cAMP sensitivity in HCN2 pacemaker channels induces generalized seizures

Verena Hammelmann, Marc Sebastian Stieglitz, Henrik Hülle, Karim Le Meur, Jennifer Kass, Manuela Brümmer, Christian Gruner, **René Dominik Rötzer**, Stefanie Fenske, Jana Hartmann, Benedikt Zott, Anita Lüthi, Saskia Spahn, Markus Moser, Dirk Isbrandt, Andreas Ludwig, Arthur Konnerth, Christian Wahl-Schott, Martin Biel

2019, **JCI Insight**, 4(9): e126418

The network activity of the thalamus is determined by two firing modes that the individual neurons can adopt and switch between: burst firing, which is characterized by stereotypic short trains of high-frequency action potentials, and tonic firing, in which the frequency of action potentials is correlated with the strength of an incoming depolarization through afferent excitatory inputs. The burst firing mode is associated with reduced transmission of information, whereas the tonic firing mode allows sensory information to be transmitted. CDR of HCN channels expressed in these neurons has been proposed to be the main mechanism controlling transition between burst and tonic firing, however specific proof that cAMP binding to HCN2 channels is the key regulator has been missing.

To study the role of cAMP-dependent regulation of thalamic HCN2 channels, a mouse line expressing cAMP insensitive HCN2 channels was investigated in this publication. Mutation of two amino acids located in the CNBD of the HCN2 channel (R591E and T592A, HCN2EA mouse line) disrupted cAMP binding completely. Patch-clamp experiments on HEK293 cells heterologously expressing HCN2EA channels have shown normal hyperpolarization-dependent gating but absent modulation by cAMP, i.e., no depolarizing shift of the activation curve. Voltage-clamp measurements, including the planar patch-clamp technique, ruled out effects of cAMP on maximum channel conductance. This indicated that the pore is stabilized with cAMP binding but not opened further and that the amplitude of the current only depends on the number of open channels.

The isoform HCN2 was shown to be expressed in the thalamic dLGN and VB nuclei, where it overlaps with HCN4 only in the VB. An altered HCN channel expression profile

in the thalamus due to the mutant channel was excluded by immunohistological staining and western blot analysis. In native cells of both nuclei, the loss of CDR was reflected in a hyperpolarized resting membrane potential. The lack of cAMP modulation and thus the missing rightward shift of the activation curve reduces the depolarizing HCN2 current under physiological conditions and hence the impact of hyperpolarizing currents such as outward potassium currents is more pronounced. Additionally, HCN2EA neurons were unable to switch from burst firing to tonic firing within a broad range of injected currents. The reduced capability of tonic firing altered network activity as demonstrated in 2-photon Ca^{2+} imaging and therefore also had to become evident *in vivo*. Since tonic firing corresponds to the transmission mode, it was expected that there would be disturbances in the forwarding of information within the CNS. Indeed, visual learning was impaired in the HCN2EA mice. Additionally, the phenotype was characterized by occurrence of generalized seizures of the absence type, which could be directly attributed to the cAMP-insensitive HCN2 channels in the VB region. Furthermore, the properties of NREM sleep seemed to be affected in this mouse line.
In summary, the study reveals that key function of the CDR of HCN2 in thalamocortical neurons is the control of the mode switches between tonic and burst firing and underlines its physiological importance.

Declaration of Contribution: I performed and analyzed the planar patch-clamp experiment.
The result showed that cAMP does not increase maximum channel conductance of open HCN2 channels and, therefore, abolishing the CDR of HCN2 only affects the cAMP induced shifts in voltage dependence and concomitantly the number of open channels. This important aspect contributes significantly to a detailed understanding of the effects of the introduced mutations. Thus, the mutant channel used was characterized. Moreover, this long-disputed finding was also clarified for the WT HCN2 channel, a result that can be extended to other HCN isoforms.

6.3 cAMP-dependent regulation of HCN4 controls the tonic entrainment process in sinoatrial node pacemaker cells

Stefanie Fenske, Konstantin Hennis*, **René D. Rötzer***, Verena F. Brox*, Elvir Becirovic, Andreas Scharr, Christian Gruner, Tilman Ziegler, Verena Mehlfeld, Jaclyn Brennan, Igor R. Efimov, Audrys G. Pauža, Markus Moser, Carsten T. Wotjak, Christian Kupatt, Rasmus Gönner, Rai Zhang, Henggui Zhang, Xiangang Zong, Martin Biel, Christian Wahl-Schott
2020, **Nature Communications**, 11, 5555
* *equal contribution*

The role of CDR of HCN4 for sinoatrial pacemaking is highly debated. It has been postulated for a long time that it underlies HR control by the ANS, but conflicting results have made it difficult to validate this assumption.
In this study we addressed this using a mouse model expressing cAMP insensitive HCN4 channels by introducing three point mutations (Y527F, R669E, and T670A, referred to as FEA) in the channel coding gene. Voltage-clamp experiments confirmed loss of cAMP-dependent regulation of mutant channels, as reflected by the absence of a depolarizing shift in the voltage-dependent activation and unchanged channel kinetics in the presence of cAMP. According to textbook knowledge HCN channels are main modulators of the chronotropic effect via their CDR by providing a depolarizing current at the beginning of the SDD which can be increased with binding of cAMP. In this theory, elevated cAMP levels cause a steeper SDD, a shorter time to fire the next action potential and thus higher firing rates. Therefore, expression of cAMP-insensitive HCN4 channels was expected to result in a lower firing rate. However, in current clamp measurements with isolated SAN cells firing parameters, e.g., firing frequency or slope of the SDD, have shown no difference between HCN4FEA cells compared to WT cells. A striking feature at the single cell level was the increased number of non-firing cells isolated from HCN4FEA SAN tissue compared to WT. Calcium imaging experiments with isolated SAN tissue have shown that the non-firing mode is manifested as cells with individual subthreshold calcium activity and is more pronounced in HCN4FEA explants. The overall firing rate of biatrial explants and isolated hearts was reduced in preparations from mutants, which can be attributed to the more frequent non-firing

mode. Based on these results, it was proposed that the mutual tonic interaction between non-firing and firing cells in the network, enabled by gap junctions, sets the HR and that the ratio of the two cell populations is controlled by the CDR of HCN4. Furthermore, the involvement of hysteresis of HCN4 to the mode switch was investigated. In non-firing cells hysteresis shifts the activation curve of the HCN4 channel to depolarized potentials, increasing the HCN current and thus rescues quiescent cells, vice versa in firing cells hysteresis shifts the activation curve to hyperpolarized potentials favouring non-firing by reduction of the HCN current.
Ex-vivo vagal nerve stimulation revealed an increased susceptibility of HCN4FEA hearts to vagal activity with an increased number of sinus pauses and larger shifts of the leading pacemaker. In line with these findings, BRS analysis of telemetric ECG and blood pressure recordings has shown a higher reflex gain for HCN4FEA mice. In addition, the ECG recordings revealed a phenotype characterized by severe sinus bradycardia and sinus dysrhythmia, but fully preserved HR regulation.
All in all, this indicates that CDR of HCN4 is not necessary for the chronotropic HR increase, but for an appropriate basal HR and rhythmicity.

Declaration of Contribution: I performed histological and immunohistological experiments, including preparations, cryosectioning, staining and data analysis. Furthermore, I contributed significantly to patch-clamp measurements (kinetics and hysteresis) in HEK293 cells and analyzed the data. Patch-clamp measurements of calcium currents in isolated SAN cells also include my efforts. I established and carried out vagal nerve stimulation (establishment includes efforts of Dr. Verena Brox) and right heart catheterization in whole-heart explants. I also contributed significantly to basal measurements of Langendorff-heart preparations.
My histological experiments and the calcium current measurements helped to exclude compensatory or secondary pathomechanisms potentially leading to the observed *in vivo* phenotype that results from abolishing cAMP sensitivity of the HCN4 channel. Patch-clamp measurements in HEK293 cells were done to obtain kinetic and hysteresis parameters, which were the base for the explanation of mode switches in isolated SAN cells. Based on these results I contributed to create our novel model, which explains the rhythmic changes of firing and non-firing cells in the SAN. My experiments with isolated hearts completed the picture of the phenotype on the network level. The paper challenges the present textbook knowledge about the role of

CDR of HCN4 and beyond that, suggests HCN4 as a regulator of the tonic entrainment of SAN cells.

6.4 Implantation of combined telemetric ECG and blood pressure transmitters to determine spontaneous baroreflex sensitivity in conscious mice

René D. Rötzer, Verena F. Brox, Konstantin Hennis, Stefan B. Thalhammer, Martin Biel, Christian Wahl-Schott, Stefanie Fenske
2021, **Journal of Visualized Experiments**, (168): e62101

The reflex adaptions of the HR to changes in blood pressure are referred to as the baroreflex. The sensitivity of this feedback mechanism includes cardiac, vascular, and nervous function and is thus used as a marker for cardiovascular or autonomic nervous system diseases. Therefore, it is frequently studied in research and multiple methods to assess BRS are being used.

This publication contains a visualized protocol (video in production) for the implantation of combined telemetric ECG and BP transmitters to determine spontaneous BRS in conscious, freely moving mice. The demanding surgical procedure comprises the insertion of a blood pressure catheter in the left common carotid artery and subcutaneous placement of ECG leads on the pectoral muscle. After recovery long-term blood pressure and ECG recordings are acquired and BRS is determined using the sequence method. A step-by-step description of the surgery and concomitant data analysis is given, supplemented with visual material. Presented positive and negative results complete a comprehensive picture of the approach.

The main advantage of the described technique is that stress responses that interfere with the BRS are circumvented; therefore, spontaneous, and physiological BRS values are obtained. Other approaches lack this critical aspect as they make use of pharmacological interventions that require entering the measurement room and physically interacting with the animals, resulting in high stress levels.

Following the video and written protocol of the publication researchers are able to reproduce the surgery and analyze their obtained data.

7 References

1 Hodgkin, A. L. & Huxley, A. F. Propagation of electrical signals along giant nerve fibers. *Proc R Soc Lond B Biol Sci* **140**, 177-183, doi:10.1098/rspb.1952.0054 (1952).

2 Hodgkin, A. L. & Huxley, A. F. A quantitative description of membrane current and its application to conduction and excitation in nerve. *J Physiol* **117**, 500-544, doi:10.1113/jphysiol.1952.sp004764 (1952).

3 Hodgkin, A. L. & Huxley, A. F. The dual effect of membrane potential on sodium conductance in the giant axon of Loligo. *J Physiol* **116**, 497-506, doi:10.1113/jphysiol.1952.sp004719 (1952).

4 Hodgkin, A. L. & Huxley, A. F. Currents carried by sodium and potassium ions through the membrane of the giant axon of Loligo. *J Physiol* **116**, 449-472, doi:10.1113/jphysiol.1952.sp004717 (1952).

5 Hodgkin, A. L., Huxley, A. F. & Katz, B. Measurement of current-voltage relations in the membrane of the giant axon of Loligo. *J Physiol* **116**, 424-448, doi:10.1113/jphysiol.1952.sp004716 (1952).

6 Del Castillo, J. & Katz, B. Biophysical aspects of neuro-muscular transmission. *Prog Biophys Biophys Chem* **6**, 121-170 (1956).

7 Neher, E. & Sakmann, B. Single-channel currents recorded from membrane of denervated frog muscle fibres. *Nature* **260**, 799-802, doi:10.1038/260799a0 (1976).

8 Doyle, D. A. *et al.* The structure of the potassium channel: molecular basis of K+ conduction and selectivity. *Science* **280**, 69-77, doi:10.1126/science.280.5360.69 (1998).

9 Yu, F. H., Yarov-Yarovoy, V., Gutman, G. A. & Catterall, W. A. Overview of molecular relationships in the voltage-gated ion channel superfamily. *Pharmacol Rev* **57**, 387-395, doi:10.1124/pr.57.4.13 (2005).

10 Madeira, F. *et al.* The EMBL-EBI search and sequence analysis tools APIs in 2019. *Nucleic Acids Res* **47**, W636-W641, doi:10.1093/nar/gkz268 (2019).

11 Brelidze, T. I., Carlson, A. E., Sankaran, B. & Zagotta, W. N. Structure of the carboxy-terminal region of a KCNH channel. *Nature* **481**, 530-533, doi:10.1038/nature10735 (2012).

12 Marques-Carvalho, M. J. & Morais-Cabral, J. H. Crystallization and preliminary X-ray crystallographic characterization of a cyclic nucleotide-binding homology domain from the mouse EAG potassium channel. *Acta Crystallogr Sect F Struct Biol Cryst Commun* **68**, 337-339, doi:10.1107/S1744309112004216 (2012).

13 Brelidze, T. I. N- and C-terminal interactions in KCNH channels: The spotlight on the intrinsic ligand. *J Gen Physiol* **151**, 400-403, doi:10.1085/jgp.201812313 (2019).

14 Brelidze, T. I., Carlson, A. E. & Zagotta, W. N. Absence of direct cyclic nucleotide modulation of mEAG1 and hERG1 channels revealed with fluorescence and electrophysiological methods. *J Biol Chem* **284**, 27989-27997, doi:10.1074/jbc.M109.016337 (2009).

15 Thomas, D. *et al.* Deletion of protein kinase A phosphorylation sites in the HERG potassium channel inhibits activation shift by protein kinase A. *J Biol Chem* **274**, 27457-27462, doi:10.1074/jbc.274.39.27457 (1999).

16 Cui, J., Melman, Y., Palma, E., Fishman, G. I. & McDonald, T. V. Cyclic AMP regulates the HERG K(+) channel by dual pathways. *Curr Biol* **10**, 671-674, doi:10.1016/s0960-9822(00)00516-9 (2000).

17 Bradley, J., Frings, S., Yau, K. W. & Reed, R. Nomenclature for ion channel subunits. *Science* **294**, 2095-2096, doi:10.1126/science.294.5549.2095 (2001).

18 Calejo, A. I. *et al.* Differences in the expression pattern of HCN isoforms among mammalian tissues: sources and implications. *Mol Biol Rep* **41**, 297-307, doi:10.1007/s11033-013-2862-2 (2014).

19 Matulef, K. & Zagotta, W. N. Cyclic nucleotide-gated ion channels. *Annu Rev Cell Dev Biol* **19**, 23-44, doi:10.1146/annurev.cellbio.19.110701.154854 (2003).

20 Chen, T. Y. *et al.* A new subunit of the cyclic nucleotide-gated cation channel in retinal rods. *Nature* **362**, 764-767, doi:10.1038/362764a0 (1993).

21 Zheng, J., Trudeau, M. C. & Zagotta, W. N. Rod cyclic nucleotide-gated channels have a stoichiometry of three CNGA1 subunits and one CNGB1 subunit. *Neuron* **36**, 891-896, doi:10.1016/s0896-6273(02)01099-1 (2002).

22 Zhong, H., Molday, L. L., Molday, R. S. & Yau, K. W. The heteromeric cyclic nucleotide-gated channel adopts a 3A:1B stoichiometry. *Nature* **420**, 193-198, doi:10.1038/nature01201 (2002).

23 Michalakis, S., Becirovic, E. & Biel, M. Retinal Cyclic Nucleotide-Gated Channels: From Pathophysiology to Therapy. *Int J Mol Sci* **19**, doi:10.3390/ijms19030749 (2018).

24 Bonigk, W. *et al.* The native rat olfactory cyclic nucleotide-gated channel is composed of three distinct subunits. *J Neurosci* **19**, 5332-5347 (1999).

25 Zheng, J. & Zagotta, W. N. Stoichiometry and assembly of olfactory cyclic nucleotide-gated channels. *Neuron* **42**, 411-421, doi:10.1016/s0896-6273(04)00253-3 (2004).

26 Craven, K. B. & Zagotta, W. N. CNG and HCN channels: two peas, one pod. *Annu Rev Physiol* **68**, 375-401, doi:10.1146/annurev.physiol.68.040104.134728 (2006).

27 Selvakumar, D. *et al.* CNGA3 is expressed in inner ear hair cells and binds to an intracellular C-terminus domain of EMILIN1. *Biochem J* **443**, 463-476, doi:10.1042/BJ20111255 (2012).

28 Kolesnikov, S. S., Rebrik, T. I., Zhainazarov, A. B., Tavartkiladze, G. A. & Kalamkarov, G. R. A cyclic-AMP-gated conductance in cochlear hair cells. *FEBS Lett* **290**, 167-170, doi:10.1016/0014-5793(91)81251-3 (1991).

29 Drescher, M. J. *et al.* Expression of subunits for the cAMP-sensitive 'olfactory' cyclic nucleotide-gated ion channel in the cochlea: implications for signal transduction. *Brain Res Mol Brain Res* **98**, 1-14, doi:10.1016/s0169-328x(01)00289-3 (2002).

30 Misaka, T. *et al.* Taste buds have a cyclic nucleotide-activated channel, CNGgust. *J Biol Chem* **272**, 22623-22629, doi:10.1074/jbc.272.36.22623 (1997).

31 Lee, H. M., Park, Y. S., Kim, W. & Park, C. S. Electrophysiological characteristics of rat gustatory cyclic nucleotide--gated channel expressed in Xenopus oocytes. *J Neurophysiol* **85**, 2335-2349, doi:10.1152/jn.2001.85.6.2335 (2001).

32 Distler, M., Biel, M., Flockerzi, V. & Hofmann, F. Expression of cyclic nucleotide-gated cation channels in non-sensory tissues and cells. *Neuropharmacology* **33**, 1275-1282, doi:10.1016/0028-3908(94)90027-2 (1994).

33 Biel, M., Zong, X. & Hofmann, F. Molecular diversity of cyclic nucleotide-gated cation channels. *Naunyn Schmiedebergs Arch Pharmacol* **353**, 1-10, doi:10.1007/BF00168909 (1995).

34 Fried, H. U., Kaupp, U. B. & Muller, F. Hyperpolarization-activated and cyclic nucleotide-gated channels are differentially expressed in juxtaglomerular cells in the olfactory bulb of mice. *Cell Tissue Res* **339**, 463-479, doi:10.1007/s00441-009-0904-9 (2010).

35 Muller, F. *et al.* HCN channels are expressed differentially in retinal bipolar cells and concentrated at synaptic terminals. *Eur J Neurosci* **17**, 2084-2096, doi:10.1046/j.1460-9568.2003.02634.x (2003).

36 Nakashima, N., Ishii, T. M., Bessho, Y., Kageyama, R. & Ohmori, H. Hyperpolarisation-activated cyclic nucleotide-gated channels regulate the spontaneous firing rate of olfactory receptor neurons and affect glomerular formation in mice. *J Physiol* **591**, 1749-1769, doi:10.1113/jphysiol.2012.247361 (2013).

37 Mobley, A. S. *et al.* Hyperpolarization-activated cyclic nucleotide-gated channels in olfactory sensory neurons regulate axon extension and glomerular formation. *J Neurosci* **30**, 16498-16508, doi:10.1523/JNEUROSCI.4225-10.2010 (2010).

38 Knop, G. C. *et al.* Light responses in the mouse retina are prolonged upon targeted deletion of the HCN1 channel gene. *Eur J Neurosci* **28**, 2221-2230, doi:10.1111/j.1460-9568.2008.06512.x (2008).

39 Gamsiz, E. D., Ouyang, Q., Schmidt, M., Nagpal, S. & Morrow, E. M. Genome-wide transcriptome analysis in murine neural retina using high-throughput RNA sequencing. *Genomics* **99**, 44-51, doi:10.1016/j.ygeno.2011.09.003 (2012).

40 Della Santina, L. *et al.* Processing of retinal signals in normal and HCN deficient mice. *PLoS One* **7**, e29812, doi:10.1371/journal.pone.0029812 (2012).

41 Jiang, Z., Yue, W. W. S., Chen, L., Sheng, Y. & Yau, K. W. Cyclic-Nucleotide- and HCN-Channel-Mediated Phototransduction in Intrinsically Photosensitive Retinal Ganglion Cells. *Cell* **175**, 652-664 e612, doi:10.1016/j.cell.2018.08.055 (2018).

42 Horwitz, G. C., Risner-Janiczek, J. R., Jones, S. M. & Holt, J. R. HCN channels expressed in the inner ear are necessary for normal balance function. *J Neurosci* **31**, 16814-16825, doi:10.1523/JNEUROSCI.3064-11.2011 (2011).

43 Kim, Y. H. & Holt, J. R. Functional contributions of HCN channels in the primary auditory neurons of the mouse inner ear. *J Gen Physiol* **142**, 207-223, doi:10.1085/jgp.201311019 (2013).

44 Stevens, D. R. *et al.* Hyperpolarization-activated channels HCN1 and HCN4 mediate responses to sour stimuli. *Nature* **413**, 631-635, doi:10.1038/35098087 (2001).

45 Gao, N. *et al.* Voltage-gated sodium channels in taste bud cells. *BMC Neurosci* **10**, 20, doi:10.1186/1471-2202-10-20 (2009).

46 Biel, M., Wahl-Schott, C., Michalakis, S. & Zong, X. Hyperpolarization-activated cation channels: from genes to function. *Physiol Rev* **89**, 847-885, doi:10.1152/physrev.00029.2008 (2009).

47 Hammelmann, V. *et al.* Abolishing cAMP sensitivity in HCN2 pacemaker channels induces generalized seizures. *JCI Insight* **4**, doi:10.1172/jci.insight.126418 (2019).

48 Yamamoto, T. Taste responses of cortical neurons. *Prog Neurobiol* **23**, 273-315, doi:10.1016/0301-0082(84)90007-8 (1984).

49 Notomi, T. & Shigemoto, R. Immunohistochemical localization of Ih channel subunits, HCN1-4, in the rat brain. *J Comp Neurol* **471**, 241-276, doi:10.1002/cne.11039 (2004).

50 Stieglitz, M. S. *et al.* Disturbed Processing of Contextual Information in HCN3 Channel Deficient Mice. *Front Mol Neurosci* **10**, 436, doi:10.3389/fnmol.2017.00436 (2017).

51 Albrecht, J. & Wiesmann, M. in *Encyclopedia of Neuroscience* (eds Marc D. Binder, Nobutaka Hirokawa, & Uwe Windhorst) 3003-3006 (Springer Berlin Heidelberg, 2009).

52 Li, N. *et al.* Molecular Mapping of Sinoatrial Node HCN Channel Expression in the Human Heart. *Circ Arrhythm Electrophysiol* **8**, 1219-1227, doi:10.1161/CIRCEP.115.003070 (2015).

53 Fenske, S. *et al.* cAMP-dependent regulation of HCN4 controls the tonic entrainment process in sinoatrial node pacemaker cells. *Nat Commun* **11**, 5555, doi:10.1038/s41467-020-19304-9 (2020).

54 Fenske, S. *et al.* Sick sinus syndrome in HCN1-deficient mice. *Circulation* **128**, 2585-2594, doi:10.1161/CIRCULATIONAHA.113.003712 (2013).

55 Herrmann, S., Layh, B. & Ludwig, A. Novel insights into the distribution of cardiac HCN channels: an expression study in the mouse heart. *J Mol Cell Cardiol* **51**, 997-1006, doi:10.1016/j.yjmcc.2011.09.005 (2011).

56 Herrmann, S., Stieber, J., Stockl, G., Hofmann, F. & Ludwig, A. HCN4 provides a 'depolarization reserve' and is not required for heart rate acceleration in mice. *EMBO J* **26**, 4423-4432, doi:10.1038/sj.emboj.7601868 (2007).

57 Hennis, K., Biel, M., Wahl-Schott, C. & Fenske, S. Beyond pacemaking: HCN channels in sinoatrial node function. *Prog Biophys Mol Biol*, doi:10.1016/j.pbiomolbio.2021.03.004 (2021).

58 Marionneau, C. *et al.* Specific pattern of ionic channel gene expression associated with pacemaker activity in the mouse heart. *J Physiol* **562**, 223-234, doi:10.1113/jphysiol.2004.074047 (2005).

59 He, W., Zhang, J., Gan, T., Xu, G. & Tang, B. Expression of hyperpolarization-activated cyclic nucleotide-gated channel isoforms in a canine model of atrial fibrillation. *Exp Ther Med* **12**, 433-436, doi:10.3892/etm.2016.3290 (2016).

60 Schweizer, P. A. *et al.* Transcription profiling of HCN-channel isotypes throughout mouse cardiac development. *Basic Res Cardiol* **104**, 621-629, doi:10.1007/s00395-009-0031-5 (2009).

61 Fenske, S. *et al.* HCN3 contributes to the ventricular action potential waveform in the murine heart. *Circ Res* **109**, 1015-1023, doi:10.1161/CIRCRESAHA.111.246173 (2011).

62 Biel, M. *et al.* Another member of the cyclic nucleotide-gated channel family, expressed in testis, kidney, and heart. *Proc Natl Acad Sci U S A* **91**, 3505-3509, doi:10.1073/pnas.91.9.3505 (1994).

63 Callaway, E. Revolutionary cryo-EM is taking over structural biology. *Nature* **578**, 201, doi:10.1038/d41586-020-00341-9 (2020).

64 Wahl-Schott, C. & Biel, M. HCN channels: structure, cellular regulation and physiological function. *Cell Mol Life Sci* **66**, 470-494, doi:10.1007/s00018-008-8525-0 (2009).

65 Sautter, A., Zong, X., Hofmann, F. & Biel, M. An isoform of the rod photoreceptor cyclic nucleotide-gated channel beta subunit expressed in olfactory neurons. *Proc Natl Acad Sci U S A* **95**, 4696-4701, doi:10.1073/pnas.95.8.4696 (1998).

66 Much, B. *et al.* Role of subunit heteromerization and N-linked glycosylation in the formation of functional hyperpolarization-activated cyclic nucleotide-gated channels. *J Biol Chem* **278**, 43781-43786, doi:10.1074/jbc.M306958200 (2003).

67 Lee, C. H. & MacKinnon, R. Structures of the Human HCN1 Hyperpolarization-Activated Channel. *Cell* **168**, 111-120 e111, doi:10.1016/j.cell.2016.12.023 (2017).

68 Li, M. *et al.* Structure of a eukaryotic cyclic-nucleotide-gated channel. *Nature* **542**, 60-65, doi:10.1038/nature20819 (2017).

69 Zheng, X. *et al.* Mechanism of ligand activation of a eukaryotic cyclic nucleotide-gated channel. *Nat Struct Mol Biol* **27**, 625-634, doi:10.1038/s41594-020-0433-5 (2020).

70 Long, S. B., Tao, X., Campbell, E. B. & MacKinnon, R. Atomic structure of a voltage-dependent K+ channel in a lipid membrane-like environment. *Nature* **450**, 376-382, doi:10.1038/nature06265 (2007).

71 Tao, X. & MacKinnon, R. Cryo-EM structure of the KvAP channel reveals a non-domain-swapped voltage sensor topology. *Elife* **8**, doi:10.7554/eLife.52164 (2019).

72 Sun, J. & MacKinnon, R. Cryo-EM Structure of a KCNQ1/CaM Complex Reveals Insights into Congenital Long QT Syndrome. *Cell* **169**, 1042-1050 e1049, doi:10.1016/j.cell.2017.05.019 (2017).

73 Payandeh, J., Scheuer, T., Zheng, N. & Catterall, W. A. The crystal structure of a voltage-gated sodium channel. *Nature* **475**, 353-358, doi:10.1038/nature10238 (2011).

74 James, Z. M. *et al.* CryoEM structure of a prokaryotic cyclic nucleotide-gated ion channel. *Proc Natl Acad Sci U S A* **114**, 4430-4435, doi:10.1073/pnas.1700248114 (2017).

75 Rheinberger, J., Gao, X., Schmidpeter, P. A. & Nimigean, C. M. Ligand discrimination and gating in cyclic nucleotide-gated ion channels from apo and partial agonist-bound cryo-EM structures. *Elife* **7**, doi:10.7554/eLife.39775 (2018).

76 Zagotta, W. N. *et al.* Structural basis for modulation and agonist specificity of HCN pacemaker channels. *Nature* **425**, 200-205, doi:10.1038/nature01922 (2003).

77 Saponaro, A. *et al.* Structural basis for the mutual antagonism of cAMP and TRIP8b in regulating HCN channel function. *Proc Natl Acad Sci U S A* **111**, 14577-14582, doi:10.1073/pnas.1410389111 (2014).

78 Lolicato, M. *et al.* Tetramerization dynamics of C-terminal domain underlies isoform-specific cAMP gating in hyperpolarization-activated cyclic nucleotide-gated channels. *J Biol Chem* **286**, 44811-44820, doi:10.1074/jbc.M111.297606 (2011).

79 Taraska, J. W., Puljung, M. C., Olivier, N. B., Flynn, G. E. & Zagotta, W. N. Mapping the structure and conformational movements of proteins with transition metal ion FRET. *Nat Methods* **6**, 532-537, doi:10.1038/nmeth.1341 (2009).

80 Altieri, S. L. *et al.* Structural and energetic analysis of activation by a cyclic nucleotide binding domain. *J Mol Biol* **381**, 655-669, doi:10.1016/j.jmb.2008.06.011 (2008).

81 Goldschen-Ohm, M. P. *et al.* Structure and dynamics underlying elementary ligand binding events in human pacemaking channels. *Elife* **5**, doi:10.7554/eLife.20797 (2016).

82 Kaupp, U. B. *et al.* Primary structure and functional expression from complementary DNA of the rod photoreceptor cyclic GMP-gated channel. *Nature* **342**, 762-766, doi:10.1038/342762a0 (1989).

83 Zhou, L. & Siegelbaum, S. A. Gating of HCN channels by cyclic nucleotides: residue contacts that underlie ligand binding, selectivity, and efficacy. *Structure* **15**, 655-670, doi:10.1016/j.str.2007.04.012 (2007).

84 Chen, S., Wang, J. & Siegelbaum, S. A. Properties of hyperpolarization-activated pacemaker current defined by coassembly of HCN1 and HCN2 subunits and basal modulation by cyclic nucleotide. *J Gen Physiol* **117**, 491-504, doi:10.1085/jgp.117.5.491 (2001).

85 Altenhofen, W. *et al.* Control of ligand specificity in cyclic nucleotide-gated channels from rod photoreceptors and olfactory epithelium. *Proc Natl Acad Sci U S A* **88**, 9868-9872, doi:10.1073/pnas.88.21.9868 (1991).

86 Liu, D. T., Tibbs, G. R., Paoletti, P. & Siegelbaum, S. A. Constraining ligand-binding site stoichiometry suggests that a cyclic nucleotide-gated channel is composed of two functional dimers. *Neuron* **21**, 235-248, doi:10.1016/s0896-6273(00)80530-9 (1998).

87 Kaupp, U. B. & Seifert, R. Cyclic nucleotide-gated ion channels. *Physiol Rev* **82**, 769-824, doi:10.1152/physrev.00008.2002 (2002).

88 Nakamura, T. & Gold, G. H. A cyclic nucleotide-gated conductance in olfactory receptor cilia. *Nature* **325**, 442-444, doi:10.1038/325442a0 (1987).

89 Porro, A. *et al.* The HCN domain couples voltage gating and cAMP response in hyperpolarization-activated cyclic nucleotide-gated channels. *Elife* **8**, doi:10.7554/eLife.49672 (2019).

90 Whicher, J. R. & MacKinnon, R. Structure of the voltage-gated K(+) channel Eag1 reveals an alternative voltage sensing mechanism. *Science* **353**, 664-669, doi:10.1126/science.aaf8070 (2016).

91 Stieglitz, M. S. *The control of neuronal activity and behavior by members of the HCN and TPC family* PhD thesis, Ludwigs-Maximilians-Universität München, (2018).

92 Contreras, J. E., Srikumar, D. & Holmgren, M. Gating at the selectivity filter in cyclic nucleotide-gated channels. *Proc Natl Acad Sci U S A* **105**, 3310-3314, doi:10.1073/pnas.0709809105 (2008).

93 Ramentol, R., Perez, M. E. & Larsson, H. P. Gating mechanism of hyperpolarization-activated HCN pacemaker channels. *Nat Commun* **11**, 1419, doi:10.1038/s41467-020-15233-9 (2020).

94 Waldeck, C., Vocke, K., Ungerer, N., Frings, S. & Mohrlen, F. Activation and desensitization of the olfactory cAMP-gated transduction channel: identification of functional modules. *J Gen Physiol* **134**, 397-408, doi:10.1085/jgp.200910296 (2009).

95 Hofmann, F., Biel, M., Kaupp, U. B. & International Union of, P. International Union of Pharmacology. XLII. Compendium of voltage-gated ion channels: cyclic nucleotide-modulated channels. *Pharmacol Rev* **55**, 587-589, doi:10.1124/pr.55.4.10 (2003).

96 Dzeja, C., Hagen, V., Kaupp, U. B. & Frings, S. Ca2+ permeation in cyclic nucleotide-gated channels. *EMBO J* **18**, 131-144, doi:10.1093/emboj/18.1.131 (1999).

97 Seifert, R., Eismann, E., Ludwig, J., Baumann, A. & Kaupp, U. B. Molecular determinants of a Ca2+-binding site in the pore of cyclic nucleotide-gated channels: S5/S6 segments control affinity of intrapore glutamates. *EMBO J* **18**, 119-130, doi:10.1093/emboj/18.1.119 (1999).

98 Eismann, E., Muller, F., Heinemann, S. H. & Kaupp, U. B. A single negative charge within the pore region of a cGMP-gated channel controls rectification, Ca2+ blockage, and ionic selectivity. *Proc Natl Acad Sci U S A* **91**, 1109-1113, doi:10.1073/pnas.91.3.1109 (1994).

99 Marchesi, A., Mazzolini, M. & Torre, V. Gating of cyclic nucleotide-gated channels is voltage dependent. *Nat Commun* **3**, 973, doi:10.1038/ncomms1972 (2012).

100 Arcangeletti, M., Marchesi, A., Mazzolini, M. & Torre, V. Multiple mechanisms underlying rectification in retinal cyclic nucleotide-gated (CNGA1) channels. *Physiol Rep* **1**, e00148, doi:10.1002/phy2.148 (2013).

101 Bohm, S. *et al.* A gene therapy for inherited blindness using dCas9-VPR-mediated transcriptional activation. *Sci Adv* **6**, eaba5614, doi:10.1126/sciadv.aba5614 (2020).

102 Stephens, A. D., Zacharopoulou, M. & Kaminski Schierle, G. S. The Cellular Environment Affects Monomeric alpha-Synuclein Structure. *Trends Biochem Sci* **44**, 453-466, doi:10.1016/j.tibs.2018.11.005 (2019).

103 Helton, T. D., Xu, W. & Lipscombe, D. Neuronal L-type calcium channels open quickly and are inhibited slowly. *J Neurosci* **25**, 10247-10251, doi:10.1523/JNEUROSCI.1089-05.2005 (2005).

104 Vasylyev, D. V., Han, C., Zhao, P., Dib-Hajj, S. & Waxman, S. G. Dynamic-clamp analysis of wild-type human Nav1.7 and erythromelalgia mutant channel L858H. *J Neurophysiol* **111**, 1429-1443, doi:10.1152/jn.00763.2013 (2014).

105 Stöckl, G. *Charakterisierung des humanen HCN3-Kanals und seiner cAMP-Modulierbarkeit im Vergleich zu den anderen humanen HCN-Kanälen* PhD thesis, Ludwig-Maximilians-Universität München, (2007).

106 Sartiani, L., Mannaioni, G., Masi, A., Novella Romanelli, M. & Cerbai, E. The Hyperpolarization-Activated Cyclic Nucleotide-Gated Channels: from Biophysics to Pharmacology of a Unique Family of Ion Channels. *Pharmacol Rev* **69**, 354-395, doi:10.1124/pr.117.014035 (2017).

107 Azene, E. M., Xue, T., Marban, E., Tomaselli, G. F. & Li, R. A. Non-equilibrium behavior of HCN channels: insights into the role of HCN channels in native and engineered pacemakers. *Cardiovasc Res* **67**, 263-273, doi:10.1016/j.cardiores.2005.03.006 (2005).

108 Mannikko, R., Pandey, S., Larsson, H. P. & Elinder, F. Hysteresis in the voltage dependence of HCN channels: conversion between two modes affects pacemaker properties. *J Gen Physiol* **125**, 305-326, doi:10.1085/jgp.200409130 (2005).

109 Elinder, F., Mannikko, R., Pandey, S. & Larsson, H. P. Mode shifts in the voltage gating of the mouse and human HCN2 and HCN4 channels. *J Physiol* **575**, 417-431, doi:10.1113/jphysiol.2006.110437 (2006).

110 Xiao, Y. F. *et al.* Hysteresis in human HCN4 channels: a crucial feature potentially affecting sinoatrial node pacemaking. *Sheng Li Xue Bao* **62**, 1-13 (2010).

111 DiFrancesco, D. Block and activation of the pace-maker channel in calf purkinje fibres: effects of potassium, caesium and rubidium. *J Physiol* **329**, 485-507, doi:10.1113/jphysiol.1982.sp014315 (1982).

112 Pal, B., Por, A., Szucs, G., Kovacs, I. & Rusznak, Z. HCN channels contribute to the intrinsic activity of cochlear pyramidal cells. *Cell Mol Life Sci* **60**, 2189-2199, doi:10.1007/s00018-003-3187-4 (2003).

113 Bucchi, A., Tognati, A., Milanesi, R., Baruscotti, M. & DiFrancesco, D. Properties of ivabradine-induced block of HCN1 and HCN4 pacemaker channels. *J Physiol* **572**, 335-346, doi:10.1113/jphysiol.2005.100776 (2006).

114 Fedorov, V. V. *et al.* Optical mapping of the isolated coronary-perfused human sinus node. *J Am Coll Cardiol* **56**, 1386-1394, doi:10.1016/j.jacc.2010.03.098 (2010).

115 Verheijck, E. E. *et al.* Electrophysiological features of the mouse sinoatrial node in relation to connexin distribution. *Cardiovasc Res* **52**, 40-50, doi:10.1016/s0008-6363(01)00364-9 (2001).

116 Liu, J., Dobrzynski, H., Yanni, J., Boyett, M. R. & Lei, M. Organisation of the mouse sinoatrial node: structure and expression of HCN channels. *Cardiovasc Res* **73**, 729-738, doi:10.1016/j.cardiores.2006.11.016 (2007).

117 Hennis, K. *et al.* Speeding Up the Heart? Traditional and New Perspectives on HCN4 Function. *Front Physiol* **12**, 669029, doi:10.3389/fphys.2021.669029 (2021).

118 Armour, J. A., Murphy, D. A., Yuan, B. X., Macdonald, S. & Hopkins, D. A. Gross and microscopic anatomy of the human intrinsic cardiac nervous system. *Anat Rec* **247**, 289-298, doi:10.1002/(SICI)1097-0185(199702)247:2<289::AID-AR15>3.0.CO;2-L (1997).

119 Armour, J. A. Potential clinical relevance of the 'little brain' on the mammalian heart. *Exp Physiol* **93**, 165-176, doi:10.1113/expphysiol.2007.041178 (2008).

120 Hanna, P. *et al.* Innervation and Neuronal Control of the Mammalian Sinoatrial Node a Comprehensive Atlas. *Circ Res* **128**, 1279-1296, doi:10.1161/CIRCRESAHA.120.318458 (2021).

121 Srinivas, M., Verselis, V. K. & White, T. W. Human diseases associated with connexin mutations. *Biochim Biophys Acta Biomembr* **1860**, 192-201, doi:10.1016/j.bbamem.2017.04.024 (2018).

122 Kanaporis, G. *et al.* Gap junction channels exhibit connexin-specific permeability to cyclic nucleotides. *J Gen Physiol* **131**, 293-305, doi:10.1085/jgp.200709934 (2008).

123 Boyett, M. R. *et al.* Connexins in the sinoatrial and atrioventricular nodes. *Adv Cardiol* **42**, 175-197, doi:10.1159/000092569 (2006).

124 Kreuzberg, M. M., Willecke, K. & Bukauskas, F. F. Connexin-mediated cardiac impulse propagation: connexin 30.2 slows atrioventricular conduction in mouse heart. *Trends Cardiovasc Med* **16**, 266-272, doi:10.1016/j.tcm.2006.05.002 (2006).

125 Fedorov, V. V. *et al.* Structural and functional evidence for discrete exit pathways that connect the canine sinoatrial node and atria. *Circ Res* **104**, 915-923, doi:10.1161/CIRCRESAHA.108.193193 (2009).

126 Fedorov, V. V., Hucker, W. J., Dobrzynski, H., Rosenshtraukh, L. V. & Efimov, I. R. Postganglionic nerve stimulation induces temporal inhibition of excitability in rabbit sinoatrial node. *Am J Physiol Heart Circ Physiol* **291**, H612-623, doi:10.1152/ajpheart.00022.2006 (2006).

127 Brox, V. F. *Optical and electrophysiological approaches to examine the role of cAMP-dependent regulation of the sinoatrial pacemaker channel HCN4* PhD thesis, Ludwig-Maximilians-Universität München, (2019).

128 O'Rourke, M. F. & Safar, M. E. Relationship between aortic stiffening and microvascular disease in brain and kidney: cause and logic of therapy. *Hypertension* **46**, 200-204, doi:10.1161/01.HYP.0000168052.00426.65 (2005).

129 Melgarejo, J. D. *et al.* Association of Fatal and Nonfatal Cardiovascular Outcomes With 24-Hour Mean Arterial Pressure. *Hypertension* **77**, 39-48, doi:10.1161/HYPERTENSIONAHA.120.14929 (2021).

130 DeMers, D. & Wachs, D. in *StatPearls* (2021).

131 Rotzer, R. D. *et al.* Implantation of Combined Telemetric ECG and Blood Pressure Transmitters to Determine Spontaneous Baroreflex Sensitivity in Conscious Mice. *J Vis Exp*, doi:10.3791/62101 (2021).

132 Kumada, M., Terui, N. & Kuwaki, T. Arterial baroreceptor reflex: its central and peripheral neural mechanisms. *Prog Neurobiol* **35**, 331-361, doi:10.1016/0301-0082(90)90036-g (1990).

133 Zeng, W. Z. *et al.* PIEZOs mediate neuronal sensing of blood pressure and the baroreceptor reflex. *Science* **362**, 464-467, doi:10.1126/science.aau6324 (2018).

134 Burke, S. D., Jordan, J., Harrison, D. G. & Karumanchi, S. A. Solving Baroreceptor Mystery: Role of PIEZO Ion Channels. *J Am Soc Nephrol* **30**, 911-913, doi:10.1681/ASN.2019020160 (2019).

135 Min, S. *et al.* Arterial Baroreceptors Sense Blood Pressure through Decorated Aortic Claws. *Cell Rep* **29**, 2192-2201 e2193, doi:10.1016/j.celrep.2019.10.040 (2019).

136 Lu, H. J. *et al.* Tentonin 3/TMEM150C senses blood pressure changes in the aortic arch. *J Clin Invest* **130**, 3671-3683, doi:10.1172/JCI133798 (2020).

137 Wehrwein, E. A. & Joyner, M. J. Regulation of blood pressure by the arterial baroreflex and autonomic nervous system. *Handb Clin Neurol* **117**, 89-102, doi:10.1016/B978-0-444-53491-0.00008-0 (2013).

138 Kirchheim, H. R. Systemic arterial baroreceptor reflexes. *Physiol Rev* **56**, 100-177, doi:10.1152/physrev.1976.56.1.100 (1976).

139 Martinka, P. *et al.* Mechanisms of blood pressure variability-induced cardiac hypertrophy and dysfunction in mice with impaired baroreflex. *Am J Physiol Regul Integr Comp Physiol* **288**, R767-776, doi:10.1152/ajpregu.00445.2004 (2005).

140 Cowley, A. W., Jr., Liard, J. F. & Guyton, A. C. Role of baroreceptor reflex in daily control of arterial blood pressure and other variables in dogs. *Circ Res* **32**, 564-576, doi:10.1161/01.res.32.5.564 (1973).

141 Thrasher, T. N. Baroreceptors, baroreceptor unloading, and the long-term control of blood pressure. *Am J Physiol Regul Integr Comp Physiol* **288**, R819-827, doi:10.1152/ajpregu.00813.2004 (2005).

142 Mussalo, H. *et al.* Baroreflex sensitivity in essential and secondary hypertension. *Clin Auton Res* **12**, 465-471, doi:10.1007/s10286-002-0069-z (2002).

143 Mortara, A. *et al.* Arterial baroreflex modulation of heart rate in chronic heart failure: clinical and hemodynamic correlates and prognostic implications. *Circulation* **96**, 3450-3458, doi:10.1161/01.cir.96.10.3450 (1997).

144 La Rovere, M. T., Bigger, J. T., Jr., Marcus, F. I., Mortara, A. & Schwartz, P. J. Baroreflex sensitivity and heart-rate variability in prediction of total cardiac mortality after myocardial infarction. ATRAMI (Autonomic Tone and Reflexes After Myocardial Infarction) Investigators. *Lancet* **351**, 478-484, doi:10.1016/s0140-6736(97)11144-8 (1998).

145 Robinson, T. G., Dawson, S. L., Eames, P. J., Panerai, R. B. & Potter, J. F. Cardiac baroreceptor sensitivity predicts long-term outcome after acute ischemic stroke. *Stroke* **34**, 705-712, doi:10.1161/01.STR.0000058493.94875.9F (2003).

146 DiFrancesco, D. The role of the funny current in pacemaker activity. *Circ Res* **106**, 434-446, doi:10.1161/CIRCRESAHA.109.208041 (2010).

8 Publications

Original publications

Böhm S*, Splith V*, Riedmayr LM, **Rötzer RD**, Gasparoni G, Nordström KJV, Wagner JE, Hinrichsmeyer KS, Walter J, Wahl-Schott C, Fenske S, Biel M, Michalakis S, Becirovic E (2020) ***A gene therapy for inherited blindness using dCas9-VPR-mediated transcriptional activation.*** Sci Adv 6(34), eaba5614, doi:10.1126/sciadv.aba5614

* *Authors contributed equally*

Hammelmann V, Stieglitz MS, Hülle H, Le Meur K, Kass J, Brümmer M, Gruner C, **Rötzer RD**, Fenske S, Hartmann J, Zott B, Lüthi A, Spahn S, Moser M, Isbrandt D, Ludwig A, Konnerth A, Wahl-Schott C, Biel M (2019) ***Abolishing cAMP sensitivity in HCN2 pacemaker channels induces generalized seizures.*** JCI Insight 4(9), doi: 10.1172/jci.insight.126418

Fenske S, Hennis K*, **Rötzer RD***, Brox VF, Becirovic E, Scharr A, Gruner C, Ziegler T, Mehlfeld V, Brennan J, Efimov IR, Pauža AG, Moser M, Wotjak CT, Kupatt C, Gönner R, Zhang R, Zhang H, Zong X, Biel M, Wahl-Schott C (2020) ***cAMP-dependent regulation of HCN4 controls the tonic entrainment process in sinoatrial node pacemaker cells.*** Nat Commun 11, 5555, doi: 10.1038/s41467-020-19304-9

* *Authors contributed equally*

Rötzer RD, Brox VF, Hennis K, Thalhammer SB, Biel M, Wahl-Schott C, Fenske S (2021) ***Implantation of Combined Telemetric ECG and Blood Pressure Transmitters to Determine Spontaneous Baroreflex Sensitivity in Conscious Mice.*** J Vis Exp, doi: 10.3791/62101

Review

Hennis K, **Rötzer RD**, Piantoni C, Biel M, Wahl-Schott C, Fenske S (2021) ***Speeding up the heart? Traditional and new perspectives on HCN4 function.*** Front Physiol

Submitted manuscripts

Hennis K, **Rötzer RD**, Rilling J, Thalhammer SB, Biel M, Wahl-Schott C, Stefanie F (2021) ***Characterization of the cardiac conduction system, atrial and ventricular vulnerability using in vivo and ex vivo electrophysiological study in the mouse heart.*** Under revision at Nature protocols.

Conference participations and posters

Rötzer R, Dirschl S, Hennis K, Yang Y, Biel M, Fenske S ***Molecular and electrophysiological characterization of novel HCN2 mutations associated with cardiac arrhythmias.*** *16th Munich Heart Alliance Meeting*, 17th July 2019, Bernried

Rötzer R ***Elucidating the effect of cAMP on HCN channel current amplitude.*** *10th Nanion User Meeting Germany*, 17th – 18th October 2019, Munich

9 Acknowledgement

Hiermit möchte ich mich bei allen bedanken, die das Entstehen dieser Doktorarbeit möglich gemacht haben. Es war eine sehr spannende und lehrreiche Zeit für mich.

Mein aufrichtigster Dank gilt im Besonderen...

... Prof. Dr. Martin Biel für die Aufnahme in den Arbeitskreis, die andauernde Förderung, die stets offene Tür bei Fragen und Problemen und die Übernahme des Zweitgutachtens.

... Prof. Dr. Christian Wahl-Schott für die gute Betreuung, die sehr guten Ideen bei bearbeiteten Projekten und nicht zuletzt für die Möglichkeit die Dissertation zu verwirklichen.

… PD Dr. Stefanie Fenske für die wissenschaftliche Unterstützung, sehr gute Betreuung und die stete Ermutigung zum Perfektionieren.

… Konstantin Hennis für die entspannte Sitznachbarschaft, super Unterstützung in anstrengenden Publikationszeiten, den steten Zusammenhalt und die Kollegialität!

... Dr. Verena Brox für die gemeinsame, lustige Zeit in der Herz-Gruppe, gute Laune und Kollegialität in meiner ersten Promotionshälfte!

… Dr. Verena Mehlfeld für die vielen exzellenten Antworten auf molekularbiologische Fragen und Hilfestellungen. Sei es mir oder den Herzgruppen-Bachelor-/Masterstudenten gegenüber. Herzlichen Dank dafür! Danke auch für die Möglichkeit am Neuro-HCN2-Projekt mitgewirkt haben zu können.

... PD Dr. Elvir Becirovic für die Möglichkeit mich an einem gentherapeutischen Projekt mitwirken zu lassen.

… Klara für die stilsichere Unterstützung im und außerhalb des Labors!

… den weiteren aktuellen „Herz“-Kollegen Stefan, Julia und Vivi. Danke Julia für deinen tierärztlichen Rat, der nicht besser sein könnte!

... den weiteren aktuellen wie auch ehemaligen Kollegen (Ella, Sybille, Lisa, Vicky etc.) des gesamten Arbeitskreises für die angenehme Arbeitsatmosphäre, lustige Mittagstische (besonders als es noch en vogue war sich zu fünfzehnt in eine Miniküche zu drängen), anregende Diskussionen und die Hilfsbereitschaft.

Ein außerordentlicher Dank gilt meinen Eltern, ohne deren konstanten Rückhalt das Ganze nicht möglich gewesen wäre!
Zu guter Letzt möchte ich mich von tiefstem Herzen bei meinem Partner Oliver bedanken, der mich mit einem stets offenen Ohr durch die Promotion begleitet hat und mit dem es so leicht fällt Gedanken auf schöne Dinge zu richten.

10 Appendix

In the following, the manuscripts I to IV are reprinted:

I. **Böhm et al.**, (2020) *A gene therapy for inherited blindness using dCas9-VP-mediated transcriptional activation*, **Science Advances**, 6(34): eaba5614

II. **Hammelmann et al.**, (2019) *Abolishing cAMP sensitivity in HCN2 pacemaker channels induces generalized seizures*, **JCI Insight**, 4(9): e126418

III. **Fenske et al.**, (2020) *cAMP-dependent regulation of HCN4 controls the tonic entrainment process in sinoatrial node pacemaker cells*, **Nature Communications**, 11, 5555

IV. **Rötzer et al.**, (2021) *Implantation of Combined Telemetric ECG and Blood Pressure Transmitters to Determine Spontaneous Baroreflex Sensitivity in Conscious Mice*, **Journal of Visualized Experiments**, (168): e62101

Manuscript I

DISEASES AND DISORDERS

A gene therapy for inherited blindness using dCas9-VPR–mediated transcriptional activation

Sybille Böhm[1,2]*, Victoria Splith[1,2]*, Lisa Maria Riedmayr[1,2], René Dominik Rötzer[1,2], Gilles Gasparoni[3], Karl J. V. Nordström[3], Johanna Elisabeth Wagner[1,2], Klara Sonnie Hinrichsmeyer[1,2], Jörn Walter[3], Christian Wahl-Schott[4], Stefanie Fenske[1,2], Martin Biel[1,2], Stylianos Michalakis[1,2,5], Elvir Becirovic[1,2†]

Catalytically inactive dCas9 fused to transcriptional activators (dCas9-VPR) enables activation of silent genes. Many disease genes have counterparts, which serve similar functions but are expressed in distinct cell types. One attractive option to compensate for the missing function of a defective gene could be to transcriptionally activate its functionally equivalent counterpart via dCas9-VPR. Key challenges of this approach include the delivery of dCas9-VPR, activation efficiency, long-term expression of the target gene, and adverse effects in vivo. Using dual adeno-associated viral vectors expressing split dCas9-VPR, we show efficient transcriptional activation and long-term expression of cone photoreceptor-specific M-opsin (*Opn1mw*) in a rhodopsin-deficient mouse model for retinitis pigmentosa. One year after treatment, this approach yields improved retinal function and attenuated retinal degeneration with no apparent adverse effects. Our study demonstrates that dCas9-VPR–mediated transcriptional activation of functionally equivalent genes has great potential for the treatment of genetic disorders.

INTRODUCTION

Various inherited disorders are caused by mutations in genes for which counterparts with similar function but distinct expression pattern exist. CRISPR-Cas–mediated transcriptional activation (transactivation) of such functionally equivalent genes is one attractive therapeutic strategy to compensate for the function of their mutant counterparts. Different transcriptional activators have been fused to catalytically inactive Cas9 (dCas9) proteins and evaluated regarding their transactivation efficiency. Among the tested candidates, the catalytically inactive dCas9 fused to transcriptional activators (dCas9-VPR) transactivating module shows high efficiency across different species and cell types (*1*). However, because of its size (5.8 kb), dCas9-VPR exceeds the genome packaging capacity of recombinant adeno-associated viral (rAAV) vectors, which are currently the gold standard for gene delivery to native tissues and for gene therapy. A previous study provided a proof of principle for reconstitution of split dCas9-VPR using dual rAAVs in vitro and in vivo in wild-type (WT) mice (*2*). Nonetheless, the therapeutic potential of this tool has not been evaluated in disease models so far. In particular, the long-term effects, such as efficiency and expression of the transactivated gene as well as the potential adverse effects, remained largely unexplored.

Inherited retinal dystrophies (IRDs) affect several million people worldwide. Retinitis pigmentosa (RP) is the most common IRD subtype and primarily affects rod photoreceptors (*3*). By contrast, achromatopsia (ACHM) is among the most frequent IRDs affecting the cones (*4*). Many genes associated with RP or ACHM encode members of the phototransduction cascade in rods or cones. The key phototransduction molecules in these cells are encoded by distinct yet functionally equivalent genes, and mutations in many of these genes, such as the visual pigments (opsins) or cyclic nucleotide-gated (CNG) ion channels, are associated with different types of blinding disorders. Mutations in the rhodopsin gene (*RHO*) are the leading cause for RP, whereas mutations in the cone CNG channel genes (*CNGA3* and *CNGB3*) are the most frequent cause for ACHM. While rods only express rhodopsin, most mammals including mice express two opsin types in cones, the short wavelength–sensitive S-opsin (*Opn1sw*) and the medium wavelength–sensitive M-opsin (*Opn1mw*). CNG channels are heterotetrameric complexes composed of the channel function defining CNG A and the modulatory CNG B subunit. The native rod CNG channels contain CNGA1 and CNGB1 and their cone counterparts CNGA3 and CNGB3 subunits, respectively. A previous study has shown that rod and cone CNG A subunits can also form functional units with the CNG B subunits from the other photoreceptor type, i.e., CNGA1 with CNGB3 and CNGA3 with CNGB1 (*5*). Given the functional similarity between native and chimeric CNG channels, activation of the respective functionally equivalent gene in rods or cones appears an attractive treatment option. Recent work on mouse models has shown that rhodopsin and cone opsins are also functionally equivalent (*6*–*9*). This suggests that activation of genes encoding for cone opsins in rods could compensate for the defective rhodopsin in the respective animal models.

Here, using dCas9-VPR, we were able to efficiently transactivate the *Rho* homolog *Opn1mw* and the rod-specific *Cnga3* homolog *Cnga1* in vitro. Using a dual rAAV vector system for split dCas9-VPR–mediated *Opn1mw* activation in a rhodopsin-deficient mouse model for RP, we also demonstrate that this treatment results in safe and efficient long-term expression, gain in retinal function, and delay of retinal degeneration.

RESULTS

Cnga1 and Opn1mw transactivation in transiently transfected 661W and MEF cells

To test for the feasibility and efficiency of ectopic activation of non-expressed or poorly expressed genes, we transfected different mouse cell lines with dCas9-VPR in combination with single guide RNAs

[1]Center for Integrated Protein Science Munich CIPSM, Munich, Germany. [2]Department of Pharmacy - Center for Drug Research, Ludwig-Maximilians-Universität München, Munich, Germany. [3]Department of Genetics, Saarland University, Saarbrücken, Germany. [4]Institute for Neurophysiology, Hannover Medical School (MHH), Hanover, Germany. [5]Department of Ophthalmology, Ludwig-Maximilians-Universität München, Munich, Germany.
*These authors contributed equally to this work.
†Corresponding author. Email: elvir.becirovic@cup.uni-muenchen.de

(sgRNAs) binding to the promoter region of either murine *Cnga1* or *Opn1mw* (Fig. 1A). As the transactivation efficiency can be increased with a growing number of sgRNAs (*1*), we used a combination of three sgRNAs for each of the genes. Transactivation of *Cnga1* was addressed in 661W cells, immortalized derivatives of murine cones lacking *Cnga1* expression (*10*). As 661W cells express *Opn1mw* endogenously, we used mouse embryonic fibroblast (MEF) cells for transactivation of this gene.

In 661W cells transiently cotransfected with the dCas9-VPR cassette and *Cnga1*-specific sgRNAs, we observed efficient transactivation of *Cnga1* on the transcript level, which was absent in control cells expressing the *lacZ* sgRNA (Fig. 1B and fig. S1A). Nevertheless, no Cnga1 protein signal was detectable in cells labeled with a specific antibody under these conditions.

When addressing the *Opn1mw* transactivation in MEF cells, we detected *Opn1mw* transcript in both naïve and in *lacZ* sgRNA–expressing cells, indicating endogenous expression of *Opn1mw* in this cell line (fig. S1B). The efficiency of dCas9-mediated transactivation is known to correlate negatively with the basal expression level of a given gene (*1*). Nevertheless, despite the basal *Opn1mw* expression, a robust transactivation of *Opn1mw* was detectable in MEF cells coexpressing dCas9-VPR and *Opn1mw*-specific sgRNAs (Fig. 1C and fig. S1B). A combination of another set of three *Opn1mw* sgRNAs could not further improve the transactivation efficiency (fig. S1, C and D). These results show that, in transiently transfected cells, both *Cnga1* and *Opn1mw* can be efficiently transactivated using dCas9-VPR.

Transactivation in cell lines stably expressing inducible dCas9-VPR sgRNA cassettes

Next, we analyzed whether Cnga1 protein can be detected in a transfection-independent system. For this, we created 661W and MEF cell lines with stable integration of expression cassettes for doxycycline (DOX)–inducible dCas9-VPR in combination with *Cnga1*, *Opn1mw*, or *lacZ*-specific sgRNAs [661W–piggyBac (pb) and MEF-pb, respectively]. When analyzing the *Cnga1* transcript in the 661W cells, we detected a DOX concentration–dependent transactivation of this gene. However, robust *Cnga1* transactivation was also present in the absence of DOX, suggesting a leaky activity of the DOX-dependent promoter driving dCas9-VPR expression. Moreover, an increase in *Cnga1* expression was only obtained for the lowest DOX concentration (5 ng/ml), whereas *Cnga1* levels were decreasing with further increase in drug concentration (Fig. 1D). Thus, when exceeding the optimal DOX concentration, there was an inverse correlation between dCas9-VPR transcript levels and the efficiency of *Cnga1* transactivation (Fig. 1E). Very similar results were obtained in MEF cells stably expressing the dCas9-VPR cassette and *Opn1mw* sgRNAs, indicating that this effect was gene independent (Fig. 1, F and G). In contrast to *Cnga1*, there was no apparent *Opn1mw* transactivation in MEFs stably expressing dCas9-VPR and *Opn1mw*-specific sgRNAs in the absence of DOX, which is most likely due to the endogenous basal expression of this gene in this cell line.

In summary, these results suggest that an optimal window for transactivation exists in which sufficient levels of dCas9-VPR protein support maximal levels of gene expression. Upon exceeding the

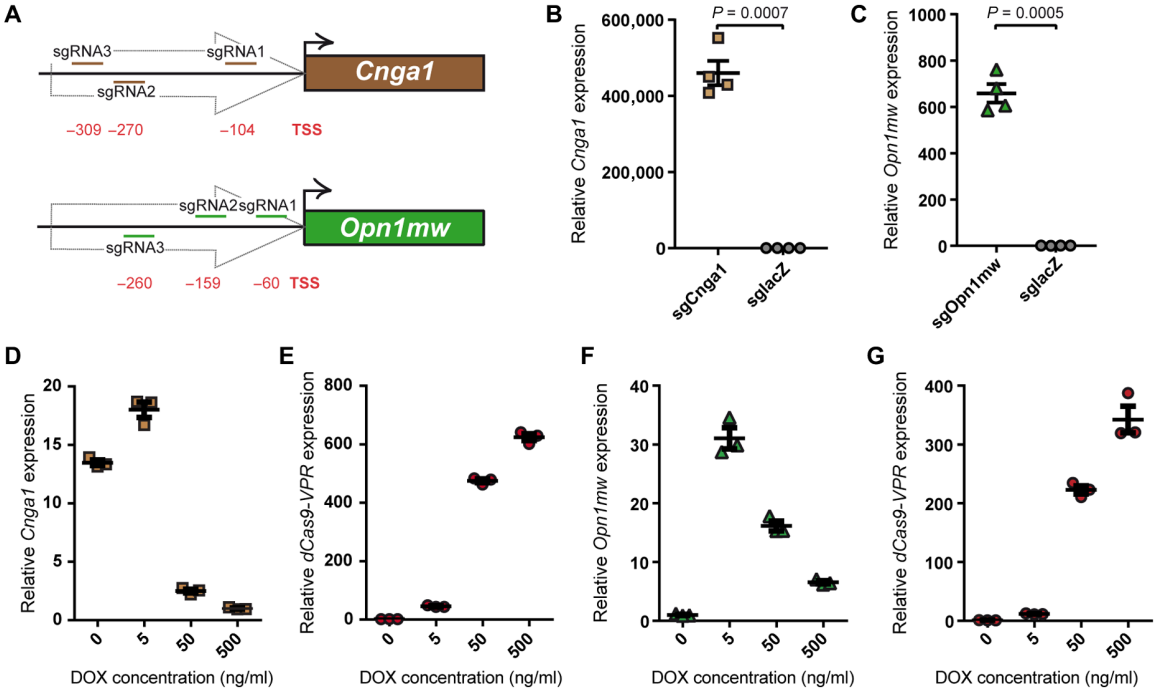

Fig. 1. Transactivation of *Cnga1* and *Opn1mw* via dCas9-VPR. (**A**) Binding position of the three sgRNAs used for targeting dCas9-VPR to the promoter of the *Cnga1* or *Opn1mw* gene, respectively. The relative distance of each sgRNA to the transcription start site (TSS) of the target gene is given in base pairs. (**B**) Quantitative reverse transcription polymerase chain reaction (qRT-PCR) from 661W cells cotransfected with dCas9-VPR and either *Cnga1* or *lacZ* sgRNAs. *Cnga1* expression was normalized to the *lacZ* control. (**C**) qRT-PCR from MEF cells cotransfected with dCas9-VPR and either *Opn1mw* or *lacZ* sgRNAs. *Opn1mw* expression was normalized to the *lacZ* control. A two-tailed unpaired *t* test with Welch's correction was used for statistical analysis in (B) and (C). (**D** to **G**) qRT-PCR from 661W-pb (D and E) or MEF-pb cells (F and G) cultured at different doxycycline (DOX) concentrations as indicated. *Cnga1* expression was normalized to DOX (500 ng/ml), and *Opn1mw* and dCas9-VPR expression was normalized to DOX (0 ng/ml).

optimal dCas9-VPR levels, there is a gradual decrease in transactivation efficiency.

Analysis of protein expression and function in transactivated cells

Next, we assessed the Cnga1 and M-opsin protein expression in the corresponding stable cell lines treated with the optimal DOX concentration. Under these conditions, no evident increase in M-opsin protein expression was detectable when compared to the control cells (fig. S1E). For Cnga1, however, we could detect a robust signal that was absent in the *lacZ* sgRNA–expressing 661W cell line (Fig. 2A). To address whether functional channels can be formed from the proteins expressed from the transactivated *Cnga1* locus, we conducted electrophysiological recordings in 661W cells cultured under optimal DOX concentration. In contrast to the *lacZ* control cell line lacking any CNG channel-like responses, several Cnga1 channel–specific characteristics including guanosine 3′,5′-cyclic monophosphate (cGMP) sensitivity, calcium, and magnesium blockage and outward rectification could be measured upon transactivation of this gene (Fig. 2, B to D). This indicates that successful transactivation by dCas9-VPR can lead to fully functional Cnga1 channels.

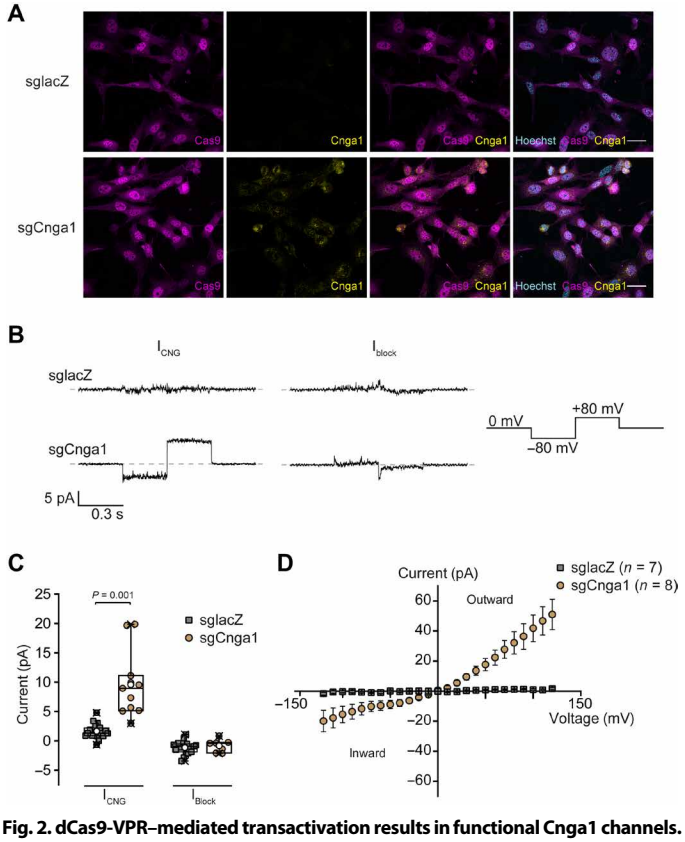

Fig. 2. dCas9-VPR–mediated transactivation results in functional Cnga1 channels. (**A**) Immunostainings of 661W-pb cells stably expressing dCas9-VPR and *lacZ*- (sglacZ, top row) or *Cnga1*-specific sgRNAs (sgCnga1, bottom row) in the presence of DOX (5 ng/ml) using Cas9- and Cnga1-specific antibodies. Scale bar, 30 μm. (**B**) Representative current traces recorded from inside out patches of DOX-induced 661W-pb cells in the presence of 300 μM cGMP (left, I_{CNG}) or cGMP and Ca^{2+}/Mg^{2+} (right, I_{block}). (**C**) Quantification of the cGMP-induced currents in the absence (I_{CNG}) or presence of Ca^{2+}/Mg^{2+} (I_{block}) (unpaired *t* test with Welch's correction, two-tailed). (**D**) Current-voltage plot of cGMP-induced currents from sgCnga1 or sglacZ membrane patches.

Cnga1 and Opn1mw transactivation in cells expressing split intein dCas9-VPR

Owing to the limited genome packaging capacity of rAAVs, the entire dCas9-VPR cassette cannot be packaged into a single rAAV vector for in vivo delivery. To circumvent this limitation, two recent studies took advantage of the split intein technology to reconstitute (d)Cas9-VPR or its derivatives at the protein level upon codelivery of two separate dual rAAVs, each of which expressing one half of the split *Sp*Cas9 cassette (*2*, *11*). The split intein-mediated reconstitution efficiency is known to depend on the position of the intein integration within the corresponding protein (*12*). The aforementioned studies addressed the transactivation of (d)Cas9-VP(R) split either after the amino acid position E573 (*11*) or V713 (fig. S1F) (*2*). Nevertheless, to our best knowledge, no quantitative or comparative data with respect to the reconstitution efficiency resulting from these two approaches are available so far. As such data would be very helpful to achieve optimal results in vivo, we first set out to compare the reconstitution efficiency for both approaches side-by-side at the protein level. To this end, we transiently cotransfected human embryonic kidney (HEK) 293 cells with plasmids encoding the *Sp*Cas9 halves intersected after the E573 or V713 position (fig. S1G) and quantified the resulting reconstitution efficiency. We found that the reconstitution efficiency of the *Sp*Cas9 variant split after V713 (56.9 ± 2.1%) was considerably higher than its counterpart split after the E573 position (33.3 ± 2.1%) (fig. S1H).

Next, we examined whether the coexpression of split dCas9-V713-VPR fragments also leads to efficient transactivation of *Cnga1* and *Opn1mw* in the respective cells. While the transactivation efficiency for both target genes originating from the split dCas9-VPR was lower than from full-length dCas9-VPR, it still appeared robust and high enough in relation to the respective controls (fig. S1, I and J). Together, we show that dCas9-VPR split after the V713 position can transactivate both *Cnga1 and Opn1mw* in cell culture experiments and was therefore used for the subsequent in vivo experiments.

Split dCas9-VPR efficiently transactivates cone opsins in WT mice

We next focused on activation of *Opn1mw* in rod photoreceptors to provide an in vivo proof of concept for transactivation of functionally equivalent genes using split dCas9-VPR dual AAVs. For this purpose, we coinjected titer-matched dual rAAVs expressing split dCas9-VPR under control of a human rhodopsin promoter and *Opn1mw*-specific sgRNAs (Fig. 3A). Given the high percentage of rods, an activation of *Opn1mw* in this cell type is expected to superimpose the endogenous *Opn1mw* mRNA and protein signal originating from the more sparse cones, which make up only 3% of the total photoreceptor population in mice. For initial experiments, we used WT (+/+) animals subretinally injected on postnatal day 28 (P28) with split dCas9-VPR dual rAAVs. Four weeks after injection, a robust increase in *Opn1mw* transcript levels was observed in eyes coinjected with dual rAAVs compared to saline-injected eyes (Fig. 3B). This up-regulation of *Opn1mw* transcript was also confirmed by RNA sequencing (RNA-seq) (fig. S2A). Moreover, we could detect a strong M-opsin signal using an M-opsin–specific antibody in rod photoreceptor outer segments (Fig. 3C). This rod photoreceptor–specific expression of M-opsin was absent in untreated retinas, which only show M-opsin signal in

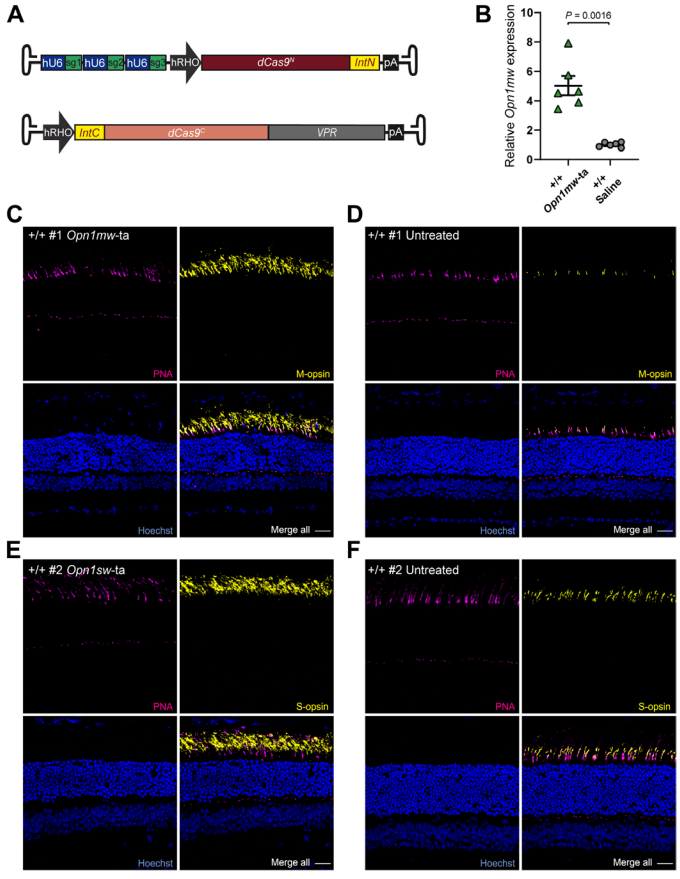

Fig. 3. Split dCas9-VPR–mediated transactivation of *Opn1mw* and *Opn1sw* in WT mice. (**A**) Scheme of split dCas9-VPR and sgRNA encoding dual rAAV vectors used for transactivation of *Opn1mw* (B to D) and *Opn1sw* (E and F) in C57Bl/6J WT (+/+) mice. (**B**) qRT-PCR for *Opn1mw* expression upon transactivation 4 weeks after injection (*Opn1mw*-ta). The expression was normalized to control eyes injected with NaCl solution (saline, $n = 6$ eyes, paired t test, two-tailed). (**C** to **F**) Immunolabeling of two +/+ mice injected with *Opn1mw*- (C) or *Opn1sw*-transactivating dual AAVs (E). The contralateral eyes (D and F) of both mice served as control (untreated) (D and F). Peanut agglutinin (PNA; magenta) was used as marker for cones. Scale bars, 30 μm.

cone photoreceptors (Fig. 3D). Encouraged by this finding, we addressed whether S-opsin (*Opn1sw*), another *Rho* homolog and potential candidate for transactivation in rhodopsin-deficient mice, can also be transactivated in rods using the same approach. Akin to *Opn1mw*, in retinas expressing split dCas9-VPR dual rAAVs and *Opn1sw*-specific sgRNAs, we could also detect S-Opsin protein in rod outer segments (Fig. 3, E and F). Notably, there was an evident variability in protein expression of transactivated M-Opsin and S-Opsin from experiment to experiment (fig. S2, B to E).

Opn1mw transactivation delays retinal degeneration and improves retinal function in Rho$^{+/-}$ mice

Next, we also tested whether *Opn1mw* transactivation is sufficient to ameliorate the RP phenotype in the heterozygous rhodopsin-deficient (Rho$^{+/-}$) RP mouse model (*13*). In contrast to Rho$^{-/-}$ mice, which completely lack rod outer segments from birth, heterozygous mice are capable of developing shortened but functional outer segments (*13*, *14*), which is expected to be an important prerequisite for treatments requiring injections at later time points. Rho$^{+/-}$ mice were subretinally injected on P14 with titer-matched dual rAAV vectors expressing the split dCas9-VPR and *Opn1mw* sgRNAs. The contralateral control eye was injected with a NaCl (saline) solution. As Rho$^{+/-}$ mice show a slow course of retinal degeneration (*13*), we assessed the effects of our treatment 1 year after injection. Retinal degeneration is accompanied by a reduction of photoreceptors, a condition that can be addressed noninvasively by optical coherence tomography (OCT) measuring the thickness of the outer nuclear layer (ONL). OCT recordings from eyes expressing split dCas9-VPR and *Opn1mw* sgRNAs revealed an increase in the ONL thickness compared to the contralateral saline-injected eye, suggesting that our treatment is capable of delaying the degeneration (Fig. 4A and fig. S2F). Similar results were obtained when comparing the ONL thickness between treated and saline-injected eyes using an independent method based on histological analysis of retinal cryosections (fig. S2G).

To assess beneficial effects of our approach on rod-mediated (scotopic) and cone-mediated (photopic) retinal function, electroretinography (ERG) measurements were performed in dark- and light-adapted Rho$^{+/-}$ mice, respectively (Fig. 4, B to G, and figs. S3 and S4). The associated statistical analysis has been conducted in two different ways: (i) We performed a multiple comparison test to compare the ERG amplitudes at the different light intensities of all three groups (WT and treated or saline-injected Rho$^{+/-}$ mice; Fig. 4), and (ii) we made a paired comparison of ERG amplitudes between treated and saline-injected eyes only (fig. S5).

In light-adapted animals, an increase in the a-wave amplitude of dual rAAV–injected eyes at the highest light flash intensity was achieved compared to saline-injected eyes and untreated WT animals (Fig. 4D). Moreover, when performing a pairwise comparison of the treated eyes to the corresponding saline-injected counterparts only, an increase in photopic a-wave amplitudes could be observed for the two highest flash intensities (fig. S5A). This suggests that under these conditions, M-opsin expressing rods might respond to cone-activating intensities. A slight tendential improvement was also detectable in the photopic b-wave amplitudes in treated eyes at the highest flash intensity (Fig. 4E and fig. S5B). When addressing the rod-mediated function in dark-adapted animals, we could measure a slight tendency for improvement of the scotopic a-wave toward WT-like responses (Fig. 4F and fig. S5C). In comparison, a robust trend toward an improvement of the scotopic b-wave was observed when comparing the treated eyes to their saline-injected counterparts (Fig. 4G and fig. S5D). This trend was more pronounced with increasing light intensities, further supporting the assumption that treated rods expressing M-opsin are capable of responding to cone-activating stimuli. The individual P values for all ERG measurements shown in Fig. 4 are summarized in fig. S5E. Conclusively, these data suggest that *Opn1mw* transactivation can ameliorate retinal degeneration and results in partially improved retinal function in the Rho$^{+/-}$ RP mouse model.

Opn1mw transactivation reduces apoptosis without inducing gliosis or invasion of immune responsive cells in Rho$^{+/-}$ mice

In another set of experiments, we also analyzed the expression of M-opsin protein and markers for potential gliosis, apoptosis, or immune response in the retinas of the mice used for OCT and ERG measurements. Analogous to the results obtained in WT mice (cf. Fig. 3C and fig. S2), we found a considerable expression of transactivated M-opsin in the rod outer segments of injected animals, which, however,

varied between animals (Fig. 5, A and B, and figs. S6 and S7). Furthermore, to assess the translational potential of this approach, we examined whether our treatment induced persistent gliosis or immune responses, which would be accompanied by proliferation of glial fibrillary acidic protein (GFAP)–positive Müller glia or ionized calcium binding adaptor molecule 1 (Iba-1)–positive microglial or mononuclear cells in the retina. Immune labeling of the retinas with these markers revealed no obvious increase in the number of glial, microglial, or mononuclear cells between the different groups in contrast to retinas of rd1 (retinal degeneration 1) mice exhibiting a fast retinal degeneration peaking on P13 (Fig. 5, C to H, and fig. S8) (*15*). To investigate whether photoreceptor degeneration is caused by apoptosis in the Rho$^{+/-}$ mouse model, we conducted a terminal deoxynucleotidyl transferase–mediated deoxyuridine triphosphate nick end labeling (TUNEL) assay on retinal sections from the treated Rho$^{+/-}$ mice (Fig. 6, A and B). In this assay, we could detect a low but considerable number of TUNEL-positive cells, indicating that apoptosis is the underlying mechanism for the photoreceptor loss in this mouse model. Moreover, by comparing the number of TUNEL-positive cells per area in the transduced versus untransduced part of the treated retinas, we show that *Opn1mw* transactivation reduces apoptosis (Fig. 6C). These data further emphasize the beneficial effects of our treatment on photoreceptor survival.

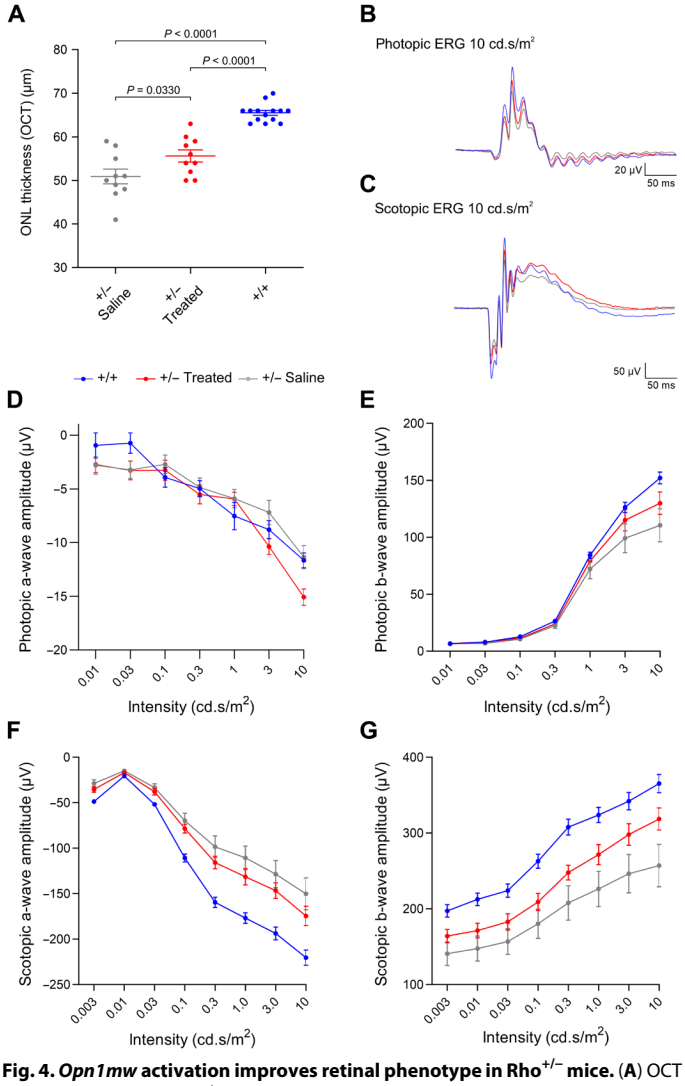

Fig. 4. *Opn1mw* activation improves retinal phenotype in Rho$^{+/-}$ mice. (**A**) OCT measurements from Rho$^{+/-}$ mice injected with a NaCl solution (+/– saline, $n = 10$ eyes) or dual rAAVs expressing split dCas9-VPR and *Opn1mw*-specific sgRNAs (+/– treated, $n = 10$ eyes). Age-matched C57Bl/6J WT mice (+/+, $n = 14$ eyes) were used as controls. Statistical analysis was performed using one-way analysis of variance (ANOVA) with Tukey's post hoc test. (**B** and **C**) Averaged photopic and scotopic traces of the same Rho$^{+/-}$ and WT mice at 10 cd.s/m^2. (**D** and **E**) Quantification of light-adapted photopic a- and b-wave amplitudes of the same groups. (**F** and **G**) Dark-adapted scotopic a- and b-wave amplitudes of the same groups plotted against different light intensities. All *P* values for each comparison (+/– treated versus +/– saline, +/– treated versus +/+, and +/– saline versus +/+) are shown in fig. S5E.

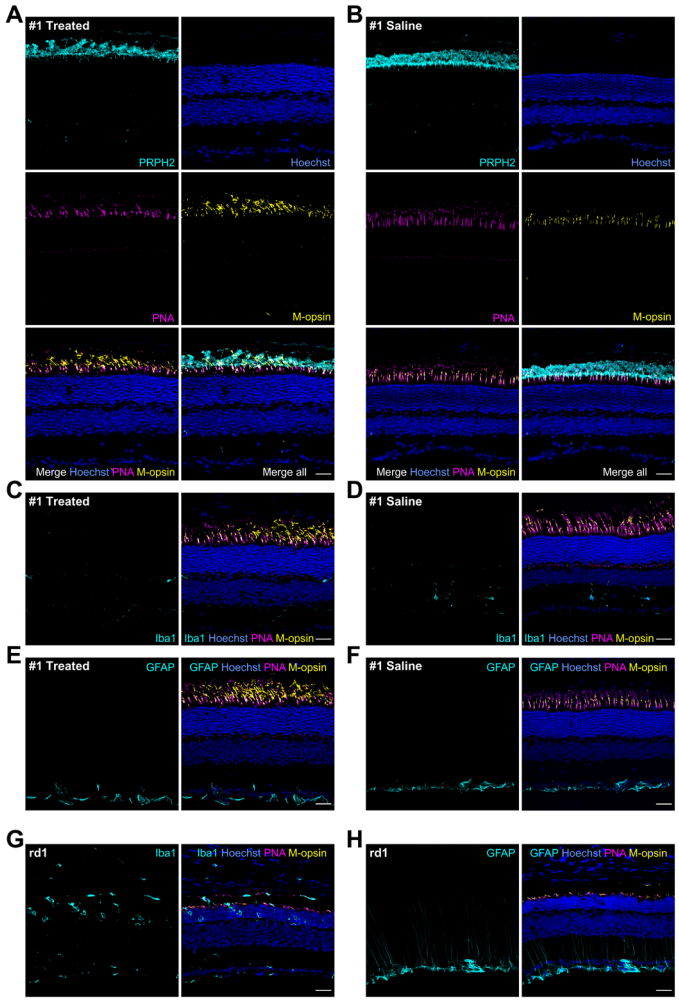

Fig. 5. Transactivation of *Opn1mw* in Rho$^{+/-}$ mice does not evoke any microglial activation or reactive gliosis. (**A** and **B**) Representative immunostainings of retinas from Rho$^{+/-}$ mouse #1 injected with either split dCas9-VPR and *Opn1mw*-specific sgRNAs (A) (treated) or NaCl (B) (saline, contralateral eye). Peripherin-2 antibody (PRPH2, cyan) was used as rod and cone outer segment marker and PNA (magenta) as marker for cones. (**C** to **F**) Immunolabeling of the same retinas with Iba1 or GFAP (cyan) to visualize microglial cells or reactive gliosis in the treated (C and E) and saline-injected contralateral eye (D and F). (**G** and **H**) Immunolabeling of retinas from *Pde6b*-deficient (rd1) mice on P13 with Iba1 (G, cyan) or GFAP (H, cyan) served as a positive control. Scale bars, 30 µm.

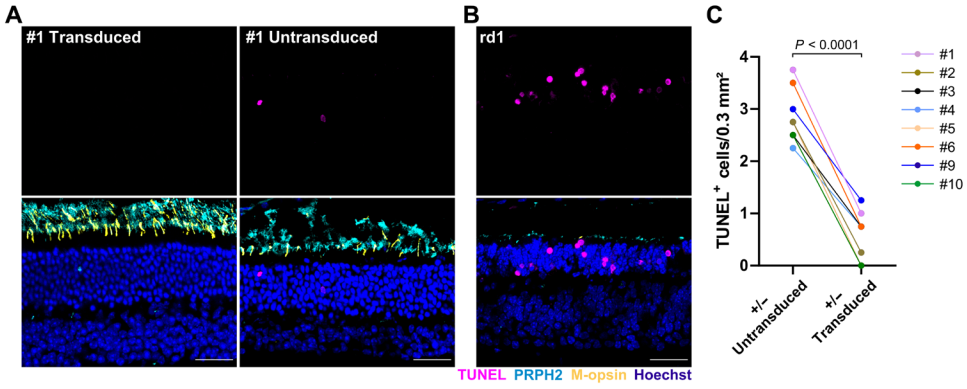

Fig. 6. Transactivation of *Opn1mw* in Rho$^{+/-}$ mice reduces apoptosis. (**A**) Representative sections of the immunolabeled retina from Rho$^{+/-}$ mouse #1 injected with split dCas9-VPR and *Opn1mw*-specific sgRNAs showing a transduced (left) or untransduced (right) area of the same retina 1 year after injection. (**B**) Immunolabeling of the rd1 mouse retina on P13 served as a positive control. TUNEL staining (magenta, top) was used to visualize apoptosis, PRPH2 (cyan) was used as rod and cone outer segment marker (bottom). Scale bar, 30 μm. (**C**) Quantification of TUNEL$^+$ cells in transduced versus untransduced areas of retinas from eight Rho$^{+/-}$ mice injected with split dCas9-VPR and *Opn1mw*-specific sgRNAs. A paired *t* test (two-tailed) was used for statistical analysis.

Characterization of untreated Rho$^{+/-}$ mice

The interpretation of the results obtained so far was largely based on the comparison of the treated Rho$^{+/-}$ mice to the saline-injected contralateral eye. To address whether the injection of saline might induce some effects on its own, we characterized the retinal degeneration and function, reactive gliosis, recruitment of immune reactive cells, and apoptosis in age-matched (1-year-old) untreated Rho$^{+/-}$ mice and compared these parameters side by side to those obtained from saline-injected control eyes. Except for a very slight decrease in the photopic b-wave amplitude at one single light flash intensity (0.1 cd.s/m^2) upon saline injection, there were no noticeable differences in any of these parameters between the two groups (fig. S9). The injection of the saline solution thus most likely does not affect the interpretation of our results and the treatment success.

DISCUSSION

In this study, we provide the first evidence that ectopic transcriptional activation of functionally equivalent genes using split dCas9-VPR can ameliorate a disease phenotype, further expanding the spectrum of possibilities for treatment of genetic disorders. Given that many IRD-linked genes expressed in rods or cones are encoded by functionally equivalent genes, the transactivation approach provides an attractive option for therapy of these diseases for several reasons: (i) Transactivation of functionally equivalent genes can be used for the treatment of large and frequent IRD genes, such as *ABCA4* or *MYO7A*, which cannot be efficiently reconstituted using classical dual AAV vectors. *ABCA4* and *MYO7A* belong each to a large protein family with many functionally equivalent partners expressed across different cell types. Some of these partners, e.g., *ABCA1* or *MYO7B*, show a very high structural conservation to *ABCA4* and *MYO7A*, respectively, with at least 50% amino acid identity and 65% amino acid similarity and therefore represent highly attractive candidates for transactivation. (ii) A transactivation approach can also be used for therapy of genes with autosomal dominant inheritance, for which gene delivery has to be combined with simultaneous knockout of the diseased allele. Recent studies demonstrated that sgRNAs with shortened spacer lengths (<16 bases) repress the catalytic activity of Cas9-VPR (*16*, *17*). A strategy combining catalytically active Cas9-VPR with sgRNAs of shortened spacer lengths for transactivation and with standard sgRNAs (usually 20 bases spacer length) for simultaneous down-regulation of the diseased gene can, e.g., be used for the treatment of the most common rhodopsin P23H gain-of-function mutation but should also be applicable to other mutations in *RHO* or to other genes with autosomal-dominant inheritance. (iii) Owing to the possibility of multiplexing in CRISPR-Cas approaches, transactivation could potentially also be used for the treatment of more complex (retinal) diseases, such as those caused by mutations in two or multiple genes (*18*–*20*). (iv) The (d)Cas9-VPR–mediated transactivation approach is mutation independent and thus allows for the treatment of a large number of patients.

Using alternative activation strategies, two recent studies demonstrated that CRISPR-Cas9–based transactivation of structurally and functionally related genes can ameliorate the phenotypes of two different mouse models for muscular dystrophy (*21*, *22*). Additional work is necessary to compare the transactivation efficiency, long-term effects, and safety between these approaches and dCas9-VPR side by side to determine the best treatment strategy for the individual disorders. It also remains to be investigated whether other split position within dCas9-VPR (*23*) or other technologies for reconstitution of large coding sequences might further improve the transactivation efficiency and/or the therapeutic outcome of dCas9-VPR–based approaches. Unlike its catalytically active counterpart, dCas9 and its fusion variants do not cause single or double strand breaks at the genomic level. Studies addressing the off-targets of dCas9-VPR at the transcript level revealed that such off-target rates are very low or nondetectable (*1*, *2*), further emphasizing the therapeutic potential of this approach. We demonstrate herein that the split dCas9-VPR technology can induce long-term expression and morphological as well as functional phenotypic changes in an animal model with no apparent adverse effects, such as gliosis or invasion of immune cells. These promising results might therefore help pushing this approach toward first clinical trials. Notably, as in previous retinal gene therapy studies in mice, we could not fully rescue the WT-like retinal function or morphology. One possible reason is that a single subretinal injection with conventional rAAV capsids usually covers only up to one third of the retina, and hence, amplitudes of up to 30% of the WT response could be expected. We suggest that functional or structural improvements can be further increased by developing

more potent rAAV vectors, which show pan-retinal expression upon subretinal injection (e.g., due to lateral spreading) or which allow for other more convenient administration routes (e.g., intravitreal injection). In addition, we use a dual rAAV vector approach that requires both vectors to be expressed and reconstituted in the same cell. Accordingly, one would benefit from more efficient dual rAAV vector strategies or techniques to increase the reconstitution efficiency of the split dCas9-VPR.

Last, we also provide the first in vitro evidence that transactivation efficiency is inversely correlated with dCas9-VPR expression in a transfection-independent system. It remains to be clarified whether this unexpected dose dependency of dCas9-VPR also occurs in vivo and whether it reflects an inherent property of other catalytically active and inactive Cas9 or other Cas variants. A precise understanding of this correlation could help to further improve and fine-tune the efficiency of these enzymes and might thus also increase the therapeutic outcome of CRISPR-Cas–based approaches.

METHODS

Animals

All animal procedures were performed with the permission of local authorities (District Government of Upper Bavaria) and in accordance with the German laws on animal welfare (Tierschutzgesetz). Animals were anesthetized via an intraperitoneal injection of ketamine (40 mg/kg body weight) and xylazine (20 mg/kg body weight). Euthanasia was performed by cervical dislocation. For all experiments, C57Bl/6J or $Rho^{+/-}$ mice (*13*) backcrossed to a C57Bl/6J background for at least eight generations were used.

sgRNA design

The Eukaryotic Promoter Database (https://epd.epfl.ch//index.php) was consulted for the identification of promoter regions (*24*). sgRNA sequences in the genomic target region were chosen using the CRISPOR website with 20bp-NGG PAM settings for *Sp*Cas9 (*25*) and elimination of sgRNAs with a specificity score (*26*) lower than 50. All sgRNA sequences used in this study are shown in table S1.

Construction and cloning of expression plasmids

The Cas9m4-VP64, SP-dCas9-VPR, pSMVP-Cas9N, pSMVP-Cas9C, and pAAV-CMV-Cas9C-VPR plasmids were obtained from Addgene (#47319, #63798, #80934, #80939, and #80933, respectively). sgRNAs expressed via a U6 promoter were added using standard cloning techniques. Cas9N and Cas9C were rendered catalytically inactive by introducing the D10A and the H840A point mutations via a standard site-directed mutagenesis protocol using the KAPA HiFi HotStart ReadyMix PCR kit (Kapa Biosystems). For the generation of stable cell lines, dCas9-VPR was subcloned into a pb expression vector containing the Tet-On system for DOX-inducible expression of dCas9-VPR. For expression in mouse photoreceptors, the split dCas9-VPR driven by a human rhodopsin promoter and corresponding sgRNAs each driven by a human U6 promoter were subcloned into the pAAV2.1 vector (*27*). All transgenes were sequenced before use (Eurofins Genomics).

Cell culture and transfection

The murine 661W cell line derived from retinal tumors was provided by M. Al-Ubaidi, University of Houston (*28*). The cells were cultured in Dulbecco's modified Eagle's medium (DMEM) GlutaMAX medium (ThermoFisher Scientific) supplemented with 10% fetal bovine serum (FBS) (Biochrom) and 1% Anti-Anti (ThermoFisher Scientific) at 37°C and 10% CO_2. Immortalized MEFs were generated as previously described (*29*, *30*). MEF cells were cultured in DMEM GlutaMAX medium supplemented with 10% FBS (Biochrom) and 1% penicillin/streptomycin (Biochrom) at 37°C and 5% CO_2. Transient transfections of 661W and MEF cells were performed using the Xfect Transfection Reagent (Takara Bio) according to the manufacturer's instructions. HEK293 cells were transfected using the standard calcium phosphate technique.

Generation of stable cell lines using pb technology

The stable cell lines were generated using the pb transposon system. Briefly, 661W or MEF cells were cotransfected with the respective dCas9-VPR and sgRNA containing pb vector and a pb transposase expression vector using the Xfect Transfection Reagent (Takara Bio) according to the manufacturer's instructions. Fourty-eight to 72 hours after transfection, cells were selected for successful integration by addition of puromycin dihydrochloride (Gibco, Thermo Fisher Scientific) for approximately 1 week at 4.5 and 1 μg/ml concentration for 661W and MEF cells, respectively. To induce dCas9-VPR expression, DOX hyclate (Sigma-Aldrich) was added directly to the medium.

RNA isolation and (quantitative) reverse transcription polymerase chain reaction

Forty-eight hours after transfection, the cells were harvested and lysed using the mixer mill MM400 (Retsch). RNA was isolated using the RNeasy Plus Mini Kit (QIAGEN) according to the manufacturer's instructions, and RNA concentration and purity were determined via the NanoDrop2000 (ThermoFisher Scientific). Complementary DNA (cDNA) was synthesized using the RevertAid First Strand cDNA Synthesis Kit (ThermoFisher Scientific) according to the manufacturer's instructions for up to 1 μg of total RNA. For reverse transcription polymerase chain reaction (RT-PCR), the Herculase II polymerase (Agilent Technologies) was used following the manufacturer's instructions. The quantitative RT-PCR (qRT-PCR) was performed on the StepOnePlus Real-Time PCR System (Applied Biosystems, ThermoFisher Scientific) using the SYBR Select Master Mix (Applied Biosystems, ThermoFisher Scientific) according to the manufacturer's instructions. The relative expression levels of *Cnga1* and *Opn1mw* were normalized to the housekeeping gene *Alas* and calculated using the $2^{-\Delta\Delta C(T)}$ method. All primers used in this study can be found in table S1.

RNA isolation and mRNA-seq library preparation and sequencing

Total RNA was isolated from retinas using the RNeasy Plus Micro Kit (QIAGEN) according to the manufacturer's protocol. For mRNA library production, we used a scaled-up version of the SMARTseq2 protocol. Briefly, from ca. 7 to 90 ng of total RNA, mRNA was captured with a mix of 0.5 μl of 20 μM oligo dT primer and 0.5 μl of 20 mM dNTPs, followed by heating to 72°C for 3 min and immediately putting into ice-water bath. Then, in a 10-μl reaction, double-stranded cDNA was generated by adding 2 μl of 5× Superscript II first-strand buffer (ThermoFisher Scientific), 2 μl of 5 M Betaine, 0.6 μl of 100 mM $MgCl_2$, 0.5 μl of 100 mM dithiothreitol (DTT), 0.4 μl of RNAsin (Promega), 0.5 μl of 20 μM template-switch oligo (20 μM), and 0.5 μl of SuperScript II reverse transcriptase (200 U/μl; ThermoFisher Scientific) and incubation for 90 min at 42°C, followed

by 14 cycles (50°C for 2 min, 42°C for 2 min) and heat inactivation (70°C for 15 min). Pre-amplification was performed by addition of 12.5 μl of 2× KAPA HiFi HotStart Ready mix, 0.25 μl of 10 μM IS PCR primers, and 2.25 μl of nuclease-free water in a thermos protocol of 98°C for 3 min, 10 pre-amplification cycles (98°C for 20 s, 67°C for 15 s, 72°C for 6 min), followed by 5 min at 72°C and hold at 4°C. Purification was performed with AMPure XP beads (Beckman Coulter), and cDNA was quantified with Qubit (ThermoFisher Scientific) and checked for fragment length distribution on an Agilent Bioanalyzer chip. Next, 7 ng of cDNA was fragmented in a 20-μl reaction by incubation with 1 μl of Tn5 enzyme from Illumina Nextera library preparation kit and 10 μl of 2× tagmentation DNA buffer for 10 min at 55°C. Tagmented cDNA was purified with MinElute columns (QIAGEN) and PCR-amplified with NEBNext High-Fidelity 2× PCR Mastermix, 1 μl of each 10 μM Nextera index 1 and Nextera index 2 primer (Illumina) with a thermos protocol of 72°C for 5 min, 98°C for 30 s, 7 cycles (98°C for 10 s, 63°C for 30 s, and 72°C for 1 min), 72°C for 5 min, and hold at 4°C. The final library was purified with AMPure beads, quantified by Qubit, and sequenced for 100 base pairs using a V3 single read flow cell on a HiSeq 2500 (Illumina). The generated data were trimmed for quality and adapter reads with TrimGalore! and then mapped with STAR aligner. Duplicates were marked with the MarkDuplicates function from Picard tools. Reads were summarized with RSEM (RNA-seq by expectation maximization) software, and FPM (fragments per million mapped fragments) count matrix was generated with DESeq2.

Immunocytochemistry

For immunocytochemistry, 661W-pb or MEF-pb cells were seeded onto sterile 12-mm-diameter cover slips coated with poly-L-lysine hydrobromide (Sigma-Aldrich). After 48 hours of DOX application, the cells were fixed with 4% paraformaldehyde (Sigma-Aldrich) and permeabilized for 30 min in 0.3% Triton X-100. Next, the coverslips were incubated with blocking solution (5% ChemiBLOCKER, Merck Millipore). To stain for Cnga1 and *Sp*Cas9 in 661W-pb cells, an anti-Cnga1 mouse monoclonal antibody (1:30; gift from R. Molday) (*31*) and the anti-*Sp*Cas9 rabbit polyclonal antibody (1:1000; C15310258, Diagenode) were used, respectively. To stain for M-opsin and *Sp*Cas9 in MEF-pb cells, the anti-opsin red/green (M-opsin) rabbit polyclonal antibody (1:300; AB5405, Merck) and an anti-*Sp*Cas9 mouse monoclonal antibody (1:500; SAB4200751, Sigma-Aldrich) were used, respectively. Hoechst 33342 solution (5 μg/ml; Invitrogen, ThermoFisher Scientific) was used as a nuclear staining. Images were obtained via the Leica TCS SP8 spectral confocal laser scanning microscope (Leica), acquired with the LASX software (Leica), and further processed with the ImageJ software (National Institutes of Health).

Patch-clamp measurements

Inside-out patches were excised from 661W stable cells that were maintained at a DOX concentration of 5 ng/ml. Currents were recorded using an EPC-10 double patch-clamp amplifier (HEKA Elektronik, Harvard Bioscience) and PatchMaster acquisition software (HEKA Elektronik, Harvard Bioscience). Data were digitized at 20 kHz and filtered at 2.9 kHz. All recordings were obtained at room temperature. The extracellular solution was composed of 140 mM NaCl, 5 mM KCl, 10 mM Hepes, and 1 mM EGTA (pH 7.4). The intracellular solution contained 140 mM KCl, 5 mM NaCl, 10 mM Hepes, and 1 mM EGTA (pH 7.4). The effect of cGMP was examined by perfusing the patch with extracellular solution supplemented with 300 μM cGMP. To investigate channel blocking, perfusion with a symmetric Ca^{2+}/Mg^{2+} solution composed of 140 mM NaCl, 5 mM KCl, 2 mM $CaCl_2$, 1 mM $MgCl_2$, and 10 mM Hepes was performed, followed by perfusion with a cGMP-supplemented Ca^{2+}/Mg^{2+} solution as a control. Currents were evoked from a holding potential of 0 mV by applying a 300-ms pulse of −80 mV followed by a 300-ms pulse of 80 mV every 3 s.

TX lysates and Western blot analysis

Transiently transfected HEK293 cells were harvested 48 hours after transfection and lysed in TX lysis buffer (0.5% Triton X-100, v/v) using the mixer mill MM400 (Retsch). The lysis buffer was supplemented with cOmplete ULTRA Protease Inhibitor Cocktail tablets (Roche). For Western blotting, 30 μg of the whole-cell protein was incubated in 1× Laemmli sample buffer supplemented with DTT at 72°C for 10 min. The proteins were separated on a 6 to 12% SDS-polyacrylamide gel via gel electrophoresis. For immunoblotting, the anti-*Sp*Cas9 antibody (1:1000; C15310258, Diagenode) was used. The relative band intensities were quantified using the ImageLab software (Bio-Rad).

rAAV production and subretinal injections

rAAV vectors containing the N- or C-terminal part of dCas9-VPR and the sgRNA expression cassette were produced using the 2/8YF capsid (*32*) as described previously (*33*, *34*). C57Bl/6J mice were injected subretinally at P28 with a single injection (1 μl) of titer-matched rAAVs (total 10^{11} vg/μl), and the retinas were harvested for immunohistochemistry 4 weeks after injection. For 10 $Rho^{+/-}$ mice, one eye was injected via a single injection (1 μl) of titer-matched rAAVs (total 10^{11} vg/μl) on P14. The contralateral eye was control injected with 1 μl of NaCl (saline). Twelve months after injection, ERG and OCT were performed on both eyes of all $Rho^{+/-}$ mice, and all retinas were harvested for immunohistochemistry.

Electroretinography

Corneal electroretinograms were recorded from 10 $Rho^{+/-}$ and 10 age-matched C57Bl/6J WT mice using the Celeris full-field ERG system from Diagnosys (model D430). Scotopic and photopic electroretinograms were carried out for each animal. Mice were dark adapted overnight, and scotopic ERG measurements were conducted first under dim red light conditions followed by photopic tests. Pupils were dilated using 1% atropine- and 0.5% tropicamide-containing eye drops (Mydriaticum Stulln, Pharma Stulln GmbH). As contact fluid, hydroxylpropyl methylcellulose (Methocel 2%, OmniVision GmbH) was applied on both eyes before placing the light guide electrodes. During the whole protocol, animals were kept warm by the integrated platform heater of the Celeris system. ERG responses were obtained simultaneously from both eyes. For scotopic measurements, single flash recordings were performed at light intensities of 0.003 (blue light, 455 nm), 0.01, 0.03, 0.1, 0.3, 1, 3, and 10 cd.s/m^2 (all remaining intensities 6500 K white light). Background intensity was 0 cd/m^2. For photopic measurements, mice were light adapted (3 cd.s/m^2) for 5 min, and single flash recordings were obtained at light intensities of 0.01, 0.03, 0.1, 0.3, 1, 3, and 10 cd.s/m^2. The background intensity for all photopic recordings was 9 cd/m^2. For both, scotopic and photopic assessments, measurements were recorded from 50 ms before stimulus onset to 300 ms poststimulus. Voltage signals were sampled at 1 Hz, and recorded responses were averages of 5 (scotopic) or 10 (photopic) sweeps depending on

signal-to-noise ratios. The measurements were analyzed using the provided Espion V6 software from Diagnosys with the a-wave amplitude measured from stimulus onset to the trough of the a-wave and the b-wave amplitude ranging from the trough of the a-wave to the peak of the b-wave.

Optical coherence tomography

Retinal morphology of the Rho$^{+/-}$ mice was assessed with OCT using an adapted Spectralis HRA + OCT system (Heidelberg Engineering) in combination with contact lenses as described previously (*35*). Pupils were dilated using 1% atropine- and 0.5% tropicamide-containing eye drops (Mydriaticum Stulln, Pharma Stulln GmbH), and hydroxylpropyl methylcellulose (Methocel 2%, OmniVision GmbH) was applied to keep the eyes moist. OCT scans (20 frames per retina) were performed in high-resolution mode with the scanner set to 30° field of view.

Immunohistochemistry and confocal microscopy

Retinas of 13-month-old injected Rho$^{+/-}$ and age-matched WT mice were dissected and processed for immunohistochemistry as described previously (*36*). The mouse monoclonal anti–PRPH2 2B7 antibody (1:100; gift from M. Naash) (*37*) served as marker for rod and cone outer segments. The guinea pig anti-iba1 antibody (1:100; 234 004, Synaptic Systems) was used to visualize microglia. As marker for potential reactive gliosis served the mouse anti–GFAP-Cy3 antibody (1:1000; C9205, Sigma-Aldrich). Fluorescein isothiocyanate–conjugated lectin from *Arachis hypogaea* [peanut agglutinin (PNA)] (1:100; L7381, Sigma-Aldrich) was applied to stain cone photoreceptors. To detect cone-specific and activated M-opsin in rod photoreceptors, the rabbit anti-opsin red/green (M-opsin) antibody (1:300; AB5405, Merck) was used. The cell nuclei were visualized with Hoechst 33342 solution. To detect apoptosis, the TUNEL assay was performed using the In Situ Cell Death Detection Kit, Fluorescein (11684795910; Roche) according to the manufacturer's instruction. The TUNEL assay was conducted for 8 of 10 injected Rho$^{+/-}$ mice except for mouse #7 and #8 (Fig. 6) as there were no cryosections left to stain from these two mice. Retinal images were obtained via the Leica TCS SP8 spectral confocal laser scanning microscope (Leica), acquired with the LASX software (Leica), and further processed with the ImageJ software (National Institutes of Health). Postmortem analysis of the ONL thickness in stained retinal sections was performed using the ImageJ software. Areas with equal distance to the optic nerve were chosen for analysis. At least three measurements were averaged per retina.

Statistics

All values are given as means ± SEM. The number of replicates (n) and the used statistical tests are indicated in each figure legend for each experiment.

SUPPLEMENTARY MATERIALS

Supplementary material for this article is available at http://advances.sciencemag.org/cgi/content/full/6/34/eaba5614/DC1

View/request a protocol for this paper from *Bio-protocol*.

REFERENCES AND NOTES

1. A. Chavez, M. Tuttle, B. W. Pruitt, B. Ewen-Campen, R. Chari, D. Ter-Ovanesyan, S. J. Haque, R. J. Cecchi, E. J. K. Kowal, J. Buchthal, B. E. Housden, N. Perrimon, J. J. Collins, G. Church, Comparison of Cas9 activators in multiple species. *Nat. Methods* **13**, 563–567 (2016).
2. W. L. Chew, M. Tabebordbar, J. K. Cheng, P. Mali, E. Y. Wu, A. H. Ng, K. Zhu, A. J. Wagers, G. M. Church, A multifunctional AAV–CRISPR–Cas9 and its host response. *Nat. Methods* **13**, 868–874 (2016).
3. S. P. Daiger, L. S. Sullivan, S. J. Bowne, Genes and mutations causing retinitis pigmentosa. *Clin. Genet.* **84**, 132–141 (2013).
4. S. Michalakis, C. Schön, E. Becirovic, M. Biel, Gene Therapy for Achromatopsia. *J. Gene Med.* **19**, e2944 (2017).
5. J. T. Finn, D. Krautwurst, J. E. Schroeder, T. Y. Chen, R. R. Reed, K. W. Yau, Functional co-assembly among subunits of cyclic-nucleotide-activated, nonselective cation channels, and across species from nematode to human. *Biophys. J.* **74**, 1333–1345 (1998).
6. Y. Fu, V. Kefalov, D.-G. Luo, T. Xue, K.-W. Yau, Quantal noise from human red cone pigment. *Nat. Neurosci.* **11**, 565–571 (2008).
7. V. J. Kefalov, Rod and cone visual pigments and phototransduction through pharmacological, genetic, and physiological approaches. *J. Biol. Chem.* **287**, 1635–1641 (2012).
8. K. Sakurai, A. Onishi, H. Imai, O. Chisaka, Y. Ueda, J. Usukura, K. Nakatani, Y. Shichida, Physiological properties of rod photoreceptor cells in green-sensitive cone pigment knock-in mice. *J. Gen. Physiol.* **130**, 21–40 (2007).
9. G. Shi, K.-W. Yau, J. Chen, V. J. Kefalov, Signaling properties of a short-wave cone visual pigment and its role in phototransduction. *J. Neurosci.* **27**, 10084–10093 (2007).
10. J. B. Fitzgerald, A. P. Malykhina, M. R. Al-Ubaidi, X.-Q. Ding, Functional expression of cone cyclic nucleotide-gated channel in cone photoreceptor-derived 661W cells. *Adv. Exp. Med. Biol.* **613**, 327–334 (2008).
11. A. M. Moreno, X. Fu, J. Zhu, D. Katrekar, Y.-R. V. Shih, J. Marlett, J. Cabotaje, J. Tat, J. Naughton, L. Lisowski, S. Varghese, K. Zhang, P. Mali, In situ gene therapy via AAV-CRISPR-Cas9-mediated targeted gene regulation. *Mol. Ther.* **26**, 1818–1827 (2018).
12. Y. Li, Split-inteins and their bioapplications. *Biotechnol. Lett.* **37**, 2121–2137 (2015).
13. M. M. Humphries, D. Rancourt, G. J. Farrar, P. Kenna, M. Hazel, R. A. Bush, P. A. Sieving, D. M. Sheils, N. McNally, P. Creighton, A. Erven, A. Boros, K. Gulya, M. R. Capecchi, P. Humphries, Retinopathy induced in mice by targeted disruption of the rhodopsin gene. *Nat. Genet.* **15**, 216–219 (1997).
14. J. Lem, N. V. Krasnoperova, P. D. Calvert, B. Kosaras, D. A. Cameron, M. Nicolò, C. L. Makino, R. L. Sidman, Morphological, physiological, and biochemical changes in rhodopsin knockout mice. *Proc. Natl. Acad. Sci. U.S.A.* **96**, 736–741 (1999).
15. J. Sancho-Pelluz, B. Arango-Gonzalez, S. Kustermann, F. J. Romero, T. van Veen, E. Zrenner, P. Ekström, F. Paquet-Durand, Photoreceptor cell death mechanisms in inherited retinal degeneration. *Mol. Neurobiol.* **38**, 253–269 (2008).
16. J. E. Dahlman, O. O. Abudayyeh, J. Joung, J. S. Gootenberg, F. Zhang, S. Konermann, Orthogonal gene knockout and activation with a catalytically active Cas9 nuclease. *Nat. Biotechnol.* **33**, 1159–1161 (2015).
17. S. Kiani, A. Chavez, M. Tuttle, R. N. Hall, R. Chari, D. Ter-Ovanesyan, J. Qian, B. W. Pruitt, J. Beal, S. Vora, J. Buchthal, E. J. Kowal, M. R. Ebrahimkhani, J. J. Collins, R. Weiss, G. Church, Cas9 gRNA engineering for genome editing, activation and repression. *Nat. Methods* **12**, 1051–1054 (2015).
18. K. Kajiwara, E. L. Berson, T. P. Dryja, Digenic retinitis pigmentosa due to mutations at the unlinked peripherin/RDS and ROM1 loci. *Science* **264**, 1604–1608 (1994).
19. M. Burkard, S. Kohl, T. Krätzig, N. Tanimoto, C. Brennenstuhl, A. E. Bausch, K. Junger, P. Reuter, V. Sothilingam, S. C. Beck, G. Huber, X.-Q. Ding, A. K. Mayer, B. Baumann, N. Weisschuh, D. Zobor, G.-A. Hahn, U. Kellner, S. Venturelli, E. Becirovic, P. C. Issa, R. K. Koenekoop, G. Rudolph, J. Heckenlively, P. Sieving, R. G. Weleber, C. Hamel, X. Zong, M. Biel, R. Lukowski, M. W. Seeliger, S. Michalakis, B. Wissinger, P. Ruth, Accessory heterozygous mutations in cone photoreceptor CNGA3 exacerbate CNG channel–associated retinopathy. *J. Clin. Invest.* **128**, 5663–5675 (2018).
20. R. G. Das, F. P. Marinho, S. Iwabe, E. Santana, K. S. McDaid, G. D. Aguirre, K. Miyadera, Variabilities in retinal function and structure in a canine model of cone-rod dystrophy associated with RPGRIP1 support multigenic etiology. *Sci. Rep.* **7**, 12823 (2017).
21. D. U. Kemaladewi, P. S. Bassi, S. Erwood, D. Al-Basha, K. I. Gawlik, K. Lindsay, E. Hyatt, R. Kember, K. M. Place, R. M. Marks, M. Durbeej, S. A. Prescott, E. A. Ivakine, R. D. Cohn, A mutation-independent approach for muscular dystrophy via upregulation of a modifier gene. *Nature* **572**, 125–130 (2019).
22. H.-K. Liao, F. Hatanaka, T. Araoka, P. Reddy, M.-Z. Wu, Y. Sui, T. Yamauchi, M. Sakurai, D. D. O'Keefe, E. Núñez-Delicado, P. Guillen, J. M. Campistol, C.-J. Wu, L.-F. Lu, C. R. Esteban, J. C. Izpisua Belmonte, In vivo target gene activation via CRISPR/Cas9-mediated *trans*-epigenetic modulation. *Cell* **171**, 1495–1507.e15 (2017).
23. C. Schmelas, D. Grimm, Split Cas9, not hairs – advancing the therapeutic index of CRISPR technology. *Biotechnol. J.* **13**, e1700432 (2018).
24. R. Dreos, G. Ambrosini, R. Groux, R. Cavin Périer, P. Bucher, The eukaryotic promoter database in its 30th year: Focus on non-vertebrate organisms. *Nucleic Acids Res.* **45**, D51–D55 (2017).
25. M. Haeussler, K. Schönig, H. Eckert, A. Eschstruth, J. Mianné, J.-B. Renaud, S. Schneider-Maunoury, A. Shkumatava, L. Teboul, J. Kent, J.-S. Joly, J.-P. Concordet, Evaluation of off-target and on-target scoring algorithms and integration into the guide RNA selection tool CRISPOR. *Genome Biol.* **17**, 148 (2016).

26. P. D. Hsu, D. A. Scott, J. A. Weinstein, F. A. Ran, S. Konermann, V. Agarwala, Y. Li, E. J. Fine, X. Wu, O. Shalem, T. J. Cradick, L. A. Marraffini, G. Bao, F. Zhang, DNA targeting specificity of RNA-guided Cas9 nucleases. *Nat. Biotechnol.* **31**, 827–832 (2013).
27. S. Michalakis, R. Mühlfriedel, N. Tanimoto, V. Krishnamoorthy, S. Koch, M. D. Fischer, E. Becirovic, L. Bai, G. Huber, S. C. Beck, E. Fahl, H. Büning, F. Paquet-Durand, X. Zong, T. Gollisch, M. Biel, M. W. Seeliger, Restoration of cone vision in the CNGA3$^{-/-}$ mouse model of congenital complete lack of cone photoreceptor function. *Mol. Ther.* **18**, 2057–2063 (2010).
28. M. R. al-Ubaidi, R. L. Font, A. B. Quiambao, M. J. Keener, G. I. Liou, P. A. Overbeek, W. Baehr, Bilateral retinal and brain tumors in transgenic mice expressing simian virus 40 large T antigen under control of the human interphotoreceptor retinoid-binding protein promoter. *J. Cell Biol.* **119**, 1681–1687 (1992).
29. P. S. Jat, C. L. Cepko, R. C. Mulligan, P. A. Sharp, Recombinant retroviruses encoding simian virus 40 large T antigen and polyomavirus large and middle T antigens. *Mol. Cell. Biol.* **6**, 1204–1217 (1986).
30. J. Xu, Preparation, culture, and immortalization of mouse embryonic fibroblasts. *Curr. Protoc. Mol. Biol.* **70**, Unit 28.1 (2005).
31. C. L. Cheng, R. S. Molday, Interaction of 4.1G and cGMP-gated channels in rod photoreceptor outer segments. *J. Cell Sci.* **126**, 5725–5734 (2013).
32. H. Petrs-Silva, A. Dinculescu, Q. Li, S.-H. Min, V. Chiodo, J.-J. Pang, L. Zhong, S. Zolotukhin, A. Srivastava, A. S. Lewin, W. W. Hauswirth, High-efficiency transduction of the mouse retina by tyrosine-mutant AAV serotype vectors. *Mol. Ther.* **17**, 463–471 (2009).
33. S. Koch, V. Sothilingam, M. Garcia Garrido, N. Tanimoto, E. Becirovic, F. Koch, C. Seide, S. C. Beck, M. W. Seeliger, M. Biel, R. Mühlfriedel, S. Michalakis, Gene therapy restores vision and delays degeneration in the CNGB1$^{-/-}$ mouse model of retinitis pigmentosa. *Hum. Mol. Genet.* **21**, 4486–4496 (2012).
34. E. Becirovic, S. Böhm, O. N. Nguyen, L. M. Riedmayr, V. Hammelmann, C. Schön, E. S. Butz, C. Wahl-Schott, M. Biel, S. Michalakis, AAV Vectors for FRET-based analysis of protein-protein interactions in photoreceptor outer segments. *Front. Neurosci.* **10**, 356 (2016).
35. C. Schön, N. A. Hoffmann, S. M. Ochs, S. Burgold, S. Filser, S. Steinbach, M. W. Seeliger, T. Arzberger, M. Goedert, H. A. Kretzschmar, B. Schmidt, J. Herms, Long-term in vivo imaging of fibrillar tau in the retina of P301S transgenic mice. *PLOS ONE* **7**, e53547 (2012).
36. S. Michalakis, H. Geiger, S. Haverkamp, F. Hofmann, A. Gerstner, M. Biel, Impaired opsin targeting and cone photoreceptor migration in the retina of mice lacking the cyclic nucleotide-gated channel CNGA3. *Invest. Ophthalmol. Vis. Sci.* **46**, 1516–1524 (2005).
37. S. M. Conley, H. M. Stricker, M. I. Naash, Biochemical analysis of phenotypic diversity associated with mutations in codon 244 of the retinal degeneration slow gene. *Biochemistry* **49**, 905–911 (2010).

Acknowledgments: We thank B. Noack, J. Koch, and K. Skokann for excellent technical support. We also thank M. Naash for the gift of the peripherin-2 antibody and R. Molday for the gift of the CNGA1 antibody. Moreover, we want to thank M. Al-Ubaidi for the gift of the 661W cells. **Funding:** This work was supported by the Deutsche Forschungsgemeinschaft, SPP2127 (to E.B., M.B., and S.M.). K.J.V.N. was funded by the BMBF grant (031L0101D) for de.NBI and is currently hired by AstraZeneca. This work was also supported, in part, by German Research Foundation Grants SFB 870 B05. **Author contributions:** E.B. designed the study and supervised the project with input from S.M. and M.B. S.B. conducted the in vivo experiments including AAV preparation, subretinal injections, OCT, immunohistochemistry, and ERG experiments with contributions from V.S., L.M.R., J.E.W., and K.S.H. V.S. designed and generated the stable cell lines, performed immunocytochemistry, and the molecular biology experiments including sgRNA design, qRT-PCR, and statistical analyses with contributions from S.B. and L.M.R. R.D.R. performed and analyzed the patch-clamp measurements with contributions from C.W.-S. and S.F. G.G. performed the RNA-seq experiment and K.J.V.N. analyzed the RNA-seq data. E.B., V.S., S.B., and L.M.R. wrote the manuscript with contributions from S.M. and M.B. E.B., S.M., M.B., C.W.-S., and J.W. acquired funding. E.B., S.M., M.B., S.B., V.S., and L.M.R. analyzed and discussed the data with input from all authors. **Competing interests:** E.B., M.B., and S.M. are authors on a patent application related to this work (no. EP19198830, filed 23 September 2019). The other authors declare that they have no competing interests. **Data and materials availability:** All data needed to evaluate the conclusions in the paper are present in the paper and/or the Supplementary Materials. Additional data related to this paper may be requested from the authors.

Submitted 13 December 2019
Accepted 8 July 2020
Published 19 August 2020
10.1126/sciadv.aba5614

Citation: S. Böhm, V. Splith, L. M. Riedmayr, R. D. Rötzer, G. Gasparoni, K. J. V. Nordström, J. E. Wagner, K. S. Hinrichsmeyer, J. Walter, C. Wahl-Schott, S. Fenske, M. Biel, S. Michalakis, E. Becirovic, A gene therapy for inherited blindness using dCas9-VPR–mediated transcriptional activation. *Sci. Adv.* **6**, eaba5614 (2020).

Science Advances

A gene therapy for inherited blindness using dCas9-VPR–mediated transcriptional activation

Sybille Böhm, Victoria Splith, Lisa Maria Riedmayr, René Dominik Rötzer, Gilles Gasparoni, Karl J. V. Nordström, Johanna Elisabeth Wagner, Klara Sonnie Hinrichsmeyer, Jörn Walter, Christian Wahl-Schott, Stefanie Fenske, Martin Biel, Stylianos Michalakis and Elvir Becirovic

Sci Adv **6** (34), eaba5614.
DOI: 10.1126/sciadv.aba5614

Science Advances (ISSN 2375-2548) is published by the American Association for the Advancement of Science, 1200 New York Avenue NW, Washington, DC 20005. The title *Science Advances* is a registered trademark of AAAS.

Science Advances
AAAS

advances.sciencemag.org/cgi/content/full/6/34/eaba5614/DC1

Supplementary Materials for

A gene therapy for inherited blindness using dCas9-VPR–mediated transcriptional activation

Sybille Böhm, Victoria Splith, Lisa Maria Riedmayr, René Dominik Rötzer, Gilles Gasparoni, Karl J. V. Nordström, Johanna Elisabeth Wagner, Klara Sonnie Hinrichsmeyer, Jörn Walter, Christian Wahl-Schott, Stefanie Fenske, Martin Biel, Stylianos Michalakis, Elvir Becirovic*

*Corresponding author. Email: elvir.becirovic@cup.uni-muenchen.de

Published 19 August 2020, *Sci. Adv.* **6**, eaba5614 (2020)
DOI: 10.1126/sciadv.aba5614

This PDF file includes:

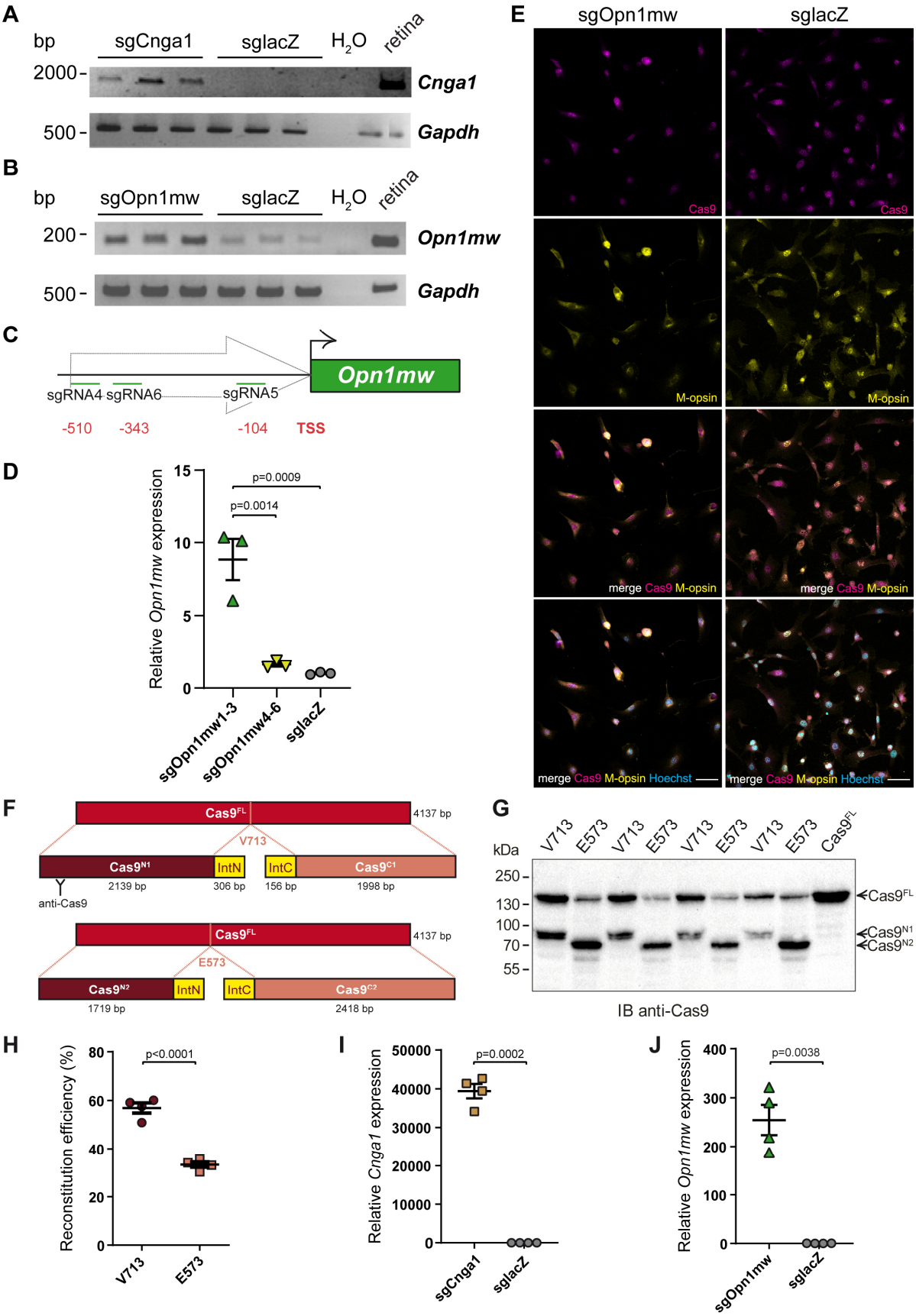

Fig. S1 *In vitro* characterization of split dCas9-VPR-mediated transactivation. A RT-PCR from 661W cells co-transfected with rAAV-sgRNA-CMVmini-dCas9^{N} and rAAV-CMVmini-dCas9^{C}-VPR using *Cnga1*-specific primers. *Gapdh* was used as loading control and cDNA from wild type mouse retinas served as positive control. **B** RT-PCR from MEF cells co-

transfected with rAAV-sgRNA-CMVmini-dCas9^{N} and rAAV-CMVmini-dCas9^{C}-VPR using *Opn1mw*-specific primers. Note the basal *Opn1mw* expression in MEF cells expressing the control *lacZ* sgRNA. **C** Binding position of three additional sgRNAs used for targeting dCas9-VPR to the promoter of the *Opn1mw* gene. The relative distance of each sgRNA to the transcription start site (TSS) of the target gene is given in bp. **D** Quantification of transactivation potency between the two different *Opn1mw*-specific sgRNA sets. Expression was normalized to MEF cells co-transfected with split dCas9-VPR and a *lacZ* sgRNA (One-way ANOVA with Dunnett´s multiple comparisons test). **E** Immunostainings of MEF-pb cells cultured with 5 ng/ml DOX using Cas9- (magenta) or M-opsin-specific antibodies (yellow). Scale bar 30 µm. **F** Scheme of the split Cas9 cassettes. N-intein and C-intein sequences of *Rhodothermus marinus* (*Rma*) were incorporated after amino acid position V713 or E573 of *Sp*Cas9. **G** Immunoblot (IB) from HEK293 cells co-transfected with the respective Cas9 halves. The uppermost band indicates successfully reconstituted full-length Cas9 (Cas9^{FL}). **H** Quantification of reconstitution efficiency by ratiometric analysis of the Cas9^{FL} and Cas9^{N} band intensities. (Unpaired t-test with Welch´s correction, two-tailed). **I, J** qRT-PCR from 661W (I) and MEF (J) cells co-transfected with dual AAVs encoding for V713 split dCas9-VPR fragments and *Cnga1, Opn1mw* or *lacZ* sgRNAs (rAAV-sgRNA-CMV-dCas9^{N} + rAAV-CMV-dCas9^{C}-VPR). Expression was normalized to cells co-transfected with split dCas9-VPR and control *lacZ* sgRNA. (Unpaired t-test with Welch´s correction, two-tailed).

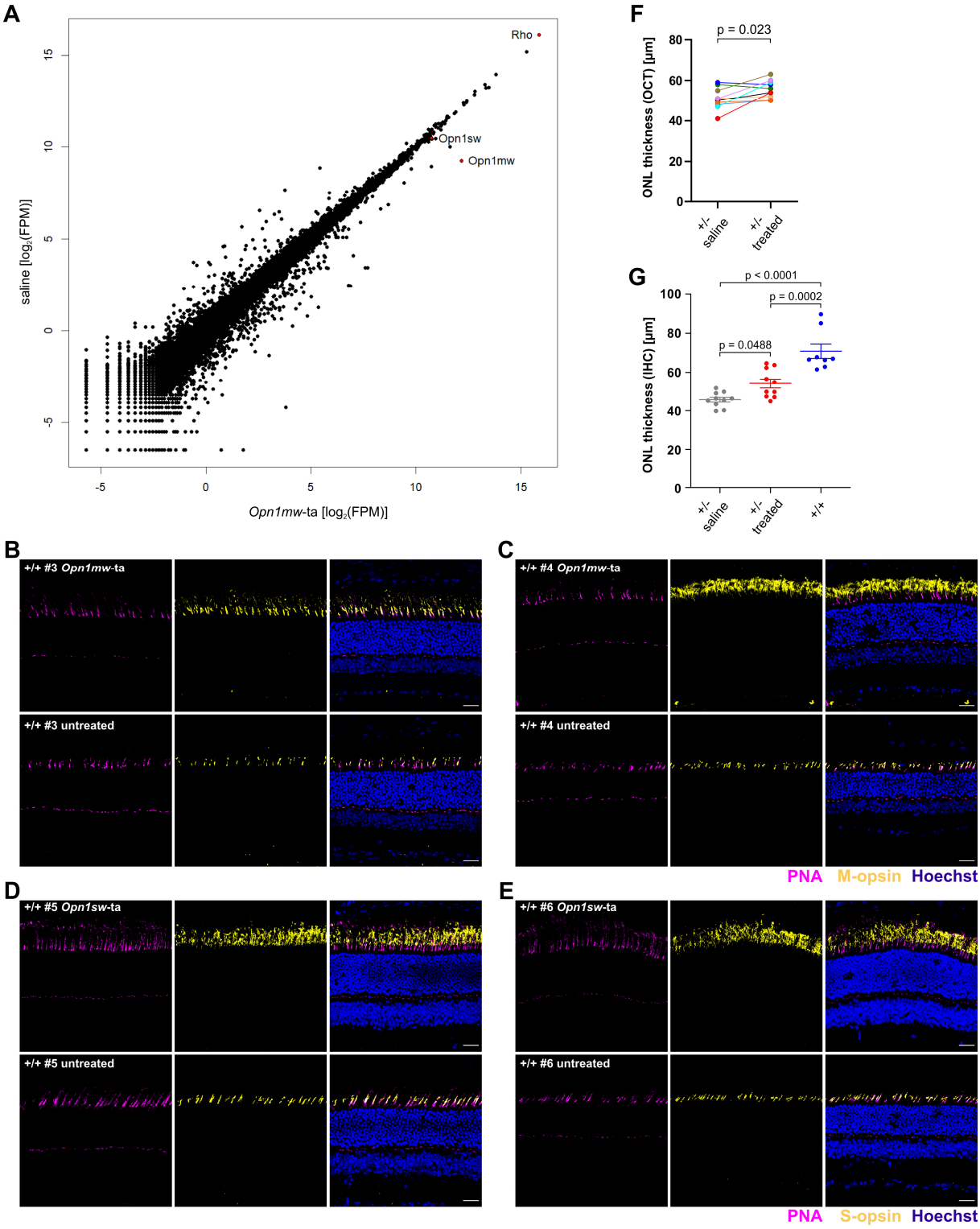

Fig. S2 Transactivation of *Opn1mw* or *Opn1sw* in wild type and ONL thickness measurements in Rho$^{+/-}$ mice. A The treated eye of a wild type (+/+) mouse (n = 1) was subretinally injected with dual rAAVs expressing split dCas9-VPR and *Opn1mw*-specific sgRNAs (*Opn1mw*-ta). The contralateral eye was injected with a NaCl solution (saline). RNA-seq was performed four weeks post-injection. Each dot represents one transcript and *Opn1mw*, *Opn1sw* and *Rho* transcripts are highlighted in red. FPM, fragments per million mapped reads. **B-E** Immunolabeling of retinas from four wild type mice (#3 - #6) injected with dual rAAVs expressing split dCas9-VPR and either *Opn1mw*-specific (B, C) or *Opn1sw*-specific sgRNAs (D, E) or untreated (lower panel) mice 4 weeks post-injection. Peanut

agglutinin (PNA, magenta) was used as marker for cones. All experiments were repeated at least once. Scale bar 30 µm. **F** Pairwise comparison of outer nuclear layer (ONL) thickness originating from OCT measurements from treated and saline-injected eyes (Paired t-test, two-tailed). **G** Histology-based (immunohistochemistry, IHC) measurements of the ONL thickness of the single groups as indicated. Statistical analysis was done using one-way ANOVA with Tukey's post-hoc test.

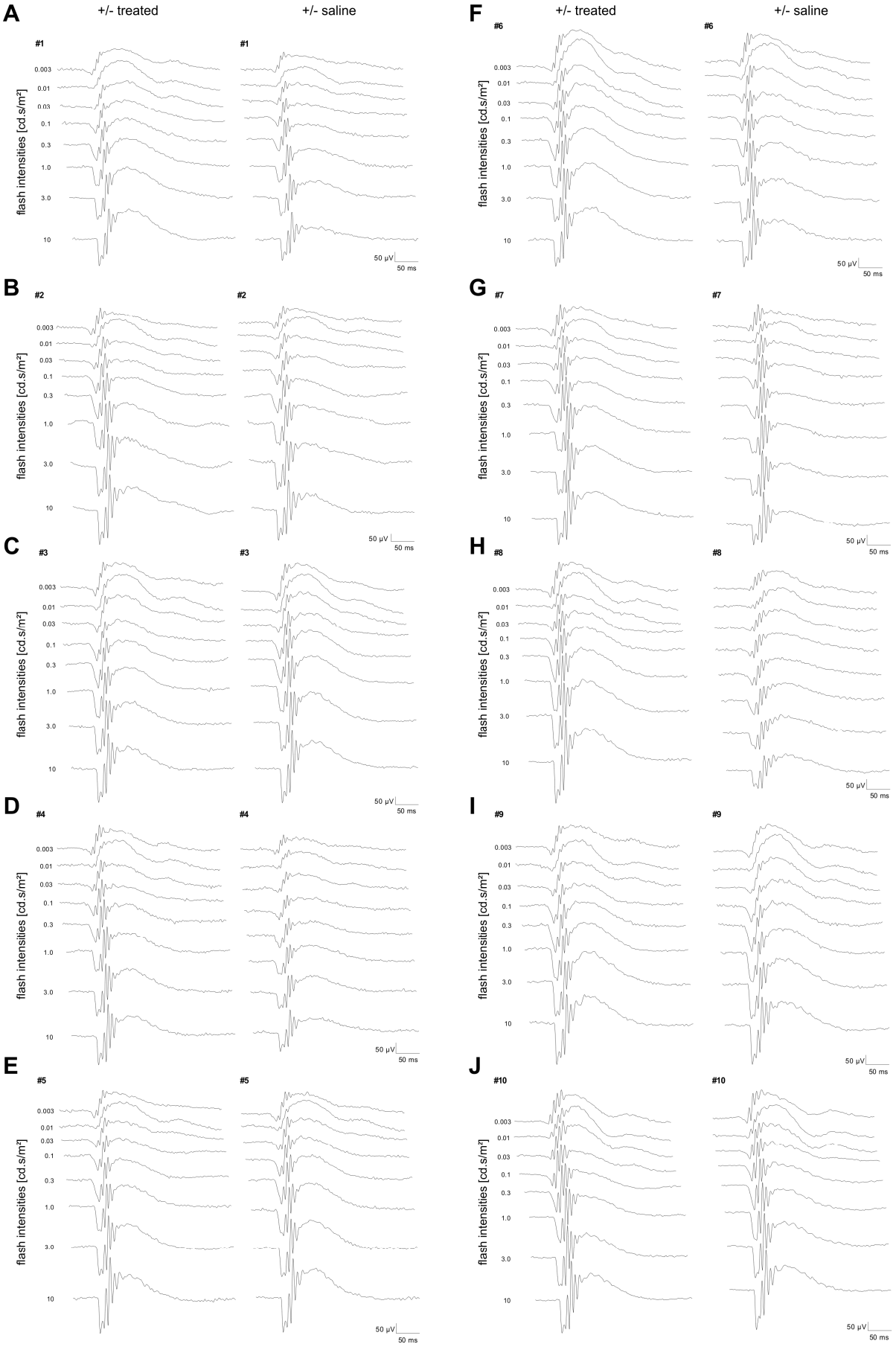

Fig. S3 Single flash scotopic ERG responses for all injected Rho$^{+/-}$ mice. A-J Serial responses to increasing flash stimuli were recorded from the *Opn1mw* expressing Rho$^{+/-}$ (+/-

treated, left) and NaCl-injected (+/- saline, right) eyes of $Rho^{+/-}$ mice (#1-10) under dark-adapted conditions one year after injection.

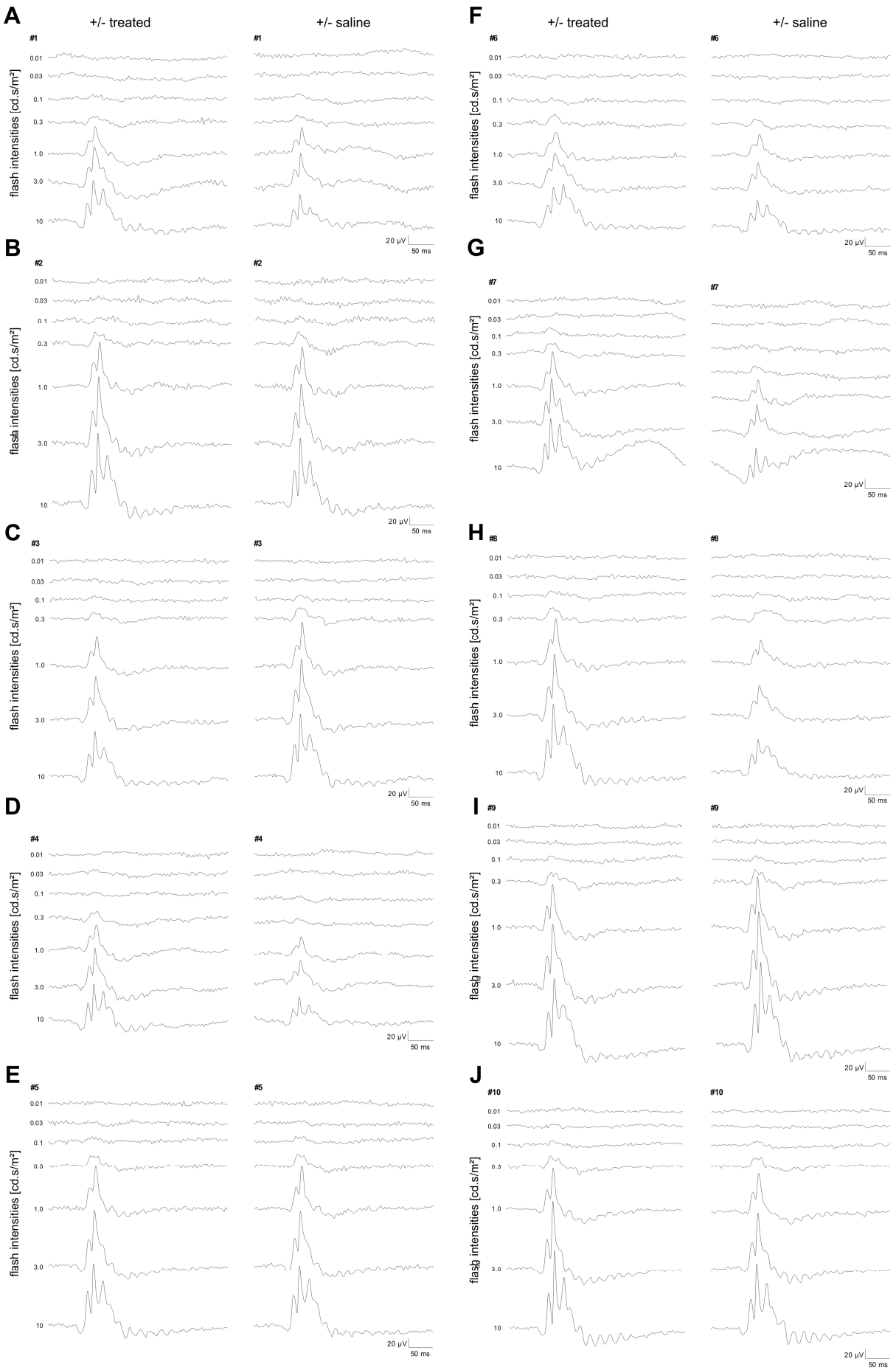
A
+/- treated
+/- saline
#1
#1
flash intensities [cd.s/m²]
0.01
0.03
0.1
0.3
1.0
3.0
10
20 µV
50 ms
B
#2
#2
C
#3
#3
D
#4
#4
E
#5
#5
F
#6
#6
G
#7
#7
H
#8
#8
I
#9
#9
J
#10
#10

Fig. S4 Single flash photopic ERG responses for all injected Rho$^{+/-}$ mice. A-J Serial responses to increasing flash stimuli were recorded from the *Opn1mw* expressing (+/- treated, left) and control NaCl-injected (+/- saline, right) eyes of Rho$^{+/-}$ mice (#1-10) under light-adapted conditions one year after injection.

A

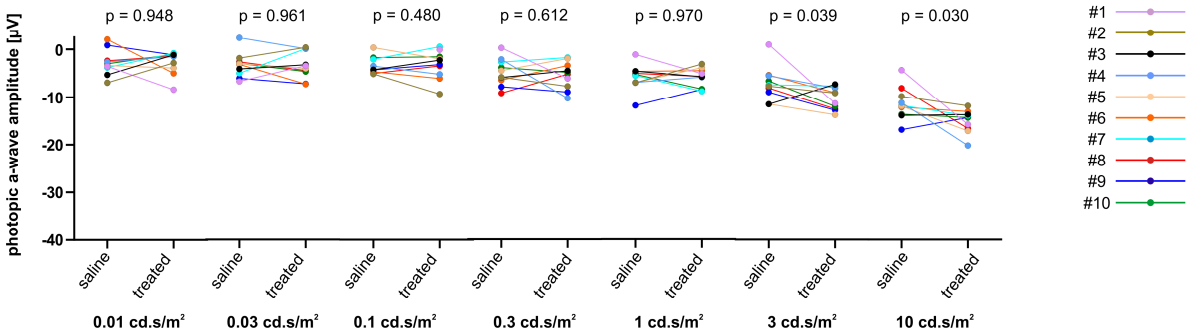

B

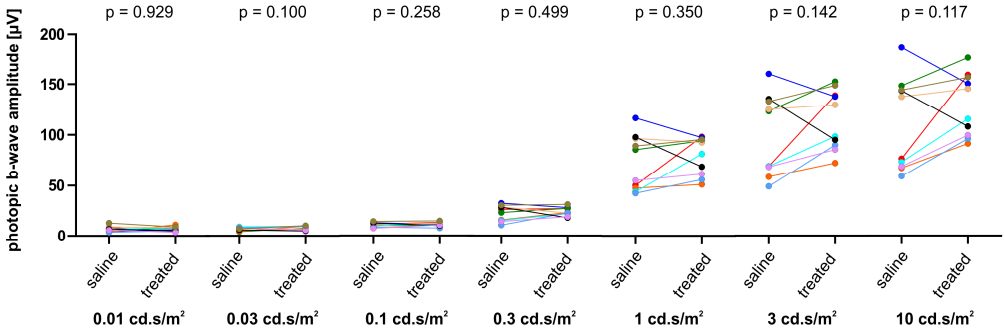

C

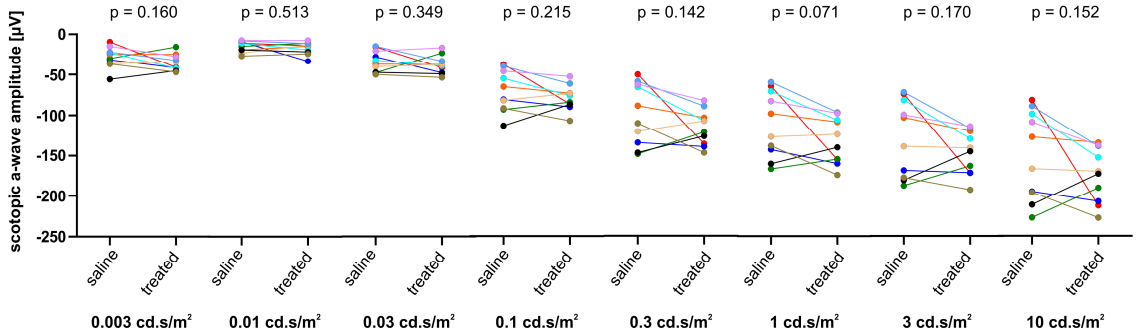

D

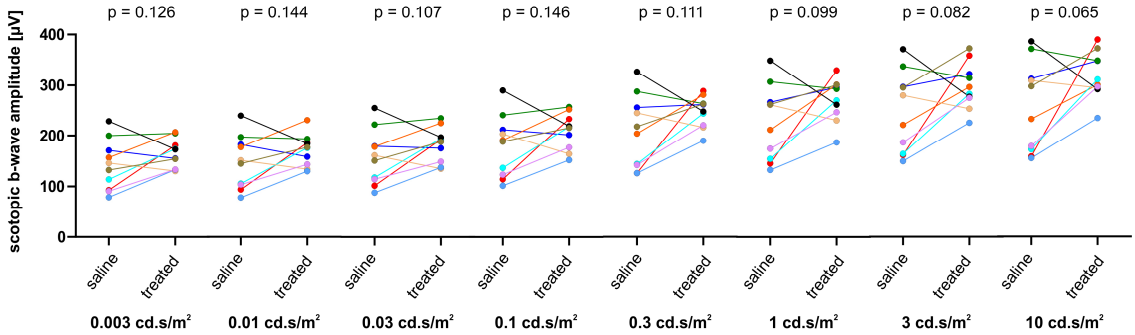

E

p-values *belonging to main Fig. 4*									
Amplitude	Comparison	0.003 cd.s/m²	0.01 cd.s/m²	0.03 cd.s/m²	0.1 cd.s/m²	0.3 cd.s/m²	1 cd.s/m²	3 cd.s/m²	10 cd.s/m²
photopic a-wave	treated *vs*. saline		0.9973	0.9992	0.9022	0.8618	0.9994	0.0769	0.031
	treated *vs*. WT		0.4187	0.1489	0.8713	0.8831	0.5076	0.3640	0.0083
	saline *vs*. WT		0.4069	0.1342	0.6110	0.9958	0.5441	0.5019	0.9716
photopic b-wave	treated *vs*. saline		0.9959	0.2891	0.6838	0.8499	0.7751	0.5844	0.5219
	treated *vs*. WT		0.9915	0.9710	0.4000	0.3592	0.7271	0.5337	0.1500
	saline *vs*. WT		0.9994	0.3523	0.1477	0.3383	0.4034	0.1510	0.0492
scotopic a-wave	treated *vs*. saline	0.4231	0.8137	0.6938	0.6365	0.4483	0.4114	0.5635	0.4817
	treated *vs*. WT	0.0083	0.3847	0.0122	0.0002	0.0002	0.0018	0.0011	0.0083
	saline *vs*. WT	0.0019	0.0849	0.0043	0.0014	0.0014	0.0013	0.0045	0.0080
scotopic b-wave	treated *vs*. saline	0.4183	0.4485	0.4236	0.4226	0.2735	0.2459	0.2129	0.1665
	treated *vs*. WT	0.0313	0.0107	0.0193	0.0038	0.0008	0.0142	0.0658	0.0554
	saline *vs*. WT	0.0160	0.0091	0.0091	0.0049	0.0040	0.0059	0.0116	0.0103

Fig. S5 Pairwise comparison of ERG amplitudes between treated and saline-injected eyes. **A-D** Pairwise plot (saline *vs.* treated) of the ERG measurements for each individual animal (#1-10) as indicated. p-values (Paired t-test, two-tailed) are shown above the corresponding measurements. **E** p-values of single comparisons (treated *vs.* saline, treated *vs.* wild type and saline *vs.* wild type) for all scotopic and photopic a- and b-wave amplitudes shown in main Fig. 4 (two-way ANOVA with Tukey's post-hoc test).

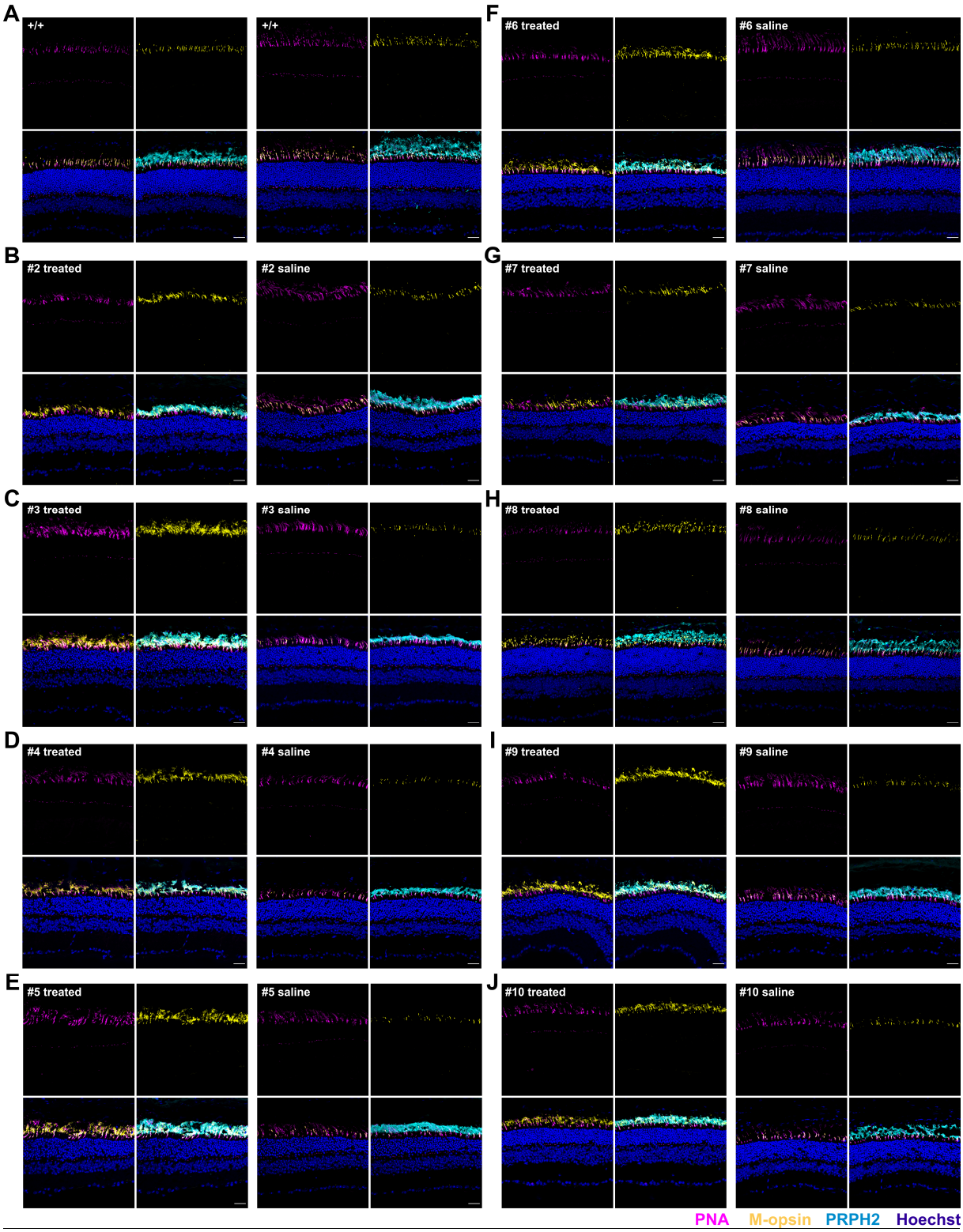

Fig. S6 Transactivation of *Opn1mw* in retinal cryosections of Rho$^{+/-}$ mice. A-J Immunolabeling of retinas from untreated WT (+/+ A) and Rho$^{+/-}$ mice #2-10 (**B-J**) either injected with split dCas9-VPR and *Opn1mw*-specific sgRNAs (treated, left panel) or with saline (right panel) at one year post-injection. PRPH2 (cyan) was used as rod and cone outer segment marker and PNA (magenta) was used as marker for cones. Scale bar 30 µm.

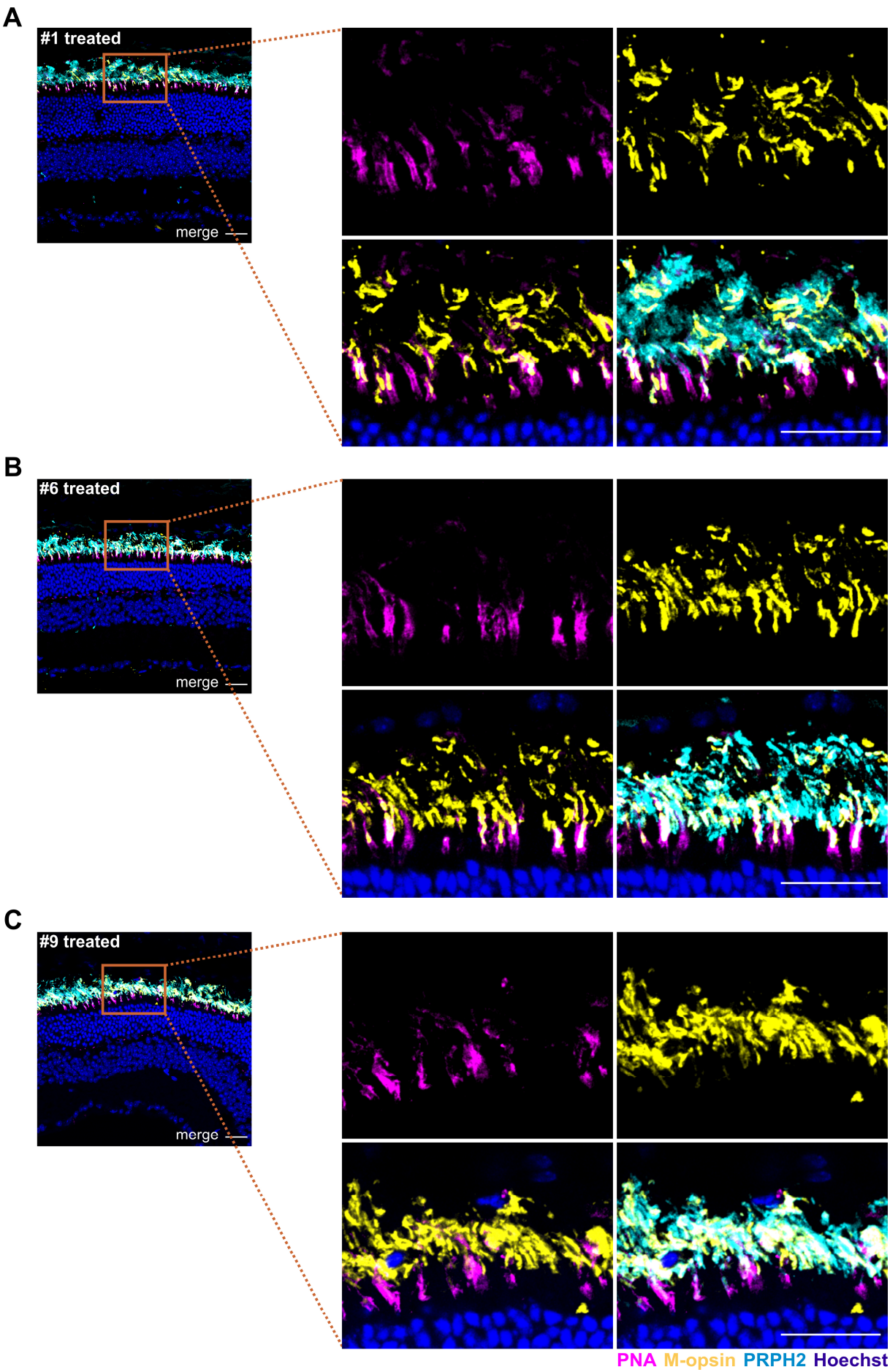
A
#1 treated
merge
B
#6 treated
merge
C
#9 treated
merge
PNA M-opsin PRPH2 Hoechst

Fig. S7 High magnification images of retinas from treated Rho$^{+/-}$ mice. A-C Left panel, Representative sections of immunolabeled retinas from Rho$^{+/-}$ mouse #1, #6 and #9 injected with split dCas9-VPR and *Opn1mw*-specific sgRNAs (treated). Right panel, Magnifications of the areas indicated by the brown rectangles in the left panel. PRPH2 (cyan) was used as rod and cone outer segment marker and PNA (magenta) was used as marker for cones. Scale bar 30 µm.

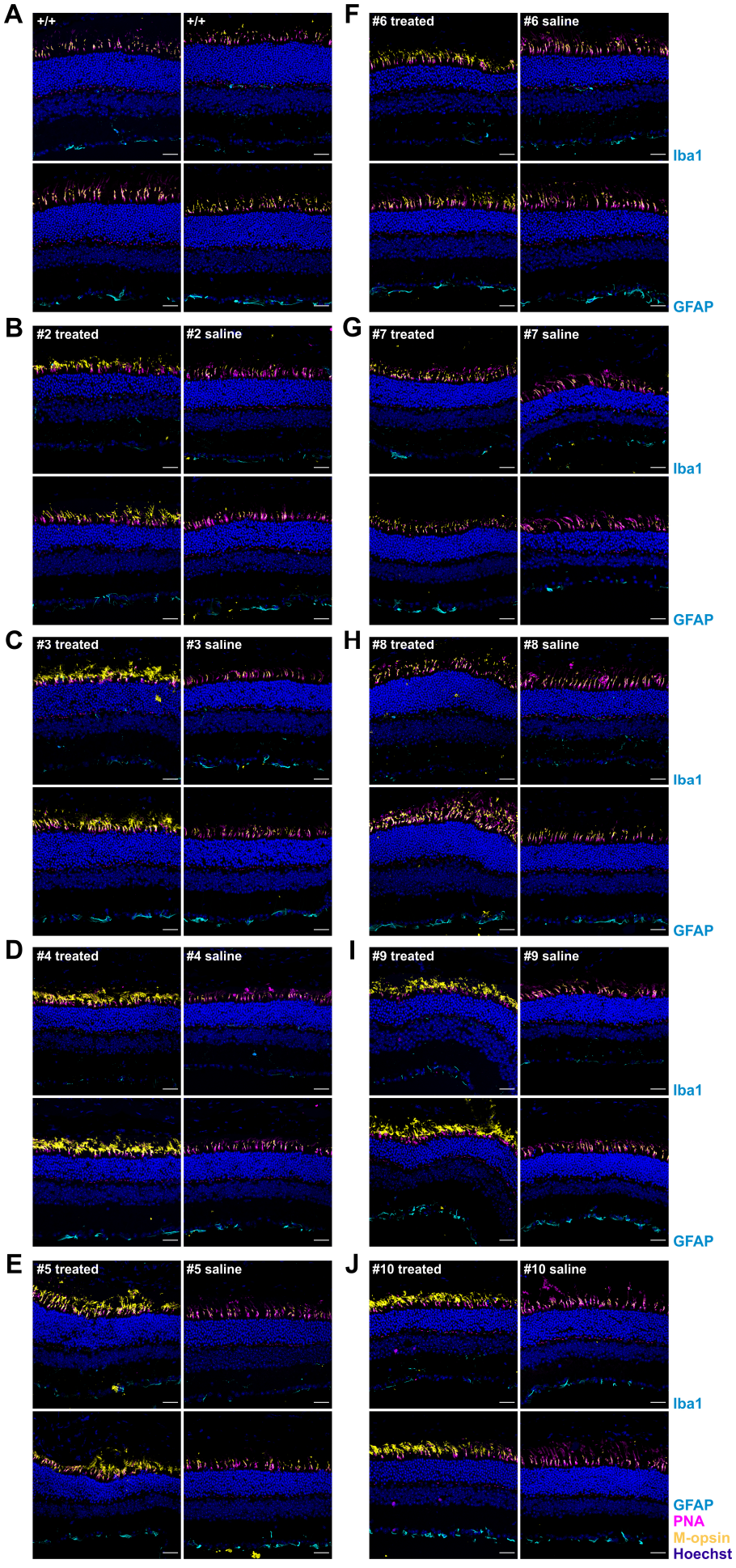
A
+/+
+/+
F
#6 treated
#6 saline
Iba1
GFAP
B
#2 treated
#2 saline
G
#7 treated
#7 saline
Iba1
GFAP
C
#3 treated
#3 saline
H
#8 treated
#8 saline
Iba1
GFAP
D
#4 treated
#4 saline
I
#9 treated
#9 saline
Iba1
GFAP
E
#5 treated
#5 saline
J
#10 treated
#10 saline
Iba1
GFAP
PNA
M-opsin
Hoechst

Fig. S8 Transactivation of *Opn1mw* in Rho$^{+/-}$ mice does not evoke any obvious gliosis or immune response. A-J Immunolabeling of retinas from untreated wild type (+/+, A) and Rho$^{+/-}$ mice #2-10 (**B-J**) either injected with split dCas9-VPR and *Opn1mw*-specific sgRNAs (treated, left panel) or with saline (right panel) at one year post-injection. Iba1-labeling (cyan, upper panel) was used to visualize microglial cells and GFAP staining (cyan, lower panel) to mark reactive gliosis. Scale bar 30 µm.

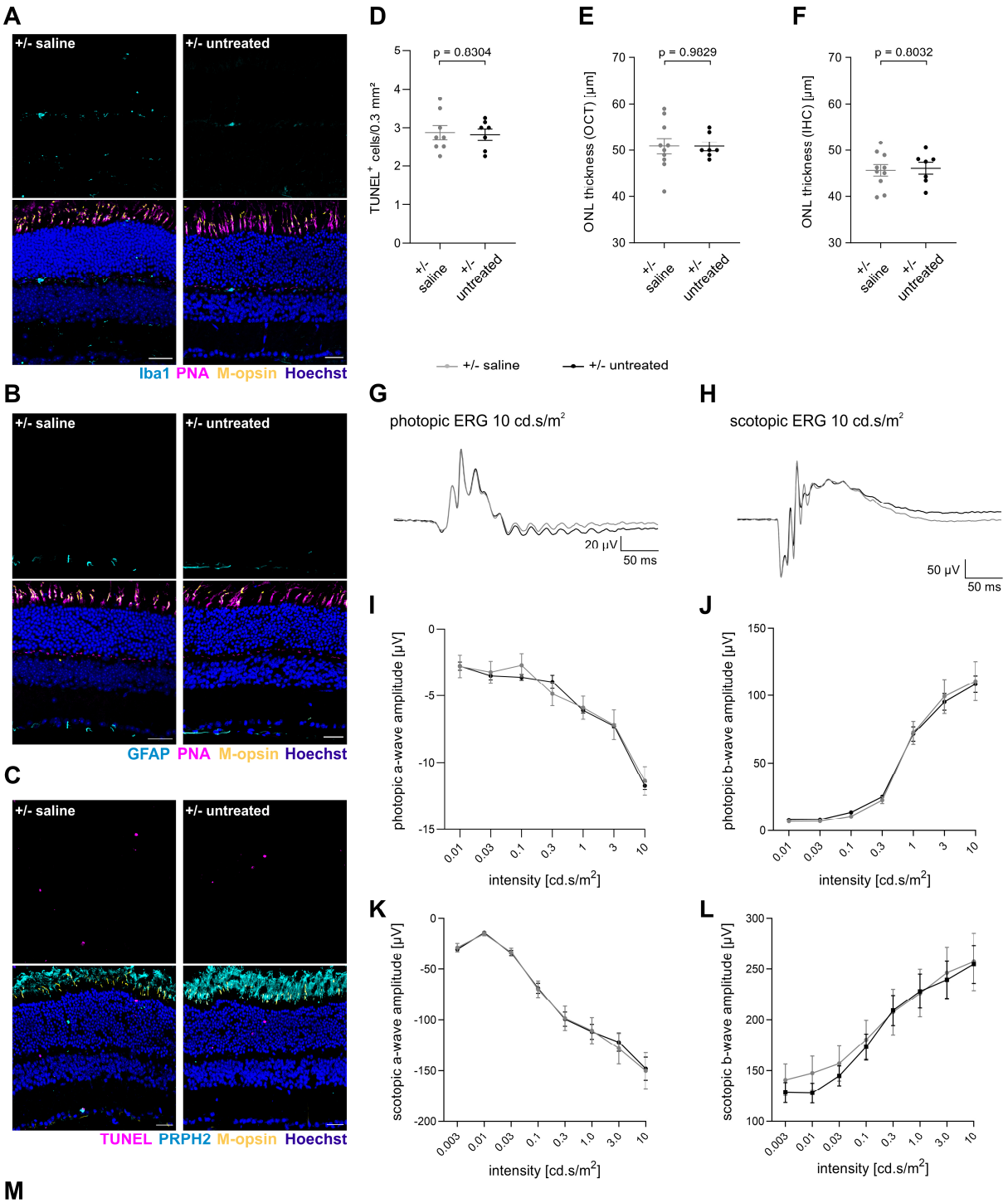

M

p-values									
	Amplitude	0.003 cd.s/m²	0.01 cd.s/m²	0.03 cd.s/m²	0.1 cd.s/m²	0.3 cd.s/m²	1 cd.s/m²	3 cd.s/m²	10 cd.s/m²
+/- saline *vs.* +/- untreated	photopic a-wave		0.9760	0.7682	0.3356	0.3938	0.8210	0.9428	0.7389
	photopic b-wave		0.2668	0.1298	0.0073	0.3862	0.9376	0.7721	0.8895
	scotopic a-wave	0.7114	0.7333	0.8772	0.9124	0.9544	0.9402	0.7185	0.9259
	scotopic b-wave	0.5111	0.3220	0.5485	0.7560	0.9549	0.9418	0.8264	0.9443

Fig. S9 Characterization of untreated one-year-old Rho$^{+/-}$ mice. A-C Representative immunostainings of the retina from a NaCl-injected Rho$^{+/-}$ mouse #8 (saline, left panel) one year post-injection and from an untreated age- and background-matched Rho$^{+/-}$ mouse (untreated, right panel). Iba1-labeling was used to visualize microglial cells (A) and GFAP staining to mark reactive gliosis (B). **C, D** TUNEL staining and the corresponding quantification. Scale bar 30 µm. **E-F** ONL thickness measurements originating from OCT recordings (E) or

post mortem histological analysis of retinal cryosections (IHC, F). **G-H** Averaged photopic (left) or scotopic (right) ERG traces for both groups at 10 cd.s/m^2. **I-L** Photopic and scotopic a- and b-wave amplitudes across different light intensities. **M** Summary of the individual p-values for the a- and b-wave amplitudes shown in **I-L**. For all panels, statistical analysis was conducted using an unpaired t-test with Welch's correction (two-tailed).

Table S1 sgRNA sequences and primers used in this study.

Target gene	**sgRNA sequence 5' – 3'**	**sgRNA position**
Cnga1 promoter	TAGGCGACCGGCTTTGAGAA CTGTGGAAGTCTCCAAACGC TCTTCTCTCTCGGCGCTATG	1 -104 bp to TSS 2 -270 bp to TSS 3 -309 bp to TSS
Opn1mw promoter	GTTTGGGGGCCTTTAAGGTA CCTGAGCCACCCCTGTGGAT TAGCTCTTGCTTGTTTACAA	1 -60 bp to TSS 2 -159 bp to TSS 3 -260 bp to TSS
	GCTCCCATGGAAAAGCGGGT CTGATCTCTTAATTGGGCCC TTGTGGACCAGAGTGTGAGT	4 -510 bp to TSS 5 -104 bp to TSS 6 -343 bp to TSS
E. coli lacZ	GTCTGACCGATGATCCGCGC	Gene body
Primer name	**Primer sequence 5' – 3'**	
qPCR mCnga1 forward	AACGAGCCATTTGTGCTGC	
qPCR mCnga1 reverse	TGGTTAGTTTAATATCTGCGCTTGT	
RT-PCR mCnga1 forward	GTCGTGGTTATTGATCCTTCAGG	
RT-PCR mCnga1 reverse	TTGACCAGCTTTTCAGTCCTGTA	
mOpn1mw forward	GGAGCAGGTACTGGCCTTATG	
mOpn1mw reverse	GGAGGTAGCAGAGCACGATG	
mOpn1sw forward	ACAAAAAGTTGCGACAGCCC	
mOpn1sw reverse	CCATCCTGTCACTAGACCTGC	
Cas9 forward	AGTACAAGGTGCCGAGCAAA	
Cas9 reverse	CCGTGCTGTTCTTTTGAGCC	
mAlas forward	TCGCCGATGCCCATTCTTATC	
mAlas reverse	GGCCCCAACTTCCATCATCT	

Manuscript II

JCI insight

Abolishing cAMP sensitivity in HCN2 pacemaker channels induces generalized seizures

Verena Hammelmann, … , Christian Wahl-Schott, Martin Biel

JCI Insight. 2019;4(9):e126418. https://doi.org/10.1172/jci.insight.126418.

Research Article Neuroscience

Hyperpolarization-activated cyclic nucleotide–gated (HCN) channels are dually gated channels that are operated by voltage and by neurotransmitters via the cAMP system. cAMP-dependent HCN regulation has been proposed to play a key role in regulating circuit behavior in the thalamus. By analyzing a knockin mouse model (HCN2EA), in which binding of cAMP to HCN2 was abolished by 2 amino acid exchanges (R591E, T592A), we found that cAMP gating of HCN2 is essential for regulating the transition between the burst and tonic modes of firing in thalamic dorsal-lateral geniculate (dLGN) and ventrobasal (VB) nuclei. HCN2EA mice display impaired visual learning, generalized seizures of thalamic origin, and altered NREM sleep properties. VB-specific deletion of HCN2, but not of HCN4, also induced these generalized seizures of the absence type, corroborating a key role of HCN2 in this particular nucleus for controlling consciousness. Together, our data define distinct pathological phenotypes resulting from the loss of cAMP-mediated gating of a neuronal HCN channel.

JCI insight

RESEARCH ARTICLE

Abolishing cAMP sensitivity in HCN2 pacemaker channels induces generalized seizures

Verena Hammelmann,[1] Marc Sebastian Stieglitz,[1] Henrik Hülle,[1] Karim Le Meur,[1] Jennifer Kass,[1] Manuela Brümmer,[1] Christian Gruner,[1] René Dominik Rötzer,[1] Stefanie Fenske,[1] Jana Hartmann,[2] Benedikt Zott,[2] Anita Lüthi,[4] Saskia Spahn,[1] Markus Moser,[3] Dirk Isbrandt,[5] Andreas Ludwig,[6] Arthur Konnerth,[2] Christian Wahl-Schott,[1,7] and Martin Biel[1]

[1]Department of Pharmacy, Center for Drug Research, Center for Integrated Protein Science Munich, Ludwig-Maximilians-Universität München, Munich, Germany. [2]Institute of Neuroscience, Technical University of Munich, Munich, Germany; and Munich Cluster for Systems Neurology (SyNergy) and Center for Integrated Protein Sciences (CIPSM), Munich, Germany. [3]Department for Molecular Medicine, Max-Planck-Institut für Biochemie, Martinsried, Germany. [4]Department of Fundamental Neurosciences, University of Lausanne, Lausanne, Switzerland. [5]DZNE Research Group, Experimental Neurophysiology, Institute for Molecular and Behavioral Neuroscience, University of Cologne, Germany. [6]Institut für Experimentelle und Klinische Pharmakologie und Toxikologie, Friedrich-Alexander-Universität Erlangen-Nürnberg, Erlangen, Germany. [7]Institut für Neurophysiologie, Medizinische Hochschule Hannover, Hannover, Germany.

Hyperpolarization-activated cyclic nucleotide–gated (HCN) channels are dually gated channels that are operated by voltage and by neurotransmitters via the cAMP system. cAMP-dependent HCN regulation has been proposed to play a key role in regulating circuit behavior in the thalamus. By analyzing a knockin mouse model (HCN2EA), in which binding of cAMP to HCN2 was abolished by 2 amino acid exchanges (R591E, T592A), we found that cAMP gating of HCN2 is essential for regulating the transition between the burst and tonic modes of firing in thalamic dorsal-lateral geniculate (dLGN) and ventrobasal (VB) nuclei. HCN2EA mice display impaired visual learning, generalized seizures of thalamic origin, and altered NREM sleep properties. VB-specific deletion of HCN2, but not of HCN4, also induced these generalized seizures of the absence type, corroborating a key role of HCN2 in this particular nucleus for controlling consciousness. Together, our data define distinct pathological phenotypes resulting from the loss of cAMP-mediated gating of a neuronal HCN channel.

Introduction

Hyperpolarization-activated cyclic nucleotide–gated (HCN) channels are voltage-gated ion channels that conduct a current termed I_h, or I_f (in heart) (1, 2). I_h differs from almost all other currents characterized in neurons, as I_h is activated upon membrane hyperpolarization (at potentials more negative than –50 mV). The channels are open at rest and are important for the determination of the resting membrane potential (RMP) (1, 2). Moreover, HCN channels have been implicated in the regulation of other cellular and circuit functions, including synaptic transmission, dendritic integration, and neuronal rhythmicity (1). All 4 members of the HCN-channel family (HCN1–4) are expressed in the brain in only partly overlapping expression patterns, suggesting that each HCN-channel subtype contributes to unique functions in a nonredundant fashion (3, 4). Knockout studies have principally confirmed this concept by elucidating specific roles for HCN1 (5–7) and HCN2 (8, 9). The function of HCN3 has been investigated in the heart (10) and brain (11) and the function of HCN4 has been studied in the heart (12). In contrast, the role of neuronal HCN4 channels remains to be elucidated.

A key feature of HCN channels is that their activation gating is facilitated by cAMP. Mechanistically, this modulation is conferred by cAMP binding to a domain in the C-terminus of HCN channels (the CNBD), which in turn induces a shift in the voltage dependence of activation towards more positive potentials (13–15). Consequently, at a given voltage, more current flows through an HCN channel if the cAMP concentration rises in a cell. Direct gating of HCN channels has been proposed to play a key role in heart rate regulation (16). With respect to the nervous system, an influence on the RMP and on the firing

Conflict of interest: The authors have declared that no conflict of interest exists.

Submitted: November 26, 2018
Accepted: April 2, 2019
Published: May 2, 2019.

Reference information: *JCI Insight*. 2019;4(9):e126418. https://doi.org/10.1172/jci.insight.126418.

of action potentials (APs) by neurons due to the direct modulation of I_h by cAMP was first demonstrated in the hippocampus (17). Since then, cAMP-mediated regulation of I_h has been implicated in diverse processes such as in the transmission of inflammatory pain (18), regulation of spatial periodicity of grid cells in the medial entorhinal cortex (19), control of working memory (20), and coincidence detection of sound (21, 22). In particular, it has been proposed that cAMP-dependent regulation (CDR) of I_h is involved in the control of thalamic network activity (23–26). Thalamocortical (TC) neurons fire in 2 main modes: the burst firing mode, which is characterized by stereotypic short trains of high-frequency APs, and the tonic mode, in which the frequency of APs is correlated with the strength of an incoming depolarization through afferent excitatory inputs (27, 28). In the tonic mode, TC neurons can process sensory information (encoded by trains of APs) and forward it to the respective regions of the cortex. In contrast, the burst mode is linked to states in which thalamic information gating is reduced, for example, during deep sleep (27). It has been proposed that CDR of I_h is a major mechanism whereby neurotransmitters regulate the transition from burst to tonic firing, and hence, the activity state of the thalamus (26, 27). However, the proposed model is mainly based on experiments using pharmacological tools. Experiments with global HCN2-knockout (HCN2-KO) mice (8) and rat models of epilepsy with an altered HCN-channel expression profile (WAG/Rij) (29) support a key role of HCN channels in thalamic firing. However, direct proof that cAMP binding to the CNBD of HCN channels regulates firing is missing. Furthermore, TC neurons express 2 distinct HCN channel subtypes that are sensitive to cAMP, HCN2 and HCN4, and it is not known which of the two regulates TC activity (3, 8), or whether both channels cooperate in this regard. This question also extends to the role of thalamic HCN channel modulation in vigilance-state control, notably in sleep and in the transition to waking.

In the present study, we have directly addressed this question by analyzing an HCN2-knockin mouse model that expresses a mutant HCN2 channel (HCN2EA) with normal voltage-dependent gating, while CDR is completely abolished. We found that HCN2EA mice show impaired firing in 2 different thalamic nuclei, the dorsal lateral geniculate nucleus (dLGN) and the ventrobasal nucleus (VB). We also demonstrate that these defects directly translate into impaired visual learning, an altered spectral profile of non–rapid eye movement (NREM) sleep, and the generation of generalized seizures (spike and wave characteristics).

Results

Generation of HCN2EA mice and basic characterization of HCN2EA-mediated I_h. Using homologous recombination in embryonic stem cells we generated a knockin mouse model (HCN2EA) that expresses an HCN2 channel carrying 2 distinct amino acid substitutions in the CNBD (R591E and T592A) (Supplemental Figure 1; supplemental material available online with this article; https://doi.org/10.1172/jci.insight.126418DS1). The R591 and T592 residues are located in the loop between the P helix and the β7 sheet of the CNBD and are highly conserved throughout the cyclic nucleotide–gated and HCN-channel family (14, 15). In high-resolution structures of the CNBD obtained for various cyclic nucleotide–modulated channels, both residues directly interact with the phosphate group of cAMP, indicating that these residues are required for high-affinity binding of cyclic nucleotides (Figure 1A). Mutation of R591 to glutamine or glutamate and/or mutation of T592 to alanine completely abolishes channel activation by cyclic nucleotides (30, 31). Indeed, when heterologously expressed in HEK293 cells, the HCN2EA channel revealed normal hyperpolarization-dependent gating, while modulation by cAMP (even at high millimolar concentrations) was completely lost (HCN2: $V_{0.5}$ [no cAMP] = –100.60 ± 0.60 mV [n = 9], $V_{0.5}$ [1 mM cAMP] = –89.50 ± 0.79 mV [n = 9]; HCN2EA: $V_{0.5}$ [no cAMP] = –101.10 ± 0.75 mV [n = 7], $V_{0.5}$ [1 mM cAMP] = –98.96 ± 2.07 mV [n = 8]; data not shown). Heterozygous matings produced wild-type (WT), HCN2EA/WT, and HCN2EA/EA mice at the expected Mendelian ratios. Here, the term HCN2EA is used to refer to mice that carry the 2 mutations on both *Hcn2* alleles. HCN2EA mice showed no gross body abnormalities, nor did they differ from their WT littermates with regard to lifespan (Supplemental Figure 2A) or body weight (Supplemental Figure 2B). Unlike HCN2-KO mice, the HCN2EA mice had neither whole-body tremor nor ataxia (Supplemental Figure 2, C and D) (8, 9). The overall brain morphology of HCN2EA mice appeared normal (Figure 1B). We examined the expression of HCN channels in the thalamus using immunohistochemistry and Western blot analysis. Western blots and quantitative reverse transcription PCR (qRT-PCR) confirmed that the dLGN expresses only HCN2, whereas the VB region contains both HCN2 and HCN4 (Figure 1C and Supplemental Figure 3D). We next compared expression levels of WT and HCN2EA channels. Western blot analysis of membrane fractions from whole brain revealed no difference in protein amounts between the

2 genotypes (Figure 1, D and E). Importantly, we also found evidence for the formation of heterotetrameric HCN2/HCN4 and HCN2EA/HCN4 channels in whole-brain membrane fractions (Supplemental Figure 3A), indicating that the principal channel architecture of HCN2 is not disturbed by the EA mutation. In agreement with this finding, HCN2EA channels interacted like WT channels with the auxiliary HCN-channel subunit TRIP8b (32, 33) (Supplemental Figure 3B). Staining of horizontal brain slices from WT mice showed broad expression of HCN2 throughout the thalamus (Figure 2A). In the VB region, a strong signal for HCN4 was detected. However, HCN4 was not detected in the dLGN (Figure 2B). The expression of HCN1 in the thalamus (VB and dLGN) was below the detection level (Supplemental Figure 3C). HCN3 is expressed in the intergeniculate leaflet, while there is no expression in the VB (11). Further characterization of HCN2 channel expression in the VB region from staining in neurons revealed that expression levels of HCN2 were higher in somata as compared with dendrites (Figure 2, C and D). Importantly, however, the distribution of HCN2 was not different between WT and HCN2EA mice (Figure 2, C and D). In agreement with this finding, analysis of the expression of HCN2 in primary neurons from WT and HCN2EA mice revealed no difference in the expression level along dendrites and in somata (Supplemental Figure 4). Expression of HCN4 was slightly enriched in dendrites and was also not different between WT and HCN2EA animals (Figure 2, E and F).

We next characterized I_h in TC neurons from thalamic slice preparations. Figure 3A shows representative traces of whole-cell currents from VB TC neurons of WT and HCN2EA. The shape of the current traces was identical; however, the opening kinetics of the HCN2EA current were somewhat slower compared with those of WT (τ at –140 mV: WT, 166.46 ± 11.29 ms [n = 7]; HCN2EA, 252.66 ± 9.09 ms [n = 8]; data not shown). The current density in the dLGN was similar for HCN2EA compared to WT (Figure 3B; current density at –140 mV: WT, 6.45 ± 0.55 pA/pF; HCN2EA, 6.65 ± 0.34 pA/pF). In the VB region current densities were generally higher than in the dLGN but were in the same range for WT and HCN2EA (current density at –140 mV: WT, 15.02 ± 1.96 pA/pF; HCN2EA, 12.23 ± 0.87 pA/pF). These experiments suggest that cAMP does not affect current density and maximal conductance of I_h. In agreement with these findings, maximal current density and maximal conductance were similar in TC neurons recorded in acute slice preparations (Supplemental Figure 5A). This conclusion was further confirmed by planar patch-clamp experiments of HEK293 cells stably expressing WT or HCN2EA channels (Supplemental Figure 5B). These experiments were carried out in a special configuration that allows for exchange of the intracellular solution with the cytosolic solution. In these experiments, we applied intracellular control solution and subsequently exchanged it with a solution containing cAMP through perfusion (Supplemental Figure 5B, inset). Together, the experiments in both TC neurons and HEK293 cells expressing HCN2 channels (Supplemental Figure 5, C and D) indicate that cAMP does not increase channel conduction and current densities. We next determined the voltage dependence of activation of I_h in the absence of cAMP and after perfusion with 1 μM cAMP, which is close to the reported apparent cAMP affinities of I_h in neurons (1). Figure 3C shows activation curves for TC neurons of dLGN from HCN2EA and WT. Unlike WT, which displayed a significant shift in the $V_{0.5}$ (ΔV = +5.05 mV: $V_{0.5}$ no cAMP, –94.57 ± 0.77 mV; +cAMP, –89.51 ± 1.31 mV), the voltage-dependent activation of HCN2EA was not affected by cAMP (ΔV = +1.10 mV: $V_{0.5}$ no cAMP, –99.97 ± 0.80 mV; +cAMP, –98.87 ± 0.43 mV). In the VB region of HCN2EA, voltage-dependent activation of I_h was still modulated by cAMP, although to a significantly lesser extent than the WT. HCN2EA (ΔV = +3.59 mV: $V_{0.5}$ no cAMP, –104.11 ± 0.77 mV; +cAMP, –100.52 ± 0.63 mV), WT (ΔV = +5.56 mV: $V_{0.5}$ no cAMP, –97.92 ± 0.55 mV; +cAMP, –92.36 ± 0.31 mV). At a saturating cAMP concentration (100 μM) the voltage shift was +18.3 mV for WT and +6.6 mV for HCN2EA. These data are consistent with the expression data showing that in the dLGN, HCN2 is the only channel expressed whereas VB neurons contain HCN2 plus HCN4, which could contribute to the residual cAMP sensitivity of I_h in HCN2EA mice.

Impaired firing in the dLGN and reduced visual learning in HCN2EA mice. We examined the intrinsic firing properties of WT TC neurons from whole-cell current-clamp measurements. In the absence of cAMP, TC neurons responded to injections of positive current at the RMP with the generation of high-frequency burst discharges (Figure 4, A and B). When measurements were performed in the presence of 1 μM cAMP in the pipette and a slight depolarization was induced, cells fired a tonic series of APs. In contrast, within the range from 50–200 pA of injected current, TC neurons from HCN2EA mice fired in the burst mode independently of the absence or presence of cAMP (Figure 4, A and B). These neurons produced tonic series of APs only in response to a strong depolarizing current injection (400 pA) (Figure 4B) or if the RMP was elevated to WT conditions (Supplemental Figure 6). As mentioned, we observed that the loss of cAMP regulation in

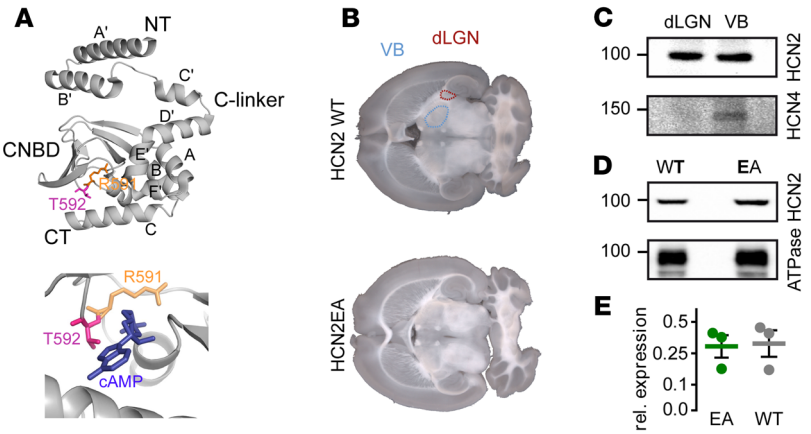

Figure 1. Impaired modulation of I_h by cAMP in thalamocortical neurons expressing HCN2EA. (**A**) Structural model of the CNBD of HCN channels. The 2 key residues R591 (yellow) and T592 (pink) that are crucial for binding of cAMP are highlighted. (**B**) Horizontal brain slices of WT and HCN2EA mice. The position of the dLGN (red) and the VB (blue) is indicated. (**C**) Detection of HCN2 and HCN4 in Western blot analysis of punched dLGN and VB regions. Images are representatives of n = 3/group. (**D**) Western blot analysis of membrane preparations of HCN2EA and WT mice probed for HCN2 and a loading control (Na^+/K^+-ATPase). Images are representatives of n = 3/group. (**E**) Quantification of HCN2 expression level in relation to the Na^+/K^+-ATPase (n = 3).

HCN2 had an effect on the RMP. The RMP of HCN2EA TC neurons differed in 2 aspects from that of WT (Figure 4C). First, it was hyperpolarized in comparison with WT (HCN2EA, –84.99 ± 1.08 mV; WT, –81.46 ± 0.72 mV) and second, it was not depolarized by cAMP (HCN2EA, –84.47 ± 0.76 mV; WT, –76.69 ± 0.71 mV). This finding supports a key role for cAMP-dependent regulation of HCN2 in the determination of the RMP in dLGN TC neurons. The consequences of the cAMP regulation could also be measured by the voltage sag, which is a characteristic feature of I_h (Figure 4D). WT neurons revealed a prominent, slow, time-dependent rectification during hyperpolarization that is caused by the activation of I_h. In HCN2EA mice the voltage sag was less pronounced (i.e., the ratio between the peak and steady-state voltages was closer to 1) and unlike in WT, was independent of cAMP. Taken together, these findings support a key role for cAMP modulation of HCN2 in regulating the basic firing properties of TC neurons in the dLGN. Because the dLGN is the main thalamic relay center of the primary visual pathway from retina to cortex (34, 35) (Figure 5A), we examined visual learning in WT and HCN2EA mice using a visual discrimination test that is sensitive to thalamic information processing via the geniculate pathway (Figure 5B). This test revealed that the visual learning capability in HCN2EA mice is significantly reduced during the first 2 test days. Only at later time points did both genotypes show comparable results in their performance (Figure 5B). In principle, reduced visual learning could simply reflect a defect in retinal function. To test this hypothesis, we performed a virtual-cliff test (Figure 5C), which allows the visual function to be evaluated. In this test, HCN2EA and WT mice performed equally well, whereas triple-KO mice, which are deficient in cyclic nucleotide–gated channel α3, rhodopsin, and melanopsin (*Cnga3*$^{-/-}$ *Rho*$^{-/-}$ *Opn4*$^{-/-}$; see ref. 36) and lack all native light responses driven by photoreceptors or photosensitive ganglion cells, failed to pass the test (Figure 5C). Finally, to demonstrate that the learning defect observed in HCN2EA mice reflects a specific failure in thalamic function, we used a Morris water-maze paradigm to test hippocampus-dependent spatial learning. In this test, HCN2EA and WT mice performed equally well (Figure 5D).

Role of cAMP modulation of HCN2 in the VB region. We also extensively studied I_h in the VB complex, which is the main relay nucleus for somatosensory stimuli. Qualitatively, loss of cAMP modulation of HCN2 had the same impact on the firing properties of TC neurons in the VB as in the dLGN (Figure 6, A and B). Under basal (cAMP-free) conditions, WT neurons fired in the burst mode and switched to tonic firing upon stronger stimuli (200 pA). In contrast, in the presence of 1 μM cAMP, TC neurons did not reveal burst activity, but consistently produced tonic series of APs. HCN2EA neurons only produced bursts of APs and showed tonic firing at very strong stimuli (400 pA) (Figure 6, A and B). The RMP of TC neurons of HCN2EA was hyperpolarized compared with WT (HCN2EA, –82.85 ± 0.67 mV; WT, –77.19 ± 0.65 mV) (Figure 5C). In agreement with the presence of a residual cAMP-dependent I_h current (Figure 3C), the RMP of HCN2EA TC neurons became more depolarized in the presence of 1 μM cAMP (–79.71 ± 0.77 mV)

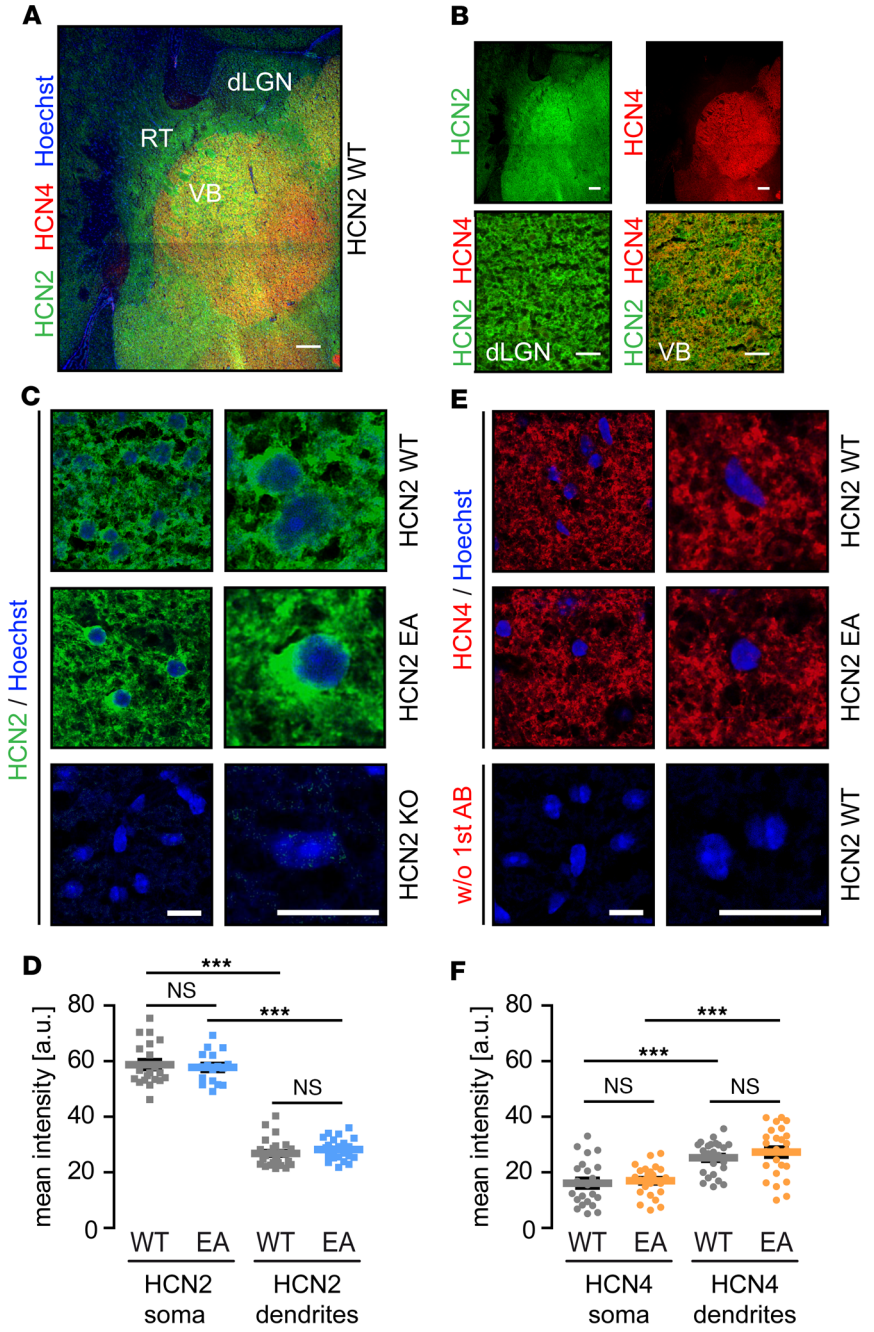

Figure 2. HCN2 and HCN4 staining in the thalamus. (**A**) Distribution of HCN2 and HCN4 in the VB region of mouse thalamus. Scale bar: 200 μm. (**B**) Overlay of anti-HCN2 (green), anti-HCN4 (red), and Hoechst (blue). Scale bars: 200 μm. Upper: Single channels for HCN2 (green) and HCN4 (red) staining. Lower: Magnification (scale bars: 25 μm) of the dLGN (left) and VB (middle). (**C**) Magnified HCN2 stainings of WT (upper), HCN2EA litters (middle), and HCN2-KO mice (lower panel) in the VB region. Scale bars: 20 μm. (**D**) Analysis of the mean intensity of the HCN2 fluorescence in WT and HCN2EA soma and dendrites (WT: gray squares, soma [n = 20], dendrites [n = 26]; EA: blue squares, soma [n = 17], dendrites [n = 26]). (**E**) Magnified HCN4 stainings of WT (upper) and HCN2EA litters (middle). Staining in the absence of primary antibody is shown in the bottom panels. Scale bars: 20 μm. (**F**) Analysis of the mean intensity of the HCN4 fluorescence in WT and HCN2EA soma and dendrites (WT: gray circles, soma [n = 23], dendrites [n = 25]; EA: orange circles, soma [n = 25], dendrites [n = 25]) ***P < 0.001 by 1-way ANOVA with Bonferroni's post hoc test. NS, not significant.

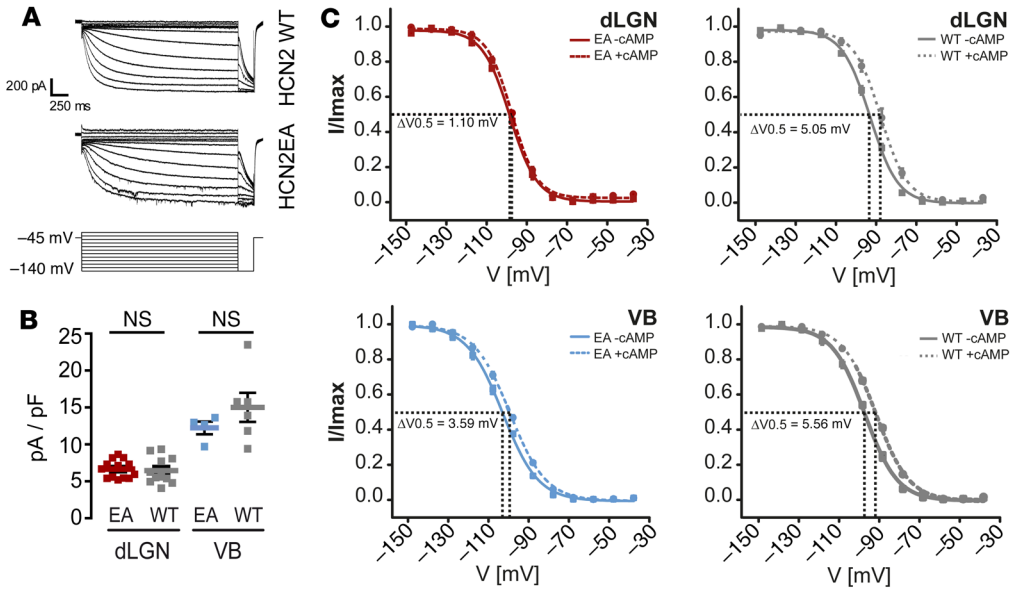

Figure 3. Impaired modulation of I_h by cAMP in thalamocortical neurons expressing HCN2EA. (**A**) Representative I_h traces from thalamocortical WT (upper) and HCN2EA neurons (lower) in the VB. Below, voltage protocol used to evoke current traces. (**B**) I_h density of thalamocortical neurons in the dLGN (HCN2EA, red squares [*n* = 13]; WT, gray squares [*n* = 11]; *P* = 0.3524 by Mann-Whitney test) and the VB (HCN2EA, blue squares [*n* = 4]; WT, gray squares [*n* = 6]; *P* = 0.6021 by Mann-Whitney test). NS, not significant. (**C**) Normalized current-voltage relationships of I_h in thalamocortical neurons of WT and HCN2EA mice in the absence (–cAMP) and presence of 1 μM cAMP (Boltzmann fit). Upper left: dLGN, HCN2EA: solid red line, –cAMP (*n* = 6); dashed red line, +cAMP (*n* = 4). Upper right: dLGN, WT: solid gray line, –cAMP (*n* = 6); dashed gray line, +cAMP (*n* = 5). Lower left: VB, HCN2EA: solid blue line, –cAMP (*n* = 4); dashed blue line, +cAMP (*n* = 5). Lower right: VB, WT: solid gray line, –cAMP (*n* = 6); dashed gray line, +cAMP (*n* = 8). The cAMP-dependent shift of the midpoint potentials ($V_{0.5}$) of activation is indicated as dashed black lines.

(Figure 6C). Similarly, HCN2EA neurons revealed a larger voltage-sag ratio (i.e., weaker contribution of I_h) than in WT neurons; however, the voltage sag was slightly increased by cAMP (Figure 6D).

To examine the effect of altered firing behavior on network activity, we used a 2-photon Ca^{2+} imaging approach as previously described for the analysis of HCN2-KO mice (8). Spontaneous discharge patterns of TC cell ensembles in the semipreserved thalamic network were investigated in horizontal slices of somatosensory thalamus in which spontaneous rhythmicity is high due to cell-intrinsic and intrathalamic mechanisms (cell-intrinsic bursting of TC cells) (37–39). Given this connectivity, intrathalamic reverberating low-frequency oscillations can be induced. As a measure of electrical activity, Ca^{2+} fluctuations of ensembles of TC neurons were monitored. Upon facilitation of neuronal activity by 4-aminopyridine (4-AP), 74 out of 153 WT cells showed spontaneous calcium transients (Figure 6E). Oscillatory behavior was not detected in any of these cells (Figure 6F). In preparations from HCN2EA mice, 70 out of 170 cells were active in the presence of 4-AP. However, more than 35% of these cells showed oscillatory activity (Figure 6, E and F), as evident by the repeated synchronous increases in fluorescence at approximately 0.5 Hz, a frequency that is typical for the clock-like delta rhythm of TC cells in the acute slice (26, 38).

Loss of cAMP modulation in HCN2 is sufficient to produce generalized seizures. In order to determine the consequences of altered thalamic network activity we performed telemetric EEG recordings in freely moving mice (Figure 7, A and B). HCN2EA mice displayed frequent spike-and-wave discharges (SWDs) and behavioral arrest, the hallmark of generalized seizures of the absence-epilepsy type (Figure 7A and Supplemental Videos 1–3). The SWDs concurred with episodes of low muscular tone as reflected in the EMG (traces below the EEG). The SWDs had a frequency of 3–5 Hz and comprised 0.30% ± 0.11% of the recording time. The mean duration of an SWD was 4.57 ± 0.50 seconds and the time between 2 SWDs was 2,175 ± 734.6 seconds (Figure 7B). Global HCN2-KO mice displayed SWDs with comparable frequency and duration as seen in HCN2EA mice (8). In contrast, SWDs were not detected in WT littermates.

Next, we examined the time spent in the different vigilance states (wake, REM sleep, NREM sleep). In animals entrained to a 12-hour light/12-hour dark cycle, both WT and HCN2EA mice showed a sleep-wake pattern characteristic of nocturnal animals with their main resting period during the light phase, in which they

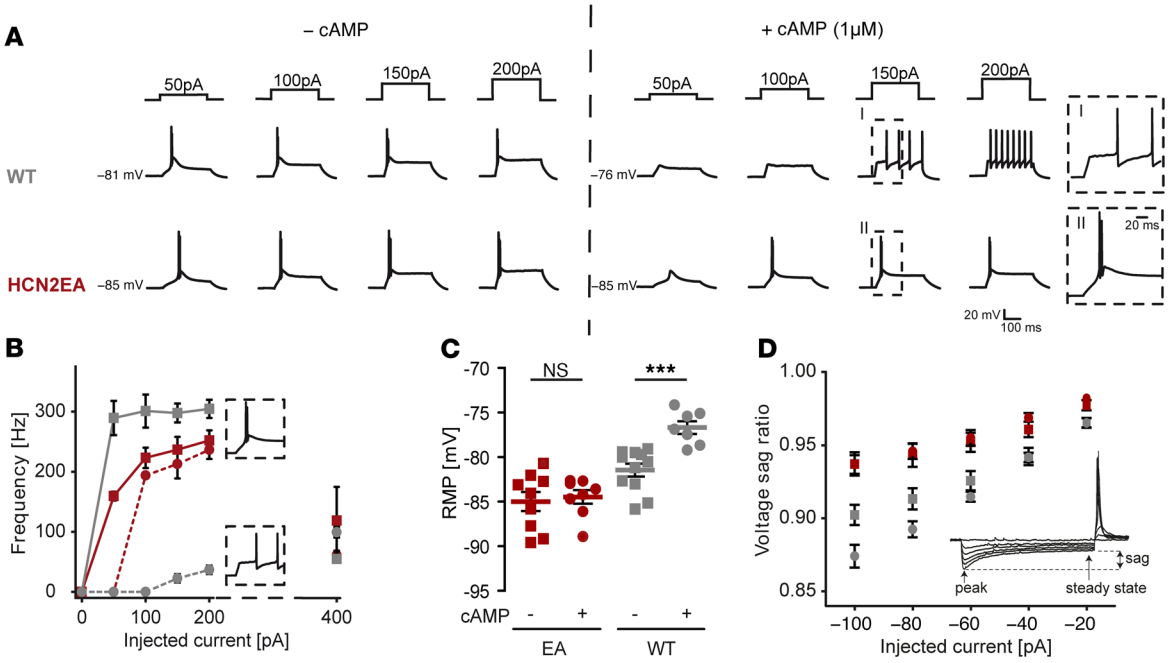

Figure 4. Lack of cAMP modulation in HCN2 alters firing properties of thalamocortical neurons in the dLGN. (**A**) Firing properties of WT and HCN2EA dLGN neurons in the absence (–cAMP, left) or presence of 1 μM cAMP (right). Current injections (300 ms) are indicated above the traces. Insets: Enlarged traces elicited at 150 pA/+cAMP for WT (I) and HCN2EA (II). Traces are representatives of measurements shown in **B**. (**B**) Firing frequencies of TC neurons at different injected currents. HCN2EA (solid red line, –cAMP [*n* = 5]; dashed red line, +cAMP [*n* = 3]); WT (solid gray line, –cAMP [*n* = 4]; dashed gray line, +cAMP [*n* = 3]). Insets: Representative examples of burst and tonic firing at 200 pA. When injecting 400 pA, neurons fired in tonic mode independently of genotype and cAMP concentration. (**C**) Resting membrane potential (RMP) of TC neurons in the absence and presence of 1 μM cAMP. HCN2EA (red squares, –cAMP [*n* = 9]; red circles, +cAMP [*n* = 8]). WT (gray squares, –cAMP [*n* = 11]; gray circles, +cAMP [*n* = 7]). NS, $P = 0.7052$ (EA), ***$P = 0.0004$ (WT) by unpaired *t* test. (**D**) Voltage-sag ratios (peak vs. steady state) at different negative current injections in the absence and presence of 1 μM cAMP. HCN2EA (red squares, –cAMP [*n* = 9]; red circles, +cAMP [*n* = 8]); WT (gray squares, –cAMP [*n* = 11]; gray circles, +cAMP [*n* = 7]). Inset: Example measurement of the voltage sag and calculation of the sag ratio.

spend approximately 70% of their time asleep (NREM and REM sleep). Both genotypes also did not differ with respect to the total time spent in the different vigilance states during the light and the dark phases (Figure 7C). However, mean normalized EEG spectral profiles from 0 to 25 Hz differed specifically for NREM but not for REM sleep (data not shown) in frequency bands known to arise within thalamocortical loops (Figure 7D). First, the sigma power band (9–16 Hz) that contains sleep spindles (40) was attenuated in the HCN2EA mice (Figure 7E; WT, 0.78 ± 0.17 vs. HCN2EA, 0.61 ± 0.05). The observed attenuation of sigma power was equally distributed across the power band. Conversely, the power in the delta band was not equally distributed. It was markedly augmented in the low-frequency slow delta (δ_1: 1.75 Hz), while the fast delta band (δ_2: 2.5–4 Hz) was unchanged. Because sleep spindles and delta rhythms depend on rhythmic activity in TC neurons, this result strongly suggests that increased cell-autonomous burst firing of TC neurons in HCN2EA mice boosted the occurrence of low-frequency thalamocortical rhythms in the EEG, yet compromised the capability of these cells to engage in reciprocal interactions with thalamic reticular nucleus (nRT) cells to generate sleep spindles.

We wondered whether impaired VB complex firing caused the absence-seizure phenotype observed in HCN2EA. To verify this hypothesis, we locally deleted the HCN2 channel in the VB by stereotactically injecting an AAV2/8 vector expressing Cre recombinase under the control of neuron-specific human synapsin promoter into the VB of *HCN2*$^{fl/fl}$ mice. Using coexpressed EGFP as a reporter, we verified that only cells in the VB, but not cells in the thalamic RT or ventromedial regions were transfected and that these cells do not have HCN2 channel expression (Figure 8, A and B). EEG measurements performed 2 weeks after injection consistently revealed the presence of SWDs that were qualitatively similar to those found in global HCN2-KO or HCN2EA mice (Figure 8C). In mice injected with an adeno-associated virus (AAV) that only expressed EGFP, SWDs were absent, indicating that the effect was caused by the deletion of HCN2

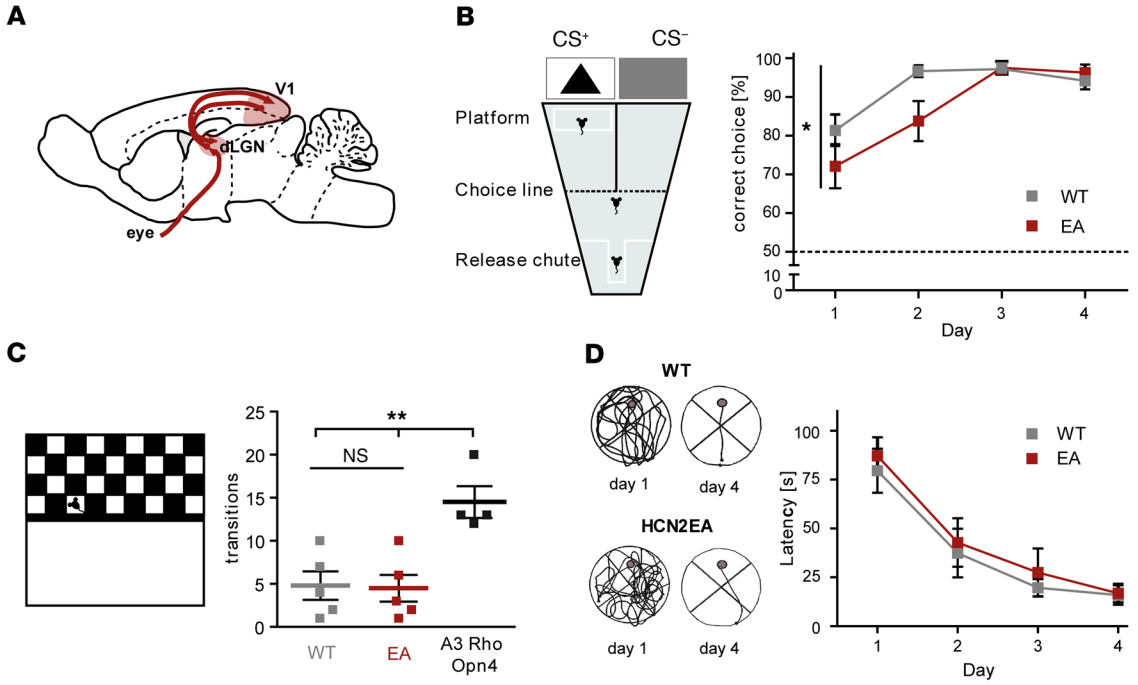

Figure 5. Lack of cAMP modulation in HCN2 impairs visual learning. (**A**) Scheme of the geniculate pathway. The dLGN receives input directly from the retina and projects towards the primary visual cortex (V1). (**B**) Left: Design of the visual discrimination task. CS^+, conditioned stimulus; CS^-, nonconditioned stimulus. Right: Learning curve of HCN2EA (red) and WT (gray) animals (n = 8). *P < 0.05 by 1-way ANOVA with Bonferroni's post hoc test. Dashed line indicates chance level. (**C**) Number of transitions over the virtual cliff for HCN2EA (red, n = 5), WT (gray, n = 5), and *Cnga3*$^{-/-}$ *Rho*$^{-/-}$ *Opn4*$^{-/-}$ triple-KO mice (black, n = 4). **P < 0.01 by 1-way ANOVA with Bonferroni's post hoc test. NS, not significant. (**D**) Swimming traces of WT (upper left) and HCN2EA mice (lower left) on day 1 and day 4 in a Morris water maze. Right: Latency of WT (gray, n = 9) and HCN2EA mice (red, n = 9) to find a hidden platform.

in the VB (Figure 8D). Finally, we sought to determine whether VB-specific deletion of HCN4 could also exert effects on the EEG, given that HCN4 is coexpressed in the VB together with HCN2 and likely underlies the residual cAMP-sensitive I_h component observed in HCN2EA. However, in the EEG of *HCN4*$^{fl/fl}$ mice injected with the same viral vector used for HCN2 deletion, as well as in *HCN4*$^{fl/fl}$ mice injected with an EGFP-expressing control vector, we did not observe SWDs (Figure 8E).

Discussion

It is known that cAMP is a crucial factor regulating I_h/HCN channel function in the heart and brain. However, so far it has not been possible to directly identify functions attributable to CDR of HCN channels in vivo without interfering with voltage-dependent functions. Most studies addressing CDR of HCN channels have been based on pharmacological blockers of I_h, or on the use of experimental approaches that involve up- or downregulation of cAMP-signaling pathways upstream of the channels. One study prevented CDR of HCN channels using a synthetic peptide based on TRIP8b (41). However, this peptide can only be used for in vitro experiments and is also not specific for a given HCN channel isoform. In the present study, we aimed to directly address this problem by genetically abolishing cAMP binding in the HCN2 channel without altering any other principal channel features. This strategy allowed us to define the specific contribution of cAMP modulation for a distinct member of the HCN-channel family (HCN2). Nevertheless, it might be possible that altered cAMP dynamics could interfere with our phenotype by pathways that do not involve direct cAMP-dependent gating of HCN2.

How do changes in CDR of HCN2 lead to changes in neuronal function, neuronal networks, and behavior? To address this question we focused on the thalamocortical circuit. In the current study, we show direct evidence that loss of CDR has profound consequences for the switch between tonic to burst-firing in thalamic neurons. We found that HCN2EA TC neurons of both dLGN and VB nuclei display a slightly hyperpolarized RMP compared with WT, indicating that basal cAMP levels in these neurons normally lead to a sustained partial preactivation of HCN2. The difference between WT and HCN2EA RMP was less pronounced in the VB, likely because VB neurons (in contrast to the dLGN) also express the highly

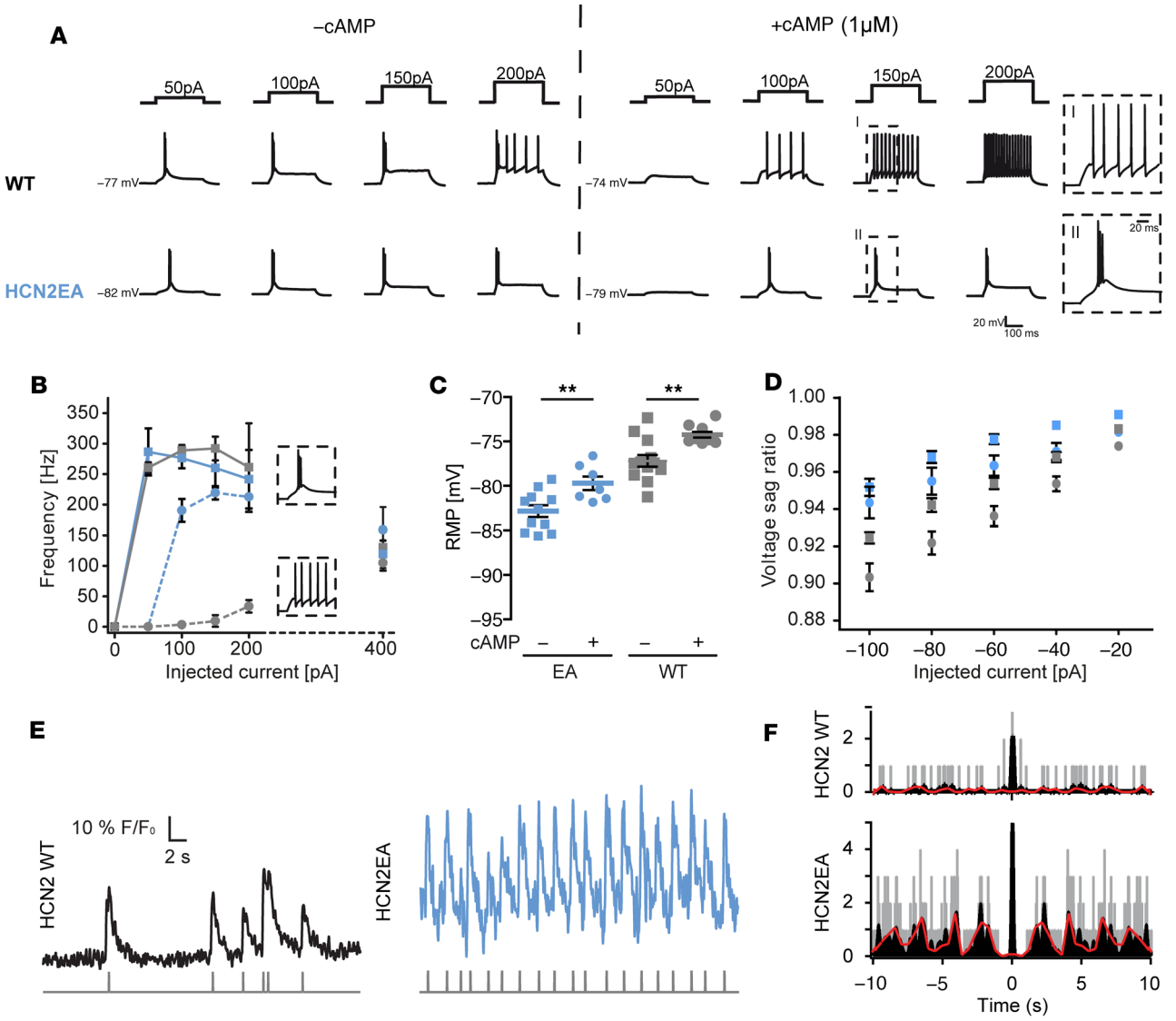

Figure 6. Analysis of neuronal network activity in the thalamic VB region. (**A**) Firing properties of WT and HCN2EA TC neurons from the VB region. Shown are action potentials elicited by 300-ms depolarizing current pulses at resting membrane potential of WT and HCN2EA TC neurons under control conditions (–cAMP) and in the presence of 1 μM cAMP. Unlike WT neurons, HCN2EA neurons fail to switch from burst to tonic firing in the presence of cAMP within the current range from 50–200 pA. The insets show representative examples of tonic (I) and burst (II) firing activity induced by injecting 150 pA in a WT and HCN2EA neuron, respectively. Traces are representatives of measurements shown in **B**. (**B**) Frequency of action potential generation as a function of the injected current. HCN2EA: solid blue line, –cAMP (n = 6); dashed blue line, +cAMP (n = 6). WT: solid gray line, –cAMP (n = 4); dashed gray line, +cAMP (n = 5). (**C**) Resting membrane potential (RMP) of TC neurons from the VB of HCN2EA (blue squares, –cAMP [n = 11]; blue circles, +cAMP [n = 7]) and WT (gray squares, –cAMP [n = 13]; gray circles, +cAMP [n = 10]).**P < 0.01 (P = 0.0083 [EA], P = 0.0013 [WT]) by Mann-Whitney test. (**D**) Voltage-sag ratios of TCs in response to injected current. HCN2EA (blue squares, –cAMP [n = 11]; blue circles, +cAMP [n = 7]); WT (gray squares, –cAMP [n = 13]; gray circles, +cAMP [n = 10]). (**E**) Original traces of spontaneous activity of individual thalamic neurons visualized using 2-photon calcium imaging. The raster plots under the traces (gray) indicate the detected peaks. All active cells from WT mice show irregular transients (left, n = 74), whereas more than one-third of the active cells from HCN2EA mice show oscillatory transients (right, n = 25). (**F**) Autocorrelograms of the traces shown in **E**. Gray, original autocorrelation function (ACF); black, smoothed ACF; red, cubic spline interpolation of the smoothed ACF.

cAMP-sensitive HCN4 channel. In both nuclei investigated, TC neurons did not switch from burst to tonic firing in response to cAMP over a broad range of injected currents (Figure 4A, Figure 6A, and Supplemental Figure 7C). A possible explanation for this finding could be that HCN4 and HCN2 operate in different compartments of TC neurons. In support of this hypothesis, we found that HCN2 is enriched in somata compared with the dendrites, while HCN4 expression shows the opposite polarity (Figure 2). An alternative explanation could be that the residual cAMP-dependent I_h upregulation provided by HCN4 is not sufficient to rescue normal firing. Importantly, HCN2EA mice showed impaired visual learning, indicating that visual

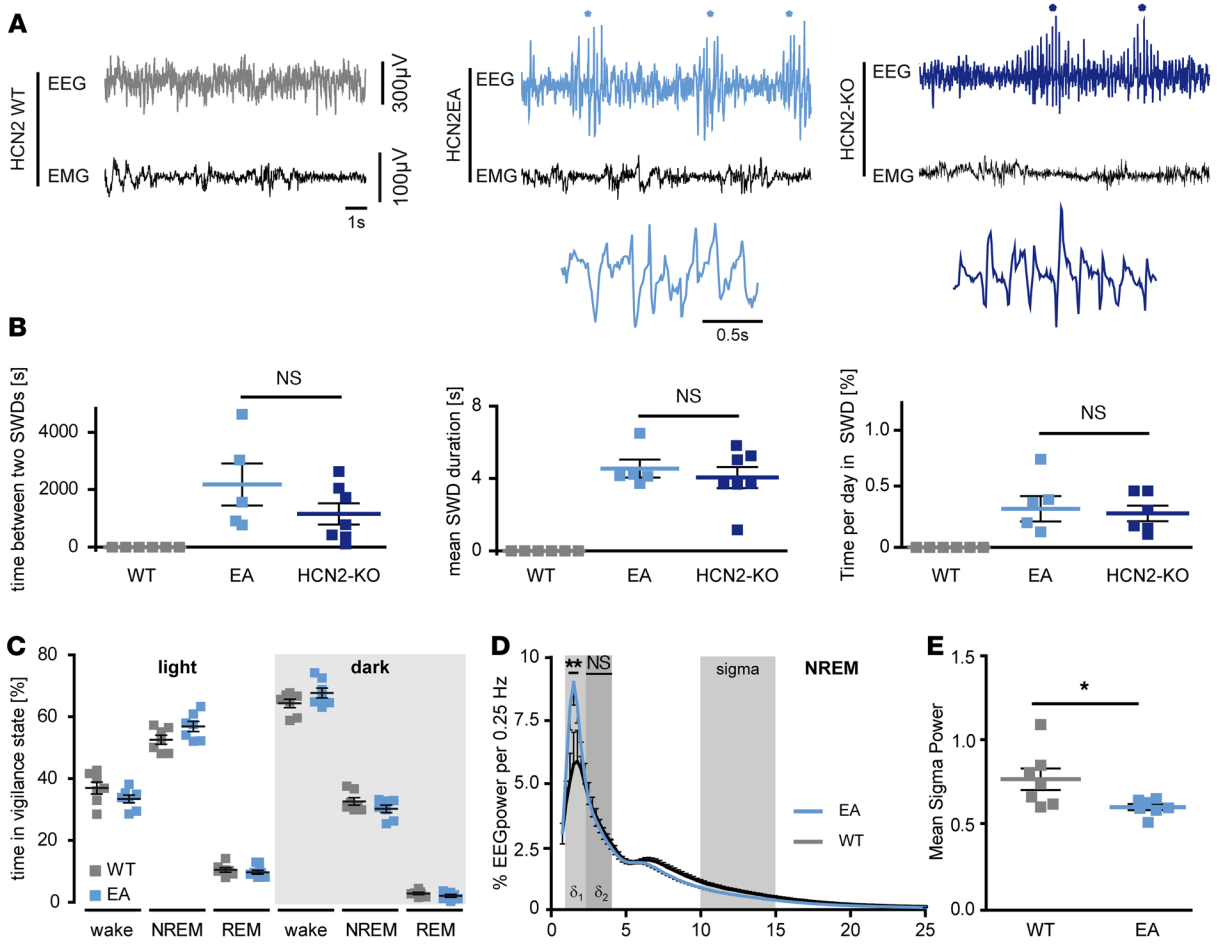

Figure 7. Absence epilepsy in HCN2EA mice. (**A**) EEG traces of WT (left), HCN2EA (middle), and global HCN2-KO mice (right panel). Spike and wave discharges (SWDs) in the EEG of HCN2EA and global HCN2-KO are marked by asterisks. SWDs concur with episodes of low activity in the EMG. Higher magnifications of SWD traces are displayed below the EEG of HCN2EA and HCN2-KO mice. Representative traces of animals analyzed in **B**. (**B**) SWD characteristics of HCN2EA (light blue, $n = 5$) and global HCN2-KO (dark blue, $n = 6$) animals compared with WT traces (gray, $n = 6$) regarding the time between 2 SDWs (left), mean SWD duration (middle), and the time per day in SWDs (right). NS, not significant (1-way ANOVA, Bonferroni's post hoc test). (**C**) Time spent in different vigilance states (wake, NREM and REM sleep) during light and dark conditions (HCN2EA, blue; WT, gray; $n = 7$). (**D**) Power spectra of NREM sleep in HCN2EA (blue, $n = 7$) and WT animals (gray, $n = 7$). $^{**}P < 0.01$ by 2-way ANOVA. (**E**) Mean sigma power in HCN2EA (blue, $n = 7$) and WT animals (gray, $n = 7$). $^{*}P = 0.0175$ by Mann-Whitney test.

learning critically relies on CDR of firing modes in the dLGN. Increased burst firing of thalamocortical cells in the dLGN may lead to a disruption of the flow of visual information to the visual cortex, and therefore cause defects in thalamus-dependent visual behavior. Notably, the impairment in visual learning observed in HCN2EA could involve multiple neuronal circuits. Given that HCN2 is by far the predominant isoform in the dLGN, the likelihood that HCN2 in this nucleus is a major contributor to the effect is very high.

The occurrence of generalized seizures in HCN2EA mice provides a striking example of absence epilepsy of thalamic origin. HCN2EA mice display some phenotypes observed in global HCN2-KO mice including absence seizures, as characterized by SWDs in EEG recordings from HCN2EA mice that were indistinguishable from those found in global HCN2-KO mice. In addition, during episodes of SWDs mice displayed behavioral arrest (Supplemental Videos 1–3), a characteristic hallmark for absence seizures. However, other phenotypes are not present, including whole-body tremor, ataxia, lower body weight, and reduced life span (Supplemental Figure 2) (8, 9). These observations suggest that the loss of dynamic cAMP modulation does not completely impair HCN2 function in vivo. Rather, it has a specific impact on a subset of functions that reflects the activity of distinct neuronal circuits. This finding also supports previous studies performed in rat models of epilepsy (WAG/Rij and GAERS) in which an upregulation of HCN1 in thalamic TC neurons, and thereby reduced cAMP regulation, was proposed to

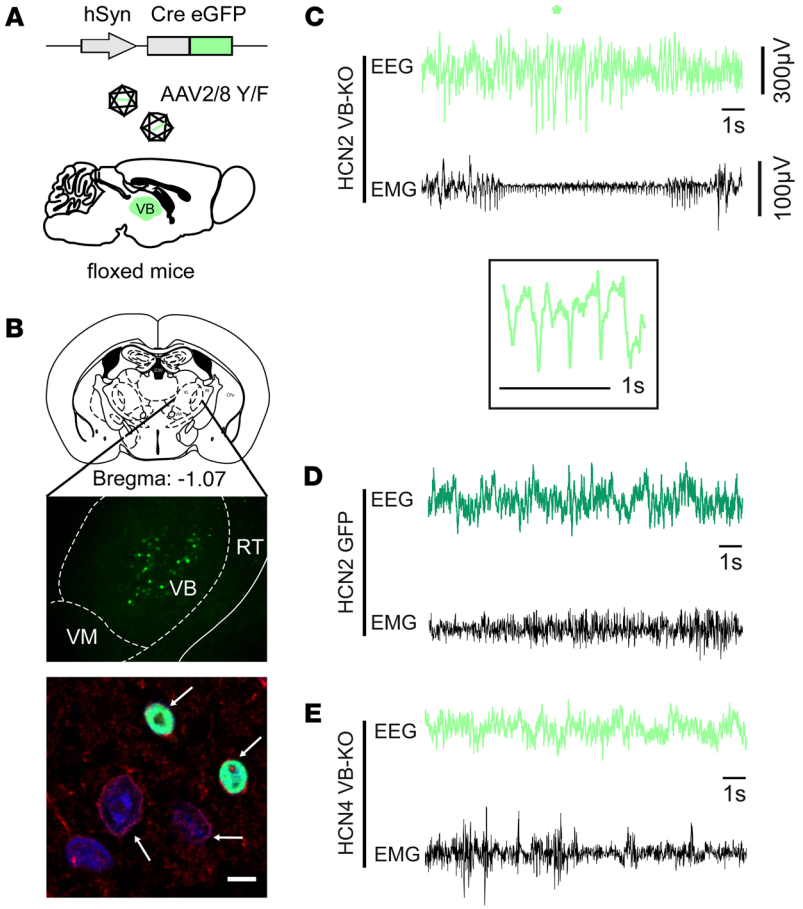

Figure 8. Absence epilepsy in VB-specific HCN2-KO mice. (**A**) Strategy for specific deletion of HCN channels in the VB. Left panel: Scheme of the AAV2/8-hSyn-Cre-EGFP vector that was injected stereotactically into the VB of *HCN*$^{fl/fl}$ mice. The schematic brain shows the injected region in the thalamus. Only cells in the VB show the green EGFP signal due to viral transfection. (**B**) Staining with anti-HCN2 antibody (red) in the VB region shows that Cre/EGFP–positive neurons (green) lack HCN2, while nontransduced (EGFP-negative) cells express HCN2 in the plasma membrane (marked by white arrows). Scale bar: 5 µm. VM, ventromedial region. (**C**) VB-specific HCN2-KO mice show SWDs (marked with an asterisk) in EEG traces (representative trace, *n* = 3). The inset shows a magnification of the SWD. (**D**) Representative EEG (green) and EMG (black) traces of an *HCN2*$^{fl/fl}$ mouse that was injected with a control AAV vector that expresses only EGFP (*n* = 3). (**D**) Representative EEG (green) and EMG (black) traces of a VB-specific HCN4-KO animal that was generated by injecting the same vector as displayed in Figure 7A into the VB of an *HCN4*$^{fl/fl}$ mouse (*n* = 3).

be part of the pathomechanism leading to seizures (29, 42). Previous rodent models for absence epilepsy have focused on abnormal cortical activity and on a perturbation of cortically controlled feedforward inhibition of TC cells through the nRT (43, 44). Absence epilepsy was also found in animals deficient in corticoreticular excitation, which leads to a hyperexcitability of TC cells due to the lack of feedforward inhibition (45). Moreover, real-time induction of thalamic burst firing using optogenetics evoked absence seizures in animal models (46).

However, it is possible that other brain regions expressing HCN2 (e.g., the cortex) could also contribute to this phenotype (47). We sought to clarify this question by acutely deleting HCN2 locally in the VB of adult mice using an AAV-mediated approach, which was designed to avoid compensatory changes in gene expression pattern that could occur in classical knockouts and also allows for the spatial control of gene deletion. In agreement with a key role of the VB, these mice displayed SWDs in EEG recordings that were qualitatively identical to those observed in HCN2EA or global HCN2-KO mice. In line with the distinct functional profile of HCN4 discussed above, mice with a VB-specific deletion of HCN4 did not show SWDs. Taken together, these findings support the key role of HCN2 in information processing in the VB and suggest that HCN4 is involved in functions that are not directly coupled to those controlled by HCN2.

Our findings on the level of the channel (voltage clamp), on the cellular level (current clamp), and systemic in vivo level are summarized in Supplemental Figure 7. The cartoon illustrates that a fixed amount of channel activity is present for a given membrane potential in the absence of cAMP dynamics (steady-state activation curve on the left [closed symbols] of WT HCN2 channels in the absence of cAMP). On top, channel activity of WT HCN2 can be gradually tuned according to cellular needs by cAMP via upstream cAMP-sensitive signaling effectors like $G_{\alpha S}$ (Supplemental Figure 7A; red area; HCN2 channels with cAMP dynamics). In contrast, HCN2EA channels cannot bind cAMP and hence, are unresponsive to changes in the cAMP concentration. The dynamic range for cAMP-sensitive tuning is represented by the red area in Supplemental Figure 7. Within the physiological range of membrane voltages, cAMP can recruit up to 300% of HCN2 channel activity, whereas in the absence of cAMP the current is greatly reduced (less than one-third).

In the thalamus, the transition between burst mode activity and the transmission mode is regulated by cAMP-sensitive upregulation of HCN2 channels. This is critically important for keeping neurons in the transmission mode during wakefulness and thereby protects the brain from absence epilepsy and behavioral arrest. First, TC neurons lacking cAMP modulation of HCN2 channels have a slightly hyperpolarized RMP, which facilitates the transition to the burst-firing mode. Consequently, in the semi-intact circuit TC cells tend to show synchronized low-frequency activity at their endogenous clock-like pace, as observed previously when blocking I_h pharmacologically (26). This will in turn facilitate the excitation of reticular cells and create conditions that are prone to hypersynchrony in reticular-thalamic and cortico-thalamic network loops in vivo. Second, the absence of CDR of HCN2 may lead to an imbalance between depolarizing inward currents carried by I_h and hyperpolarizing currents such as potassium currents. As a result, the membrane potential during the transmission mode (tonic firing) would be less stable and prone to perturbing influences. This hypothesis is consistent with a similar stabilizing role for HCN channels regarding the RMP in other systems (48, 49). In vivo, this excitatory-inhibitory imbalance would manifest on the behavioral level as sleep-like episodes, behavioral arrest, spike and wave discharges in EEG recordings, as well as episodes of behavioral arrest, all of which are consistent with the clinical symptoms of absence episodes. The transition between sleep and waking is accompanied by marked changes in the activity of forebrain and brainstem arousal systems. In these arousal-promoting mechanisms, neurotransmitters are released that lead to cAMP upregulation of I_h, membrane depolarization, and promotion of tonic firing in thalamic cells (27). However, in spite of the pronounced deficiency of cAMP signaling, animals spent comparable time in wakefulness. Although these data argue against a major role of CDR of HCN2 in the control of waking from sleep during arousal, it should be noted that arousal promotion also includes cAMP-independent neurotransmitter signaling, such as G protein–mediated closure of K^+ channels to depolarize TC cells (50, 51). The redundancy of wake-promoting mechanisms could therefore overcome the deficiency in CDR of HCN2.

Thalamic HCN channel–dependent activities have also been implicated in the control of low-frequency sleep waves, particularly in the sigma (10–15 Hz) and delta (0.5–4 Hz) frequency range (1). The decrease in sigma power noted in the NREM sleep spectral profile is in line with the notion that HCN channels are relevant for sleep spindle generation (23, 52). The augmentation of power in the slow delta range (1–2.5 Hz) in HCN2EA animals suggests that thalamic activity regulates low-frequency oscillatory activity in the delta band and indicates a complex interplay of thalamic and cortical rhythm generators in the composition of the delta band, which is a major frequency band of NREM sleep. Our observations are in line with increasing evidence showing that slow and fast delta-frequency components serve different roles in homeostatic sleep regulation (53). Furthermore, the mouse model generated in this study will be a valuable tool to examine the contribution of HCN2 in other systems in which CDR of I_h has been proposed.

Our findings on HCN2-cAMP–dependent burst control and absence epilepsy are thus fully consistent with a central role of thalamic burst propensity in thalamic epileptogenesis. In addition, we show that HCN2 channels are a molecular target in which burst firing of TC cell activity can be regulated, thereby expanding the range of proposed anti-absence drug strategies.

Methods

PyMOL. The figure of the CNBD structure was prepared using PyMOL Molecular Graphic System, version 1.3 (Schrodinger LLC). The structure is based on the sequence 483–607 of the human HCN1 structure in complex with cAMP (15), downloaded from the RCSB protein database (https://www.rcsb.org/, accession code 5U6P).

Generation of HCN2EA mice. The targeting construct was amplified using a BAC clone (Genome Systems) isolated from a genomic 129/SvJ library. Base pairs in exon 7 of murine HCN2 gene coding for amino acids R591 and T592 of mHCN2 were mutated to E591 and A592 by site-directed mutagenesis [(CGT) R591E(GAA)/(ACG)T592A(GCG)]using a QuikChange II XL site-directed mutagenesis kit (Agilent) according to the manufacturer's protocol. For embryonic stem cell selection, an ACN-selection cassette (54) flanked by loxP sites was inserted in intron 5 of the targeting construct. The construct was electroporated into R1 embryonic stem cells, and G418-resistant clones were screened by Southern blot analysis. Correctly targeted clones were injected into C57BL/6N blastocysts, and the resulting chimeric mice were mated with C57BL/6N mice for germline transmission. Primers for genotyping the offspring were 5′-AGTTGTACTCAACCAGTGGC-3′ (sense) and 5′-TAGTCACGGTCACTGCCAAG-3′ (antisense). The correct integration of the mutated base pairs was verified by amplifying exon 7 (sense: 5′-GGAAGAAGATGTACTTCATCCAG-3′; antisense: 5′-TGCCCCACTGGAATGGAGCC-3′) and subsequent sequencing (Eurofins).

Immunohistochemistry. Adult mice were sacrificed and brains were deep-frozen in isobutane. Immunohistochemistry was performed in 12-μm-thick cryosections as described previously (55). The following primary antibodies were used: anti-HCN1 (1:300, Alomone, APC-056), anti-HCN2 (1:300, Alomone, APC-030), anti-HCN3 (1:300, Alomone, APC-057), anti-HCN4 (1:300, Alomone, APC-052), Cy3 donkey anti-rabbit IgG (711-165-152, Jackson ImmunoResearch), or Alexa488 donkey anti-rabbit IgG (711-545-152, Jackson ImmunoResearch). Images were acquired at a minimum of 3208 × 3208 pixel resolution in an inverted Leica TCS-SP8 confocal microscope, 10–40×, 1.4-NA objective and 600 Hz. For the comparison of WT and HCN2EA littermates, slices were processed using the same protocol on the same day. The acquisition was performed with identical laser intensities and scanner settings. The intensities of the HCN fluorescence were analyzed using the plot profile tool of ImageJ software (56).

Primary neurons. Primary neurons from WT and HCN2EA mice were isolated as described previously and transfected with either HCN2 (mHCN2_pcDNA3) or HCN2EA DNA (mHCN2EA_pcDNA3) using high–calcium phosphate transfection on DIV4 (57). Immunocytochemistry was performed on DIV14 as described (57). The following primary antibodies were used: anti-HCN2 (1:300, Alomone, APC-030), anti-MAP2 (1:500, Sigma-Aldrich, M9942) followed by Cy3 donkey anti-rabbit IgG (1:400, Jackson ImmunoResearch, 711-165-152) or DyLight 488 anti-mouse (1:800, Jackson ImmunoResearch, 715-485-151).

Western blot. Samples from the dLGN and the VB were punched from adult mouse brain and homogenized in RIPA buffer containing 50 mM Tris pH 8.0, 150 mM NaCl, 1% Triton X-100, 0.5% sodium deoxycholate, 0.1% SDS, and Protease Inhibitor Cocktail (Complete, Mini, Roche). The preparation of brain membranes has been described previously (58). Western blotting was performed using standard methods. Primary antibodies used were anti-HCN2 (1:1000, Alomone, APC-030), anti-HCN4 (1:1000, Alomone, APC-052), anti-ATP1A1 (1:1000, a6F, DSHB, University of Iowa), and anti-Trip8b (1:1000, N212/7, Neuromab). Secondary horseradish-peroxidase-conjugated antibodies were used (rabbit: 1:1000, sc-2030; mouse: 1:2000, sc-2031; Santa Cruz Biotechnology). Signals were acquired with a luminescence image analyzer (ChemiDoc MP; Bio-Rad) and quantified using ImageLab software (Bio-Rad).

Coimmunoprecipitation. Co-IPs were performed with anti-HCN2 antibody (Alomone, APC-030), anti-HCN4 (Alomone, APC-052), or anti-Trip8b (N212/7, Neuromab) using Novex Protein G magnetic beads (Thermo Fisher Scientific) according to the manufacturer's protocol.

qRT-PCR. The VB and dLGN regions of 4- to 5-month-old mice were dissected in 400-μm coronal slices (Vibratome; Leica VT1200S). RNA was isolated using the RNeasy Micro Kit (Qiagen). cDNA was synthesized with the RevertAid First Strand cDNA Synthesis Kit (Thermo Fisher Scientific). qRT-PCR was performed using the following primer sequences: HCN1 for: CTGCTGCAGGACTTCCCACCA, HCN1 rev: ATGCTGACAGGGGCTTGGGC, HCN2 for: CAGGAACGCGTGAAGTCGGCG, HCN2 rev: TCCAGGGCGCGGTGGTCTCG, HCN3 for: TGGCCATGGACCGGCTTCGG, HCN3 rev: GAGCCAGGCCCCGAACACCAC, HCN4 for: AGGGCCTTCGAGACGGTTGCGC, HCN4 rev: GGCCATCTCACGGTCATGCCG, ALAS for: TCGCCGATGCCCATTCTTATC, ALAS rev: GGCCCCAACTTCCATCATCT.

rAAV preparation and stereotaxic injections. Recombinant AAV particles (pAAV-hSyn-Cre-p2A-EGFP or pAAV-hSyn-EGFP) were produced with a 2/8 Y/F capsid variant as described previously (59). Viral particles (1×10^{10}) were delivered bilaterally to the VB region of the thalamus of adult (P60–P70) HCN2 L2 or HCN4 L2 mice anesthetized with isoflurane by stereotaxic injection using a 34-G Hamilton syringe. The stereotaxic coordinates for bilateral targeting were as follows: A/P, −1.2; M/L, ±1.7; D/V, −3.2; and A/P, −3.2 (from bregma). Volume (0.5 μl at each injection site) and speed (100 nl/min) of the injections were

controlled by a WPI Micro4 pump. The Hamilton syringe was retracted from the brain after a 3-minute waiting period to allow diffusion to occur. After suturing and disinfecting, mice were allowed to recover for 2 weeks prior to the start of the in vivo EEG experiments.

Telemetric EEG measurements. To measure the EEG and EMG traces, a telemetric EEG transmitter (F20-EET, Data Science International) was implanted using the following procedure. The head of the mouse was fixed in a stereotactic apparatus and the body temperature was maintained constant at 37°C via a rectal feedback control system. By a small (1.5-cm-long) incision, the scalp was first opened along the median of the head and the skullcap (cranium cerebrale) was dissected. A second incision was made caudally between the scapulae along the longitudinal axis. Using blunt scissors, a small pocket was opened for the transmitter and the 2 electrodes for electromyography (EMG) were sutured on the shoulder muscle. Two tiny holes were drilled into the skullcap (0.7 mm in diameter) using the following coordinates: A/P, –2.0; M/L, 1.8 (from bregma; recording electrode) and A/P, –1.0; M/L, –0.5 (from lambda; reference electrode). After suturing and disinfection, mice were allowed to recover for 2 weeks before in vivo EEG experiments.

Cortical electroencephalogram (EEG/ECoG) and EMG traces of freely moving mice were recorded using A.R.T. software (Data Science International) and videotaped. EMG traces were high-pass filtered at 10 Hz. The vigilance states (wake, NREM sleep, and REM sleep) were scored using Neuroscore3.2.1 (Data Science International). The EEG traces were Fourier transformed (DFT) in a frequency range from 0 to 26 Hz and an epoch size of 4 seconds for NREM sleep using a Hamming Window. Spike trains (spike and wave discharges, SWDs) were defined as a minimum number of 10 spikes with a maximal spike interval of 0.6 seconds.

Behavioral analysis. Behavioral studies were performed with male adult mutant mice and WT littermates. Mice were housed in standard cages in a 12-hour light/12-hour dark cycle. Water and rodent chow were available ad libitum during all tests. All tests were performed during the light phase of the light/dark cycle by trained observer blind to genotype. The virtual-cliff test and the Morris water maze were videotaped using a computer-assisted data acquisition system (VideoMot, TSE). The experiments were performed and analyzed blindly with respect to the animals' genotype.

Footprint analysis. Mice were trained to walk on a sheet of blank paper along a runway (7 × 30 cm). Their front and hind paws were painted with nontoxic paint in blue and green colors, respectively. The resulting footprint traces were analyzed by measuring the following morphometric parameters: stride length, hind base width (normalized to the body length), and hindpaw angle.

Visual discrimination task. The procedure is a test for discrimination of visual stimuli, processed by the geniculate pathway in the dLGN of the thalamus (60, 61). Briefly, mice were trained to discriminate between a conditioned stimulus (CS^+) that is connected to a hidden platform in a water maze and nonconditioned stimulus (CS^-) images. The CS^+ was connected to a hidden platform at the open side of a trapezoid-shaped swimming pool. Each mouse was given 3 blocks of 10 training units per day in 4 consecutive days. One training unit consisted of no more than 5 trials for swimming consecutively into the wrong arm. One training unit was terminated once a mouse crossed the choice line and climbed onto the platform. To avoid the effect of positional learning, the side of the CS^+ image and the platform were pseudorandomly changed after each trial using a Gellerman schedule (LRLLRLRR; L = left, R = right). To assess the visual discrimination capacity, the mean probability of a correct choice per day was analyzed.

Virtual-cliff test. The open field consisted of a white acrylic glass arena of 48 × 48 × 30 cm under uniform (25 lux) lightning condition. Mice were allowed to explore the arena for 10 minutes. The arena was subdivided into 2 zones using the SMART software: zone 1, the central square area of 25 × 25 cm equidistant from the walls; and zone 2, the remaining borders. The transitions between the 2 zones were monitored.

Morris water maze. The Morris water maze is a test designed for hippocampus-dependent learning (62). Briefly, mice were trained for 4 days (8 trials per day) to locate a stable platform (10 cm in diameter). The platform was placed in a circular swimming pool (120 cm in diameter, 70 cm high, white plastic) filled with water. The starting position of the mouse was changed from trial to trial in a pseudorandom order, whereas the platform was kept in a constant location. Distal cues in the testing room and the water maze, such as patterned cardboards, were provided as spatial references. Trials were terminated if the mouse had climbed onto the platform or after swimming for 2 minutes.

Acute thalamic slice patch recordings. Horizontal or coronal slices (250–300 μm) containing the VB complex or the dLGN, respectively, were prepared on a vibratome (HM 650V, Microme) in an ice-cold oxygenated (95% O_2, 5% CO_2) solution containing (mM): 65.5 NaCl, 2.5 KCl, 1.25 NaH_2PO_4, 26 $NaHCO_3$, 0.5 $CaCl_2$, 7 $MgCl_2$, 105 sucrose, 24.7 glucose, and 1.7 ascorbic acid. Slices were incubated at 35°C for 30 minutes and

left at room temperature in an oxygenated artificial cerebrospinal fluid (ACSF) solution containing (mM): 131 NaCl, 2.5 KCl, 1.25 NaH_2PO_4, 26 $NaHCO_3$, 2 $CaCl_2$, 1.2 $MgCl_2$, 18 glucose, and additionally with 1.7 ascorbic acid for storage until recording.

Whole-cell recordings were obtained from TC neurons of the VB or dLGN in slices perfused at 31°C–33°C with oxygenated ACSF. TC neurons were visualized with an upright microscope (Axioskop 2 FS plus, Zeiss) with an IR CCD camera (VX55, Till Photonics). A horizontal puller (DMZ Universal Electrode Puller, Zeitz-Instruments) was used to pull patch pipettes from borosilicate glass tubing (GC150TF-10, Harvard Apparatus). Patch pipettes were filled with the following solution (mM): 140 $KMeSO_4$, 10 HEPES, 10 KCl, 0.1 EGTA, 10 phosphocreatine, and 4 MgATP. The osmolarity was adjusted to 305 mOsm/l, and the pH was adjusted to 7.3. In addition, 0.2 mM GTP was added freshly before each experiment. For experiments including cAMP, 1 μM 8-bromo cAMP (Sigma-Aldrich, B7880) was added to the pipette solution. The resistance of the electrode was 2.5–6.0 MΩ. A liquid junction potential of –8.9 mV was calculated using the Junction Potential tool of the Clampex 10.5 software and corrected off-line (63).

Voltage clamp recordings. For measurement of I_h, slices were perfused with an oxygenated ACSF plus 1 mM $BaCl_2$ and 0.5 μM tetrodotoxin.

To determine I_h steady-state activation curves, TC neurons were clamped at a holding potential of –45 mV from which pulses of 2.5-second duration were applied from –140 mV to –30 mV in 10-mV increments, followed by a 250-ms test pulse to –140 mV. Tail currents measured immediately after the final step to –140 mV were normalized to the maximal current (I_{max}) and plotted as a function of the preceding membrane potential (10). The curves were fitted with a Boltzmann function: $I/I_{max} = (A1 - A2)/(1 + e^{[V-V_{0.5}]/k}) + A2$, where $V_{0.5}$ and k represent the half-maximal voltage and Boltzmann slope factor, respectively, and A1 and A2 represent the initial and final I/I_{max} values. The current density was calculated as the amplitude recorded at –140 mV divided by the cell capacitance. Time constants were fitted by a single exponential function.

Current-clamp recordings. To record firing patterns, slices were perfused with an oxygenated ACSF. TCs were clamped at their RMP and 300-ms depolarizing pulses ranging from 50 to 400 pA were applied. To test for the influence of the membrane potential on firing modes, TCs were first clamped at their RMP and 300-ms depolarizing pulses from 50 to 200 pA were applied. Next, by application of constant currents ranging from –15 to –30 pA or from +10 to +30 pA, TCs were brought to a more hyperpolarized or depolarized potential and experiments were repeated. The voltage sag was determined by negative-current injections for 2.5 seconds in 20-pA increments from –100 to –20 pA. The sag ratio was calculated by dividing the steady state of the sag measurement by the peak voltage deflection (64).

Cell culture and heterologous expression. HEK293T cells (ATCC, CRL-3216) were maintained in DMEM medium (Gibco, Life Technologies, Inc.) supplemented with 10% fetal bovine serum, 100 units/ml penicillin, and 100 μg/ml streptomycin, and incubated at 37°C with 10% CO_2. At 80% confluence, HEK293T cells were seeded on 6-well plates (diameter 3.5 cm) for transfection. After 24 hours, cells were transfected with expression plasmid DNA (4 μg of each plasmid per well) using the Turbofect transfection reagent (Thermo Fisher Scientific). For electrophysiological measurements, transfected cells were detached using 0.05% trypsin-EDTA (Gibco, Life Technologies, Inc.) and replated on to 12-mm poly-L-lysine–coated coverslips in 24-well plates.

Stable HCN2 or HCN2EA HEK293 cells were generated using the Flp-In-293 Cell Line (Thermo Fisher Scientific).

Electrophysiology of HEK cells. Currents of heterologously expressed HCN2 and HCN2EA channels were measured using the whole-cell patch-clamp technique as previously described with slight changes (65). The extracellular solution was composed of (mM): 135 NaCl, 0.5 $MgCl_2$, 1.8 $CaCl_2$, 5 HEPES, 5 KCl, pH 7.4 adjusted with NaOH. The effect of cAMP was tested for by adding 100 μM cAMP to the intracellular solution the day of recording. Steady-state activation curves were determined by applying a hyperpolarizing voltage of –130 mV from a holding potential of –40 mV for 2 seconds (for both WT and HCN2EA). The amplitude of I_h was calculated by subtracting the instantaneous current amplitude from the steady-state current. The density of I_h was calculated by dividing the I_h current amplitude at –130 mV by the membrane capacitance obtained during whole-cell recordings.

Internal perfusion experiments. Planar patch-clamp technology combined with a fast internal perfusion system (Port-a-Patch, Nanion Technologies) was used to examine the kinetics and current density of HCN2 and HCN2EA channels in stably transfected HEK293 cells. Data were digitized at 20 kHz and filtered at 2.9 kHz. Fast and slow capacitive transients were cancelled by the compensation circuit of the EPC-10 double amplifier. All recordings were obtained at room temperature. The extracellular solution was composed of (mM): 110

NaCl, 5 KCl, 1.8 $CaCl_2$, 0.5 $MgCl_2$ and 5 HEPES (pH adjusted to 7.4 with NaOH). The intracellular solution contained (mM): 70 KCl, 60 KF, 10 NaCl, 0.5 $MgCl_2$ and 5 HEPES (pH adjusted to 7.4 with KOH). All solutions were sterile filtered before use. Currents were evoked from a holding potential of –40 mV by applying 2-second pulses of –150 mV every 10 seconds. The effect of 10 μM cAMP was examined by exchanging the standard internal solution with internal solution supplemented with cAMP using the internal perfusion system after the cells reached steady state after rundown.

Two-photon calcium imaging. Experiments were carried out in horizontal brain slices as described previously (8, 66–68). We guided a micropipette with a resistance of 3 to 5 MΩ to the VB region in the thalamus and applied pressure (10 psi) for 2–4 minutes to eject the solution from the pipette. Activity of thalamic neurons was monitored by imaging the fluorescence changes with a custom-built 2-photon microscope based on a Ti:sapphire pulsing laser operating at a wavelength of 800 nm and resonant galvo-mirror system (8 or 12 kHz, GSI) through a 40×, 0.8 numerical aperture (Nikon) water immersion objective. Full-frame images were acquired at 40 Hz using custom-written software based on LabView (National Instruments). We performed image analysis offline. Regions of interest (ROIs) were drawn around individual somata, and then relative fluorescence change (ΔF/F) versus time traces were generated for each ROI. Based on the original fluorescence recordings, binary traces were generated in which time points of fluorescence peaks were assigned the value "1" in contrast to "0" for all other time points. A cubic spline interpolation was performed on smoothed autocorrellograms that were calculated for 120-second-long binary traces using Igor Pro software (Wavemetrics). A regular pattern of satellite peaks revealed oscillatory activity.

Statistics. Electrophysiology data were analyzed using PatchMaster software (HEKA Elektronik, Harvard Bioscience). Data plotting and statistical analysis were performed using GraphPad Prism 5. All values are presented as mean ± SEM for the indicated number n of experiments. P values were calculated by Mann-Whitney test or 1- or 2-way analysis of variance (ANOVA) with Bonferroni's post hoc test. $^*P < 0.05$, $^{**}P < 0.01$, and $^{***}P < 0.001$ were considered statistically significant.

Study approval. The studies were carried out in accordance with the approved guidelines of the local committee of laboratory animal care (District Government of Upper Bavaria) and German Laws on animal welfare (Tierschutzgesetz). The HCN2-KO and HCN2 L2 mouse lines have already been published (8) as well as the *Cnga3*$^{-/-}$ *Rho*$^{-/-}$ *Opn4*$^{-/-}$ triple-KO mouse (36).

Author contributions

VH designed and performed behavioral experiments, viral knockdown, immunohistochemistry, Western blots, EEG measurements, generated HCN2EA expression vectors and the HEK293 stable HCN2EA cell line, and analyzed data. SS performed EEG measurements and analyzed sleep parameters. MSS, HH, and KLM performed electrophysiological experiments in thalamic slices. JK, RDR, and SF performed electrophysiological experiments in HEK293 cells. M. Brümmer performed qRT-PCR analysis. CG generated the HCN2EA mouse together with MM. A. Ludwig generated the floxed HCN2 and HCN4 mice. JH, BZ, and AK performed calcium imaging in thalamic slices. DI helped to implement telemetric EEG recordings. A. Lüthi helped to implement electrophysiology in thalamic slice preparations. CWS and M. Biel designed experiments and analyzed data. CWS and M. Biel wrote the manuscript.

Acknowledgments

We thank Mario R. Capecchi, Department of Human Genetics and Howard Hughes Medical Institute, University of Utah School of Medicine, Salt Lake City, USA for providing the ACN cassette. This work was supported by the Deutsche Forschungsgemeinschaft SFB870, projects B05 (to CWS), B10 (to M. Biel), and B18 (to AK).

Address correspondence to: Martin Biel, Department of Pharmacy - Ludwig-Maximilians-Universität München, Butenandtstrasse 5-13, D 81377 München, Germany. Phone: 49.892.1807.7328; Email: martin.biel@lmu.de (M. Biel). Or to: Christian Wahl-Schott, Institut für Neurophysiologie - Medizinische Hochschule Hannover (MHH), Carl-Neuberg-Str. 1, 30625 Hannover, Germany, Email: christian.wahl@cup.uni-muenchen.de or Wahl-Schott.Christian@mh-hannover.de (C. Wahl-Schott).

1. Biel M, Wahl-Schott C, Michalakis S, Zong X. Hyperpolarization-activated cation channels: from genes to function. *Physiol Rev*. 2009;89(3):847–885.
2. Robinson RB, Siegelbaum SA. Hyperpolarization-activated cation currents: from molecules to physiological function. *Annu Rev Physiol*. 2003;65:453–480.
3. Notomi T, Shigemoto R. Immunohistochemical localization of Ih channel subunits, HCN1-4, in the rat brain. *J Comp Neurol*. 2004;471(3):241–276.
4. Moosmang S, Biel M, Hofmann F, Ludwig A. Differential distribution of four hyperpolarization-activated cation channels in mouse brain. *Biol Chem*. 1999;380(7-8):975–980.
5. Nolan MF, et al. The hyperpolarization-activated HCN1 channel is important for motor learning and neuronal integration by cerebellar Purkinje cells. *Cell*. 2003;115(5):551–564.
6. Nolan MF, et al. A behavioral role for dendritic integration: HCN1 channels constrain spatial memory and plasticity at inputs to distal dendrites of CA1 pyramidal neurons. *Cell*. 2004;119(5):719–732.
7. Thuault SJ, et al. Prefrontal cortex HCN1 channels enable intrinsic persistent neural firing and executive memory function. *J Neurosci*. 2013;33(34):13583–13599.
8. Ludwig A, et al. Absence epilepsy and sinus dysrhythmia in mice lacking the pacemaker channel HCN2. *EMBO J*. 2003;22(2):216–224.
9. Chung WK, et al. Absence epilepsy in apathetic, a spontaneous mutant mouse lacking the h channel subunit, HCN2. *Neurobiol Dis*. 2009;33(3):499–508.
10. Fenske S, et al. HCN3 contributes to the ventricular action potential waveform in the murine heart. *Circ Res*. 2011;109(9):1015–1023.
11. Stieglitz MS, et al. Disturbed processing of contextual information in HCN3 channel deficient mice. *Front Mol Neurosci*. 2017;10:436.
12. Stieber J, et al. The hyperpolarization-activated channel HCN4 is required for the generation of pacemaker action potentials in the embryonic heart. *Proc Natl Acad Sci USA*. 2003;100(25):15235–15240.
13. Pedarzani P, Storm JF. Protein kinase A-independent modulation of ion channels in the brain by cyclic AMP. *Proc Natl Acad Sci USA*. 1995;92(25):11716–11720.
14. Zagotta WN, Olivier NB, Black KD, Young EC, Olson R, Gouaux E. Structural basis for modulation and agonist specificity of HCN pacemaker channels. *Nature*. 2003;425(6954):200–205.
15. Lee CH, MacKinnon R. Structures of the human HCN1 hyperpolarization-activated channel. *Cell*. 2017;168(1–2):111–120.e11.
16. DiFrancesco D. The role of the funny current in pacemaker activity. *Circ Res*. 2010;106(3):434–446.
17. Pedarzani P, Storm JF. Dopamine modulates the slow Ca(2+)-activated K^+ current IAHP via cyclic AMP-dependent protein kinase in hippocampal neurons. *J Neurophysiol*. 1995;74(6):2749–2753.
18. Emery EC, Young GT, Berrocoso EM, Chen L, McNaughton PA. HCN2 ion channels play a central role in inflammatory and neuropathic pain. *Science*. 2011;333(6048):1462–1466.
19. Heys JG, Hasselmo ME. Neuromodulation of I(h) in layer II medial entorhinal cortex stellate cells: a voltage-clamp study. *J Neurosci*. 2012;32(26):9066–9072.
20. Wang M, et al. Alpha2A-adrenoceptors strengthen working memory networks by inhibiting cAMP-HCN channel signaling in prefrontal cortex. *Cell*. 2007;129(2):397–410.
21. Shaikh AG, Finlayson PG. Excitability of auditory brainstem neurons, in vivo, is increased by cyclic-AMP. *Hear Res*. 2005;201(1–2):70–80.
22. Yamada R, Kuba H, Ishii TM, Ohmori H. Hyperpolarization-activated cyclic nucleotide-gated cation channels regulate auditory coincidence detection in nucleus laminaris of the chick. *J Neurosci*. 2005;25(39):8867–8877.
23. Lüthi A, McCormick DA. Modulation of a pacemaker current through Ca(2+)-induced stimulation of cAMP production. *Nat Neurosci*. 1999;2(7):634–641.
24. Frère SG, Lüthi A. Pacemaker channels in mouse thalamocortical neurones are regulated by distinct pathways of cAMP synthesis. *J Physiol (Lond)*. 2004;554(Pt 1):111–125.
25. McCormick DA. Neurotransmitter actions in the thalamus and cerebral cortex and their role in neuromodulation of thalamocortical activity. *Prog Neurobiol*. 1992;39(4):337–388.
26. McCormick DA, Pape HC. Properties of a hyperpolarization-activated cation current and its role in rhythmic oscillation in thalamic relay neurones. *J Physiol (Lond)*. 1990;431:291–318.
27. McCormick DA, Bal T. Sleep and arousal: thalamocortical mechanisms. *Annu Rev Neurosci*. 1997;20:185–215.
28. Llinás RR, Steriade M. Bursting of thalamic neurons and states of vigilance. *J Neurophysiol*. 2006;95(6):3297–3308.
29. Budde T, et al. Impaired regulation of thalamic pacemaker channels through an imbalance of subunit expression in absence epilepsy. *J Neurosci*. 2005;25(43):9871–9882.
30. Liu DT, Tibbs GR, Paoletti P, Siegelbaum SA. Constraining ligand-binding site stoichiometry suggests that a cyclic nucleotide-gated channel is composed of two functional dimers. *Neuron*. 1998;21(1):235–248.
31. Chen S, Wang J, Siegelbaum SA. Properties of hyperpolarization-activated pacemaker current defined by coassembly of HCN1 and HCN2 subunits and basal modulation by cyclic nucleotide. *J Gen Physiol*. 2001;117(5):491–504.
32. Santoro B, Wainger BJ, Siegelbaum SA. Regulation of HCN channel surface expression by a novel C-terminal protein-protein interaction. *J Neurosci*. 2004;24(47):10750–10762.
33. Zolles G, et al. Association with the auxiliary subunit PEX5R/Trip8b controls responsiveness of HCN channels to cAMP and adrenergic stimulation. *Neuron*. 2009;62(6):814–825.
34. Niell CM, Stryker MP. Modulation of visual responses by behavioral state in mouse visual cortex. *Neuron*. 2010;65(4):472–479.
35. Linden ML, Heynen AJ, Haslinger RH, Bear MF. Thalamic activity that drives visual cortical plasticity. *Nat Neurosci*. 2009;12(4):390–392.
36. Laprell L, et al. Photopharmacological control of bipolar cells restores visual function in blind mice. *J Clin Invest*. 2017;127(7):2598–2611.
37. Huguenard JR, Prince DA. Intrathalamic rhythmicity studied in vitro: nominal T-current modulation causes robust antioscillatory effects. *J Neurosci*. 1994;14(9):5485–5502.

38. Leresche N, Lightowler S, Soltesz I, Jassik-Gerschenfeld D, Crunelli V. Low-frequency oscillatory activities intrinsic to rat and cat thalamocortical cells. *J Physiol (Lond)*. 1991;441:155–174.
39. Jacobsen RB, Ulrich D, Huguenard JR. GABA(B) and NMDA receptors contribute to spindle-like oscillations in rat thalamus in vitro. *J Neurophysiol*. 2001;86(3):1365–1375.
40. Astori S, et al. The Ca(V)3.3 calcium channel is the major sleep spindle pacemaker in thalamus. *Proc Natl Acad Sci USA*. 2011;108(33):13823–13828.
41. Saponaro A, et al. A synthetic peptide that prevents cAMP regulation in mammalian hyperpolarization-activated cyclic nucleotide-gated (HCN) channels. *Elife*. 2018;7:null.
42. Kuisle M, et al. Functional stabilization of weakened thalamic pacemaker channel regulation in rat absence epilepsy. *J Physiol (Lond)*. 2006;575(Pt 1):83–100.
43. Paz JT, Huguenard JR. Microcircuits and their interactions in epilepsy: is the focus out of focus? *Nat Neurosci*. 2015;18(3):351–359.
44. David F, et al. Suppression of hyperpolarization-activated cyclic nucleotide-gated channel function in thalamocortical neurons prevents genetically determined and pharmacologically induced absence seizures. *J Neurosci*. 2018;38(30):6615–6627.
45. Paz JT, et al. A new mode of corticothalamic transmission revealed in the Gria4(-/-) model of absence epilepsy. *Nat Neurosci*. 2011;14(9):1167–1173.
46. Sorokin JM, et al. Bidirectional control of generalized epilepsy networks via rapid real-time switching of firing mode. *Neuron*. 2017;93(1):194–210.
47. Stroh A, et al. Making waves: initiation and propagation of corticothalamic Ca^{2+} waves in vivo. *Neuron*. 2013;77(6):1136–1150.
48. Fenske S, et al. Comprehensive multilevel in vivo and in vitro analysis of heart rate fluctuations in mice by ECG telemetry and electrophysiology. *Nat Protoc*. 2016;11(1):61–86.
49. Fenske S, et al. Sick sinus syndrome in HCN1-deficient mice. *Circulation*. 2013;128(24):2585–2594.
50. McCormick DA, Bal T. Sensory gating mechanisms of the thalamus. *Curr Opin Neurobiol*. 1994;4(4):550–556.
51. Budde T, et al. Reciprocal modulation of I (h) and I (TASK) in thalamocortical relay neurons by halothane. *Pflugers Arch*. 2008;456(6):1061–1073.
52. Bal T, McCormick DA. What stops synchronized thalamocortical oscillations? *Neuron*. 1996;17(2):297–308.
53. Vassalli A, Franken P. Hypocretin (orexin) is critical in sustaining theta/gamma-rich waking behaviors that drive sleep need. *Proc Natl Acad Sci USA*. 2017;114(27):E5464–E5473.
54. Bunting M, Bernstein KE, Greer JM, Capecchi MR, Thomas KR. Targeting genes for self-excision in the germ line. *Genes Dev*. 1999;13(12):1524–1528.
55. Hammelmann V, Zong X, Hofmann F, Michalakis S, Biel M. The cGMP-dependent protein kinase II is an inhibitory modulator of the hyperpolarization-activated HCN2 channel. *PLoS ONE*. 2011;6(2):e17078.
56. Schneider CA, Rasband WS, Eliceiri KW. NIH Image to ImageJ: 25 years of image analysis. *Nat Methods*. 2012;9(7):671–675.
57. Beaudoin GM, et al. Culturing pyramidal neurons from the early postnatal mouse hippocampus and cortex. *Nat Protoc*. 2012;7(9):1741–1754.
58. Much B, et al. Role of subunit heteromerization and N-linked glycosylation in the formation of functional hyperpolarization-activated cyclic nucleotide-gated channels. *J Biol Chem*. 2003;278(44):43781–43786.
59. Koch S, et al. Gene therapy restores vision and delays degeneration in the CNGB1(-/-) mouse model of retinitis pigmentosa. *Hum Mol Genet*. 2012;21(20):4486–4496.
60. Treviño M. Stimulus similarity determines the prevalence of behavioral laterality in a visual discrimination task for mice. *Sci Rep*. 2014;4:7569.
61. Treviño M, Oviedo T, Jendritza P, Li SB, Köhr G, De Marco RJ. Controlled variations in stimulus similarity during learning determine visual discrimination capacity in freely moving mice. *Sci Rep*. 2013;3:1048.
62. Morris R. Developments of a water-maze procedure for studying spatial learning in the rat. *J Neurosci Methods*. 1984;11(1):47–60.
63. Barry PH. JPCalc, a software package for calculating liquid junction potential corrections in patch-clamp, intracellular, epithelial and bilayer measurements and for correcting junction potential measurements. *J Neurosci Methods*. 1994;51(1):107–116.
64. Pillai AG, Anilkumar S, Chattarji S. The same antidepressant elicits contrasting patterns of synaptic changes in the amygdala vs hippocampus. *Neuropsychopharmacology*. 2012;37(12):2702–2711.
65. Cao-Ehlker X, et al. Up-regulation of hyperpolarization-activated cyclic nucleotide-gated channel 3 (HCN3) by specific interaction with K^+ channel tetramerization domain-containing protein 3 (KCTD3). *J Biol Chem*. 2013;288(11):7580–7589.
66. Stosiek C, Garaschuk O, Holthoff K, Konnerth A. In vivo two-photon calcium imaging of neuronal networks. *Proc Natl Acad Sci USA*. 2003;100(12):7319–7324.
67. Jia H, Rochefort NL, Chen X, Konnerth A. In vivo two-photon imaging of sensory-evoked dendritic calcium signals in cortical neurons. *Nat Protoc*. 2011;6(1):28–35.
68. D'Arcangelo G, D'Antuono M, Biagini G, Warren R, Tancredi V, Avoli M. Thalamocortical oscillations in a genetic model of absence seizures. *Eur J Neurosci*. 2002;16(12):2383–2393.

Supplemental Information

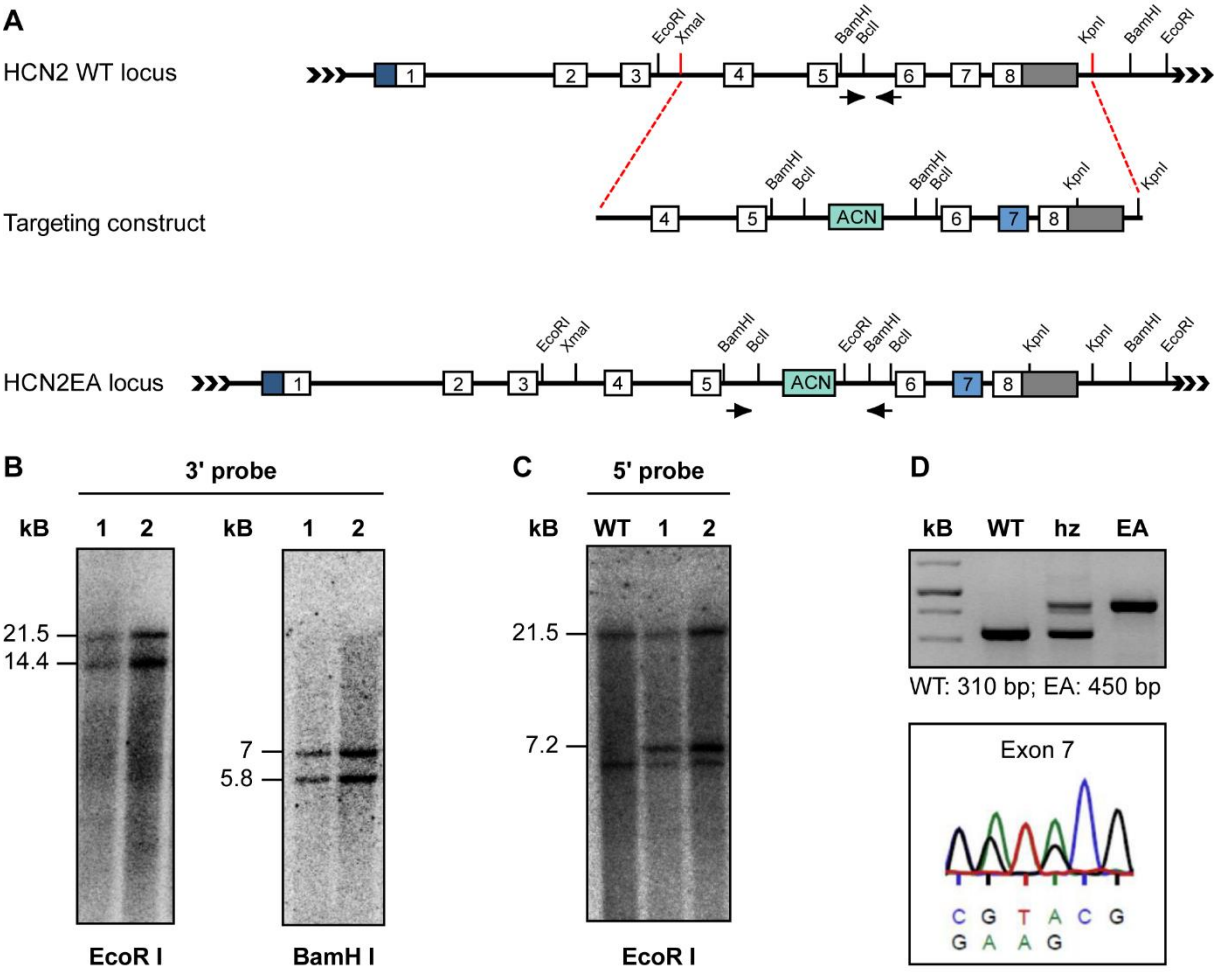

Supplemental Figure 1. Generation of the HCN2EA mouse model. **(A)** Top: wild-type HCN2 locus and targeting vector. Exons 1-8 are indicated by open boxes. The targeting vector contains an ACN self-excision neomycine resistance cassette (54) (green) and carries point mutations in exon 4 (marked in blue) to generate the R591E, T592A exchanges. Bottom: knockin HCN2EA allele obtained after homologous recombination in ES cells **(B)** Southern Blots showing the correct 3' integration of the targeting construct. **(C)** Southern Blots showing the correct 5' integration of the targeting construct. **(D)** Genotyping results of WT, heterozygous and HCN2EA mice (upper panel). The locations of the sense and antisense primer are indicated as small arrows in S1a. Electropherogram of the mutated base pairs in exon 7 in heterozygous mice (lower panel). See Methods for primer sequences.

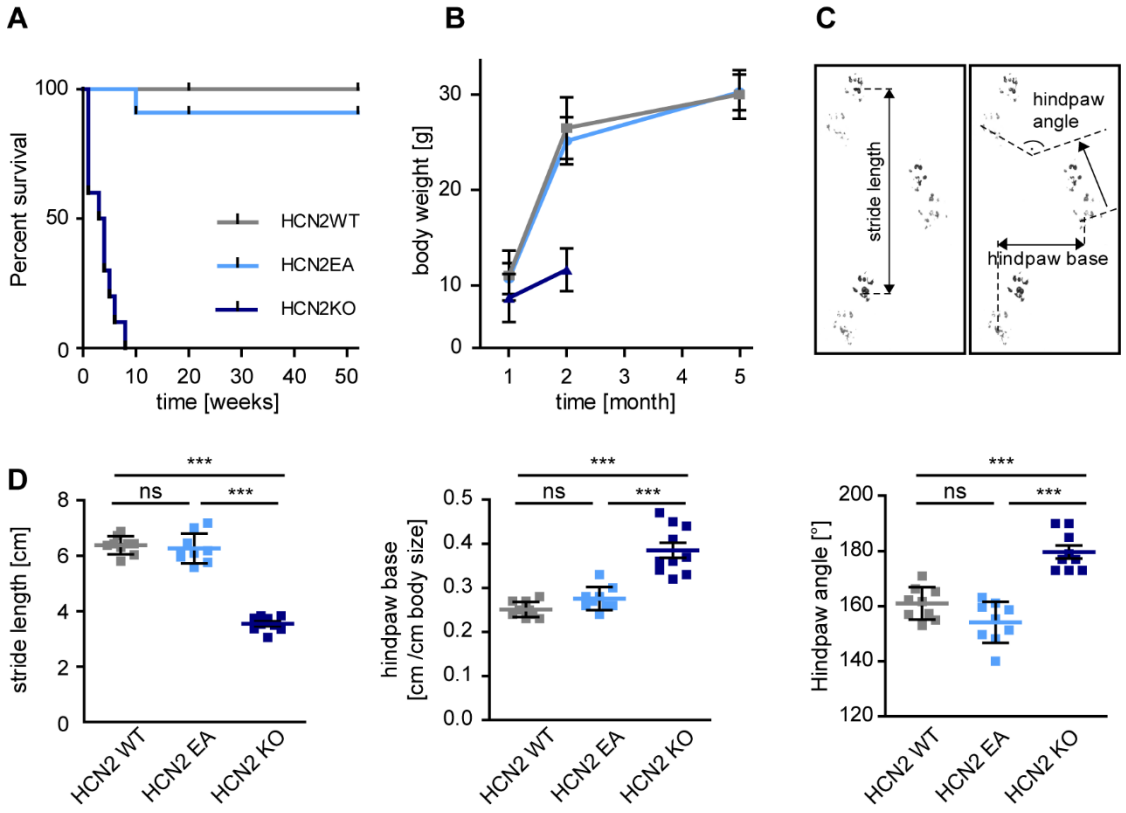

Supplemental Figure 2. Phenotype of the HCN2EA mouse. **(A)** Meier-Kaplan blot of WT (gray, n=16), HCN2EA littermates (light blue, n=16) and HCN2 KO mice (dark blue, n=10). **(B)** Body weight of WT (gray, n=33), HCN2EA littermates (light blue, n=31) and HCN2 KO mice (dark blue, n=18) over time. **(C)** Example of a footprint analysis showing stride length, hindpaw angle and hindpaw base. **(D)** Stride length (left panel), hindpaw base (middle panel) and hindpaw angle (right panel) of WT (gray) and HCN2EA littermates (light blue) and HCN2 KO mice (dark blue) (WT: n=8, HCN2EA: n=9, HCN2 KO: n=10; One-Way ANOVA, Bonferroni's post hoc test).

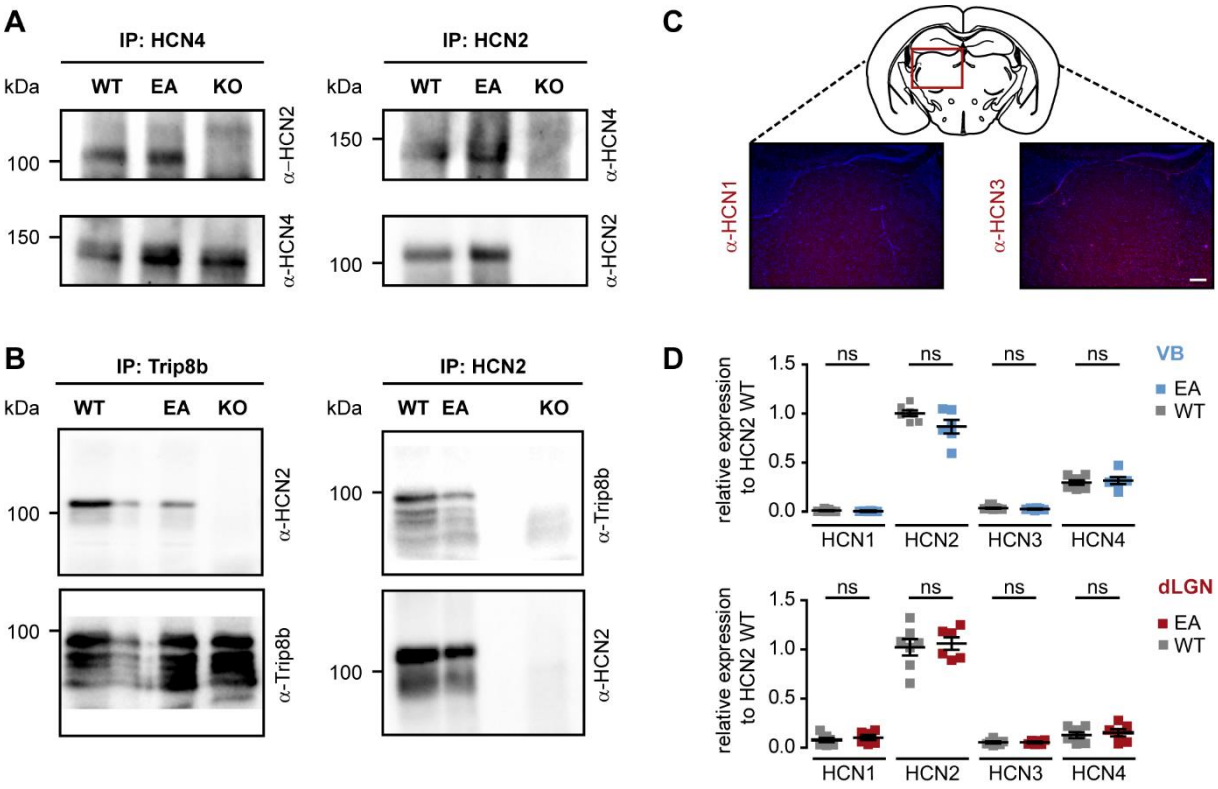

Supplemental Figure 3. Interaction and localization of HCN channels in the brain. **(A)** Co-Immunoprecipitations of lysates of whole WT brain (left lanes), HCN2EA (middle lanes) and HCN2-KO (right lanes), precipitated either with anti-HCN2 (alomone) or anti-HCN4 (alomone). **(B)** Co-Immunoprecipitations of lysates of whole WT brain (left lanes), HCN2EA (middle lanes) and HCN2-KO (right lanes), precipitated either with anti-Trip8b (alomone) or anti-HCN2 (alomone). **(C)** Immunostainings for HCN1 and HCN3 in coronal brain slices of the thalamus (as marked by the red square in the scheme of the mouse brain). Specific immunosignal is in red. Nuclei have been counterstained with Hoechst (blue), scale 200 µm. **(D)** Lack of cAMP modulation in HCN2 does not alter the expression level of HCN isoforms in VB and dLGN in WT and HCN2EA mice. The expression levels of HCN isoforms are shown for the VB (upper) and dLGN (lower panel) in WT (gray, n=7) and HCN2EA mice (blue (VB) and red (dLGN), n=6). One-Way ANOVA, Bonferroni's post hoc test showed no significant diffenrence between WT and HCN2EA.

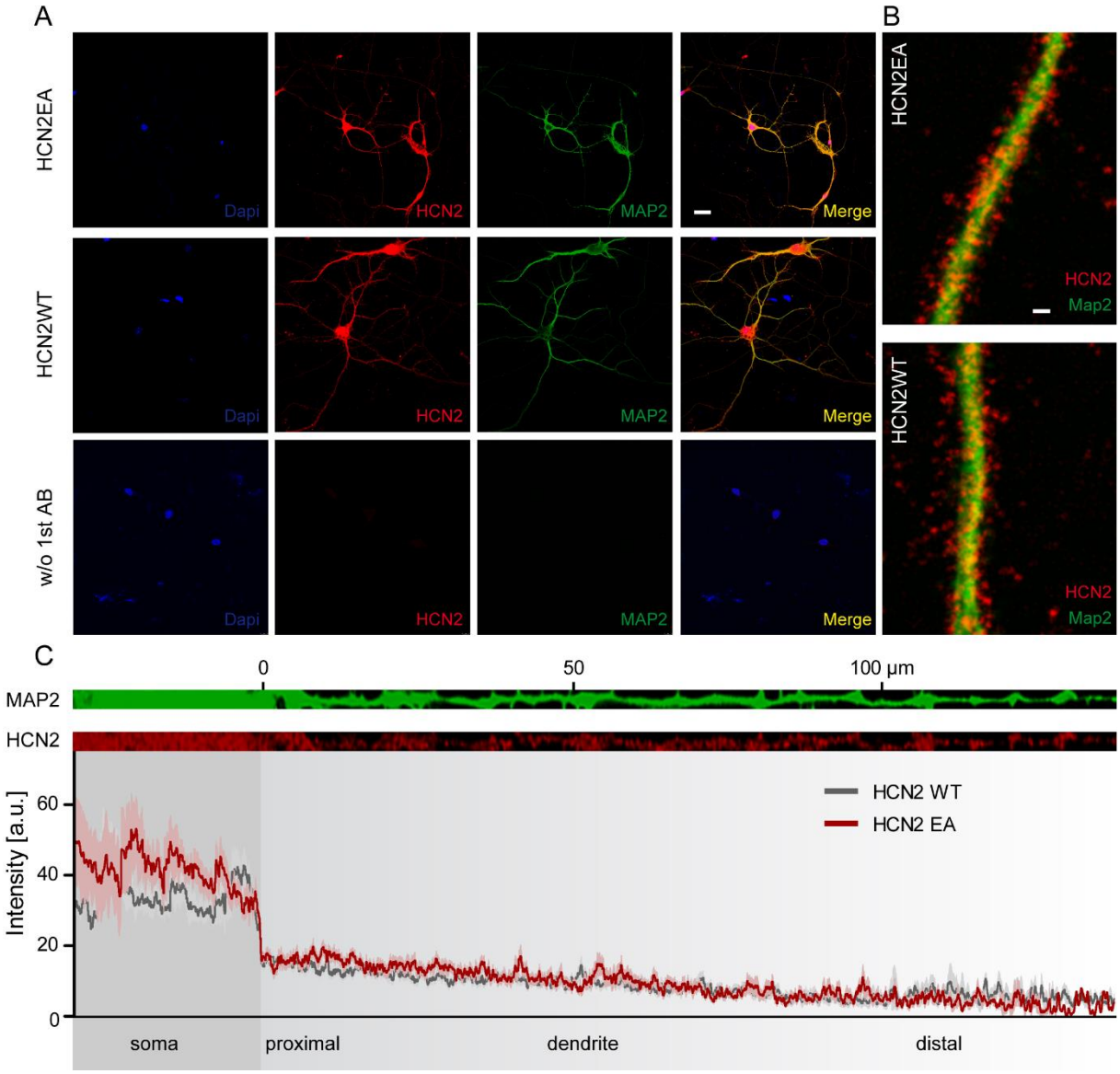

Supplemental Figure 4. Localization of HCN2 channels in soma and dendrites of primary neurons. **(A)** Primary hippocampal neurons of P0 HCN2EA or HCN2WT mice were transfected with either HCN2EA (upper) or HCN2WT DNA (middle panel). Neurons were stained at DIV14 for cell nuclei (Dapi; blue), HCN2 (α-HCN2; red) and dendrites (α-MAP2; green). Merged pictures show colocalization of HCN2 and MAP2 in the dendrites of primary neurons. Negative control (lower panel) showed specificity of the antibodies used. Scale: 20 µm. Representative primary neuron of cells analyzed in (C). **(B)** High-resolution images of dendrites shown in (A) revealed HCN2 staining at dendritic spines. Scale: 3 µm **(C)** Dendrites were identified using MAP2 (upper panel, green) and the intensity of HCN2 (middle panel; red) was measured using the Plot Profile Plugin (ImageJ). The intensity was plotted against the distance from the soma for WT (grey; n=17) and the HCN2EA mutant (red; n=16) (lower panel) and revealed no difference in the expression along dendrites and somata.

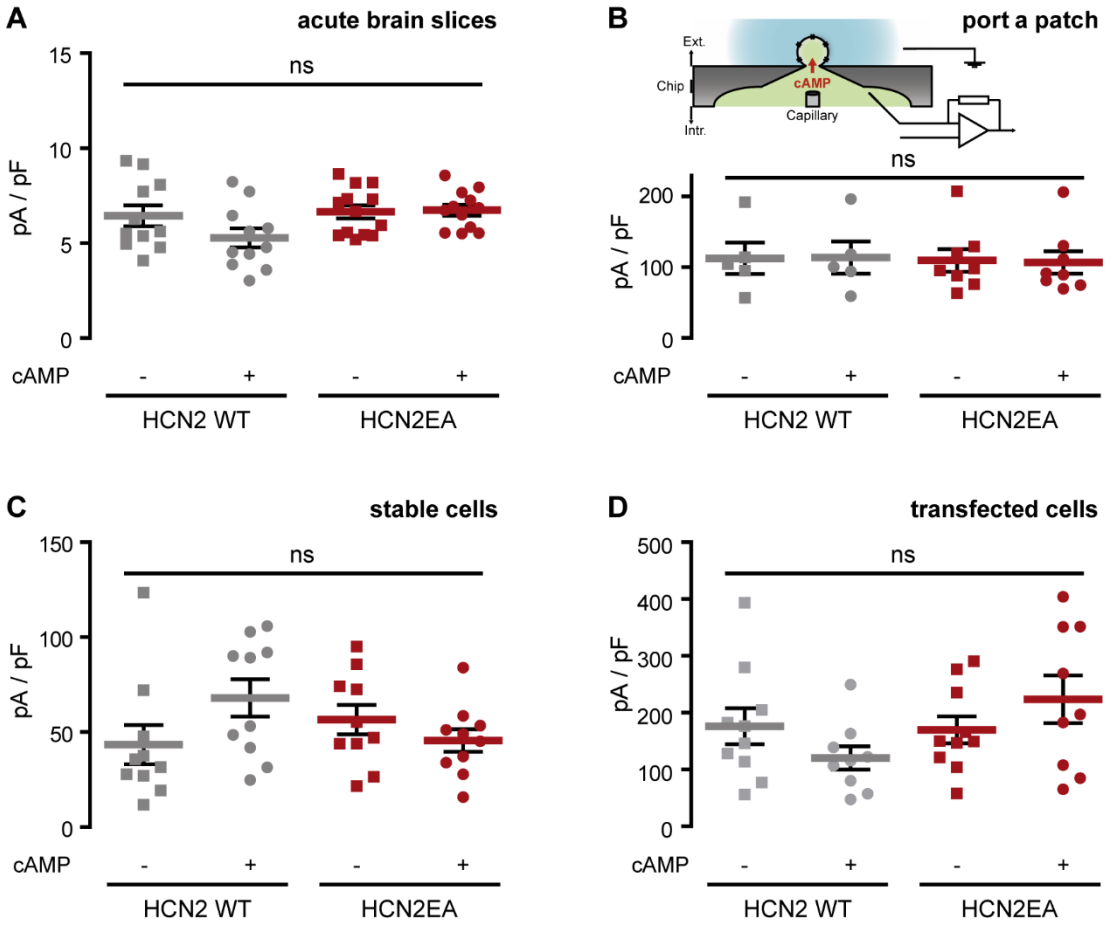

Supplemental Figure 5. (A) Current densities in acute brain slices. WT (gray squares: -cAMP, n=11; gray circles: +cAMP, n=11), HCN2EA (red squares: -cAMP, n=13; red circles: +cAMP, n=12). **(B)** Current densities in internally perfused cells using the port-a-patch system**.** WT (gray squares: -cAMP, n=5; gray circles: +cAMP, n=5), HCN2EA (red squares: -cAMP, n=8; red circles: +cAMP, n=8). **(C)** Current densities in stable HEK293 cells. WT (gray squares: -cAMP, n=10; gray circles: +cAMP, n=11), HCN2EA (red squares: -cAMP, n=10; red circles: +cAMP, n=10). **(D)** Current densities in transfected HEK293 cells. WT (gray squares: -cAMP, n=10; gray circles: +cAMP, n=9), HCN2EA (red squares: -cAMP, n=10; red circles: +cAMP, n=9). WT HCN2 current densities (gray) were compared to HCN2EA current densities (red) in absence (squares) and presence (circles) of cAMP (One-way ANOVA; Bonferroni post-hoc test).

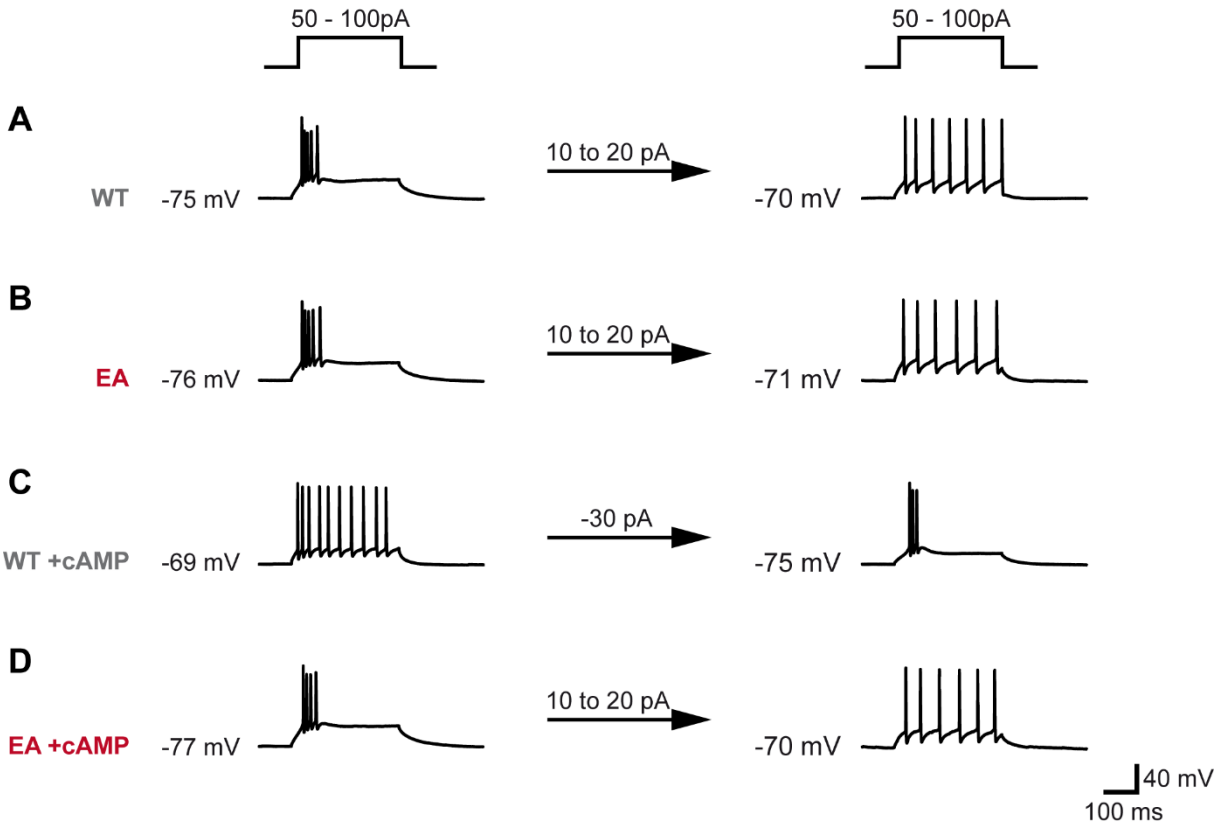

Supplemental Figure 6. Firing modes depend on the membrane potential. Shown are firing patterns elicited by 300 ms depolarizing current steps of 50 or 100 pA. Without cAMP, WT **(A)** and EA **(B)** neurons fire in burst mode when depolarized from their RMP. When bringing the membrane potential to higher values by constant current injection of 10-20 pA, cells show tonic firing upon step current injections. Application of cAMP in WT **(C)** and EA **(D)** neurons leads to different RMPs (-69 mV and -77 mV, respectively). Depolarizing step current injections elicit different responses in WT + cAMP (tonic, C) and EA + cAMP (burst, D) neurons. Constant negative current injections brings the membrane potential of WT + cAMP to a more negative value and step current injections applied thereafter lead to these cells firing in burst mode (C). Vice versa, the membrane potential of EA + cAMP neurons was elevated to a more positive value by constant current injections of 10-20 pA and step current injections now elicit tonic firing (D).. Shown are representative traces (WT: n = 6, HCN2EA: n = 7, WT + cAMP: n = 4, HCN2EA + cAMP: n = 7).

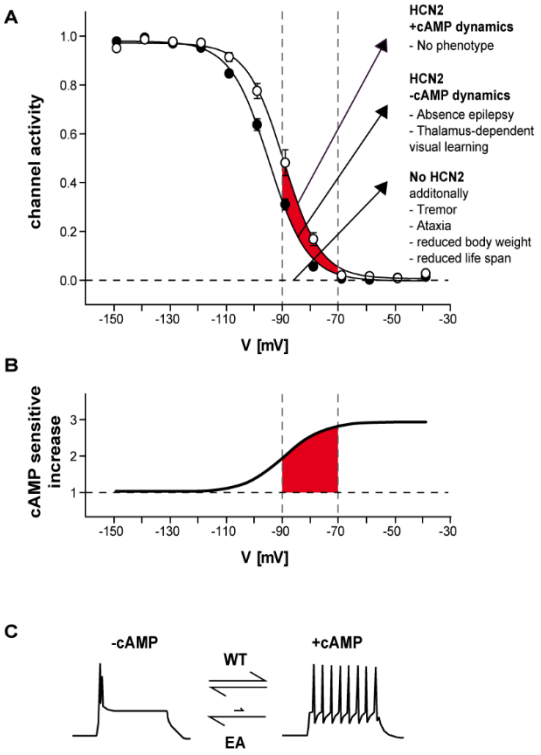

Supplemental Figure 7. Model for the physiological role of cAMP-sensitive modulation of HCN2 on the level of the channel, at the level of the cell and the in vivo level. **(A)** Cartoon for the steady state activation curve of HCN2 in the absence (closed circles) and presence (open circles) of intracellular cAMP in TC neurons. The physiological range of membrane potentials is indicated by vertical broken lines (-90 mV to -70 mV). In the absence of cAMP, only a fixed amount of channel activity is available in wild type HCN2 channels (steady state activation curve on the left). On top, a cAMP-sensitive proportion of channel activity of wild-type HCN2 can be gradually tuned according to cellular needs by cAMP. The red region indicates the dynamic range of channel activity, which can be recruited by cAMP. HCN2EA channels cannot bind cAMP and, hence, are unresponsive to changes in the cAMP concentration. Right panel: phenotypes which correspond to individual regions **(B)** from steady state activation curves shown in panel (a), cAMP-sensitive increase in the presence of cAMP as compared to control conditions without cAMP is calculated as I_{+cAMP}/I_{-cAMP}. The red region indicates the dynamic range of cAMP sensitive increase in channel activity. **(C)** Cartoon of typical burst firing in the absence of cAMP (left) and tonic firing in the presence of cAMP (right) for TC neurons of WT mice. In these neurons, increase and decrease in intracellular cAMP can switch between these firing modes. In contrast, TC neurons of HCN2EA mice are less likely to switch from burst to tonic firing in response to cAMP and rather stably remain in the burst firing mode.

Manuscript III

nature COMMUNICATIONS

ARTICLE

https://doi.org/10.1038/s41467-020-19304-9 OPEN

cAMP-dependent regulation of HCN4 controls the tonic entrainment process in sinoatrial node pacemaker cells

Stefanie Fenske[1,2], Konstantin Hennis[1,12], René D. Rötzer[1,12], Verena F. Brox[1,12], Elvir Becirovic[1], Andreas Scharr[1], Christian Gruner[1], Tilman Ziegler[2,3], Verena Mehlfeld[1], Jaclyn Brennan[4], Igor R. Efimov[4], Audrys G. Pauža[5], Markus Moser[6], Carsten T. Wotjak[7,8], Christian Kupatt[2,3], Rasmus Gönner[1], Rai Zhang[9], Henggui Zhang[10], Xiangang Zong[1], Martin Biel[1✉] & Christian Wahl-Schott[11✉]

It is highly debated how cyclic adenosine monophosphate-dependent regulation (CDR) of the major pacemaker channel HCN4 in the sinoatrial node (SAN) is involved in heart rate regulation by the autonomic nervous system. We addressed this question using a knockin mouse line expressing cyclic adenosine monophosphate-insensitive HCN4 channels. This mouse line displayed a complex cardiac phenotype characterized by sinus dysrhythmia, severe sinus bradycardia, sinus pauses and chronotropic incompetence. Furthermore, the absence of CDR leads to inappropriately enhanced heart rate responses of the SAN to vagal nerve activity in vivo. The mechanism underlying these symptoms can be explained by the presence of nonfiring pacemaker cells. We provide evidence that a tonic and mutual interaction process (tonic entrainment) between firing and nonfiring cells slows down the overall rhythm of the SAN. Most importantly, we show that the proportion of firing cells can be increased by CDR of HCN4 to efficiently oppose enhanced responses to vagal activity. In conclusion, we provide evidence for a novel role of CDR of HCN4 for the central pacemaker process in the sinoatrial node.

[1] Center for Integrated Protein Science (CIPS-M) and Center for Drug Research, Department of Pharmacy, Ludwig-Maximilians-Universität München, 81377 Munich, Germany. [2] German Center for Cardiovascular Research (DZHK), Partner Site Munich Heart Alliance, 80802 Munich, Germany. [3] Klinikum Rechts der Isar, TU Munich, 81675 Munich, Germany. [4] Department of Biomedical Engineering, George Washington University, Washington, DC 20052, USA. [5] Institute of Anatomy, Lithuanian University of Health Sciences, LT, 44307 Kaunas, Lithuania. [6] Max Planck Institute of Biochemistry, Department of Molecular Medicine, 82152 Martinsried, Germany. [7] Max Planck Institute of Psychiatry, Research Group Neuronal Plasticity, 80804 Munich, Germany. [8] Central Nervous System Diseases Research, Boehringer Ingelheim Pharma GmbH & Co. KG, 88397 Biberach Riß, Germany. [9] Department of Aerospace Engineering, University of Bristol, Bristol BS8 1QU, UK. [10] Department of Physics and Astronomy, The University of Manchester, Manchester M13 9PL, UK. [11] Hannover Medical School, Institute for Neurophysiology, 30625 Hannover, Germany. [12] These authors contributed equally: Konstantin Hennis, René D. Rötzer, Verena F. Brox. ✉email: martin.biel@cup.uni-muenchen.de; wahl-schott.christian@mh-hannover.de

Throughout life, the human heart beats up to 3 billion times with high precision and without rest. The heartbeat is initiated in the leading pacemaker region within the sinoatrial node. This region is a small cluster of pacemaker cells that display a faster firing rate than the residual cells in the SAN and cardiac conduction system. Within this region individual pacemaker cells synchronize to a common rhythm by mutual, electrical interaction via gap junctions. This mechanism is called mutual entrainment[1–4] and is important for the ability of the leading pacemaker region to generate regular electrical discharges that drive the electrical activation of the whole heart. The assumption that spontaneous activity of the leading pacemaker region of the SAN is characterized by the fastest firing rate and that this drives the heart rate (HR) represents the central premise of the pacemaker process. Spontaneous firing of pacemaker cells is initiated by the slow diastolic depolarisation[5]. Hyperpolarization-activated cyclic nucleotide-gated cation (HCN) channels are considered essential for the slow diastolic depolarisation[6]. The four HCN1–4 subtypes are principally operated by hyperpolarisation; however, activation is also controlled by cyclic adenosine monophosphate (cAMP). It is known that cAMP binds to a cyclic nucleotide-binding domain in the C-terminus of the channels[7]. Within the physiological voltage range, HCN channel activity increases in parallel with intracellular cAMP concentrations[8]. Moreover, it has been proposed that CDR of HCN4 is key for heart rate control by the autonomic nervous system (ANS). Specifically, cAMP-dependent increase of HCN4-mediated current was believed to be required for the acceleration of the HR upon high activity of the sympathetic division of the ANS, whereas a drop in cAMP levels following vagal stimulation would decrease HCN4 activity and slow down the HR[5,6,9].

While the assumption, that CDR of HCN4 underlies HR control by the ANS has been postulated for quite a long time, it has been difficult to validate this concept in vivo and it is therefore still a matter of controversy. In particular, there are conflicting results and conclusions about a potential role of cAMP binding to the cyclic nucleotide-binding domain of HCN4 channels during the chronotropic response. While experiments on embryonic mouse hearts expressing a mutant HCN4 channel lacking CDR indicated that CDR of HCN4 is crucial for HR control[10], results of tamoxifen-induced knockout of HCN4 in adult mouse hearts argued against a major role for HCN4 in HR control[11,12]. Moreover, several HCN4 channelopathies in humans (congenital diseases caused by mutations in genes coding for ion channels) lead to heterogeneous cardiac syndromes including bradycardia, yet in some of these channelopathies the response to β-adrenergic stimulation is preserved[13,14]. Unfortunately, the only two known human mutations that directly impair cAMP-modulation (573X and 695X) lead to large truncations of the HCN4 C-terminus and affect general HCN4 architecture[15,16]. Therefore, a straight-forward interpretation of the impact of these mutations on CDR is not possible. Moreover, all patients with HCN4 channelopathies identified so far are heterozygous for the respective mutation and thus also express a "healthy" copy of the HCN4 channel.

Recently, alternative concepts emerged indicating that HCN channels might have an entirely different role for HR regulation than originally postulated. There is evidence that mechanisms are required, which oppose and control HR responses to sympathetic or parasympathetic activity during the chronotropic response, ensuring balanced and well-tuned HR changes. Importantly, HCN channels, together with other signalling proteins[17–19], could play a major role within this context and represent key targets, which control and oppose the HR-lowering effect of the parasympathetic nervous system and thereby prevent parasympathetic override, inappropriate HR decreases and severe bradycardia[1,20–22].

In order to directly investigate the role of HCN4 CDR in SAN function we generated a knockin mouse line expressing cAMP-insensitive HCN4 channels. In vivo and in vitro characterization of this mouse line revealed a complex cardiac phenotype characterized by severe sinus bradycardia and sinus dysrhythmia, but fully preserved HR regulation. Furthermore, the absence of CDR leads to inappropriately enhanced HR responses of the SAN to vagal nerve activity during the baroreceptor reflex in vivo. Moreover, arrhythmia arises in the absence of HCN4 CDR during high adrenergic activity because subsidiary pacemaker regions take over pacemaker function in place of the SAN. Finally, we elaborate and propose a model based on cellular, organ and in vivo experiments which explains the cellular mechanism underlying this complex cardiac phenotype. Together, our study provides evidence for a novel role of CDR of HCN4 for pacemaking in the SAN and in particular for the central pacemaker process.

Results

Generation and validation of HCN4FEA mice. To examine the role of HCN4 CDR in the heart, we generated HCN4FEA knockin mice that contain three amino acid exchanges in HCN4 (Y527F, R669E, and T670A; Fig. 1). The R669E and T670A mutations disrupt cAMP binding and completely abolish channel activation by cyclic nucleotides (Supplementary Data 1a, b)[7,10,23]. Previous studies indicated that abolishing the cAMP binding capability of the HCN4 cyclic nucleotide-binding domain is associated with embryonic lethality[10,24]. This finding possibly reflects the fact that the activation thresholds of these HCN4 mutants are more negative than the maximum diastolic potential of pacemaker cells, which is essentially as if no cAMP was present in the cell. This causes an almost complete loss of HCN4 activity at physiological voltages, which is similar to knocking out HCN4[12].

It has been shown that in SAN cells, basal intracellular cAMP concentrations are never zero[25,26], and that basal cAMP increases HCN4-mediated currents at any given membrane potential in the physiological voltage range. To account for this scenario, we introduced a third mutation in the C-linker of the channel (Y527F). This mutation causes a parallel shift of the activation curve to more positive potentials and acceleration of activation kinetics in the same range as expected in WT channels under basal cAMP levels, i.e. $V_{0.5}$ and activation time constants values are in between those obtained for WT channels measured in the absence and in the presence of cAMP (Supplementary Data 1as).

The HCN4Y527F channels combined with R669E/T670A display (1) a constant and cAMP-independent shift of the half-maximal activation voltage ($V_{0.5}$) towards more depolarised potentials and (2) an acceleration of activation kinetics. These parameters were in between respective parameters obtained for wild-type channels in the absence and presence of cAMP. Channel properties were not modulated by cAMP-even at high micromolar concentrations (Fig. 1d–f and Supplementary Data 1a, b).

Heterozygous breeding produced offspring at the expected Mendelian ratios. Homozygous HCN4FEA mice did not show any morphological abnormalities and body weights were similar to those of WT littermates (Supplementary Data 2a). Overall cardiac morphology appeared normal, histological sections of WT and HCN4FEA hearts were indistinguishable (Fig. 2a, b), and echocardiographic analysis demonstrated normal cardiac structure as well as diastolic and systolic function in both groups of mice (Fig. 2c, Supplementary Data 2b). Detailed analysis of SAN cross sections revealed no evidence of fibrosis or myofibrillar disarray (Fig. 2d, e, Supplementary Data 2c).

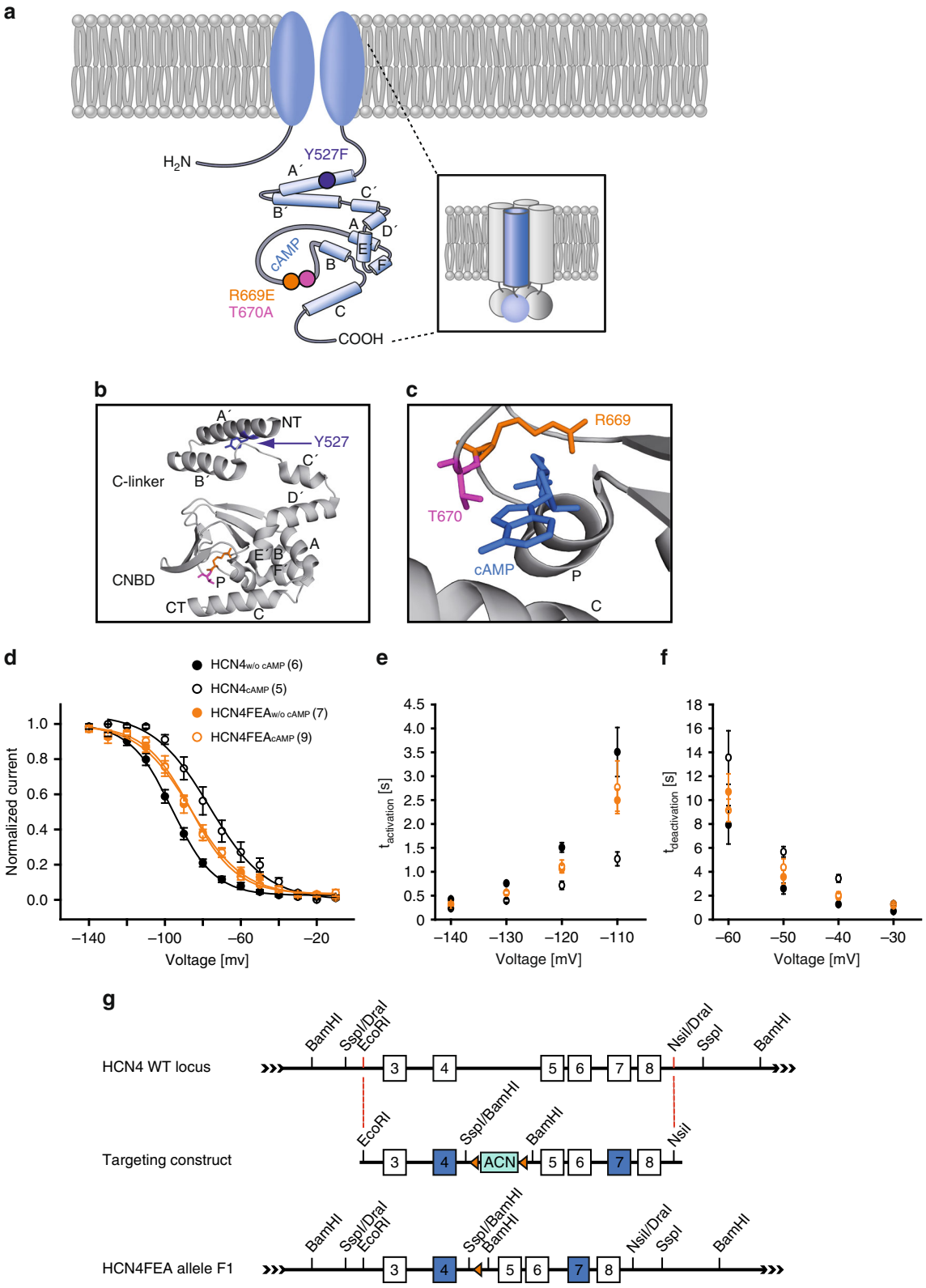

Expression of HCN channels in the heart. Quantitative reverse-transcription polymerase chain reaction confirmed that HCN4 WT and HCN4FEA are expressed at similar levels in the SAN of WT and HCN4FEA mice, respectively (Fig. 2h, Supplementary Data 2d). This finding is supported by a western blot analysis of the membrane fractions of SAN preparations (Fig. 2f), which indicated similar levels of a 135-kDa signal corresponding to the mature glycosylated HCN4 or HCN4FEA protein that was present in the SAN of WT and HCN4FEA mice. Protein distribution of HCN4 and HCN1 channels in the head, body and tail region of the SAN and surrounding atrial tissue were similar (Fig. 2f, g; Supplementary Data 2e). Gene expression profiles of isolated SAN tissue (Supplementary Data 3) confirmed that the expression levels of major depolarising and repolarising ion channels or

Fig. 1 Generation of HCN4FEA mice and basic characterisation of HCN4FEA-mediated I_f. **a** Illustration depicting the HCN4 channel tetramer (inset) and single subunit. The C-terminus contains the C-linker composed of six α-helices (A′–F′) and a cyclic nucleotide-binding domain (autonomic) composed of three α-helices (A–C) and a β-roll between helix A and B. Localisation of the three introduced point mutations is indicated with coloured circles. **b** C-terminus of the human HCN4 channel (PDB #Q9Y3Q4). Residues Y527 (purple), R669 (orange), and T670 (pink) are highlighted. The R669E and T670A mutations were introduced to completely disrupt cAMP binding. Both residues are located in the loop between the P helix and the β7 sheet of the CNBD and are highly conserved throughout the CNG (cyclic nucleotide-gated) and HCN channel family[7,53]. **c** cAMP bound to the CNBD of human HCN4. Residues R669 and T670 are required for cAMP binding. **d** Activation curves of WT HCN4 and HCN4FEA channels transiently expressed in HEK293 cells in the absence and presence of 100 μM cAMP in the pipette solution. A holding potential of −40 mV was used. cAMP shifts the activation curve of WT HCN4 to more depolarised potentials, whereas HCN4FEA activation curves are not affected by cAMP. **e** Activation time constants determined from HCN4 and HCN4FEA-mediated currents measured at test potentials ranging from −140 mV to −110 mV. Values from HCN4FEA mutant channels lie between values determined from WT channels with and without cAMP. **f** Deactivation time constants determined from currents measured at test potentials ranging from −60 mV to −30 mV. Values from HCN4FEA mutant channels lie between values determined from WT channels with and without cAMP. **g** Targeting strategy of HCN4FEA knockin animals. The HCN4 WT locus comprises exons 3–8. Exons depicted in blue carry the mutations. In the targeting construct, two substitutions were located in the CNBD (R669E, T670A) and one in the C-linker (Y527F) of the channel protein. Residues R669 and T670 are located in the loop between the P helix and the β7 sheet of the CNBD. Both residues directly interact with the phosphate group of cAMP. Data represent the mean ± SEM, n numbers are given in parentheses. Source data are provided as a Source Data file.

proteins contributing to SAN action potentials were not altered in HCN4FEA mice. Together, the results indicate that compensatory remodelling or changes in gene expression profile were not relevant issues in the HCN4FEA heart.

Native I_f properties in isolated SAN pacemaker cells. In single pacemaker cells isolated from the SAN, hyperpolarising voltage steps activated robust I_f (Fig. 2i). Steady-state I_f current densities of WT and HCN4FEA cells, determined at −140 mV in whole-cell mode, were similar in the absence of exogenous cAMP and in presence of 100 μM cAMP in the intracellular recording solution (Supplementary Data 1b). The slow (τau1) and fast (τau2) activation time constants representing activation of HCN4 and HCN1 channels, were similar in WT and HCN4FEA cells (Supplementary Data 1b) in the absence of cAMP. In contrast, intracellular cAMP accelerated the activation kinetics of WT, but not HCN4FEA channels. Steady-state activation curves were determined to derive the half-maximal activation voltage ($V_{0.5}$) and the slope values (k) (Fig. 2j, k, Supplementary Data 1b). In the absence of cAMP, $V_{0.5}$ values in HCN4FEA cells were more positive than WT values, which is in agreement with data from heterologously expressed HCN4FEA channels (Fig. 1d and Supplementary Data 1a). Cyclic AMP induced a significant right shift of the $V_{0.5}$ value of WT but not HCN4FEA activation curves. Slope factors in the absence and presence of cAMP were similar between WT and HCN4FEA cells. In perforated-patch measurements where endogenous cAMP concentrations are present[27], $V_{0.5}$ values were similar in WT and HCN4FEA cells (Fig. 2k, Supplementary Data 1c).

Sinus node bradycardia in HCN4FEA mice. Telemetric ECG recordings[1,20] (Fig. 3a–d, Supplementary Data 4a) revealed that the average and minimum HRs were significantly decreased in HCN4FEA mice indicating pronounced bradycardia. In addition, HCN4FEA animals were not able to increase their maximum HR to the same level as their WT littermates. This condition is clinically defined as chronotropic incompetence. Strikingly, HR regulation dynamics (HR_{max}/HR_{min}) and HR range (HR_{max}-HR_{min}) were preserved in the HCN4FEA mouse (Supplementary Data 4a–b). Seventy-two-hour HR histograms were shifted toward lower values in the HCN4FEA animals (Fig. 3d). Furthermore, WT histograms of HR were symmetrical with a centred peak. In contrast, histograms of HCN4FEA showed left-skewed distribution with a peak in the low HR range. In-line with the manifest bradycardia observed in vivo, markedly reduced beating rates were also present in vitro in preparations containing the intact sinoatrial node network with surrounding tissue (isolated whole hearts and biatrial preparations) of the HCN4FEA mouse (Supplementary Data 6a–b, 8a).

To further investigate the integrity of sinus node automaticity and conduction in vivo an intracardiac electrophysiological study was performed (Supplementary Fig. 1). This revealed an increase in sinus node recovery time, which is defined as the time required to reinitiate spontaneous firing following overdrive pacing. This indicated a delayed impulse formation within the HCN4FEA SAN. In addition, premature atrial stimulation[20] (Supplementary Fig. 1b, c and Supplementary Data 5a) as well as optical imaging (Fig. 3e, f and Supplementary Data 6d) uncovered prolonged sinoatrial conduction time in HCN4FEA SAN, yet the conduction pathway throughout the SAN and atria was similar to WT (Supplementary Fig. 2a–d). The combination of impaired impulse formation and conduction causes severe sinus bradycardia and a reduction in cardiac output. Furthermore, electrophysiological study revealed that atrioventricular (AV) node function was normal in HCN4FEA mice (Supplementary Fig. 1d–k and Supplementary Data 5a). Qualitative immunohistochemical experiments and Sirius red/Fast green stainings suggested that HCN4 protein levels and distribution, and amount of fibrous tissue in the AV node were similar to WT (Supplementary Fig. 1l, m).

Sinus dysrhythmia in HCN4FEA mice. Besides bradycardia and chronotropic incompetence, severe sinus dysrhythmia was dominating ECG traces of HCN4FEA mice (Fig. 3b). Sinus dysrhythmia is clinically defined as irregular HR characterized by large beat to beat variations originating in the SAN. Sinus dysrhythmia was quantified by applying signal processing tools developed for the analysis of heart rate variability in the time- and frequency domain[1]. This revealed, that time domain parameters were significantly higher for HCN4FEA animals compared to the WT (Supplementary Data 4c). Likewise, Poincaré plots displayed higher beat-to-beat dispersion and a broad comet-shaped pattern (Fig. 3g). Frequency domain analysis of HR variability (HRV) revealed markedly increased power across all frequency bands for HCN4FEA compared with WT (Fig. 3h, Supplementary Data 4d). Overall, fluctuations were more pronounced during phases of slow HR. To study the effect of complete autonomic blockade on HRV parameters, atropine and propranolol were administered consecutively. Treatment of WT and HCN4FEA mice with propranolol reduced HR fluctuations, which was further reduced upon subsequent treatment with atropine (Fig. 3i, Supplementary Data 4e). This indicates that the major part of severe HR fluctuations in HCN4FEA animals are attributable to ANS inputs. However, HR fluctuations were still more pronounced in

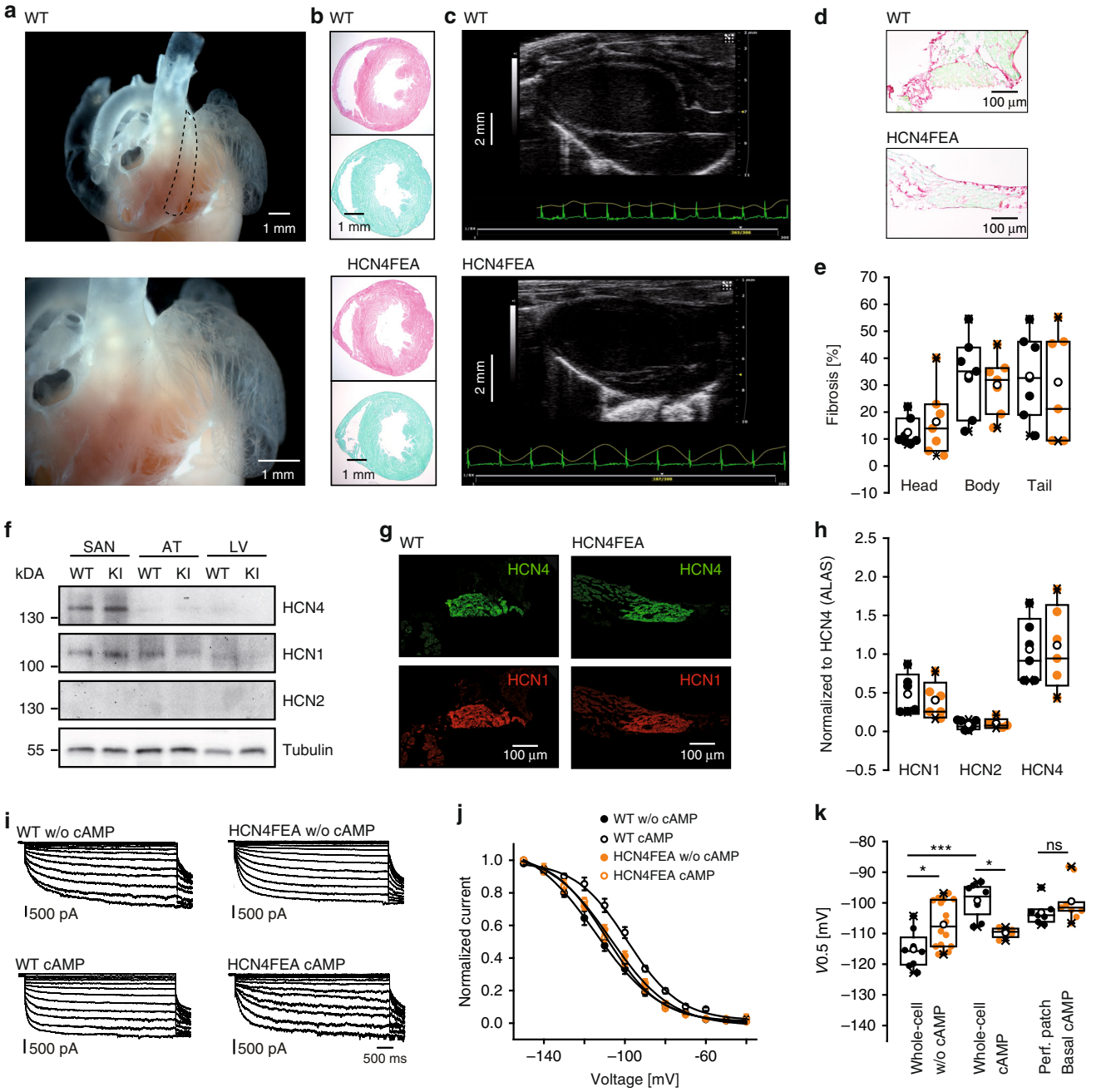

Fig. 2 Similar expression and distribution of HCN channels in the WT and HCN4FEA heart. a Gelatin-inflated heart preparation depicting the anatomy of the SAN region ($n = 5$ biologically independent samples). **b** Hematoxylin and eosin (H&E, $n = 6$ WT + 6 HCN4FEA biologically independent samples) and fibrosis stainings (Sirius red/ Fast green, $n = 7$ WT + 7 HCN4FEA biologically independent samples) of ventricular cross sections. **c** Representative long-axis echocardiograms ($n = 12$ WT + 11 HCN4FEA animals). **d** Sirius red/Fast green stained transverse sections of the central SAN (SAN head, $n = 7$ WT + 7 HCN4FEA biologically independent samples). **e** Quantification of fibrosis in the SAN head ($n = 7$ WT + 7 HCN4FEA biologically independent samples), body ($n = 7$ WT + 7 HCN4FEA biologically independent samples), and tail ($n = 7$ WT + 6 HCN4FEA biologically independent samples). **f** HCN channel expression in SAN, atria (AT), and left ventricle (LV) of WT and HCN4FEA (KI) mice (one blot with pooled tissue from 6 WT + 6 HCN4FEA animals). Tubulin: loading control. **g** Consecutive sections of the central SAN shown in **d** demonstrating the transmural distribution of HCN4 (green) and HCN1 (red) in WT and HCN4FEA ($n = 3$ WT + 3 HCN4FEA biologically independent samples). **h** Quantitative PCR analysis of HCN channel transcript levels from SANs normalised to HCN4 channel expression ($n = 6$ WT + 6 HCN4FEA biologically independent samples). Expression levels of HCN1 and HCN2 were also comparable between both genotypes. **i** Representative whole-cell I_f recordings from isolated SAN cells under conditions without (upper panel) and with (lower panel) 100 µM cAMP in the pipette solution. **j** Averaged I_f activation curves determined from current measurements as shown in **i** (WT w/o cAMP $n = 8$ cells, WT cAMP $n = 8$ cells, HCN4FEA w/o cAMP $n = 16$ cells, HCN4FEA cAMP $n = 4$ cells; data are presented as mean values ±:SEM). **k** Half-maximal activation voltage determined from I_f activation curves in whole-cell configuration without ($n = 8$ WT + 16 HCN4FEA cells) and with 100 µM cAMP in the pipette solution ($n = 8$ WT + 4 HCN4FEA cells) and from perforated-patch configuration with basal cAMP levels ($n = 7$ WT + 9 HCN4FEA cells). WT w/o cAMP vs HCN4FEA w/o cAMP: $p = 0.0075$; WT w/o cAMP vs WT cAMP: $p = 0.00003$; WT cAMP vs HCN4FEA cAMP: $p = 0.0127$; WT basal cAMP vs HCN4FEA basal cAMP (perforated-patch): $p = 0.2126$. All experiments were performed using male mice. Boxplots show the median line, perc 25/75, and min/max value; open symbols represent the mean value. Significance levels: *two-way ANOVA. Source data are provided as a Source Data file.

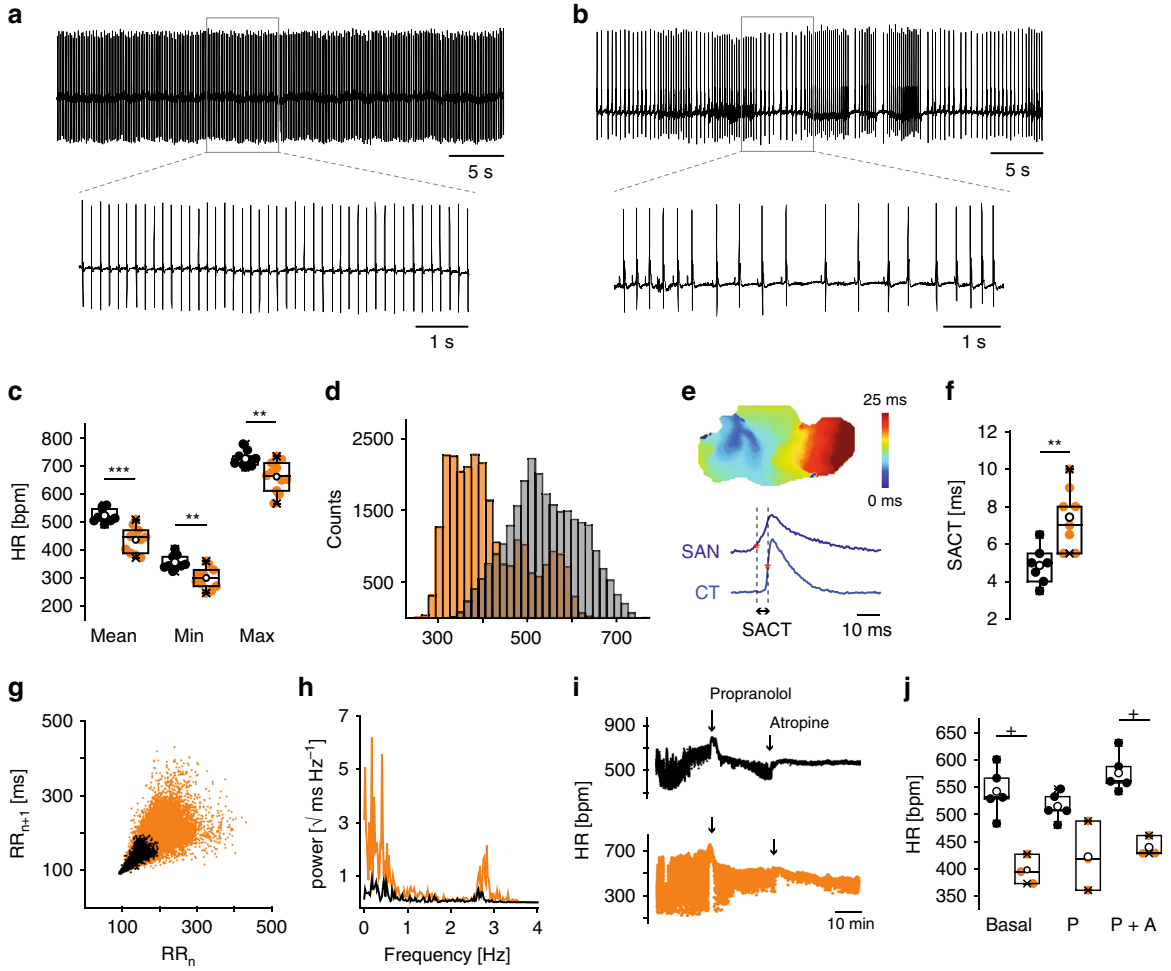

Fig. 3 HCN4FEA mice display bradycardia and sinus dysrhythmia. a, b Telemetric ECG traces obtained from a conscious, freely moving **a** WT mouse and **b** HCN4FEA mouse. Insets: Extended ECG traces. **c** Mean, minimum, and maximum HR determined from 72-h RR intervals (WT: $n = 9$, HCN4FEA: $n = 11$; two-sided *t*-test; mean HR: $p = 0.0019$, min HR: $p = 0.0040$, max HR: $p = 0.0383$). **d** HR histograms of a WT (light gray) and HCN4FEA mouse (orange) determined from 72-h (12 h/12 h light/dark cycle) ECGs. **e** Determination of sinoatrial conduction time) with optical imaging measurements. Activation map of a biatrial WT SAN preparation (upper panel) and optical action potentials (OAP) (lower panel) from the leading pacemaker site in the SAN (dark blue) and from the earliest atrial excitation site within the crista terminalis (CT; light blue). SACT is determined as the time difference of activation time points indicated by asterisk. **f** SACT in WT and HCN4FEA SAN preparations ($n = 7$ WT + 8 HCN4FEA biologically independent samples; two-sided *t*-test; $p = 0.0029$). **g** Comet-shaped Poincaré plots in HCN4FEA mice (orange). **h** Frequency domain power spectral density plots obtained from a WT (black) and HCN4FEA (orange) mouse. **i** Tachograms of WT (black) and HCN4FEA (orange) mice before and after subsequent injection of propranolol (20 mg/kg i.p) and atropine (1 mg/kg i.p). Arrows indicate timepoint of injection (WT: $n = 5$, HCN4FEA: $n = 3$). **j** Mean basal HR and HR after successive injection of propranolol and atropine ($n = 5$ WT + 3 HCN4FEA animals; Mann–Whitney U test; basal: $p = 0.03571$, P: $p = 0.07143$, P + A: $p = 0.03571$). In vivo experiments were performed using male animals. In vitro experiments were performed using tissue isolated from female animals. Boxplots show the median line, perc 25/75, and min/max value; open symbols represent the mean value. Significance levels: *student´s paired *t*-test; $^{+}$Mann–Whitney U test. Source data are provided as a Source Data file.

HCN4FEA after complete autonomic blockade, indicating that a second, but minor part of HR fluctuations observed in vivo is independent of the ANS and attributable to intrinsic sinus node dysfunction. In support of this conclusion, HR fluctuations in in vitro preparations (isolated perfused hearts and biatrial preparations; Supplementary Data 6a, 8a)—in which intrinsically autonomic regulation is lacking—were lower than those observed in vivo for both mouse groups but were still more pronounced in HCN4FEA preparations.

Long-lasting periods of nonfiring in HCN4FEA SAN cells. To test SAN activity at the cellular level, spontaneous firing of pacemaker cells was investigated using long-term perforated-patch-clamp experiments, which allow for stable recordings for up to 1 h (Fig. 4). Cells from either WT or HCN4FEA mice fired rhythmic, spontaneous pacemaker potentials (Fig. 4a, b, and Supplementary Data 7a) and averaged action potential shape, mean rate of spontaneous firing, slope of slow diastolic depolarisation and maximum diastolic potential were similar (Fig. 4d–g). Upon application of the β-adrenoceptor agonist isoproterenol (100 nM) AP firing rate increased in WT and HCN4FEA cells to the same extent (Fig. 4e and Supplementary Data 7e). From these findings we can conclude, that at least CDR of HCN4 and also most likely HCN4 channels in general are not involved in baseline firing of pacemaker cells.

Surprisingly, in 90% of HCN4FEA cells rhythmic firing was often accompanied by a slow and progressive hyperpolarisation (HCN4FEA: $\Delta V_m = 7.17 \pm 0.36$ mV; $n = 9$; WT: $\Delta V_m = 8.16 \pm 1.36$ mV; $n = 5$; Fig. 4a, b, j), leading to extended periods of nonfiring which lasted for 28.9 ± 3.3 seconds. Subsequently,

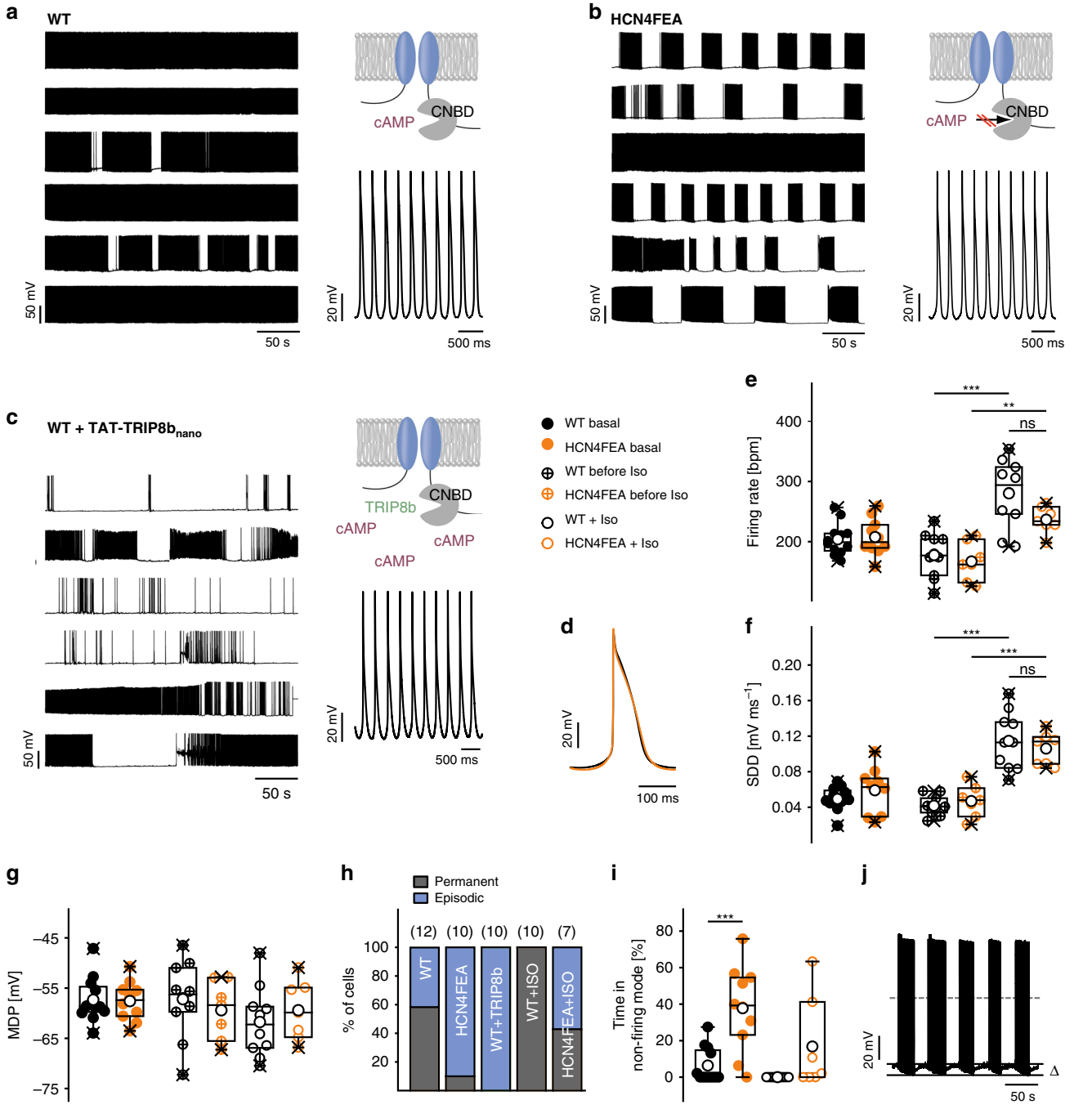

Fig. 4 Long-lasting periods of nonfiring in isolated pacemaker cells of HCN4FEA mice. a–c (right, upper panel) Cartoons of channel variant used in experiments shown in the right panel. (Left panel) long-term perforated-patch-clamp recordings of spontaneous action potentials under baseline conditions in six SAN cells isolated from **a** WT and **b** HCN4FEA mice and **c** WT cells after application of TAT-TRIP8b$_{nano}$. (Right, lower panel) Magnification of action potential recordings shown in the left panels. **d** Averaged action potentials obtained from representative perforated-patch-clamp recordings of a WT and HCN4FEA pacemaker cell. **e–g** firing rate (WT before Iso vs WT Iso: $p = 0.000004$; HCN4FEA before Iso vs HCN4FEA Iso: $p = 0.0035$; WT Iso vs HCN4FEA Iso: $p = 0.0386$), slope of slow diastolic depolarisation (SDD) (WT before Iso vs WT Iso: $p = 0.00000003$; HCN4FEA before Iso vs HCN4FEA Iso: $p = 0.00002$; WT Iso vs HCN4FEA Iso: $p = 0.4315$), and maximum diastolic potential (MDP) under basal conditions ($n = 12$ WT + 10 HCN4FEA cells) as well as before ($n = 10$ WT + 7 HCN4FEA cells) and during ($n = 10$ WT + 7 HCN4FEA cells) application of isoproterenol (100 nM). Values were determined from episodes with constant firing in WT and HCN4FEA cells. **h** Quantification of different firing patterns determined from similar recordings as shown in **a–c** (left panels). **i** Percentage of time spent in the nonfiring mode (basal $n = 12$ WT + 10 HCN4FEA cells, Iso $n = 10$ WT + 7 HCN4FEA cells; WT basal vs HCN4FEA basal: $p = 0.0004$). **j** Representative sequence of firing and nonfiring in an HCN4FEA pacemaker cell. The difference between MDP during firing and nonfiring was 7.14 ± 0.36 mV (ΔVm; $n = 9$). All experiments were performed using male animals. Boxplots show the median line, perc 25/75, and min/max value; open symbols represent the mean value. Significance levels: *Holm's–Sidak post-hoc test following two-way ANOVA. Source data are provided as a Source Data file.

pacemaker cells slowly recovered from the hyperpolarised potential and depolarised until they restarted regular firing. This firing pattern occurred less frequently in WT cells (42%; Fig. 4h), where nonfiring episodes lasted for 16.2 ± 1.5 seconds. In total, HCN4FEA cells interrupted firing for 37.7 ± 7.4% of the total measurement time, whereas WT cells stopped firing for only 6.4 ± 2.8% of the time (Fig. 4i and Supplementary Data 7a). This finding suggests the presence of a thus far unknown, nonfiring mode of SAN cells. To test whether nonfiring can be induced by acutely switching off CDR of HCN4, we employed a plasma membrane permeable peptide (TAT-TRIP8b$_{nano}$) derived from TRIP8b—an auxiliary subunit of neuronal HCN channels[28]. TAT-TRIP8b$_{nano}$ was shown to bind to the cyclic nucleotide-binding domain of HCN channels, inhibiting CDR. Application of the peptide induced the nonfiring mode in WT cells followed by firing recovery (Fig. 4c); these responses were more pronounced than in HCN4FEA cells. To mimic vagal activity and to test whether a reduction in cAMP levels can induce the nonfiring state, we applied carbachol to WT and HCN4FEA cells. Indeed, carbachol induced the nonfiring state in single pacemaker cells of WT and HCN4FEA cells (Fig. 5a–d and Supplementary Data 7b). To test the effect of increased cAMP levels we applied isoproterenol to the cells. This completely abolished the nonfiring mode in WT cells and reduced the amount of HCN4FEA cells that displayed the nonfiring mode (WT = 0%; HCN4FEA = 57.1%; Fig. 4h). Cellular capacitances and HCN current densities determined in perforated-patch mode were similar in WT and HCN4FEA cells with permanent and episodic firing, respectively, (WT, permanent firing: −12.6 ± 3.0 pA pF^{-1}, $n = 5$; WT, episodic firing: −15.4 ± 4.3 pA pF^{-1}, $n = 4$; HCN4FEA, permanent firing: −10.0 ± 3.0 pA pF^{-1}, $n = 4$; HCN4FEA, episodic firing: −15.0 ± 2.5 pA pF^{-1}, $n = 6$; Supplementary Data 7a, 7c). T-type and L-type calcium current density and response to cAMP were also similar in WT and HCN4FEA cells (Supplementary Data 7d).

Dynamic mode-shifts in the voltage dependence of HCN4. Compared to firing, nonfiring is characterized by hyperpolarized membrane potentials. To test whether this hyperpolarized potential influences voltage-dependent activation of HCN4 channels, we recorded steady-state activation curves from different holding potentials (HP) corresponding to membrane potentials during the firing (−55 mV) and nonfiring mode (−65 and −75 mV). These experiments revealed that the activation curves and $V_{0.5}$ values are strongly dependent on the HP (Supplementary Fig. 3a, Supplementary Data 1a). The most negative $V_{0.5}$ value ($V_{0.5}$: −100.1 ± 1.9 mV) was obtained for WT channels without cAMP using a HP of −55 mV. $V_{0.5}$ values are shifted to more positive values for HPs of −65 ($V_{0.5}$: −90.7 ± 4.0 mV) or −75 mV ($V_{0.5}$: −77.6 ± 3.1 mV). cAMP shifted $V_{0.5}$ values to more positive potentials in WT channels. $V_{0.5}$ was −82.1 ± 2.8 mV in the presence of cAMP using a HP of −55 mV and shifted to a more positive value of −62.0 ± 2.8 mV at a HP of −65 mV and even to −51.3 ± 1.7 mV at a HP of −75 mV. For HCN4FEA channels, the $V_{0.5}$ values in the absence and presence of cAMP at each holding potential were similar and were positioned in between $V_{0.5}$ values obtained in the absence or presence of cAMP for WT channels. Taken together, these results indicate that HCN4 channels are characterized by a history-dependent and dynamic voltage dependence. This phenomenon has been described as hysteresis and mode shift of voltage-dependent channel activation[29–33].

Nonfiring pacemaker cells in the SAN network. At this point, the question arises of how the nonfiring observed in single pacemaker cells becomes apparent in the SAN network (Fig. 6). To address this question, confocal Ca^{2+} imaging experiments of in vitro preparations containing the SAN network and surrounding tissue were performed in which global Ca^{2+} signals were used as readout for firing and nonfiring states in single pacemaker cells. The vast majority of individual WT pacemaker cells displayed rhythmic and global Ca^{2+} transients (Fig. 6a, d left panels, and Supplementary Movie 1) without exhibiting a nonfiring state. However, in a fraction of HCN4FEA cells, distinct subthreshold Ca^{2+} signals were observed (Supplementary Movie 2). Some of these cells displayed spontaneous and highly localised Ca^{2+} events during diastole and global Ca^{2+} transients during systole (Supplementary Movie 4). Another cell population displayed Ca^{2+} waves propagating from one end of the cell to the other (Fig. 6d middle panel; Supplementary Movie 5) or central Ca^{2+} waves spreading bidirectionally along the long axis (Supplementary Movie 6). These Ca^{2+} signals were self-limiting, did not trigger global Ca^{2+} transients, and were temporally and spatially unrelated to global Ca^{2+} transients of neighbouring cells; this indicates that these cells are indeed nonfiring. Sometimes, Ca^{2+} waves were not restricted to a single cell in the network but were also transmitted to neighbouring cells, resulting in small cell clusters with irregular Ca^{2+} activity (Supplementary Movie 2). This indicates an interaction between these cells and a functional impact of single, nonfiring cells on the SAN network. In WT SANs, localised Ca^{2+} activity and Ca^{2+} waves were rarely observed; however, they could reliably be induced after application of TAT-TRIP8b$_{nano}$ (Fig. 6a, d right panels; Supplementary Movie 3). This confirms that the Ca^{2+} signals are specifically caused by acutely switching off HCN4 CDR. Subthreshold Ca^{2+} activity was never observed during the nonfiring state in isolated single pacemaker cells and only occurred in the SAN network.

In vitro HR response to vagal nerve stimulation. Loss of HCN4 CDR induced nonfiring of single SAN cells, led to moderate firing fluctuations in in vitro SAN preparations and isolated whole hearts and very pronounced HR fluctuations in vivo (Supplementary Data 4c, 6a, 8a). HR fluctuations in vivo mainly arose from ANS activity (Fig. 3i). To test whether firing rate fluctuations can be induced in vitro by stimulation of the ANS, we utilised in vitro preparations containing the vagal nerve (Fig. 7). The advantage of this experiment is that electrical stimulation of the vagal nerve induces physiological, pulsatile, and transient release of acetylcholine from nerve terminals. Vagal nerve stimulation evoked a pronounced and stable decrease in the firing rate of WT whole-heart preparations (Fig. 7b, Supplementary Data 8b), which persisted throughout stimulation. In contrast, it induced short and inappropriately enhanced bradycardic periods characterized by very slow firing or sinus pauses in HCN4FEA hearts that were frequently interrupted by short periods of recovery to faster HR (Fig. 7c, d). Optical imaging of biatrial preparations (Supplementary Fig. 2a–d) demonstrated that the leading pacemaker region position, which is defined as the region of earliest excitation, was similar, remained stable, and was localised within the anatomical territory of the SAN in WT and HCN4FEA preparations. Application of carbachol shifted the leading pacemaker region towards the interatrial septum, inferior caval vein, or AV junction, but these shifts were similar in WT and HCN4FEA SANs (Supplementary Fig. 2e–f and Supplementary Data 6b). In stark contrast, vagal nerve stimulation doubled shifts of the leading pacemaker in HCN4FEA preparations (Fig. 7e–g and Supplementary Data 6c). Altogether, the findings suggest that CDR of HCN4 channels dampens and antagonises the effect of the vagal nerve.

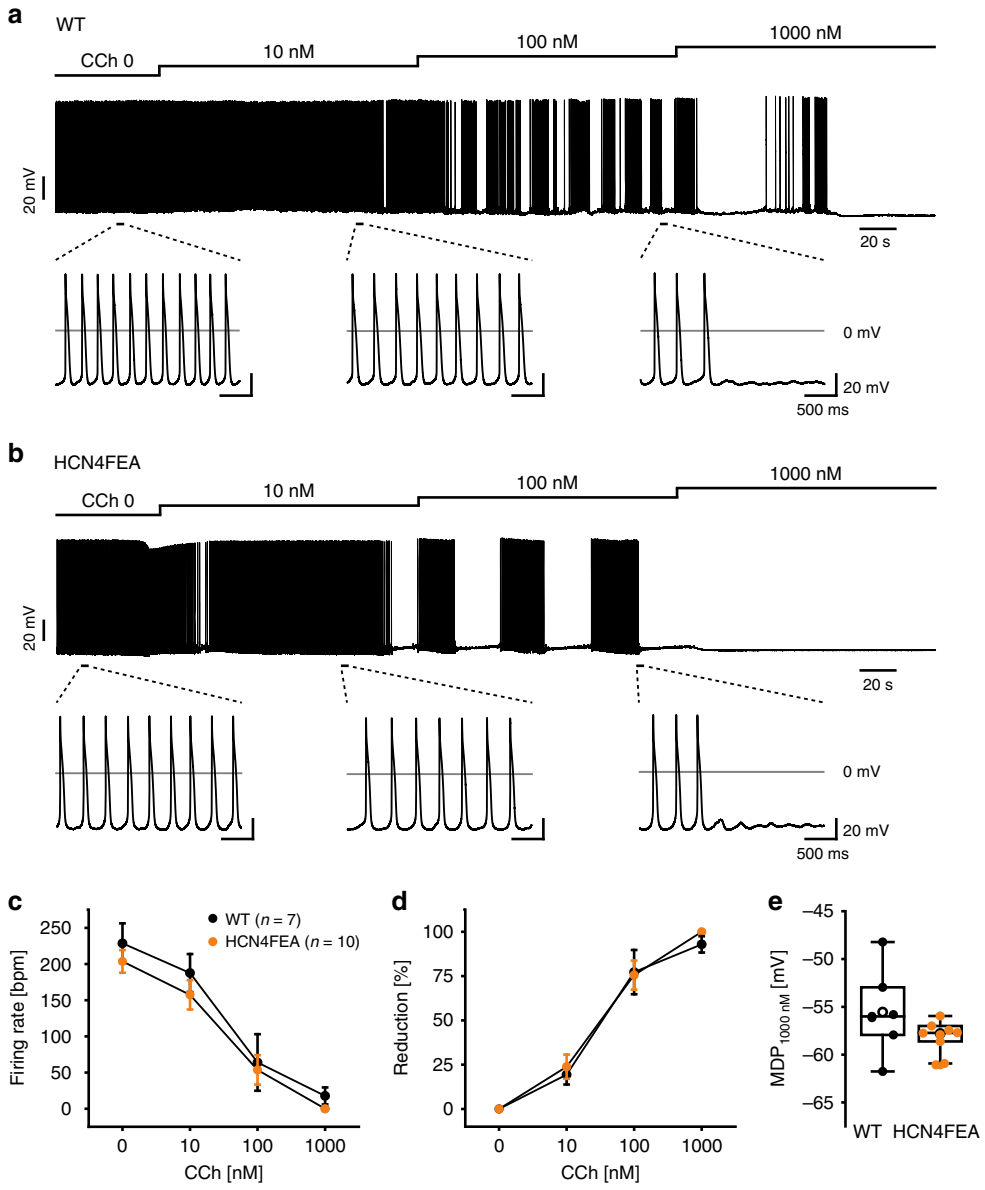

Fig. 5 Carbachol induces episodic firing patterns with nonfiring states in both WT and HCN4FEA SAN cells. a, b Representative current-clamp recordings obtained in perforated-patch-clamp mode from **a** WT and **b** HCN4FEA cells. Increasing concentrations of carbachol consecutively reduced the firing frequency and caused an episodic firing pattern with nonfiring states upon successive hyperpolarisation. **c** Cumulative carbachol dose response of WT and HCN4FEA cells ($n = 7$ WT + 10 HCN4FEA cells; data are presented as mean values ± SEM). **d** Percentage reduction was calculated by normalising each value to the basal firing rate ($n = 7$ WT + 10 HCN4FEA cells; data are presented as mean values ± SEM). **e** Maximum diastolic potential after application of 1000 nM Carbachol ($n = 7$ WT + 10 HCN4FEA cells). All data were obtained from SAN cells of male WT (black) and HCN4FEA (orange) mice. Boxplots show the median line, perc 25/75, and min/max value; open symbols represent the mean value. Source data are provided as a Source Data file.

In vivo HR response to dynamic vagal nerve activity. Dynamic interaction between vagal activity and the heart in vivo was investigated using combined telemetric blood pressure and ECG recordings (Fig. 7h–k). Therefore, 3-h recordings were screened for up and down sequences[34,35]. Up sequences were defined as a sequential increase in blood pressure over three heart beats (arrow in Fig. 7h) that lead to a reflectory increase in vagal activity, which subsequently slows down HR (increase in RR interval; Fig. 7h). Conversely, blood pressure sequentially drops over three heart beats in down sequences, inducing a subsequent increase in HR (decrease in RR interval; Fig. 7i). Importantly, HR responses mainly reflect rapid changes in vagal activity, while sympathetic activity can be assumed constant. For WT and HCN4FEA mice, a similar amount of total sequences was identified indicating similar vagal tone (Fig. 7j, Supplementary Data 9). Inspection of the graphical relationship between HR and systolic blood pressure revealed a higher amplitude and steeper slope for up and down sequences in HCN4FEA mice compared with WT (Fig. 7k). Overall, this indicates that HCN4 CDR dampens and antagonises vagal effects on the heart, which is functionally relevant for the baroreceptor reflex[34,36,37].

In vivo HR response to sympathetic nervous system activation. In HCN4FEA mice, HR acceleration during spontaneous activity of the sympathetic system induced alternating episodes of junctional escape rhythm and sinus rhythm (Fig. 8a, b). Junctional

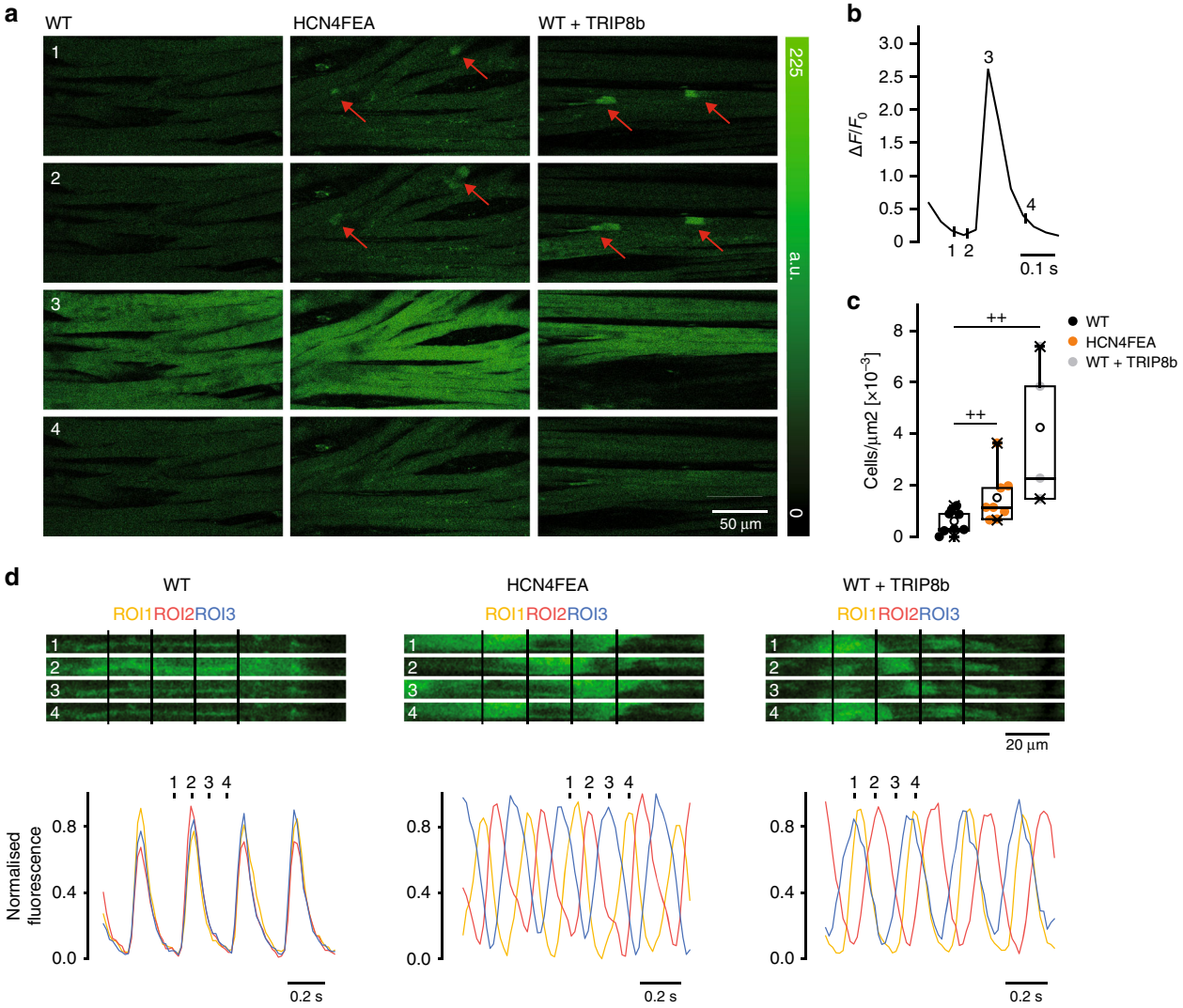

Fig. 6 Nonfiring pacemaker cells can be identified in the SAN network. a Time-lapse of confocal calcium recordings (Fluo-4 AM; fluorescence in arbitrary units [a.u.]) of intact SAN explants of WT, HCN4FEA, and WT after application of TAT-TRIP8b$_{nano}$ ($n = 7$ WT + 8 HCN4FEA + 4 WT + TRIP8b biologically independent samples). Red arrows indicate subthreshold calcium signals. Images were taken at time points 1–4 during WT calcium transient shown in **b**. **c** Number of cells per µm^2 displaying subthreshold calcium signals determined from the entire SAN region ($n = 7$ WT + 8 HCN4FEA + 4 WT + TRIP8b biologically independent samples; Mann–Whitney U test; WT vs HCN4FEA: $p = 0.0330$; WT vs WT + TRIP8b: $p = 0.0040$). **d** (upper panel) Time-lapse of confocal calcium recordings of intact SAN explants of WT, HCN4FEA, and WT after application of TAT-TRIP8b$_{nano}$ ($n = 7$ WT + 8 HCN4FEA + 4 WT + TRIP8b biologically independent samples). Images were taken at time points 1–4 indicated in the corresponding calcium transients (lower panel). Ca^{2+} transients were determined from indicated regions of interest (ROI). All experiments were performed using tissue isolated from female animals. Boxplots show the median line, perc 25/75, and min/max value; open symbols represent the mean value. Significance levels: $^{+}$Mann–Whitney U test. Source data are provided as a Source Data file.

escape rhythm is defined as a specific arrhythmia in which a second, independent, subsidiary pacemaker is present, which is faster than the SAN and thereby suppresses SAN activity. Optical imaging and intracardiac ECG recordings of Langendorff-perfused hearts revealed that the position of the secondary pacemaker was close to the AV junction. This subsidiary pacemaker paces the ventricle and retrogradely activates the atria (Fig. 8c–f, right). In-line with this activation pattern a His bundle potential preceded ventricular and atrial activity in intracardiac ECG recordings of Langendorff-perfused hearts (Fig. 8f, right). Together, these results suggest that the subsidiary pacemaker is localised proximal to the bundle of His and distal to the SAN. When the firing rate of the subsidiary pacemaker approached that of the SAN, isorhythmic AV dissociation occurred in HCN4FEA mice (Fig. 9), which in turn caused oscillations of blood pressure and cardiac output because atrial and ventricular contraction are not properly timed. The presence of isorhythmic AV dissociation and junctional escape rhythm indicates that the coordinated response of the SAN and the AVN (or another subsidiary pacemaker) to changes in ANS activity during HR regulation is impaired in HCN4FEA mice. Furthermore, their presence indicates that the SAN shows chronotropic incompetence (i.e. the SAN cannot accelerate firing rate to maximum rate observed in WT), whereas the chronotropic competence of the subsidiary pacemaker is preserved (i.e. it can accelerate firing rate).

Discussion

Here we utilized a novel mouse model to investigate the physiological role of HCN4 CDR in the heart. We found that CDR of HCN4 is not required for principal HR regulation by the ANS

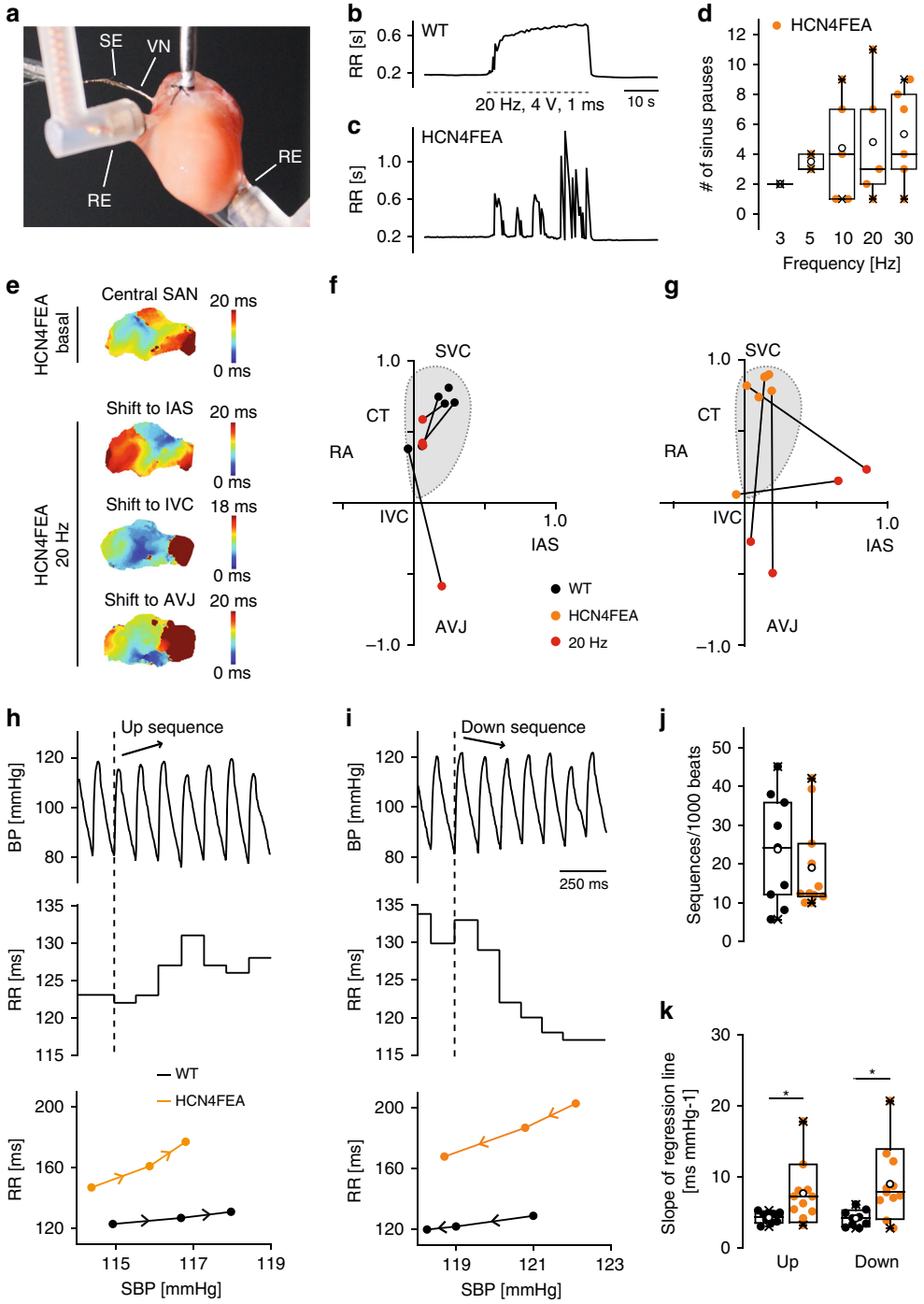

Fig. 7 Vagal nerve stimulation in vitro and spontaneous vagal nerve activity in vivo induce overshooting HR responses. a Experimental setup consisting of a Langendorff-perfused heart preparation. VN vagal nerve, SE stimulating electrode, RE ECG recording electrodes. **b, c** RR tachograms of **b** WT and **c** HCN4FEA ECGs before, during (dotted lines), and after vagal nerve stimulation (VNS). **d** Mean number of sinus pauses in HCN4FEA hearts at different stimulation frequencies during VNS (3 Hz $n = 1$, 5 Hz $n = 2$, 10 Hz $n = 5$, 20 Hz $n = 5$, 30 Hz $n = 6$ biologically independent samples). Sinus pauses were not observed in WT hearts. **e** Activation map of a HCN4FEA biatrial preparation (top) before and (bottom) during VNS. **f, g** Position of the leading pacemaker in WT and HCN4FEA preparations before and during VNS. IAS: intra-atrial septum; IVC: inferior vena cava. **h, i** Combined telemetric blood pressure (BP) and ECG recordings. **h** (top) Arterial BP trace of a WT mouse during a short sequence of three consecutive beats with increasing systolic BP (up sequence; arrow). **h** (middle) Corresponding RR intervals. **h** (bottom) Plot of systolic BP (SBP) and corresponding RR intervals for a WT and HCN4FEA mouse (see methods for details). **i** BP trace during a short sequence of three consecutive beats with decreasing systolic BP (down sequence). **j** Total amount of up and down sequences ($n = 9$ WT + 11 HCN4FEA animals). **k** Mean slope of the RR/SBP relationship ($n = 9$ WT + 11 HCN4FEA animals; two-sided *t*-test; slope up: $p = 0.0238$; slope down: $p = 0.0103$). In vivo experiments were performed using male animals. In vitro experiments were performed using tissue isolated from female animals. Boxplots show the median line, perc 25/75, and min/max value; open symbols represent the mean value. Significance levels: *student´s paired *t*-test. Source data are provided as a Source Data file.

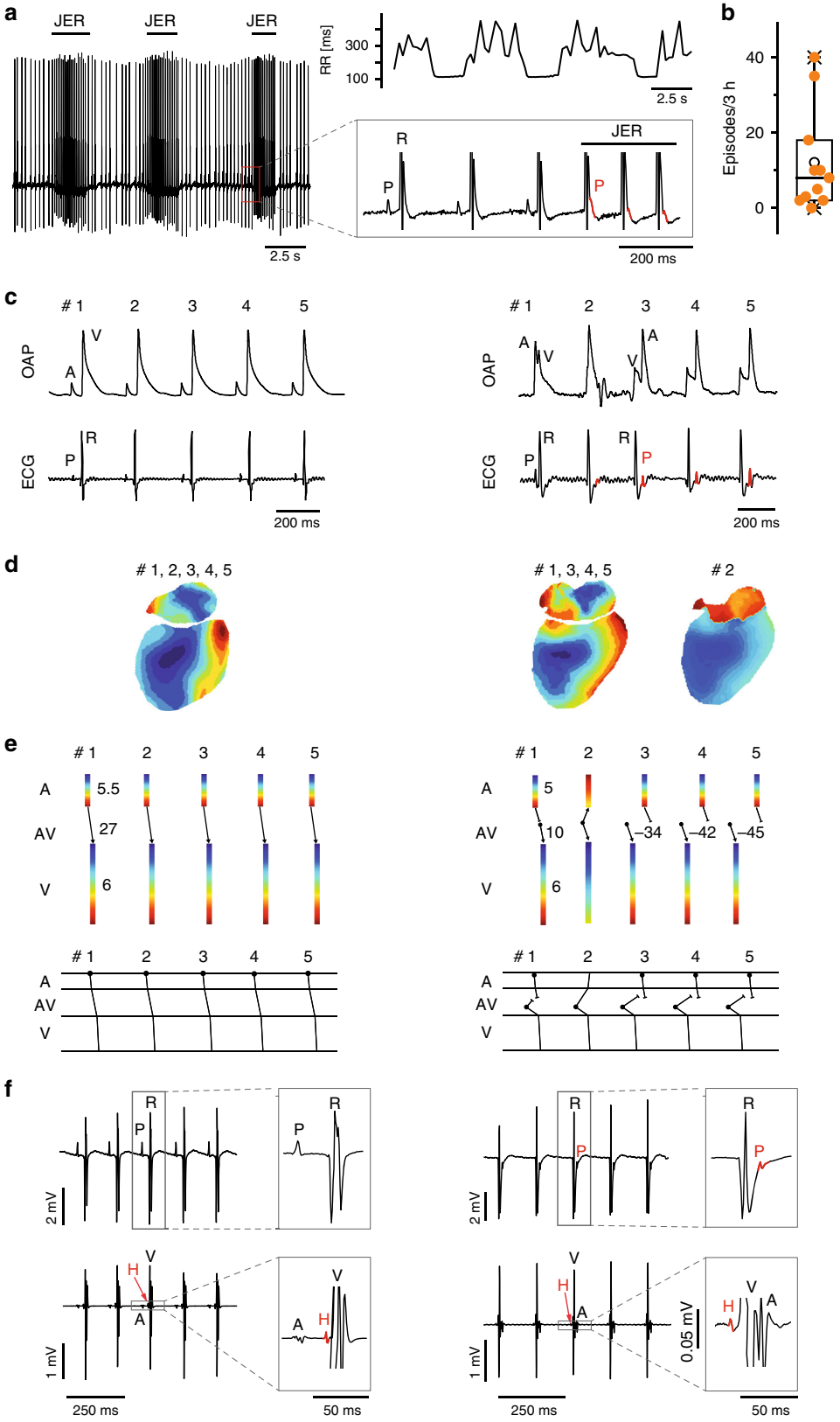

indicating that the chronotropic response is carried mainly by other ion channels and transporters. In-line with these conclusions are recent studies which also provide evidence that HCN4 channels are not required for the chronotropic response[11,12]. Importantly, our study revealed a complex cardiac phenotype in the absence of CDR characterized by sinus dysrhythmia, severe sinus bradycardia, sinus pauses and chronotropic incompetence, leading to escape arrhythmias, which together reduced cardiac output. Furthermore, the absence of CDR leads to inappropriately enhanced HR responses of the SAN to vagal nerve activity during the baroreceptor reflex. Finally, we discovered a thus far uncharacterised nonfiring mode in single SAN pacemaker cells,

Fig. 8 Junctional escape rhythm due to chronotropic incompetence of the HCN4FEA SAN. a Telemetric ECG traces from a male HCN4FEA mouse with alternating episodes of sinus rhythm and junctional escape rhythm (JER) rhythm (left) and corresponding RR tachogram (right, top). Inset: During escape rhythm the P wave (red) occurs after the QRS complex. **b** Number of JER episodes during 3 h in low activity phase ($n = 11$ HCN4FEA animals). **c** Optical action potentials (OAP) and surface ECGs recorded from a WT (left) and HCN4FEA (right) Langendorff-perfused heart explanted from female mice. The HCN4FEA heart displays JER. The ventricular signal precedes the atrial signal in beat #3–5. **d** Activation maps determined from the OAP measurements shown in **c**. Right, activation maps for beats #1, and 3–5 were similar. Activation map for beat #2: anterograde activation of ventricles and retrograde activation of atria from the junction. **e** (upper panel) Conduction times determined from **d**. Numbers indicate atrial (top), atrioventricular (middle), and ventricular (bottom) conduction times in ms. Right, Beat 1: ventricles were activated 10 ms after atrial activation. Beat 3–5: ventricles were activated by a subsidiary pacemaker close to the AV junction before atria activation by the SAN. Beat 2: atrial and ventricular activation occurred simultaneously. **e** (lower panel) Schematic ladder diagrams were determined from the measurements shown in **d, e**. **f** Right heart catheterisation of a Langendorff-heart preparation via the superior vena cava from male WT (left) and HCN4FEA (right) animals. Surface (upper panel) and intracardiac ECGs (lower panel). Right, HCN4FEA Langendorff-perfused heart during JER induced by isoproterenol application. Inset: magnification of ECG traces. A His deflection (H, red) precedes the ventricular and atrial signal indicating that the subsidiary pacemaker is localised proximal to the bundle of His. Boxplots show the median line, perc 25/75, and min/max value; open symbols represent the mean value. Source data are provided as a Source Data file.

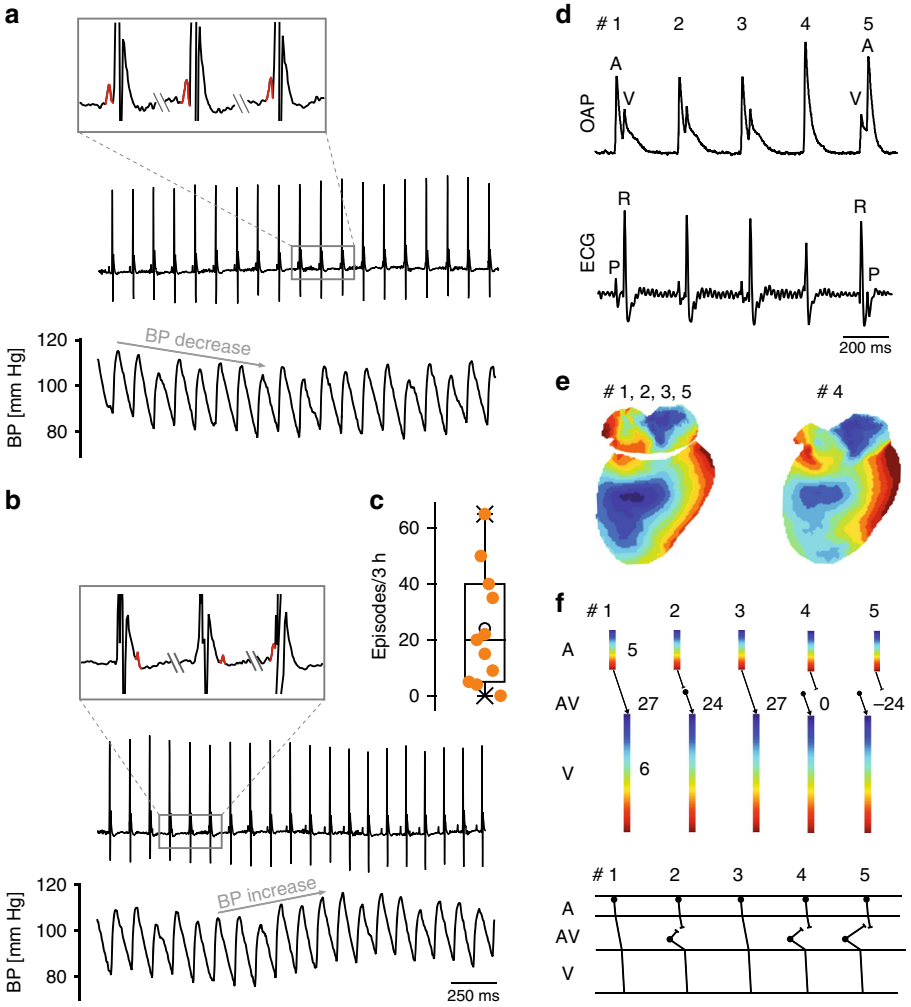

Fig. 9 Isorhythmic AV dissociation (IAVD) due to chronotropic incompetence of the HCN4FEA SAN. a, b Telemetric ECG trace (top) and corresponding arterial blood pressure recordings **(bottom)** from a male HCN4FEA mouse during IAVD. Characteristic flirtatious P waves indicate the presence of two independent pacemakers (top and inset). Concomitantly with the successive decrease in PR intervals, blood pressure dropped (bottom). **b** (top and inset) The P wave is hidden within the QRS complex, located behind or before the QRS complex. Blood pressure starts to normalise when PR normalises (bottom). **c** Number of IAVD episodes during 3 h in low activity phase ($n = 11$ HCN4FEA animals). **d** OAPs and surface ECG recorded from a female HCN4FEA whole-heart preparation during IAVD. **e** (left) Activation maps of beat #1 determined from the recordings presented in **d** showing IAVD ex vivo. Activation maps for beats 1, 2, 3, and 5 were similar. Right: activation map of beat #4. **f** Ladder diagrams for beats #1–5. Beat #1 and 3: normal activation arising from SAN with regular and constant PR; beat #2, 4, and 5: IAVD with shortened or negative PR indicating that the atria are activated by SAN and ventricles by a subsidiary pacemaker close to the AV junction. Schematic ladder diagrams were determined from the measurements shown in **d, e**. Boxplots show the median line, perc 25/75, and min/max value; open symbols represent the mean value. Source data are provided as a Source Data file.

which mechanistically can explain the observed phenotype on the single cell level.

The nonfiring mode is not only present in HCN4FEA cells but also spontaneously adopted in single WT SAN pacemaker cells (Fig. 10a) and lasts up to a minute. Importantly, this nonfiring mode is by far more pronounced when CDR of HCN4 is lacking. In WT cells, nonfiring can be increased by lowering intracellular cAMP levels by carbachol application or by acute blocking of cAMP binding to HCN4 channels by TAT-TRIP8b$_{nano}$. Reversely, increasing intracellular cAMP by application of isoproterenol markedly reduced nonfiring by shifting nonfiring cells into the firing mode. In-line with the observed induction of nonfiring by carbachol, recent studies revealed that nonfiring can be induced by application of cholinergic drugs in wild-type SAN cells[17,22] and knockout models in which cholinergic signalling is exaggerated, e.g. the RGS4[18] or RGS6[19] knockout mice. In summary, CDR of HCN4 is critically important for maintaining firing and for restoring firing in pacemaker cells that adopt the nonfiring mode. In contrast, lack of CDR leads to reduced stability of firing and thus pacemaker cells spontaneously switch to and remain in the nonfiring mode (Fig. 10a–b).

Our results suggest the following model, which explains the rhythmic changes of firing and nonfiring (Supplementary Fig. 3; note that for the physiological model all values are corrected for liquid junction potential). One important prerequisite for this model is that kinetic parameters of HCN4 (and also other HCN channel subtypes[38]) are much slower than the duration of the pacemaker potential. Therefore, HCN4 currents can be assumed as being almost constant during the pacemaker potential with only minor and low amplitude oscillations around a constant mean. Thus, the effective voltage, which determines overall HCN4 currents during firing is the average voltage of a pacemaker potential (pink line in Supplementary Fig. 3c). A typical cycle of firing and nonfiring is shown in Supplementary Fig. 3c. Firing starts at a maximum diastolic potential of −67 mV and slowly declines to −75 mV. At the same time, the average membrane potential declines from −51 mV (beginning of firing; pink curve) to −59 mV (end of firing; pink curve). When firing terminates, membrane potential abruptly drops to −75 mV (pink curve). During nonfiring the membrane potential slowly rises to −67 mV until firing is reinitiated, which leads to an abrupt increase in average potential to −51 mV. We propose that during firing and nonfiring pronounced shifts in the activation curves of HCN4 channels occur (Supplementary Fig. 3b), which are driven by the large voltage steps at the beginning and the end of firing (step-like jumps in the pink curve). We suggest that by the end of the firing mode (−59 mV) the activation curve of HCN4 is positioned to more hyperpolarised potentials (black curve, Supplementary Fig. 3b). After the abrupt jump to −75 mV at the beginning of nonfiring the activation curve shifts towards more depolarised potentials (red curve). Once the threshold for firing is reached pacemaker cells switch to firing mode and voltage abruptly jumps to −51 mV shifting voltage-dependent activation to more hyperpolarized potentials (black curve) and the cycle repeats. Voltage-dependent activation of HCN4 is therefore a dynamic and history-dependent process[29–33]. Given the voltage-dependent hysteresis of HCN4 channels[31,33], the shifts in activation curves lag behind the rather fast voltage jumps due to the slow activation and deactivation time constants of the HCN4 channels. The slow hysteresis of HCN4 maintains firing until the shift of the activation curve to the left is completed. Analog reasoning applies to nonfiring. Together, hysteresis behaviour and slow kinetics of HCN4 channels match slow changes of firing and nonfiring. During firing, HCN4 currents slowly decline and set the timepoint at which firing is terminated. By contrast, HCN4 currents do not influence SDD or firing rate during firing mode.

In WT channels, cAMP/isoproterenol shifts activation curves to more depolarised potentials. It thereby decreases the frequency and length of nonfiring by changing the timepoint at which firing is initiated and terminated. In HCN4FEA cells nonfiring is observed more frequently than in WT with high cAMP (isoproterenol) and with basal cAMP. Also, the duration of nonfiring is longest in HCN4FEA cells, indicating that in the absence of CDR activation curves cannot be sufficiently shifted to depolarised potentials and hence currents cannot be increased to a sufficiently high level to reduce or suppress nonfiring. Finally, our data indicate that basal cAMP levels actually might shift activation curves of WT channels to slightly more depolarised $V_{0.5}$ values as compared to the HCN4FEA mutant.

Our data show that shifts in $V_{0.5}$ parallel respective changes in time constants. Importantly, activation time constants of HCN4FEA channels expressed in HEK293 cells are in between the respective values obtained for WT channels in absence of cAMP and presence of saturating cAMP concentrations (order of activation time constants: WT w/o cAMP > HCN4FEA w/o cAMP = HCN4FEA cAMP > WT cAMP). Deactivation time constants of HCN4FEA are similar to WT under conditions without cAMP (order of deactivation time constants: WT w/o cAMP = HCN4FEA w/o cAMP = HCN4FEA cAMP < WT cAMP). Assuming simple Hodgkin-Huxley formalism for HCN4 channels, one would expect that the peaks of the kinetic-voltage-relationship follow the same order as respective $V_{0.5}$ values. Shifts of $V_{0.5}$ and peaks of the kinetic-voltage-relationship to more positive potentials together with faster activation and unchanged deactivation in the mutant increase availability of HCN4FEA channels as compared to WT channels without cAMP. However, in the presence of cAMP, the availability of HCN4FEA and the constitutive current is smaller as compared to WT HCN4 channels, because $V_{0.5}$ and the peak of the kinetic-voltage-relationship are less positive, the activation time constant is slower and the deactivation constant faster. Lower availability of the mutant versus the wild-type could lead to nonfiring more easily. While this explains how intermittent firing might arise more frequently in HCN4FEA compared to WT pacemaker cells, future experiments and modelling studies need to be performed to complement and confirm this.

In addition to mode-shifts and kinetic-related issues, other factors could contribute to intermittent firing. Possible explanations include slow oscillations of cAMP, which could directly change CDR and thereby the activity of HCN4. In addition, slow intracellular Ca^{2+} rhythms could stimulate Ca^{2+}-dependent K^+ channels, which then induce hyperpolarization and induce nonfiring in SAN pacemaker cells. At the same time, Ca^{2+} could activate Ca^{2+}-dependent adenylyl cyclases which in turn increase cAMP levels, activate CDR of HCN4 leading to an delayed increase in HCN4 activity which then effectively opposes the hyperpolarizing effect of K^+ channels and terminates the nonfiring cycle.

In the SAN network, pacemaker cells are electrically coupled via gap junctions. If a single SAN cell fires slower than the network rhythm, it is briefly depolarized during its slow diastolic depolarisation phase by action potentials fired in surrounding cells. This depolarization is caused by transient inter-cellular currents that pass through gap junctions and elicits an action potential in the slower cell to bring it back to the network rhythm. Vice versa, if a single pacemaker cell is faster than the SAN network rhythm it is slowed by neighbouring cells. These processes are known as mutual, phasic entrainment. By contrast, the interactions between nonfiring cells and firing cells last longer and are therefore assumed to be tonic (Fig. 10). We suggest the term tonic entrainment in order to specifically discuss the interaction between firing and nonfiring cells. The assumption is,

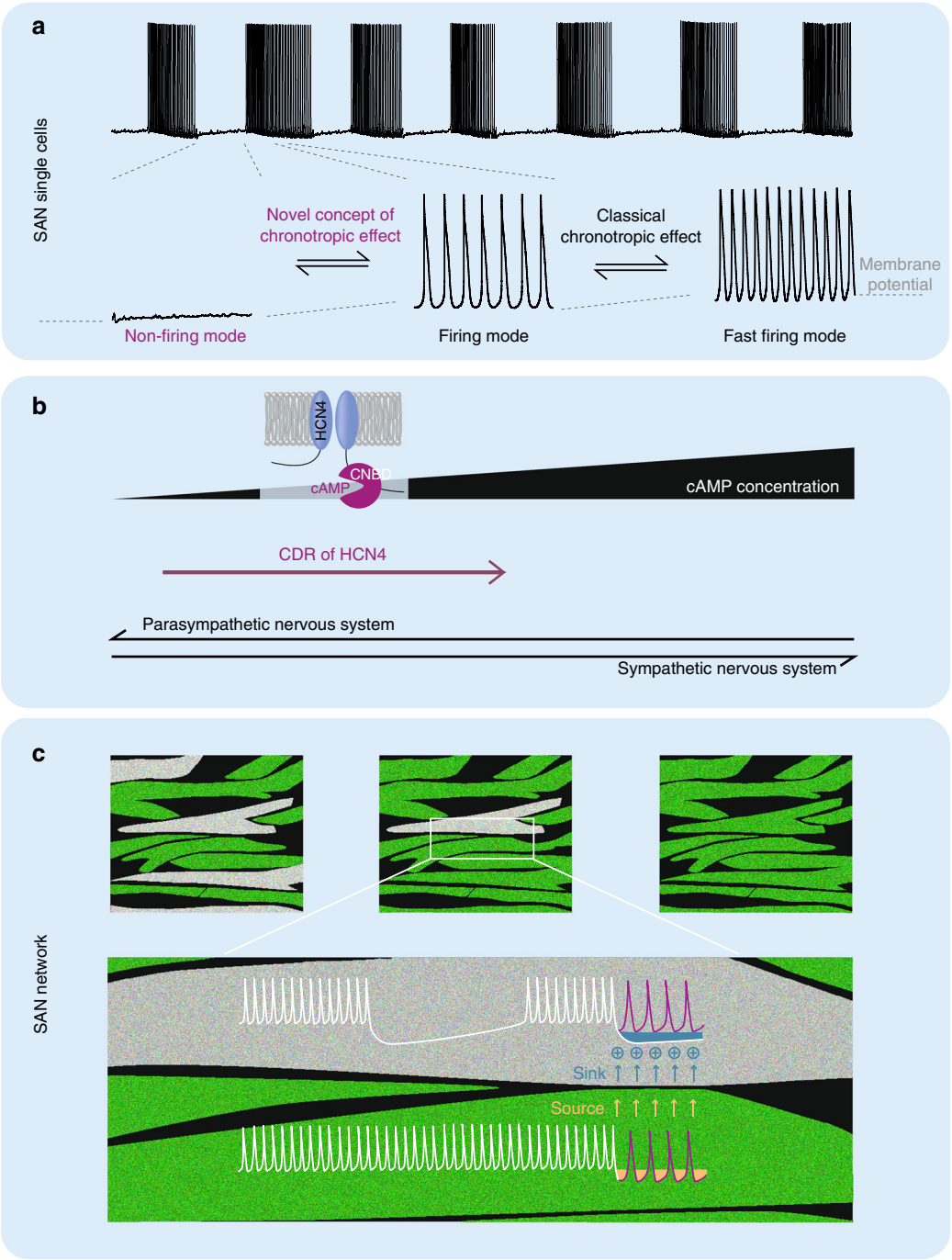

Fig. 10 CDR of HCN4 regulates the firing mode of SAN pacemaker cells. a (top) Alternating firing and nonfiring episodes in SAN pacemaker cells. During firing cells hyperpolarise and then depolarise during nonfiring. **a** (bottom) Expanded view of nonfiring, slowly firing, and fast firing modes from marked sequences. **b** Illustration of the HCN4 channel. Black ramp indicates cAMP concentration close to the cyclic nucleotide-binding domain (CNBD) which increases from left to right during sympathetic activity. Increased binding of cAMP to the CNBD of HCN4 channels successively switches the activity mode of pacemaker cells from nonfiring (left) to slow firing (middle). Increasing activity of the VN reduces cAMP levels and favours nonfiring. CDR of HCN4 antagonises the response to VN activity and acts synergistically with sympathetic nerve activity. **c** Tonic entrainment process in the SAN network. Pacemaker cells are connected via gap junctions. Nonfiring cells (gray) are more hyperpolarised and draw tonic currents from neighbouring firing cells, which slightly hyperpolarises neighbouring firing cells and depolarises nonfiring cells. Nonfiring cells either remain nonfiring or begin to fire slowly. We suggest that all nonfiring cells form a functional inhibitory cell pool that can be modulated by the ANS via CDR of HCN4. For further details see Discussion.

that whenever a pacemaker cell in the SAN network hyperpolarizes in order to enter the nonfiring mode this cell would electrotonically draw tonic flows of cations from more depolarised firing cells via gap junctions (Fig. 10c). As a consequence, firing cells would slightly hyperpolarize and fire more slowly and the nonfiring cell would slightly depolarize. Thus, a bradycardic network rhythm emerges, which is slower than the intrinsic firing rate of firing cells. Finally, the cation flow caused by the tonic entrainment process would redistribute Ca^{2+} ions towards nonfiring cells, giving rise to subthreshold Ca^{2+} activity. Our model predicts that in the WT SAN the balance between inhibition (nonfiring cells) and excitation (firing cells) is stabilised by CDR

of HCN4. In the absence of CDR, this balance is shifted towards inhibition. If too many cells are in the nonfiring mode, impulse formation and conduction is slowed down, and bradycardia and chronotropic incompetence arise. The presence of slow and fast-conducting SAN cells side by side induces a dispersion in conduction velocity and discontinuous conduction, contributing to fluctuations in firing rate and intrinsic sinus dysrhythmia. The tonic entrainment might be similar to interactions between atrial cells, which have a more hyperpolarized resting membrane potential than pacemaker cells, and SAN pacemaker cells at atrio-sinoatrial contact sites[20,39–42].

How does the tonic entrainment fit to the classical mechanism of the chronotropic effect? According to the classical view of the chronotropic effect, SAN pacemaker cells are continuously firing and the ANS induces the chronotropic response by modulation of the firing frequency (Fig. 10a; classical chronotropic effect). By considering nonfiring pacemaker cells in the SAN this model can be extended (Fig. 10a; novel concept of chronotropic effect). All cells that are nonfiring at a given moment contribute to an inhibitory pool of cells within the SAN, which is able to slow down firing in neighbouring firing cells by tonic entrainment. Activation of the vagal nerve increases the number of nonfiring cells and thereby also increases the impact of this inhibitory cell pool, whereas CDR of HCN4 can effectively counteract this effect. Increasing sympathetic activity gradually reduces the population of cells in the nonfiring mode (Fig. 10a; nonfiring to firing mode) and subsequently increases activity of firing cells (Fig. 10a; firing to fast firing mode). Thus, the role of CDR of HCN4 during activity of the sympathetic nervous system is to drive nonfiring cells to the firing mode. Furthermore, CDR sets the average HR, and shifts the position of the HR range to higher HR values. Reversely, in the absence of CDR, the average HR and the full HR range is shifted towards lower HR values (Fig. 3d). Furthermore, CDR opposes inappropriately enhanced responses to vagal activity, which tend to shift more firing cells into the nonfiring mode and thereby lead to severe bradycardia and sinus pauses. Finally, by adjusting the balance between firing and nonfiring cells CDR stabilizes the HR by reducing HR fluctuations. Together, the effects described above define novel roles of CDR of HCN4 within the framework of the chronotropic effect.

Our model also explains the shifts in the leading pacemaker region in response to activation of the ANS. The role of CDR is most pronounced in the head region of the SAN, where HCN4 expression is highest. In this region, the leading pacemaker is localised at baseline and during high activity of the sympathetic nervous system. Upon activation of the vagal nerve, cells in the head region of the SAN preferentially switch to nonfiring mode, slowing down firing. This effect is less pronounced in the more peripheral parts of the SAN and at the AV junction where HCN4 expression is lower. As a result, pacemaker cells close to the AV junction fire faster than cells in the head of the SAN and the leading pacemaker region shifts downwards towards the AV junction. In the absence of CDR, the response to vagal nerve activity is more pronounced and larger shifts occur.

In vivo and in vitro, vagal nerve activity leads to inadequately enhanced HR responses in HCN4FEA, indicating that in the absence of CDR of HCN4, the SAN is highly susceptible to perturbations induced by the ANS, giving rise to pronounced HR fluctuations, which clinically manifest as sinus dysrhythmia. Conversely, CDR of HCN4 is required to dampen and counteract HR-lowering vagal effects. These properties fit the role of HCN channels in stabilising and dampening transient changes in membrane potentials and firing rates of the SAN[1,20]. Together, our results indicate that while the tone and dynamic regulation of the ANS is unchanged (e.g. number of up and down sequences are equal and full ranges of spontaneous HRs and blood pressure regulation are preserved in telemetry), inadequately enhanced HR responses arise from an intrinsic change in responsiveness of the SAN caused by lack of HCN4 CDR.

Finally, the concerted response of the SAN and AVN during chronotropic response is disrupted in the absence of CDR. While the SAN is bradycardic and unable to accelerate the firing rate to the maximum values observed in wild-type in the absence of CDR (i.e. the SAN is chronotropically incompetent), the AVN is chronotropically competent, possibly due to lower expression of HCN4 and the presence of other mechanisms that independently accelerate firing of the AVN. In-line with this, HCN4 channel expression and I_f is lower and I_{Ca} is higher in AVN as compared to the SAN[11,21,43,44]. Therefore, I_{Ca} could provide an independent mechanism for accelerating the firing rate in the AVN. During sympathetic activation, the SAN firing rate frequently lags behind that of the AVN leading to escape phenomena, such as isorhythmic AV dissociation and junctional escape rhythm. When the AVN firing rate approaches and roughly matches that of the SAN, isorhythmic AV dissociation occurs. When the AVN firing rate exceeds that of the SAN, junctional escape rhythm occurs (Supplementary Fig. 4).

Sinus dysrhythmia and chronotropic incompetence are clinically highly relevant and well-known manifestations of the sick sinus syndrome in humans, which is connected to susceptibility to sudden cardiac arrest and sudden cardiac death. While mouse and human absolute HR values differ, the relative dynamic range of HR regulation and the underlying mechanisms are similar, corroborating the general relevance and validity of our findings for cardiac function and disease in human patients. We demonstrated that cells in the pacemaker region can stop firing for up to a minute, which is in stark contrast to intuitive knowledge that our heart is continuously beating. Furthermore, we showed that CDR regulates the concerted action on nonfiring and firing cells during the chronotropic response. The major overall benefit of regulating nonfiring cells is that heartbeat precision and the dynamic range of HR regulation are markedly elevated. In conclusion, CDR of HCN4 is essential for protecting the heart during destabilising and harmful activation of the ANS, but is not crucial for changing HR. Stable and precise HR control via ANS is of major clinical importance during development and progression of cardiovascular disease, including hypertension, heart failure, arrhythmias, and sudden cardiac death.

Methods

Ethics statement. All animal studies were approved by the Regierung von Oberbayern, were in accordance with German laws on animal experimentation, and were performed in compliance with widely accepted ethical standards. Effort was taken to keep the number of animals at a minimum.

Generation of the HCN4FEA mouse line. Using homologous recombination in ES cells we generated a global knockin mouse model (HCN4FEA) that expresses HCN4 channels with two amino acid substitutions in the cyclic nucleotide-binding domain (R669E, T670A) and one substitution in the C-linker (Y527F, Fig. 1e). The targeted HCN4 WT locus comprises exons 3-8. The C-linker mutation is located in exon 4 and both cyclic nucleotide-binding domain mutations are located in exon 7.

Animal studies. WT and HCN4FEA mice (*Hcn4*$^{tm3(Y527F;R669E;T670A)Biel}$) were obtained by in-house breeding and maintained on a mixed C57BL/6 N and 129/SvJ background. Breedings of one male and two female animals were kept in conventional Eurostandard Type III cages under SPF conditions in a 12 h dark-light-cycle environment with food and water ad libitum. Ambient temperature was 22 °C and humidity 60%. At P21 offspring were separated and group housed (2–5 animals/cage; Eurostandard Type II Long) under the same environmental conditions. Animals were kept for 2–6 months and littermates of the same sex were randomly assigned to experimental groups as indicated at the respective paragraph in the Method Details section.

Cell lines. HEK293 (human [*Homo sapiens*] embryonic kidney) cells were obtained from ATCC [https://www.atcc.org/] and cultured in Dulbecco´s Modified Eagle

Medium (DMEM, low glucose, GlutaMax™ Supplement, pyruvate) supplemented with 10% fetal bovine serum, 100 I.U. ml^{-1} penicillin, 100 µg ml^{-1} streptomycin, and 1.0 mg ml^{-1} G418. Flp-In™-293 (human [Homo sapiens] embryonic kidney) cells were obtained from Thermo Fisher Scientific and stable cell lines were generated using the Flp-In™ system from Invitrogen (Thermo Fisher Scientific, USA). Flp-In™-293 cells were cultured in DMEM (high glucose, GlutaMax™ Supplement, pyruvate) supplemented with 10% fetal bovine serum, 100 I.U. ml^{-1} penicillin, 100 µg ml^{-1} streptomycin, and 100 µg ml^{-1} hygromycin B. All cell lines were incubated at 37 °C with 10% CO_2.

RNA isolation, ChIP processing, and bioinformatics analysis. RNA from SAN of male WT and HCN4FEA mice ($n = 3$ each) was isolated using the RNeasy Micro Kit (Qiagen, Netherlands). Quality of RNA specimen was checked on an Agilent BioAnalyzer 2100 (Agilent Technologies, Germany) and processed for Affymetrix Gene Chips using Affymetrix whole transcript sense target labeling kit (Affymetrix, USA). Fragmented and labeled cDNA was hybridized onto murine MouseGene1.1-ST Gene Chips. Staining of biotinylated cDNA and scanning of arrays were performed according to the manufacturer's recommendations. Raw CEL-files were imported into Expression Console 1.0. RMA (Affymetrix, USA), which was used for array normalization and signal calculation. Normalized signal values were imported into Partek Genomics Suite 6.5. The probe sets were used to calculate differentially expressed transcripts using Welch's *t*-test with a *p* value cutoff of 0.05 and a fold-change of 1.5.

RNA isolation and quantitative RT-PCR. RNA from SAN of 3-month-old WT and HCN4FEA mice ($n = 3$ each) was isolated using the RNeasy Micro Kit (Qiagen, Netherlands). cDNA was synthetized with the RevertAid First Strand cDNA Synthesis Kit (Thermo Fisher Scientific, USA). RT-PCR was performed as described previously[9] and was repeated three times.

PyMOL. The figure of the C-terminus structure was prepared using PyMOL. The structure is based on sequence 521–723 of the human HCN4 structure in complex with cAMP[45], downloaded from the protein data base (accession code: 3U11).

Conventional electrophysiology in HEK293 cells. HEK293 cells transiently expressing WT HCN4 or mutated HCN4FEA channels were used for recordings. Currents were measured at room temperature (RT) using the whole-cell voltage-clamp technique with an Axon 200B amplifier and Clampex 10.5.2.6 software and analyzed with Clampfit 10.5.2.6 software. The extracellular solution was composed of 135 mM NaCl, 5 mM KCl, 1.8 mM $CaCl_2$, 0.5 mM $MgCl_2$, and 5 mM HEPES (pH adjusted to 7.4 with NaOH). The intracellular solution contained 130 mM KCl, 10 mM NaCl, 0.5 mM MgCl2, 1 mM EGTA, 5 mM HEPES, 3 mM MgATP, and 0.5 mM NaGTP (pH adjusted to 7.4 with KOH). 100 µM cAMP was added to the solution and the pH was readjusted. Steady-state activation curves were determined by hyperpolarizing voltage steps from −140 to −30 mV in 10 mV increments from a holding potential of −40 mV for 4.5 s (pulse interval of 20 s) followed by a step to −140 mV. To reflect more physiological conditions, steady-state activation curves were also measured at 30 °C from more hyperpolarised holding potentials (−55 mV, −65 mV, −75 mV) and voltage steps from −140 to 0 mV were applied in 10 mV increments for 5.0 s (pulse interval of 30 s) followed by a step to −140 mV for 0.5 s. Currents measured immediately after the final step to −140 mV were normalized to the maximum current (I_{max}) and plotted as a function of the preceding membrane potential. The data points were fitted with the Boltzmann function: $(I - I_{min})/(I_{max} - I_{min}) = (1 - \exp((V_m - V_{0.5})/k))$, where I_{min} is an offset caused by a nonzero holding current, V_m is the test potential, $V_{0.5}$ is the membrane potential for half-maximal activation, and k is the slope factor.

To determine activation and deactivation kinetics, WT HCN4, HCN4F, and HCN4FEA channels stably expressed in Flip-In™-293 cells were measured at RT using the whole-cell voltage-clamp technique. For determination of activation kinetics the same solutions as described above were used, whereas for determination of deactivation kinetics potassium concentration in the extracellular solution was increased to 30 mM by equimolar replacement of NaCl with KCl. For cAMP supplemented measurements 100 µM cAMP was added to the intracellular solution and the pH was readjusted. Activation and deactivation kinetics were determined after hyperpolarizing the cell to −140 mV for 3.75 s from a holding potential of −40 mV, with subsequent voltage steps back to −30 mV to −60 mV applied for 9 s. For activation kinetics current traces at potentials ranging from −140 mV to −110 mV and for deactivation kinetics current traces at −30 mV to −60 mV following maximal hyperpolarization were fit with a single exponential function ($I = I_{ss} + A \exp[-t/\tau]$) after an initial delay. I_{ss} represents the steady-state current, and τ represents the time constant. Linear leak current was subtracted.

Gelatine-inflated hearts. Gelatine-inflated hearts were prepared as described previously[1]. The mouse was anesthetized with 5% isoflurane (CP-Pharma, Germany) inhalation and sacrificed by cervical dislocation. The chest was opened and several incisions were made into the liver. The heart was perfused via the left ventricle with PBS until it was free from blood, followed by perfusion with warm 2% aqueous gelatine solution. Immediately, cold PBS was poured onto the gelatine-filled heart and the whole body was stored at 4 °C for 1 h to let the gelatine solidify. The heart was then carefully excised and transferred into a dish containing cold PBS to remove excess gelatine and tissue. Images were taken using a stereo-microscope (Stemi 508, Carl Zeiss AG, Germany) equipped with a color camera (AxioCam 512 color, Carl Zeiss AG, Germany) and ZenCore 5.3 software.

Echocardiography. Echocardiographic images were obtained using an ultrasound imaging system for rodents (Vevo 2100, FUJIFILM VisualSonics, Canada), utilizing the systems 22–55 MHz transducer (MS550D). Prior to the measurements, male mice were sedated by inhalation of isoflurane (Abbott, Germany). After achieving sedation, the animals were placed on the systems mouse handling table to monitor body temperature, heart rate, and respiratory rate. Long axis, M-Mode, and PW-Doppler images were taken and analyzed using the system software. During experiments and analysis, the investigators were blinded to genotype and experimental group. Animals were identified by earmarks.

HE staining. Hearts from 3-month-old male WT and HCN4FEA mice were removed, fixed in 4% paraformaldehyde for 2 h and incubated in sucrose at 4 °C overnight. Hearts were then embedded in optimum cutting temperature compound (Tissue Tek, Sakura Finetek, Germany) and cut into 12-µm thick sections using a cryostat. Sections were stained with hematoxylin and eosin according to standard protocols.

SAN cross section immunohistochemistry and fibrosis analysis. Three-month-old male animals were sacrificed and hearts were perfused with PBS as described in the gelatine-inflated hearts section. After PBS perfusion the hearts were excised and the SAN dissected. The tissue was fixed with 4% PFA in PBS for 25 min, washed with PBS and afterwards incubated for 2 h in 25% sucrose in PBS. The SAN was embedded in optimum cutting temperature compound (Tissue Tek, Sakura Finetek, Germany) and cut into 4-µm thick sections using a cryostat. Sections were permeabilized for 1–1.5 h with 0.5% Triton X-100 in 20% DMSO in PBS. After washing three times with PBS, blocking was achieved by 1 h incubation in 5% normal donkey serum in PBS. Another three washing steps were followed by overnight incubation at 4 °C with the guinea pig anti-HCN4 and rabbit anti-HCN1 antibodies (1:200 in PBS, Alomone labs, Israel). The slides were washed with PBS before incubation with the secondary antibodies (FITC-conjugated donkey anti-guinea pig, 1:100 and Cy3-conjugated donkey anti-rabbit, 1:400, Merck Millipore, Germany) for 4 h at RT under exclusion of light. Sections were washed, mounted with mounting medium (Vectashield, Vector Laboratories, UK) and analyzed using a Leica SP8 confocal microscope with ×10 magnification. In order to quantify protein distribution of HCN1 and HCN4 in the SAN, ImageJ software was used to analyse fluorescent areas. Thresholds for red fluorescence (HCN1) and green fluorescence (HCN4) were set to ranges that exclude unspecific background signal from surrounding SAN and atrial tissue. The same threshold ranges were used for all images. The remaining SAN area was measured and the ratio of HCN1/HCN4 area was calculated for head, body and tail regions. Consecutive cross sections of the same SAN were incubated overnight in Bouin´s solution, washed for 10 min under running tap water and subsequently stained for 20 min at RT with 0.1% Fast green solution. Slides were rinsed in 1 % acetic acid for 1 min followed by washing for 5 min in tap water. In a last staining step the cross sections were incubated for 30 min in 0.01% Sirius red solution. Finally, slides were dehydrated (70% ethanol, 10 s; 100% ethanol, 3 min; 100% xylole, 3 min) before mounting with Entellan (Merck KGaA, Germany). Images were taken with an Olympus BX41 microscope and cellSens 2.3 software using a ×10 objective. For quantification of red and green areas ImageJ software was used. To assess fibrosis levels, the percentage of red areas in the nodal region was calculated.

Western Blot. For protein isolation, mouse SAN, atrial, and left ventricular tissue from 3-month-old female WT and HCN4FEA mice was snap-frozen in liquid nitrogen. Samples were homogenized on dry ice using a mortar and pestle and suspended in homogenization buffer (2% sodium dodecyl sulfate, 50 mM Tris and proteinase inhibitor cocktail mix). After heating at 95 °C for 15 min followed by centrifugation at 1000 × *g* for 10 min to remove cell debris, the resulting supernatant was used in western blot analysis as previously described[38]. The following antibodies were used: mouse anti-HCN1 (1:1000; Abcam, UK), rat anti-HCN4 (1:500; Santa Cruz Biotechnology, USA), rabbit anti-HCN2 L (1:500[46]), and mouse anti-beta-tubulin (E7, 1:2000; Developmental Studies Hybridoma Bank, USA).

Isolation and electrophysiology of mouse SAN cells. Eight- to ten-week-old male WT and HCN4FEA mice were sacrificed by cervical dislocation under deep inhalation anaesthesia consisting of 5% isoflurane (CP-Pharma, Germany) in carbogen (5% O_2, 95% CO_2), and death was confirmed by subsequent decapitation. Beating hearts were quickly removed and transferred to warm (37 °C) Tyrode's solution (Tyrode III) containing: 140 mM NaCl, 5.4 mM KCl, 1 mM $MgCl_2$, 1.8 mM $CaCl_2$, 5 mM HEPES-NaOH (pH 7.4), and 5.5 mM D-glucose. The SAN region was excised and 2–3 incisions were made to increase the surface for optimized enzymatic digestion. The tissue was then transferred into a ´low-Ca^{2+}-low-Mg^{2+}´ (Tyrode low) solution containing: 140 mM NaCl, 5.4 mM KCl, 0.5 mM $MgCl_2$, 0.2 mM $CaCl_2$, 1.2 mM KH_2PO_4, 50 mM taurine, 5 mM HEPES-NaOH (pH 6.9), and 5.5 mM D-glucose. Digestion was carried out in a dry block heater

for 26–28 min (depending on tissue size) at 37 °C and 450 rpm after adding BSA (1 mg ml^{-1}, Merck KGaA, Germany), elastase (18.4 U ml^{-1}, Merck KGaA, Germany), collagenase B (0.3 U ml^{-1}, Roche Diagnostics, Germany), and protease (1.8 U ml^{-1}, Merck KGaA, Germany). Subsequently, the SAN was centrifuged at 200 × *g* for 2 min at 4 °C. The supernatant was discarded and following the same centrifugation protocol the tissue was washed twice with Tyrode low and twice with a modified ´Kraftbrühe´ (KB) medium containing: 80 mM L-glutamic acid, 25 mM KCl, 3 mM $MgCl_2$, 10 mM KH_2PO_4, 20 mM taurine, 10 mM HEPES-KOH (pH = 7.4), 0.5 mM EGTA, and 10 mM D-glucose. After 3–4 h recovery at 4 °C in 350 µl KB medium and further 15 min adaption to RT, SAN cells were mechanically separated by pipetting the tissue 4–8 times. Fifty microliter of cell suspension were placed on a poly-L-lysine coated coverslip in a vapour-saturated incubation chamber and for proper cell attachment sedimentation was allowed for 15 min. The coverslip was then transferred to the recording chamber and by adding Tyrode III cells were stepwise readapted to a physiological extracellular Ca^{2+} concentration. For current-clamp recording, cells were superfused with Tyrode III at 32 °C. For voltage-clamp experiments, cells were superfused with extracellular solution consisting of 140 mM NaCl, 5.4 mM KCl, 1 mM $MgCl_2$, 1 mM $CaCl_2$, 5 mM HEPES-NaOH (pH 7.4), 5 mM D-glucose, 0.3 mM $CdCl_2$, and 2 mM $BaCl_2$ at 32 °C. Pipettes were filled with intracellular solution containing: 90 mM potassium aspartate, 10 mM NaCl, 2.0 mM $MgCl_2$, 2.0 mM $CaCl_2$, 5.0 mM EGTA, 2.0 mM Na_2-ATP, 0.1 mM Na_2-GTP, and 5.0 mM creatine phosphate (pH 7.2). For measurements under saturating cAMP concentrations, 100 µM cAMP (Merck KGaA, Germany) was added to the solution and the pH was readjusted. Recording electrodes were fabricated using a WZ DMZ-Universal microelectrode puller (Zeitz-Instruments Vertriebs GmbH, Germany). We applied the whole-cell and perforated-patch variation of the patch-clamp technique as indicated at the respective experiments. For perforated-patch variation, amphotericin B (EDQM, France) was dissolved in DMSO and added to the pipette solution to obtain a final concentration of 200 µg ml^{-1}. Data were recorded using a HEKA EPC10 USB double patch-clamp amplifier (HEKA Elektronik, Germany) and Patchmaster v2x90.2 software. Data were analyzed using Fitmaster v2x90.2 software.

HCN steady-state activation curves were determined in whole-cell configuration by hyperpolarizing voltage steps from −150 to −40 mV in 10 mV increments from a holding potential of −40 mV for 4.5 s (pulse interval of 20 s) followed by a step to −150 mV for 500 ms. Linear leak current was subtracted. Activation kinetics were determined as follows. Current traces at −140 mV were fit with a double exponential function ($I = I_{ss} + A_1 \exp[-t/\tau_1]$ + $A_2 \exp[-t/\tau_2]$) after an initial delay. I_{ss} represents the steady-state current, and τ represents the time constant. The current density was calculated as the steady-state current amplitude at −140 mV divided by the cell capacitance. Linear leak current was subtracted. Time constants representing activation of HCN4 and HCN1 channels were determined from double exponential fits of I_f traces activated by a voltage step to −140 mV from a holding potential of −40 mV.

Calcium currents were recorded in sodium free extracellular solution consisting of 120 mM TEA-Cl, 25 mM HEPES, 10 mM 4-AP, 2 mM $CaCl_2$, 1 mM $MgCl_2$ (TEA-OH pH = 7.4) at 26 °C. Pipettes were filled with intracellular solution containing: 135 mM CsCl, 5 mM EGTA, 5 mM HEPES, 4 mM Mg-ATP, 1 mM $MgCl_2$, 0.1 mM Na-GTP (CsOH pH = 7.2). For measurements under saturating cAMP concentrations, 100 µM cAMP (Merck KGaA, Darmstadt, Germany) was added to the solution and the pH was readjusted. Current densities of $I_{Ca\text{-}T+L}$ and $I_{Ca\text{-}L}$ were determined at a test potential of −50 mV from a holding potential of −90 and −60 mV, respectively. For determination of $I_{Ca\text{-}T}$ the peak inward current of $I_{Ca\text{-}L}$ was subtracted from $I_{Ca\text{-}T+L}$.

Long-term current-clamp recordings of spontaneous firing activity were carried out in perforated-patch variation and gap-free recordings with a duration of at least 5 min were analyzed. Cells were categorized as "episodic firing" when they displayed continuous periods of at least 10 seconds without spontaneous action potential firing, during which the membrane potential remained at physiological values (average MDP ±10 mV). Cells that displayed no such periods were categorized as "permanent firing". Upon occurrence of an episodic firing pattern the difference in membrane potential between onset and termination of nonfiring episodes was determined (ΔVm). In order to quantify the incidence of the nonfiring mode the percentage of cells displaying the different firing patterns was calculated. The total duration of nonfiring episodes was assessed and expressed as the percentage of time spent in the nonfiring mode. The shortest nonfiring episode included in the statistics was 3.5 s. For the purpose of studying I_f current density and the percentage of permanently and episodically firing SAN cells expressing I_f, spontaneous firing activity was recorded in perforated-patch variation for 15 min during superfusion with Tyrode III at 32 °C. Subsequently, Tyrode III was replaced with extracellular solution containing $CdCl_2$ and $BaCl_2$, and voltage-clamp experiments were carried out at 32 °C as described before. Dose-response curves for carbachol were determined as follows. Using the perforated-patch variation, the basal firing rate of spontaneously active SAN cells was measured for 1 min during superfusion with Tyrode III solution. Subsequently, the perfusion was switched to Tyrode III containing carbachol (Merck KGaA, Germany) and the concentration was increased stepwise to 10 nM, 100 nM, and 1 µM, followed by washout with Tyrode III. Only cells that regained rhythmic firing upon washout were included in the analysis (data not shown). Each concentration was administered for a duration of 150 s and cumulative dose-response curves were plotted as the firing rate against the respective concentration of carbachol. To study the effect of isoproterenol, the spontaneous firing activity of SAN cells was first recorded in drug-free Tyrode III solution for 150 s. Afterwards, isoproterenol (100 nM) was washed in and action potentials were recorded for 5 further min. The effect of TAT-TRIP8b$_{nano}$ was determined as follows. WT cells were treated with Tyrode III containing 10 µM TAT-TRIP8b$_{nano}$[28] at RT for 30 min prior to experiments. Following incubation, current-clamp measurements were carried out in perforated-patch variation during superfusion with peptide-free Tyrode III solution within a timeframe of 60 min. During data analysis, the investigators were blinded to genotype. Animals were identified by earmark numbers.

Telemetric ECG recordings. Litter-matched 5–6-month-old male WT and HCN4FEA mice were anaesthetized (i.p.; 20 mg kg^{-1} xylazine; 100 mg kg^{-1} ketamine) and radiotelemetric ECG transmitters (ETA-F10, Data Sciences International, USA) were implanted into the intraperitoneal cavity. The ECG leads were sutured subcutaneously onto the upper right chest muscle and the upper left abdominal wall muscle, approximately representing ECG lead II. Carprofen (i.p.; 5 mg kg^{-1}; twice daily for 5 days) was given for postsurgical analgesia. The animals were allowed to recover for at least 14 days before measurements were performed. Analog telemetric signals were digitized at 1 kHz and recorded by Dataquest A.R.T. data acquisition software (Data Sciences International, USA). Data were sampled over the whole period of the recording in freely moving animals. For pharmacological interventions drugs were injected intraperitoneally after 2 h prerun. Thereafter, ECGs were recorded for 3–24 h. The animals were allowed to recover for at least 48 h between injections. The following drug concentrations were used in [mg kg^{-1}]: propranolol: 20; atropine: 1. Data analysts of all in vivo experiments including ECG data were not blinded to genotype because of obvious differences in the ECG traces of WT compared to HCN4FEA animals.

Combined telemetric ECG and blood pressure recordings. Litter-matched 4-month-old male WT and HCN4FEA mice were anaesthetized (i.p.; 15 mg kg^{-1} xylazine; 100 mg kg^{-1} ketamine; 1 mg kg^{-1} acepromazine). Combined radiotelemetric ECG and blood pressure transmitters (HD-X11, Data Sciences International, USA) were implanted. Briefly, the pressure sensor was introduced into the aortic arch via the left common carotid artery. The ECG leads were sutured subcutaneously onto the upper right chest muscle and the upper left abdominal wall muscle, approximately representing ECG lead II and the transmitter core unit was placed subcutaneously at the left flank. Carprofen (i.p.; 5 mg kg^{-1}; twice daily for 5 days) was given for postsurgical analgesia. The animals were allowed to recover for at least 14 days before measurements were performed. Data analysts of all in vivo experiments including ECG data were not blinded to genotype because of obvious differences in the ECG traces of WT compared to HCN4FEA animals.

Analysis of heart rate and heart rate variability (HRV). ECG and HRV analysis was performed using ecgAUTO v3.3.5.10 software (EMKA technologies, France). Mean, minimum, and maximum heart rates were determined from continuous recordings over 72 h, 12 h dark cycle, and 12 h light cycle, respectively. To determine differences in HR dynamics, HR histograms were obtained from 72 h intervals by calculating mean heart rate values every 10 s. Heart rate values were binned using 50 equal distributed windows in the range from 150 to 950 bpm. HRV was determined using an analysis based on previous reports[1]. Briefly, for frequency domain analysis, raw ECG strips from low activity phase were manually inspected to confirm stable sinus rhythm. 103 s time series of RR intervals were plotted as tachograms. These tachograms were interpolated by third-degree spline interpolation at 50 ms intervals to create equidistant points suitable for Fast Fourier Transform (FFT). After detrending, FFT was performed using 1024 spectral points and multiplying with three half overlapping Hamming windows and power spectral density plots were determined. For each time segment, the total power (TP) was calculated as the integral sum of total variability after FFT over the frequency range recorded (0–4.0 Hz). In addition, for each time segment, the cutoff frequencies previously determined to be accurate for mice were used to divide signals into three major components, very low frequency (VLF: 0.0–0.4 Hz), low frequency (LF: 0.4–1.5 Hz), and high frequency (HF: 1.5–4.0 Hz). The data obtained for each time segment were averaged. For time domain analysis, 2 h of ECG recordings were recorded during low activity period. Standard deviation (SD) of all normal RR intervals in sinus rhythm (SDNN) and the square root of mean of squared differences between successive normal RR intervals (RMSSD) were calculated from three representative 10 minute intervals. In addition, 20,000 data points from the cleaned RR time series were used for Poincaré Plots. Here, RR intervals (n; *x*-axis) were plotted against the next RR interval (n + 1; *y*-axis).

Analysis of interaction between vagal activity, HR, and BP. The beat-to-beat series of systolic BP (SBP) and RR interval during low activity phase was screened using ecgAUTO v3.3.5.10 software (EMKA technologies, France) for spontaneous sequences of increases (up sequences) or decreases (down sequences) in SBP associated with parallel changes in RR interval[35]. The length of the sequences included in the analysis was three consecutive beats. The duration of three consecutive beats (~0.3–1.2 s) is short in comparison with the sympathetic drive, which is characterised by very slow fluctuations in the range of 2–10 s[36]. Therefore, sympathetic drive can be assumed constant during the time window of observation.

In contrast, changes in vagal drive are in the millisecond range (200–650 ms)[36,37]; therefore, changes in the RR interval during a sequence are almost entirely related to changes in vagal activity[34,36,37]. The delay between systolic BP and RR was 1 beat, the threshold for BP and RR changes was 0.5 mmHg and 2 ms, respectively, and the slope of the regression line from RR/SBP plots had a correlation coefficient >0.85. Sections of ECG traces exhibiting isorhythmic atrioventricular dissociation in HCN4FEA ECG recordings were excluded to avoid misinterpretation of a BP decrease due to arrhythmia.

Intracardiac electrophysiological study. Litter-matched 2–3-month-old male WT and HCN4FEA mice were anesthetized with isoflurane and standard intervals were measured in 6-limb leads. For intracardiac electrogram recordings we used a digital electrophysiology lab (EP Tracer, CardioTek, Netherlands). The surgical area was locally anaesthetized by subcutaneous injection of xylocaine (1.7 mM kg^{-1}). An octapolar 0.54 mm (1.7 French) electrode catheter (CIBer mouse cath, NuMed Inc., USA) was placed via the right jugular vein into the right atrium and ventricle, guided by the morphology of intracardiac electrical signals. The eight electrodes directly contact the endocardial surface of the heart. Bipolar recordings of the atrial and ventricular depolarizations were obtained from adjacent electrodes in the superior right atrium just past the superior vena cava and right ventricular apex, respectively. Standard clinical electrophysiological pacing protocols were used to determine electrophysiological parameters including sinus node recovery time (SNRT), sinoatrial conduction time (SACT), sinoatrial node effective refractory period (SNERP), refractory periods of the atria, the AV node, and the ventricle as well as AV-nodal conduction properties including Wenckebach periodicity (WBP)[20]. Impulses were delivered at twice diastolic threshold (1 mA) using a pulse duration of 1.0 ms. Each mouse underwent an identical pacing and programmed stimulation protocol. The sinus node function was evaluated by indirect measurement of SNRT by pacing for 30 s at various cycle lengths, starting from a pacing cycle length just below the intrinsic sinus cycle length and measuring the duration of the return cycle, which corresponds to the interval between the last stimulation spike and first spontaneous, sinus node triggered atrial activation. After a pause of 60 s the protocol was repeated by progressively reducing the pacing cycle length in 10 ms steps until a pacing cycle length of 80 ms was reached. Rate corrected SNRT (cSNRT) was calculated by subtracting the averaged sinus cycle length (SCL) from SNRT. SACT was indirectly determined by premature atrial stimulation technique, which was carried out as described[20]. The responses are shown in Supplementary Fig. 1b, c. Premature atrial stimuli were introduced via the stimulation electrode during spontaneous sinus rhythm. The entire sinus cycle was scanned by up to 80 extra stimuli. Spontaneous sinus cycle length (A1A1 interval), coupling interval of the premature atrial stimulus (A1A2), the atrial return cycle length (A2A3) and the postreturn cycle length (A3A4) were measured. Supplementary Fig. 1b illustrates the response of the SAN to premature atrial stimulation. Upon progressively decreasing the coupling interval of the premature atrial stimulus (A1A2), the return cycles A2A3 progressively prolongs. The corresponding A2A3 data points fall on the upper diagonal line indicating fully compensatory pauses [A1A2 + A2A3 = 2(A1A1)]. The pause is compensatory because late diastolic atrial depolarizations do not penetrate and reset the SAN before it fires spontaneously. As soon as the coupling interval A1A2 is decreased below a certain point of the spontaneous cycle length, the return cycles A2A3 is no longer fully compensatory. The data points fall below the line of full compensatory pause but remain greater than one expected sinus cycle length (A1A1; horizontal line). In some animals during this phase A2A3s remained constant yielding a plateau. A1A2 plus A2A3 is shorter than twice the A1A1 interval because the premature atrial depolarization penetrates, depolarizes and resets the SAN prior to its next expected spontaneous firing. The postreturn cycle A3A4, which is the first spontaneous cycle after the return cycle, was also plotted (closed circles). By comparing A3A4 with A1A1 intervals it is possible to assess the sinus cycle variability and SAN automaticity. For calculation of SACT we determined the A2A3 interval, which deviates from the diagonal line. The A1A2 interval at this point represents the shortest premature beat interval whose retrograde excitation front does not reach the sinus node, whereas earlier premature beats reset the pacemaker[20]. The return interval A2A3 at this point, minus the spontaneous atrial cycle A1A1, is equivalent to the sum of conduction time from atrium to the sinus node plus from sinus node to atrium. Half of the total sum of conduction time gives the sinoatrial conduction time. This calculation is based on the assumptions that SACT reflects the time for the paced impulse A1 to enter the SAN, which is then reset plus the spontaneous sinoatrial cycle lengths plus the time it takes for the subsequent spontaneous beat to exit the SAN, and that the times into and out of the SAN are approximately equivalent. Atrioventricular nodal refractory period (AVNERP) was evaluated by programmed atrial stimulation. To allow for reasonable stabilization of refractoriness the premature atrial stimulus (S2) was preceded by a train of 8 paced beats (S1). The train of 8 stimuli was applied at a S1S1 cycle length of 100 ms followed by one extrastimulus (S2). The coupling interval S1S2 was stepwise reduced in 2 ms steps to 20 ms. Subsequently, the protocol was repeated after a recovery time of 30 s using S1S1 cycle length of 90 ms and 80 ms. AVNERP was defined as the longest S1S2 pacing interval with loss of AV-nodal conduction. The minimum cycle length required to maintain 1:1 AV conduction, the Wenckebach paced cycle length, and the maximum paced cycle length causing 2:1 AV block were determined for each animal. The ventricular effective refractory period (VERP) was evaluated analogously to AVNERP. The S1S1 intervals were 100, 90, and 80 ms. The coupling interval S1S2 was stepwise reduced in 2 ms steps to 30 ms. Using a similar protocol, the right atrial effective refractory period (AERP) could not reliably be determined due to superposition of atrial and ventricular electrograms at premature coupling intervals below 40 ms. To circumvent this problem the following three-step protocol was used: After applying a train of 8 S1 stimuli, an extrastimulus (S2) was given to induce AV conduction block at an S1S2 coupling interval 5 ms shorter than the determined AVNERP, followed by an increasingly premature S3. AERP was determined as longest S2S3 with absent atrial response. AV conduction curves were determined from data obtained by the AVERP protocol described above by plotting V1V2 or H1H2 intervals versus A1A2. Latency curves were constructed by plotting A2V2 intervals versus A1A2 intervals as in ref. [20]. Supplementary Fig. 1d shows the responses to premature stimulation in a single experiment. As atrial responses occurred progressively earlier in the cardiac cycle, ventricular intervals also progressively decreased. Up to a coupling interval of approximately 85 ms, the decrease of V1V2 is proportional to that of A1A2 and therefore the points fall on the line, which represents the theoretical curve of no AV conduction delay. For points on this curve V1V2 is equal to A1A2. At shorter A1A2 intervals, V1V2 decrease less than A1A2. The points lie above the line, indicating that AV conduction of the premature impulse A2 is delayed. The point at which the points start to deviate from the line marks the beginning of the relative refractory period of the AV conduction system. At a critical A1A2 interval V1V2 reaches a minimum and then begins to increase, even though the atrial interval shortened further until complete block of conduction of the premature impulse occurred. From this graph, the functional refractory period of the AV conduction system was determined as the shortest V1V2 interval. We also plotted the intervals between His bundle responses (H1H2 intervals) and premature atrial stimulations (A1A2) for the same experiment. The H1H2 intervals correspond exactly to the V1V2 values indicating that the increase in AV conduction time occurring with premature atrial stimulation was confined entirely to the region of the AV node, i.e. between the atrial and His bundle electrogram. Finally, A2V2 latencies were plotted versus A1A2 intervals. As A1A2 intervals decreases, the A2V2 latency increases (Supplementary Fig. 1f). The A2V2 lengthening is slight for relatively long A1A2 intervals and becomes larger as these intervals shorten. The diagonal line indicates A2V2 lengthening equal to the A1A2 shortenings (slope = -1).

Langendorff hearts. Ten-week-old female WT and HCN4FEA mice were anesthetized using 5% isoflurane in Carbogen (95% O_2, 5% CO_2) and sacrificed by cervical dislocation. After decapitation, the heart was carefully excised and placed in oxygenated, warm (37°C) Krebs Henseleit buffer containing 118.5 mM NaCl, 20 mM $NaHCO_3$, 4.7 mM KCl, 1.2 mM $MgSO_4$, 1.8 mM $CaCl_2$, 1.2 mM $KH2PO_4$ and 11 mM glucose (pH = 7.3). Immediately, the aorta was cannulated, mounted on a Langendorff apparatus (Basic Langendorff System, Hugo Sachs Elektronik & Harvard Apparatus GmbH, Germany) and retrogradely perfused with Krebs Henseleit buffer at a constant pressure of 80 mmHg. ECGs were recorded (PowerLab 8/35, LabChart 8, Animal Bio Amp, ADInstruments, New Zealand) by placing electrodes on the right atrium and left ventricle. The hearts were equilibrated for ~10 min prior to measurement. Mean basal HR and HRV parameters were determined from 120 s RR tachograms. Right heart catheterization of Langendorff hearts was performed as follows. Three-month-old male WT and HCN4FEA mice were injected intraperitoneally with heparin (100 IU kg^{-1}). Ten-minutes post-injection mice were anesthetized and Langendorff hearts were prepared as described above. For intracardiac electrogram recordings we used a digital electrophysiology lab (EP Tracer, CardioTek, Netherlands). An octapolar 0.54 mm (1.7 French) electrode catheter (CIBer mouse cath, NuMed Inc., USA) was placed via the right jugular vein into the right atrium and ventricle. The mounted hearts were equilibrated before starting the measurements. 100 µl of 200 nM isoproterenol in KH buffer was applied via an injection port within a few seconds to induce IAVD. For recording and analysis LabChart8 (ADInstruments, New Zealand) and EP-Tracer_V1.05 software (Schwarzer Cardiotek, Germany) were used. Vagal nerve stimulation in Langendorff-perfused hearts was performed as follows. Three-month-old female WT and HCN4FEA mice were injected intraperitoneally with heparin (100 IU kg^{-1}). Ten-minutes post-injection mice were anesthetized with 5% isoflurane and sacrificed by cervical dislocation. A small incision on the right side of the neck gave access to the vagal nerve and a silk suture was tied around the nerve. The hearts combined with the intact vagal nerve were then carefully removed and mounted on the Langendorff apparatus as described before. For nerve stimulation a custom-made Ag/AgCl electrode was used. A pulse width of 1 ms at 4 V was applied for 30 s using the stimulation frequencies 3, 5, 10, 20, and 30 Hz. Between each stimulation a recovery period of 2 min was inserted. For recording and analysis LabChart8 software (ADInstruments, New Zealand) was used. Calculations were done with Origin 2015. A sinus pause was defined as two consecutive beats with an RR interval >two times higher than the mean RR during stimulation. During data analysis, the investigators were blinded to genotype. Animals were identified by earmark numbers.

Optical imaging. Langendorff-heart preparations of 3-month-old female mice were used for optical imaging and performed as described above, with the following alterations. Briefly, the mice were injected intraperitoneally with heparin (100 IU kg^{-1}). Ten-minutes post-injection mice were sacrificed as described above and the explanted hearts were placed in warm (37 °C) Tyrode solution oxygenated with

95% O_2 5% CO_2, and immediately cannulated. The Tyrode solution contained (in mM) 128.2 NaCl, 4.7 KCl, 1.19 NaH_2PO_4, 1.05 $MgCl_2$, 1.3 $CaCl_2$, 20.0 $NaHCO_3$, 11.1 glucose; pH = 7.35[47]. The lung, thymus and fat tissue were dissected and removed. The cannula was mounted to a custom-made Langendorff apparatus and the heart was retrogradely perfused and superfused with Tyrode solution passed through a 10 µm filter. Perfusion pressure in the cannula was monitored with the use of a pressure transducer (MLT0699, ADInstruments, New Zealand) and held at a constant pressure of 80 mm Hg as previously described[48]. ECG traces were recorded (PowerLab 8/35, LabChart 8, Animal Bio Amp, ADInstruments, New Zealand) by placing needle electrodes close to the isolated heart in an approximate Einthoven I configuration. To eliminate motion artifacts, 1 ml of blebbistatin (Cayman Chemical Company, USA), dissolved in DMSO (10 mg ml^{-1}) and diluted in Tyrode solution to obtain a final concentration of 0.2 mg ml^{-1}, was injected slowly through a drug port located close to the perfusion cannula. After equilibrating for 10 min, 1 ml of Di-4-ANEPPS (Merck KGaA, Germany), dissolved in DMSO (1.25 mg ml^{-1}) and diluted in Tyrode solution to obtain a final concentration of 37.5 µg ml^{-1}, was applied via the same port. After an equilibration time of 15 min Langendorff hearts were mounted. A high-speed complementary metal-oxide-semiconductor (CMOS) camera (MiCAM05 Ultima-L Single Camera System, SciMedia, USA) faced the posterior side of the heart, which allowed for a clear view of the ventricles, the SAN and both atria. The optical apparatus consisted of an excitation light generated by a 150 W halogen light source (MHAB-150W, Mortitex, Japan), a band-pass filter of 531/40 nm and a fluorescence beam splitting system (THT-FLSP Box, SciMedia, USA). The emitted light was filtered by a 600 nm long-pass filter. The acquired fluorescent signals were collected per pixel and digitalized by the manufacturer´s software (MiCAM05 data acquisition software Ver. 2.5.4, Brainvision Inc., Japan). The following settings were used for optical imaging; a sampling rate of 2 kHz, a frame number of 4096, a spatial resolution of approximately 100 µm/pixel (obtained through a condenser lens (50 mm, M5095 + AD, SciMedia) and a 1.6x objective lense (Planapo, SciMedia, USA). Background fluorescence of optical data was automatically removed and the signals were inverted to correspond with action potentials. The manufacturer´s analysis software (BV_Ana Ver. 1604, Brainvision Inc., Japan) as well as a MATLAB-based graphical user interface (ref. [49], RHYTHM 2012) were used for data processing. Isochronal activation maps were built to visualize the first activation site, and action potential propagation through the tissue during sinus rhythm, junctional escape rhythm and IAVD in HCN4FEA mouse hearts.

Optical imaging of biatrial SAN preparations followed the same procedure as described above for Langendorff-heart preparations, with the following modification. Briefly, biatrial preparations of 12-week-old female mice were optically mapped under basal conditions and after application of carbachol. After cannulation and perfusion of the heart, the SAN was dissected together with the right and left atrium, the superior caval vein, the inferior caval vein, the AV junction and was pinned to expose the endocardial surface as described previously[50]. The SAN explant was continuously superfused with Tyrode solution (37 °C). Electrical recordings were performed using three needle electrodes to calculate the beating rate and HRV parameters. To perform optical imaging recordings, the same concentration of blebbistatin (Cayman Chemical Company, USA) and Di-4-ANEPPS (Merck KGaA, Germany) were used as described above. Blebbistatin was directly applied to the preparation followed by Di-4-ANEPPS after an interval of 10 min. After 15 min of equilibration the SAN preparation was optically mapped. The location of the leading pacemaker site and SACT were determined[47,51]. After basal measurements carbachol (Merck KGaA, Germany) (1 µM in Tyrode solution) was delivered through the perfusion system for 5–7 min until it reached steady state. The location of the maximum shift of the leading pacemaker was identified and the distance to the leading pacemaker site under basal conditions was calculated and normalized to the size of the preparation.

Biatrial preparations containing the intact right vagal nerve were prepared as the preparations described above, except that the right vagal nerve was preserved. The vagal nerve was stimulated at 4 V, 1 ms pulse width, 20 Hz for 30 s[52]. The location of the leading pacemaker site was identified as described above.

Confocal calcium imaging of SAN explants. Intact SAN preparations of 12-week-old female WT and HCN4FEA animals were prepared as described above and loaded with the Calcium indicator Fluo-4 AM (Thermo Fisher Scientific, USA) at RT for 45 min. To this end, Fluo-4 AM was dissolved in DMSO (2 mM), diluted 1:1 with Pluronic F 127 (13% in H_2O) (Merck KGaA, Germany) and added to Tyrode solution to reach an end concentration of 20 µM Fluo-4 AM. Afterwards, the preparations were continuously superfused with Tyrode solution containing blebbistatin (0.2 mg ml^{-1}) at 28 °C. Calcium signals from the head, body, and tail region of the SAN were recorded using a Leica SP8 confocal microscope with a 20x water lens objective. Each frame (440 $µm^2$) was recorded for 10 s with an optically pumped semiconductor laser (OPSL) in-line scan configuration (8 Hz scan speed, 28 frames/s). An excitation wavelength of 488 nm was used and emission was collected >500 nm. Cells displaying highly localized and spontaneous Ca^{2+} release during diastole were counted and normalized to the total surface area measured. Image analysis was performed using Leica LasX software. The change in fluorescence intensity (ΔF) was assessed after background subtraction and normalized to baseline fluorescence F_0. After basal measurements, TAT-TRIP8b_{nano} (15 µM in Tyrode solution) was added to 4 of the WT preparations and after 30 min incubation, tissue samples were scanned as described above.

Primer list. HCN1 for: CTGCTGCAGGACTTCCCACCA, HCN1 rev: ATGCTGACAGGGGCTTGGGC, HCN2 for: CAGGAACGCGTGAAGTCGGCG, HCN2 rev: TCCAGGGCGCGGTGGTCTCG, HCN3 for: TGGCCATGGACCGGCTTCGG, HCN3 rev: GAGCCAGGCCCCGAACACCAC, HCN4 for: AGGGCCTTCGAGACGGTTGCGC, HCN4 rev: GGCCATCTCACGGTCATGCCG, ALAS for: TCGCCGATGCCCATTCTTATC, ALAS rev: GGCCCCAACTTCCATCATCT.

Quantification and statistical analysis. Statistical analysis was performed using Origin 2015 (OriginLab Corporation, USA). All data are given as mean ± SEM. N represents the number of animals, preparations or cells as indicated in the Supplementary Data files. For all statistical tests $p < 0.05$ was considered significant (***$p < 0.001$, **$p < 0.005$, *$p < 0.05$, ns = not statistically significant $p > 0.05$). Differences between two groups were analysed by Student's unpaired two-sample *t*-test. The *p* values were adjusted using the Holm–Bonferroni correction as indicated in the Supplementary Data files. Experiments with two different variables were analysed with two-way ANOVA. When significant, the analysis was followed by Holm–Sidak multiple comparison test. For EPS parameters that were determined at different coupling intervals data were analysed by two-way repeated measures ANOVA based on general linear model (GLM) or mixed-effect model (REML) in case of missing data due to technical problems. For the experiment in which HCN channel activation and deactivation time constants were determined at different test potentials in HEK293 cells, the data were analysed by three-way ANOVA since the measurements include three independent factors. These factors are (1) Genotype (WT and HCN4FEA), (2) Drug (without and with cAMP), and (3) Potential (several test potentials and repeated measurements within the same specimens). Three-way ANOVA tests the interdependencies of the three factors while taking repeated measurements into account. For data, which do not follow normal distribution or for experiments with low n numbers ($n = 3$) we applied the nonparametric Mann–Whitney U test.

Reporting summary. Further information on research design is available in the Nature Research Reporting Summary linked to this article.

Data availability

The Microarray dataset generated and analysed during the current study is available in the National Center for Biotechnology Information Gene Expression Omnibus (GEO) repository and is accessible through the GEO Series accession number GSE138086. Any other datasets generated during and/or analysed during the current study are available from the corresponding author upon reasonable request. Source data are provided with this paper.

Code availability

A MATLAB-based graphical user interface (RHYTHM 2012) was used for optical imaging data processing. The current version can be downloaded on Github using this link: [https://github.com/rrasheed/rhythm-analysis-software].

Received: 11 September 2019; Accepted: 8 October 2020;
Published online: 03 November 2020

References

1. Fenske, S. et al. Comprehensive multilevel in vivo and in vitro analysis of heart rate fluctuations in mice by ECG telemetry and electrophysiology. *Nat. Protoc.* **11**, 61–86 (2016).
2. Jalife, J. Mutual entrainment and electrical coupling as mechanisms for synchronous firing of rabbit sino-atrial pace-maker cells. *J. Physiol.* **356**, 221–243 (1984).
3. Anumonwo, J. M., Delmar, M., Vinet, A., Michaels, D. C. & Jalife, J. Phase resetting and entrainment of pacemaker activity in single sinus nodal cells. *Circ. Res.* **68**, 1138–1153 (1991).
4. Michaels, D. C., Matyas, E. P. & Jalife, J. Dynamic interactions and mutual synchronization of sinoatrial node pacemaker cells. A mathematical model. *Circ. Res.* **58**, 706–720 (1986).
5. Mangoni, M. E. & Nargeot, J. Genesis and regulation of the heart automaticity. *Physiol. Rev.* **88**, 919–982 (2008).
6. Biel, M., Wahl-Schott, C., Michalakis, S. & Zong, X. Hyperpolarization-activated cation channels: from genes to function. *Physiol. Rev.* **89**, 847–885 (2009).
7. Zagotta, W. N. et al. Structural basis for modulation and agonist specificity of HCN pacemaker channels. *Nature* **425**, 200–205 (2003).

8. DiFrancesco, D. & Tortora, P. Direct activation of cardiac pacemaker channels by intracellular cyclic AMP. *Nature* **351**, 145–147 (1991).
9. Herrmann, S., Layh, B. & Ludwig, A. Novel insights into the distribution of cardiac HCN channels: an expression study in the mouse heart. *J. Mol. Cell Cardiol.* **51**, 997–1006 (2011).
10. Harzheim, D. et al. Cardiac pacemaker function of HCN4 channels in mice is confined to embryonic development and requires cyclic AMP. *EMBO J.* **27**, 692–703 (2008).
11. Baruscotti, M. et al. Deep bradycardia and heart block caused by inducible cardiac-specific knockout of the pacemaker channel gene Hcn4. *Proc. Natl Acad. Sci. USA* **108**, 1705–1710 (2011).
12. Herrmann, S., Stieber, J., Stockl, G., Hofmann, F. & Ludwig, A. HCN4 provides a 'depolarization reserve' and is not required for heart rate acceleration in mice. *EMBO J.* **26**, 4423–4432 (2007).
13. Verkerk, A. O. & Wilders, R. Pacemaker activity of the human sinoatrial node: effects of HCN4 mutations on the hyperpolarization-activated current. *Europace* **16**, 384–395 (2014).
14. Verkerk, A. O. & Wilders, R. Pacemaker activity of the human sinoatrial node: an update on the effects of mutations in HCN4 on the hyperpolarization-activated current. *Int. J. Mol. Sci.* **16**, 3071–3094 (2015).
15. Schulze-Bahr, E. et al. Pacemaker channel dysfunction in a patient with sinus node disease. *J. Clin. Invest.* **111**, 1537–1545 (2003).
16. Schweizer, P. A. et al. cAMP sensitivity of HCN pacemaker channels determines basal heart rate but is not critical for autonomic rate control. *Circ. Arrhythm. Electrophysiol.* **3**, 542–552 (2010).
17. Mesirca, P. et al. The G-protein-gated K+ channel, IKACh, is required for regulation of pacemaker activity and recovery of resting heart rate after sympathetic stimulation. *J. Gen. Physiol.* **142**, 113–126 (2013).
18. Cifelli, C. et al. RGS4 regulates parasympathetic signaling and heart rate control in the sinoatrial node. *Circ. Res.* **103**, 527–535 (2008).
19. Yang, J. et al. RGS6, a modulator of parasympathetic activation in heart. *Circ. Res.* **107**, 1345–1349 (2010).
20. Fenske, S. et al. Sick sinus syndrome in HCN1-deficient mice. *Circulation* **128**, 2585–2594 (2013).
21. Mesirca, P. et al. Cardiac arrhythmia induced by genetic silencing of 'funny' (f) channels is rescued by GIRK4 inactivation. *Nat. Commun.* **5**, 4664 (2014).
22. Kozasa, Y. et al. HCN4 pacemaker channels attenuate the parasympathetic response and stabilize the spontaneous firing of the sinoatrial node. *J. Physiol.* **596**, 809–825 (2018).
23. Chen, S., Wang, J. & Siegelbaum, S. A. Properties of hyperpolarization-activated pacemaker current defined by coassembly of HCN1 and HCN2 subunits and basal modulation by cyclic nucleotide. *J. Gen. Physiol.* **117**, 491–504 (2001).
24. Alig, J. et al. Control of heart rate by cAMP sensitivity of HCN channels. *Proc. Natl Acad. Sci. USA* **106**, 12189–12194 (2009).
25. Iancu, R. V. et al. Cytoplasmic cAMP concentrations in intact cardiac myocytes. *Am. J. Physiol. Cell Physiol.* **295**, C414–C422 (2008).
26. Vinogradova, T. M. et al. High basal protein kinase A-dependent phosphorylation drives rhythmic internal Ca2+ store oscillations and spontaneous beating of cardiac pacemaker cells. *Circ. Res.* **98**, 505–514 (2006).
27. DiFrancesco, D., Ferroni, A., Mazzanti, M. & Tromba, C. Properties of the hyperpolarizing-activated current (if) in cells isolated from the rabbit sino-atrial node. *J. Physiol.* **377**, 61–88 (1986).
28. Saponaro, A. et al. A synthetic peptide that prevents cAMP regulation in mammalian hyperpolarization-activated cyclic nucleotide-gated (HCN) channels. *elife* **7**, e35753 (2018).
29. Mannikko, R., Pandey, S., Larsson, H. P. & Elinder, F. Hysteresis in the voltage dependence of HCN channels: conversion between two modes affects pacemaker properties. *J. Gen. Physiol.* **125**, 305–326 (2005).
30. Azene, E. M., Xue, T., Marban, E., Tomaselli, G. F. & Li, R. A. Non-equilibrium behavior of HCN channels: insights into the role of HCN channels in native and engineered pacemakers. *Cardiovasc. Res.* **67**, 263–273 (2005).
31. Elinder, F., Mannikko, R., Pandey, S. & Larsson, H. P. Mode shifts in the voltage gating of the mouse and human HCN2 and HCN4 channels. *J. Physiol.* **575**, 417–431 (2006).
32. Zhao, X. et al. In vitro characterization of HCN channel kinetics and frequency dependence in myocytes predicts biological pacemaker functionality. *J. Physiol.* **587**, 1513–1525 (2009).
33. Xiao, Y. F. et al. Hysteresis in human HCN4 channels: a crucial feature potentially affecting sinoatrial node pacemaking. *Sheng Li Xue Bao* **62**, 1–13 (2010).
34. Laude, D., Baudrie, V. & Elghozi, J. L. Tuning of the sequence technique. *IEEE Eng. Med. Biol. Mag.* **28**, 30–34 (2009).
35. Laude, D., Baudrie, V. & Elghozi, J. L. Applicability of recent methods used to estimate spontaneous baroreflex sensitivity to resting mice. *Am. J. Physiol. Regul. Integr. Comp. Physiol.* **294**, R142–R150 (2008).
36. Baudrie, V., Laude, D. & Elghozi, J. L. Optimal frequency ranges for extracting information on cardiovascular autonomic control from the blood pressure and pulse interval spectrograms in mice. *Am. J. Physiol. Regul. Integr. Comp. Physiol.* **292**, R904–R912 (2007).
37. Just, A., Faulhaber, J. & Ehmke, H. Autonomic cardiovascular control in conscious mice. *Am. J. Physiol. Regul. Integr. Comp. Physiol.* **279**, R2214–R2221 (2000).
38. Fenske, S. et al. HCN3 contributes to the ventricular action potential waveform in the murine heart. *Circ. Res.* **109**, 1015–1023 (2011).
39. Kirchhof, C. J., Bonke, F. I., Allessie, M. A. & Lammers, W. J. The influence of the atrial myocardium on impulse formation in the rabbit sinus node. *Pflug. Arch.* **410**, 198–203 (1987).
40. Kurata, Y., Matsuda, H., Hisatome, I. & Shibamoto, T. Roles of hyperpolarization-activated current If in sinoatrial node pacemaking: insights from bifurcation analysis of mathematical models. *Am. J. Physiol. Heart Circ. Physiol.* **298**, H1748–H1760 (2010).
41. Verheijck, E. E. et al. Electrophysiological features of the mouse sinoatrial node in relation to connexin distribution. *Cardiovasc. Res.* **52**, 40–50 (2001).
42. Verheijck, E. E., Wilders, R. & Bouman, L. N. Atrio-sinus interaction demonstrated by blockade of the rapid delayed rectifier current. *Circulation* **105**, 880–885 (2002).
43. Mesirca, P., Torrente, A. G. & Mangoni, M. E. Functional role of voltage gated Ca(2+) channels in heart automaticity. *Front. Physiol.* **6**, 19 (2015).
44. Marger, L. et al. Functional roles of Ca(v)1.3, Ca(v)3.1 and HCN channels in automaticity of mouse atrioventricular cells: insights into the atrioventricular pacemaker mechanism. *Channels (Austin)* **5**, 251–261 (2011).
45. Lolicato, M. et al. Tetramerization dynamics of C-terminal domain underlies isoform-specific cAMP gating in hyperpolarization-activated cyclic nucleotide-gated channels. *J. Biol. Chem.* **286**, 44811–44820 (2011).
46. Ludwig, A. et al. Absence epilepsy and sinus dysrhythmia in mice lacking the pacemaker channel HCN2. *EMBO J.* **22**, 216–224 (2003).
47. Glukhov, A. V., Fedorov, V. V., Anderson, M. E., Mohler, P. J. & Efimov, I. R. Functional anatomy of the murine sinus node: high-resolution optical mapping of ankyrin-B heterozygous mice. *Am. J. Physiol. Heart Circ. Physiol.* **299**, H482–H491 (2010).
48. Lang, D., Sulkin, M., Lou, Q. & Efimov, I. R. Optical mapping of action potentials and calcium transients in the mouse heart. *J. Vis. Exp.* **55**, e3275 (2011).
49. Laughner, J. I., Ng, F. S., Sulkin, M. S., Arthur, R. M. & Efimov, I. R. Processing and analysis of cardiac optical mapping data obtained with potentiometric dyes. *Am. J. Physiol. Heart Circ. Physiol.* **303**, H753–H765 (2012).
50. Lang, D. & Glukhov, A. V. High-resolution optical mapping of the mouse sino-atrial node. *J. Vis. Exp.* **118**, e54773 (2016).
51. Efimov, I. R., Fedorov, V. V., Joung, B. & Lin, S. F. Mapping cardiac pacemaker circuits: methodological puzzles of the sinoatrial node optical mapping. *Circ. Res.* **106**, 255–271 (2010).
52. Choate, J. K. & Feldman, R. Neuronal control of heart rate in isolated mouse atria. *Am. J. Physiol. Heart Circ. Physiol.* **285**, H1340–H1346 (2003).
53. Lee, C. H. & MacKinnon, R. Structures of the human HCN1 hyperpolarization-activated channel. *Cell* **168**, 111–120 e111 (2017).

Acknowledgements

We thank Mario R. Capecchi (University of Utah School of Medicine) for providing the ACN cassette. We thank Dainius H. Pauža (Lithuanian University of Health Sciences) and Peter Grafe (Ludwig-Maximilian-University of Munich) for sharing their expertise and for fruitful discussions. We thank Phuong Nguyen for experimental support. We thank Sandra Dirschl, Marina Wolf, and Katrin Gruner for excellent technical assistance. This work was supported by the German Research Foundation [WA 2597/3-1, BI 484/5-1 and FE 1929/1-1].

Author contributions

Conceptualization, C.W.S., S.F., and M.B.; Methodology, C.W.S., S.F., and M.B.; Formal analysis, S.F., K.H., V.B., R.R., C.W., and T.Z.; Validation, S.F.; Investigation, S.F., K.H., V.B., R.R., E.B., V.M., A.P., A.S., C.G., X.Z., T.Z., R.Z., and H.Z.; Resources, I.E., J.B., M.M., and C.K.; Data Curation, S.F., Writing, C.W.S., S.F., and M.B.; Visualization, S.F., V.B., R.R., and K.H, Project administration, C.W.S. and S.F.; Funding Acquisition, C.W.S. and M.B.

Funding

Open Access funding enabled and organized by Projekt DEAL. This work was supported by the German Research Foundation [WA 2597/3-1, BI 484/5-1 and FE 1929/1-1].

Competing interests

The authors declare no competing interests.

Additional information

Supplementary information is available for this paper at https://doi.org/10.1038/s41467-020-19304-9.

Correspondence and requests for materials should be addressed to M.B.; or C.W.-S.

Peer review information *Nature Communications* thanks Robert Rose and the other, anonymous, reviewer(s) for their contribution to the peer review of this work.

Reprints and permission information is available at http://www.nature.com/reprints

Publisher's note Springer Nature remains neutral with regard to jurisdictional claims in published maps and institutional affiliations.

SUPPLEMENTARY INFORMATION

cAMP-dependent regulation of HCN4 controls the tonic entrainment process in sinoatrial node pacemaker cells.

Table of contents:

Supplementary Figure 1

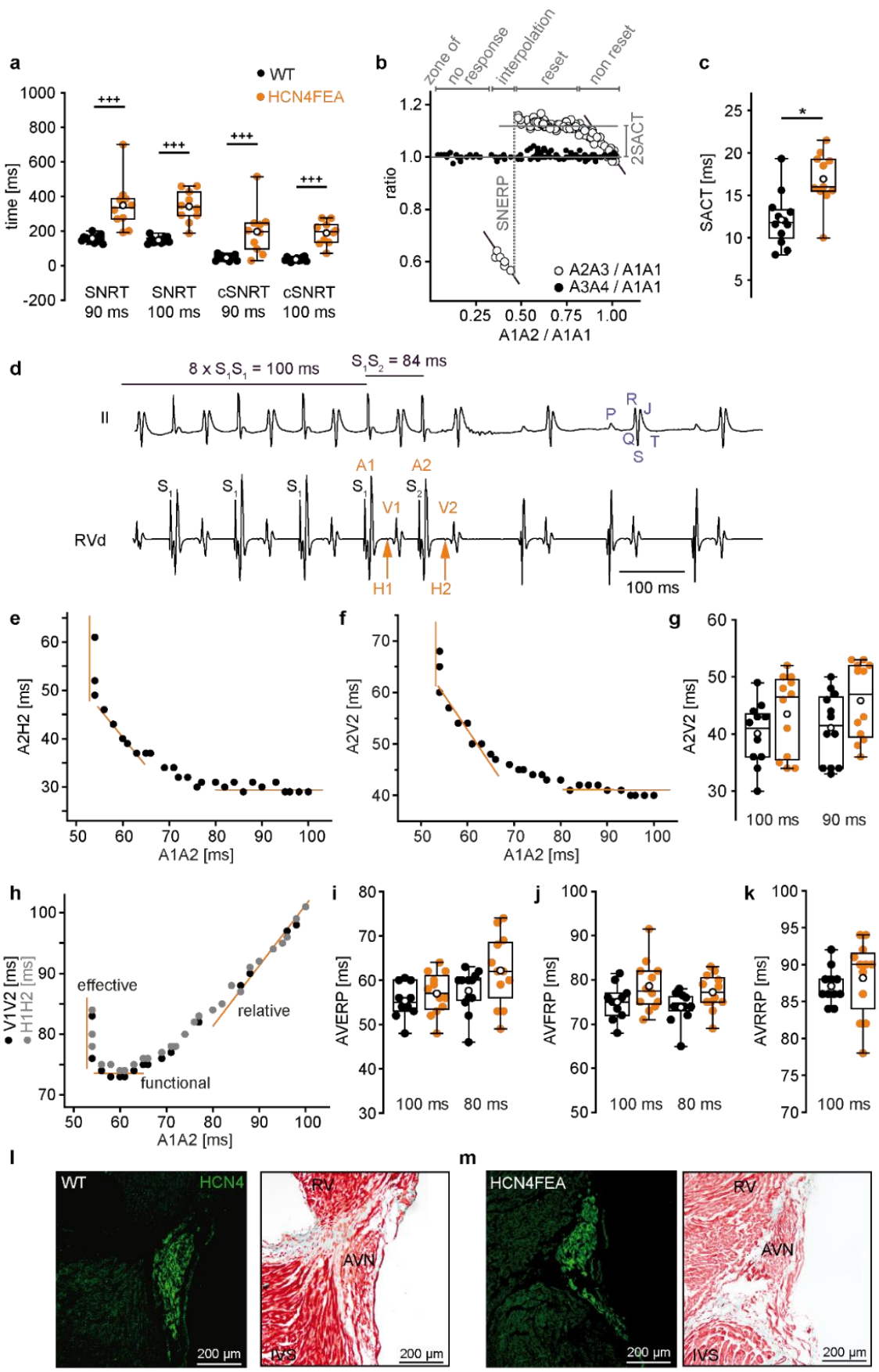

Supplementary Figure 1: Disrupted SAN but preserved AV function in HCN4FEA animals determined via *in vivo* EPS. a, Increased sinus node recovery time (SNRT) in HCN4FEA mice determined from invasive EPS (n = 12 WT + 10 HCN4FEA animals; SNRT90: p=0.00001; SNRT100: p=0.00001; cSNRT90: p=0.00006, cSNRT100: p=0.00005). **b,** Determination of sinoatrial conduction time (SACT) by programmed premature atrial stimulation. The normalised return cycle (A2A3/A1A1) and post return cycles (A3A4/A1A1) are plotted as a function of the normalised coupling interval of the premature atrial stimulus (A1A2/A1A1). Each point represents one test cycle. The diagonal line represents the line of full compensatory pauses [A1A2 + A2A3 = 2A1A1]. **c,** SACT is prolonged in HCN4FEA mice (n = 12 WT + 11 HCN4FEA animals; two-sided t-test, Holm-Bonferroni method: p=0.0075). **d,** AVN function and AV conduction was analysed by premature atrial stimulation. A train of eight stimuli (S1) was applied at S1S1 cycle lengths (100 ms or 80 ms) followed by a premature extra-stimulus (S2) at decreasing S1S2 coupling intervals. Top trace: surface ECG, lead II; bottom trace: intracardial atrial electrogram. S: pacing stimulus artefact; A: atrial signal; H: His bundle signal; V: ventricular signal. **e and f,** AV nodal latency curves were determined by plotting A2H2 or A2V2 delay versus A1A2 intervals. The horizontal line represents the shortest A2V2 interval shown in **(g)** (n = 12 WT + 12 HCN4FEA animals). **h,** AV nodal conduction curves were generated by plotting V1V2 intervals and H1H2 intervals versus the A1A2 coupling interval of the premature atrial stimulus. **i-k,** From AVN conduction curves, AVN effective refractory period (AVERP; 2-way repeated measures ANOVA, mixed effects model REML), functional refractory period (AVFRP; 2-way repeated measures ANOVA, mixed effects model REML), and relative refractory period (AVRRP; two-sided t-test, Holm-Bonferroni method) were determined. Furthermore, AVN function was evaluated using data obtained by telemetric ECG recordings. Analysis of telemetry data revealed that AV conduction was normal in HCN4FEA mice compared with that of WT mice (PQ interval, WT: 38.1 ± 0.8 ms, n = 9; HCN4FEA: 35.2 ± 1.2 ms, n = 11; p = 0.06; Supplementary Data 4). **l, m, (Left)** Cross-sections of the AVN demonstrate similar expression and distribution of HCN4 in WT **(l)** and HCN4FEA **(m). (Right)** Consecutive sections were additionally stained by masson's trichrome (n = 3 WT + 3 HCN4FEA biologically independent samples). For *in vivo* EPS and cross-sections male mice were used. Boxplots show the median line, perc 25/75, and min/max value; open symbols represent the mean value.

Significance levels: *student´s paired t-test adjusted for multiple comparisons by Holm-Bonferroni correction; + Holm's-Sidak post-hoc test after two-way ANOVA for repeated measures (general linear model). Source data are provided as a Source Data file.

Supplementary Figure 2

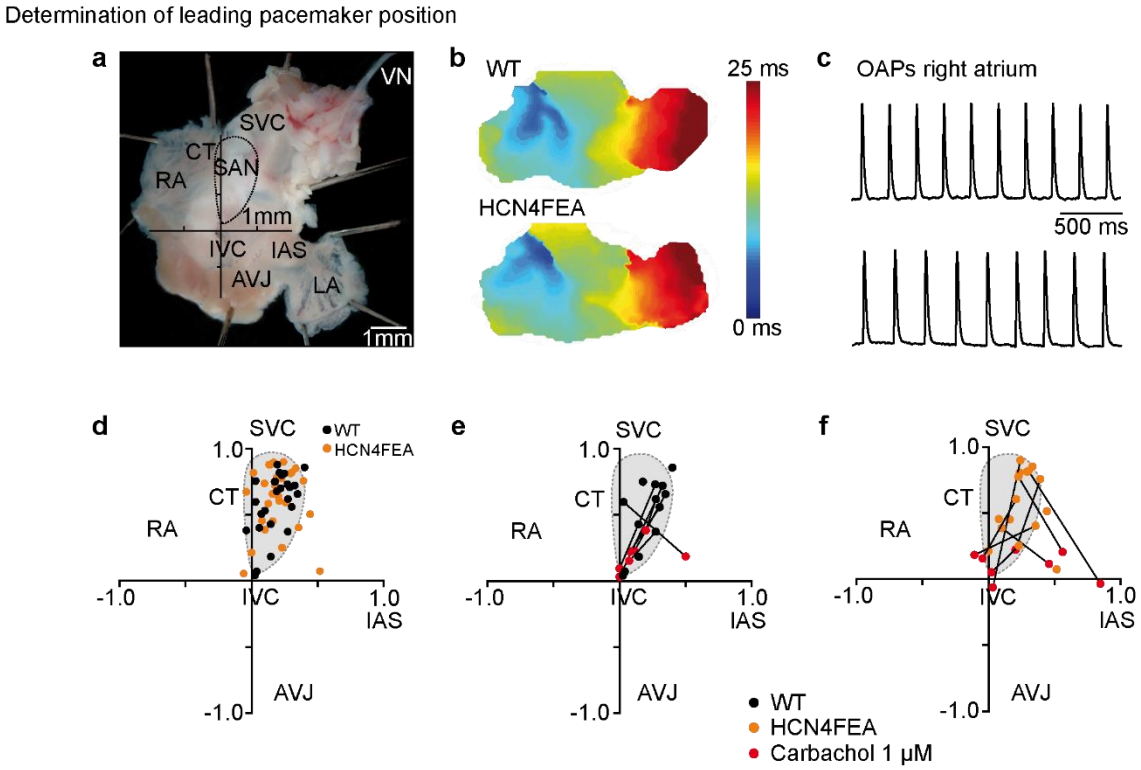

Supplementary Figure 2: Leading pacemaker site before and after application of a parasympathomimetic drug. a, Anatomy of a biatrial preparation with intact vagal nerve used for optical imaging. RA: right atrium; SAN: sinoatrial node; CT: crista terminalis; IVC: inferior caval vein; SVC: superior caval vein; AVJ: atrioventricular junction; IAS: interatrial septum; LA: left atrium; VN: vagal nerve. Orthogonal axes crossing at the IVC were used to plot the location of the leading pacemaker site and to quantify the magnitude of the leading pacemaker shift (n = 26 WT + 31 HCN4FEA biologically independent samples). **b,** Representative biatrial activation maps and **c,** corresponding

OAPs of WT and HCN4FEA preparations during spontaneous rhythm. **d,** Position of the leading pacemaker site within the SAN territory for each WT (n = 26) and HCN4FEA (n = 31) preparation. **e,** Leading pacemaker position before (black dots) and during application of carbachol (1 µM; red dots) in WT (n = 13). **f,** Leading pacemaker position before (orange dots) and during application of carbachol (1 µM; red dots) in HCN4FEA (n = 16). Shifts were larger in SANs of HCN4FEA mice. Female mice were used for optical imaging experiments. Source data are provided as a Source Data file.

Supplementary Figure 3

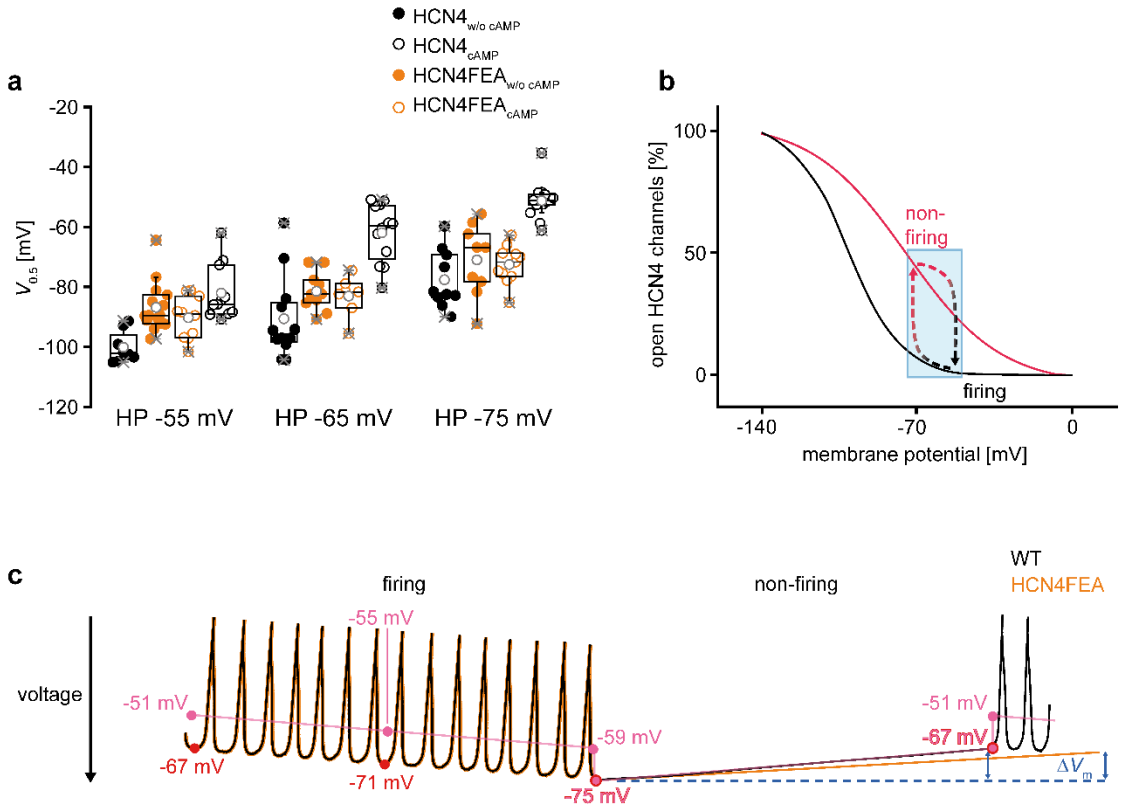

Supplementary Figure 3: Transition of the voltage dependence of HCN4 during firing and non-firing. a, $V_{0.5}$ values obtained from measurements of HCN4 currents in stably transfected HEK293 cells using different holding potentials. More negative holding potentials shift $V_{0.5}$ values to more positive potentials. Values from HCN4FEA mutant channels lie in between values determined from wild-type HCN4 channels without and with cAMP (HP -55 mV: HCN4 w/o cAMP n=8 cells, HCN4 cAMP n=11 cells, HCN4FEA w/o cAMP n=15 cells, HCN4FEA cAMP n=10 cells; HP -65 mV: HCN4 w/o cAMP n=12 cells, HCN4 cAMP n=12 cells, HCN4FEA w/o cAMP n=10 cells, HCN4FEA cAMP n=7 cells; HP -75 mV: HCN4 w/o cAMP n=10 cells, HCN4 cAMP n=13 cells, HCN4FEA w/o cAMP n=9 cells, HCN4FEA cAMP n=11 cells). **b,** Qualitative model to describe the transition of voltage dependence of HCN4 in SAN cells during firing and non-firing. **c,** Qualitative model for a typical cycle of firing and non-firing in SAN pacemaker cells. Firing starts at a MDP of -67 mV which slowly declines to -75 mV. At the same time, the average membrane potential declines from -51 mV (beginning of firing; pink curve) to -59 mV (end of firing; pink curve). When firing terminates, membrane potential abruptly drops to -75 mV (pink curve). During non-firing the membrane potential slowly rises to -67 mV until firing is reinitiated which leads to an abrupt increase in average potential to -51 mV. We propose that during firing and non-firing pronounced shifts in the activation curves of HCN4 channels **(b)** occur, which are driven by the large voltage steps at the beginning and the end of firing (**c**, step-like jumps in the pink curve). We suggest that by the end of the firing mode (-59 mV) the activation curve of HCN4 is positioned to more hyperpolarised potentials (**b**, black curve). After the abrupt jump to -75 mV at the beginning of non-firing the activation curve shifts towards more depolarised potentials (**b**, red curve). Once the threshold for firing is reached pacemaker cells switch to firing mode and voltage abruptly jumps to -51 mV, shifting voltage dependent activation to more hyperpolarised potentials (**b**, black curve) and the cycle repeats. Note that for the physiological model (**c**) all values are corrected for liquid junction potential. Boxplots show the median line, perc 25/75, and min/max value; grey open symbols represent the mean value. Source data are provided as a Source Data file.

Supplementary Figure 4

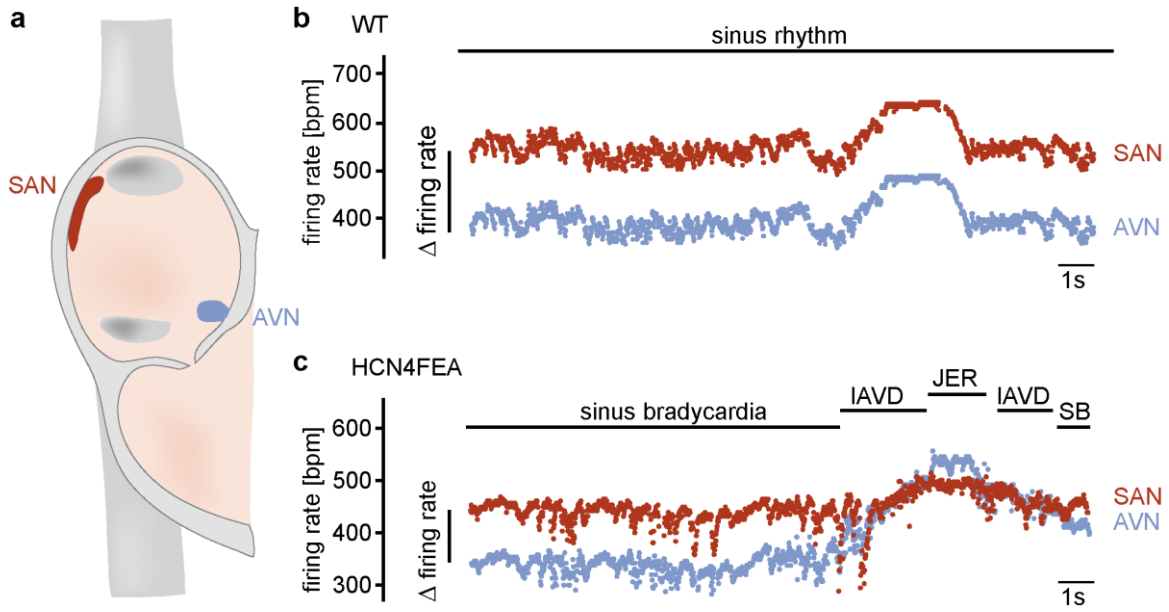

Supplementary Figure 4: Bradycardia and chronotropic incompetence disrupt the concerted action of SAN and AVN. a, Scheme depicting the positioning of SAN and AVN within the right atrium of the heart. **b,** SAN firing rate and putative AVN firing rate in a WT heart during regular sinus rhythm, HR acceleration, high HRs, and HR deceleration. SAN firing rate is always higher than the AVN firing rate and suppresses AVN activity. **c,** Sinus bradycardia (SB) caused by lack of CDR in HCN4FEA positions the SAN firing rate closer to that of the AVN. The combination of chronotropic incompetence of the SAN and preserved chronotropic competence of the AVN leads to escape phenomena (IAVD and JER) during sympathetic stimulation (see Discussion for details).

Supplementary Data files (Excel files) are not reprinted.

Manuscript IV

jove

Implantation of Combined Telemetric ECG and Blood Pressure Transmitters to Determine Spontaneous Baroreflex Sensitivity in Conscious Mice

René D. Rötzer[1], **Verena F. Brox**[1], **Konstantin Hennis**[1], **Stefan B. Thalhammer**[1], **Martin Biel**[1,2], **Christian Wahl-Schott**[3], **Stefanie Fenske**[1,2]

[1] Center for Integrated Protein Science (CIPS-M) and Center for Drug Research, Department of Pharmacy, Ludwig-Maximilians-Universität München [2] German Center for Cardiovascular Research (DZHK), Partner Site Munich Heart Alliance [3] Hannover Medical School, Institute for Neurophysiology

Corresponding Authors

Christian Wahl-Schott
Wahl-Schott.Christian@mh-hannover.de

Stefanie Fenske
stefanie.fenske@cup.uni-muenchen.de

Citation

Rötzer, R.D., Brox, V.F., Hennis, K., Thalhammer, S.B., Biel, M., Wahl-Schott, C., Fenske, S. Implantation of Combined Telemetric ECG and Blood Pressure Transmitters to Determine Spontaneous Baroreflex Sensitivity in Conscious Mice. *J. Vis. Exp.* (168), e62101, doi:10.3791/62101 (2021).

Date Published

February 14, 2021

DOI

10.3791/62101

URL

jove.com/video/62101

Abstract

Blood pressure (BP) and heart rate (HR) are both controlled by the autonomic nervous system (ANS) and are closely intertwined due to reflex mechanisms. The baroreflex is a key homeostatic mechanism to counteract acute, short-term changes in arterial BP and to maintain BP in a relatively narrow physiological range. BP is sensed by baroreceptors located in the aortic arch and carotid sinus. When BP changes, signals are transmitted to the central nervous system and are then communicated to the parasympathetic and sympathetic branches of the autonomic nervous system to adjust HR. A rise in BP causes a reflex decrease in HR, a drop in BP causes a reflex increase in HR.

Baroreflex sensitivity (BRS) is the quantitative relationship between changes in arterial BP and corresponding changes in HR. Cardiovascular diseases are often associated with impaired baroreflex function. In various studies reduced BRS has been reported in e.g., heart failure, myocardial infarction, or coronary artery disease.

Determination of BRS requires information from both BP and HR, which can be recorded simultaneously using telemetric devices. The surgical procedure is described beginning with the insertion of the pressure sensor into the left carotid artery and positioning of its tip in the aortic arch to monitor arterial pressure followed by the subcutaneous placement of the transmitter and ECG electrodes. We also describe postoperative intensive care and analgesic management. After a two-week period of post-surgery recovery long-term ECG and BP recordings are performed in conscious and unrestrained mice. Finally, we include examples of high-quality recordings and the analysis of spontaneous baroreceptor sensitivity using the sequence method.

Introduction

The arterial baroreceptor reflex is the major feedback control system in humans which provides a short-term - and possibly also longer term[1,2] - control of arterial blood pressure (ABP). This reflex buffers perturbations in BP that occur in response to physiological or environmental triggers. It provides prompt reflex changes in heart rate, stroke volume, and total peripheral arterial resistance. The reflex originates in sensory nerve endings in the aortic arch and carotid sinuses. These nerve terminals make up the arterial baroreceptors. The somata of nerve terminals in the aortic arch are located in the nodose ganglion while those of nerve terminals in the carotid sinus are located in the petrosal ganglion. The reflex is triggered by an increase in blood pressure, which stretches and activates the baroreceptor nerve terminals (**Figure 1A**). Activation results in action potential volleys which are transmitted centrally via the afferent aortic depressor and carotid sinus nerves to cardiovascular brain stem nuclei such as the nucleus tractus solitarii and the dorsal nucleus of the vagal nerve. Changes in afferent nerve activity in turn modulate the autonomic efferent activity. Increased activity of baroreceptor nerves decreases sympathetic and increases parasympathetic nerve activity. Thus, the consequences of activation of baroreceptors are a reduction in heart rate, cardiac output, and vascular resistance which together counteract and buffer the increase in blood pressure[3]. By contrast, decreased activity of baroreceptor nerves increases sympathetic and decreases parasympathetic nerve activity, which increases heart rate, cardiac output, and vascular resistance and thus counteract the decrease in blood pressure.

Numerous studies in humans and animals have demonstrated that the baroreceptor reflex can be adjusted under physiological conditions such as exercise[4], sleep[5], heat stress[6], or pregnancy[7]. Additionally, there is evidence that the baroreflex is chronically impaired in cardiovascular diseases, such as hypertension, heart failure, myocardial infarction, and stroke. In fact, baroreflex dysfunction is also utilized as a prognostic marker in several cardiovascular diseases[8,9,10]. Furthermore, dysfunction of the baroreflex is also present in disorders of the ANS. Given the importance of the baroreceptor reflex for health and disease states, in vivo estimation of this reflex is an important component of autonomic and cardiovascular research with certain serious clinical implications.

Genetic mouse lines are essential tools in cardiovascular research. In vivo studies of such mouse lines provide valuable insights into cardiovascular physiology and pathophysiology and in many cases serve as preclinical model systems for cardiovascular diseases. Here we provide a protocol for telemetric in vivo ECG and BP recording in conscious, unrestrained, freely moving mice and describe how baroreflex sensitivity can be determined from these recordings using the sequence method (**Figure 1B**). The applied method is called the sequence method, because the beat-to-beat series of systolic BP (SBP) and RR intervals are screened for short sequences of three or more beats during spontaneous increase or decrease in SBP with reflex adaption of the HR. This method is the gold-standard for baroreflex sensitivity determination since only spontaneous reflex mechanisms are investigated. The technique is superior to older techniques that involved invasive procedures such as injection of vasoactive drugs to induce BP changes.

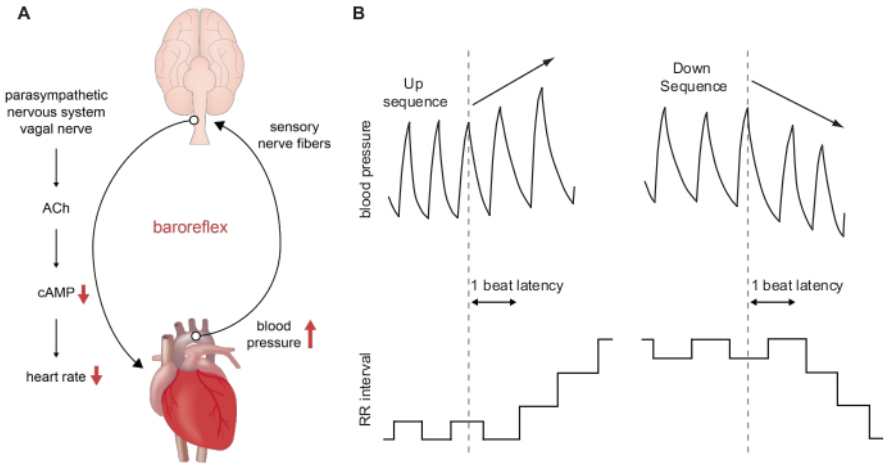

Figure 1: Schematic representation of the baroreflex and baroreflex sensitivity assessment using the sequence method. (**A**) Course of the baroreflex during an acute increase in blood pressure. A short-term rise in ABP is sensed by baroreceptors located in the aortic arch and carotid sinus. This information is transmitted to the central nervous system and induces a decrease in sympathetic nerve activity in parallel with an increase in parasympathetic activity. Release of acetylcholine from nerve endings located in the sinoatrial node region induces a decrease of the second messenger cAMP in sinoatrial node pacemaker cells and hence a reduction in heart rate. A short-term decrease in blood pressure has the opposite effect. (**B**) Schematic BP traces during an up sequence (upper left panel) and down sequence (upper right panel) of three consecutive beats. An up sequence is associated with a parallel increase in RR intervals (lower left panel) which is equivalent to a decrease in HR. A down sequence is associated with a parallel decrease in RR intervals (lower right panel) which is equivalent to an increase in HR. Please click here to view a larger version of this figure.

Protocol

Perform all animal studies in compliance with local institutional guidelines and national laws on animal experimentation. For this experiment, the studies were approved by the Regierung von Oberbayern and were in accordance with German laws on animal experimentation. WT animals (C57BL/6J background) and animals of a sick sinus syndrome mouse model displaying increased BRS sensitivity ($Hcn4^{tm3(Y527F;R669E;T670A)Biel}$)[11] (mixed C57BL/6N and 129/SvJ background) were used for this study.

1. Equipment setup

1. Remove a telemetric transmitter from its sterile package and shorten the ECG leads to the length appropriate for the size of the mouse. For a 12-week-old male black six mouse (C57BL/6J), weighing ~30 g, shorten the positive lead (red) to a length of ~45 mm and the negative lead (colorless) to a length of ~40 mm using scissors.
   NOTE: These values are given as orientation and must be adapted as necessary (**Figure 2**).

2. Remove approximately 6 mm of the ECG lead´s silicone tubing using a scalpel to expose the wire. Cover the tips of the wire with excessive tubing leaving a ~2 mm portion of ECG wire uncovered to record electrical signals. Secure the silicone tubing with non-absorbable 5-0 silk suture material (**Figure 2A**).
3. Write down the transmitter serial number into the operation protocol (**Supplemental File 1**).
4. Hydrate the transmitter in warm, sterile 0.9 % NaCl solution.
5. Weigh the mouse and record its weight.
6. Autoclave all surgical instruments prior to the surgery. Sterilize them during surgery and between operating different animals by dry heat using a hot glass bead sterilizer.
   NOTE: Surgical instruments must cool down to room temperature before use to prevent skin burns.
7. Disinfect the work bench to assure aseptic conditions.

2. Surgical implantation of telemetric transmitters for combined ECG and blood pressure measurements

1. Dissection of the left common carotid artery.
   1. Anesthetize a mouse by intraperitoneal injection of anesthesia mix (100 mg/kg ketamine; 15 mg/kg xylazine; 1 mg/kg acepromazine). Perform a toe pinch test to ensure that the mouse is fully anesthetized before commencing surgery.
   2. Use a trimmer to shave the surgical area from below the chin towards the transversal pectoral muscles.
   3. Place the mouse in a supine position on a temperature-controlled surgery plate set to 37 °C. Secure the limbs with surgical tape and continuously monitor body temperature with a rectal thermometer (**Figure 2C**). If body temperature drops below 37 °C cover the animal´s body with sterile cotton gauze during surgery.
   4. Apply eye ointment to protect the animal´s eyes during anesthesia.
   5. Apply depilatory cream to the previously shaved surgical area. Remove hair and depilatory cream using a cotton pad and warm water after 3-4 min. Make sure that the skin is clean and free of any residual hair and depilatory cream, so that the wound will not be contaminated during the operation.
   6. Disinfect the skin with skin disinfection spray.
   7. Place the animal under a dissecting microscope.
   8. Make a 1-1.5 cm midline incision through the skin of the neck, starting immediately below the chin. Take effort to make the incision as straight as possible. (**Figure 2D**).
      NOTE: During the following steps, the surgical area must be kept moist by regular application of sterile, warm (37 °C) 0.9 % NaCl.
   9. Create a subcutaneous space at both sides of the incision by separating the skin from underlying connective tissue with blunt dissection scissors. Be careful not to pinch the skin too strongly with the forceps, as this can cause necrosis and lead to impaired wound healing after surgery.
   10. Separate the parotid and submandibular glands using cotton tip applicators to expose the musculature overlying the trachea.

11. Retract the left salivary gland with curved dissection forceps to identify the left carotid artery located laterally to the trachea (**Figure 2E**).

12. Carefully dissect the carotid artery from adjacent tissue using curved forceps. Be very careful not to injure the vagal nerve that is running along the vessel. Continue blunt dissection to expose the left carotid artery to about 10 mm in length and fully separate it from vascular fascia and the vagus nerve (**Figure 2F**).

13. Pass a non-absorbable, 5-0 silk suture underneath the isolated portion of the carotid artery while slightly lifting the blood vessel with curved forceps to reduce friction between the suture and the carotid artery, as this could easily damage the vascular wall.

14. Place the suture cranially, just proximally to the bifurcation of the carotid artery, form a knot and tie it to permanently ligate the vessel (**Figure 2G**). Fix both ends of the cranial occlusion suture to the surgery table with surgical tape.

15. Pass a second occlusion suture underneath the carotid artery and place it caudally at ~5 mm distance to the cranial suture (**Figure 2H**). It is needed for temporary occlusion of blood flow during cannulation of the artery. Therefore, tie a loose knot and fix both suture ends with surgical tape.

16. Position a third suture (secure suture) between the cranial and caudal occlusion suture and make a loose knot (**Figure 2I**). This suture is needed to keep the catheter in place while cannulating the artery. Tape one end of the suture to the surgery table.

2. Cannulation of the left common carotid artery.

NOTE: The sensor area of the blood pressure catheter is located 4 mm from the distal end and consists of a tube containing a non-compressible fluid and a biocompatible gel (**Figure 2B**). Since this area is very sensitive, make sure it is free of air bubbles and do not touch it at any time during the procedure.

1. Bend the tip of a 24 G needle to an angle of ~100° to use it as a catheter introducer.

2. Gently pull the caudal occlusion suture and fix it with tension to temporarily stop blood flow and to slightly lift the artery.

3. Carefully penetrate the artery proximal to the cranial occlusion suture with the bent needle (**Figure 2J**). Grip the catheter with vessel cannulation forceps, introduce it into the small puncture and let it slide slowly into the vessel. Gently pull back the bent needle simultaneously (**Figure 2K**).

4. When the catheter reaches the caudal occlusion suture slightly tighten the secure suture to keep the catheter in place (**Figure 2L**).

5. Loosen the caudal occlusion suture so that the catheter can be further moved until its tip is positioned in the aortic arch.

   NOTE: Be sure to determine the correct insertion length of the catheter, as this depends on the size of the mouse. For male mice with a C57BL/6J background at 12 weeks of age and ~30 g body weight, we recommend inserting the catheter until the integrated notch reaches the cranial occlusion suture. The correct insertion depth and placement of the catheter for the specific mouse line can be verified after euthanasia of the animal.

6. Once positioned properly, secure the catheter with all three sutures and cut the ends as short as possible. Do not pull the knots too tight as this could damage the fragile blood pressure catheter.

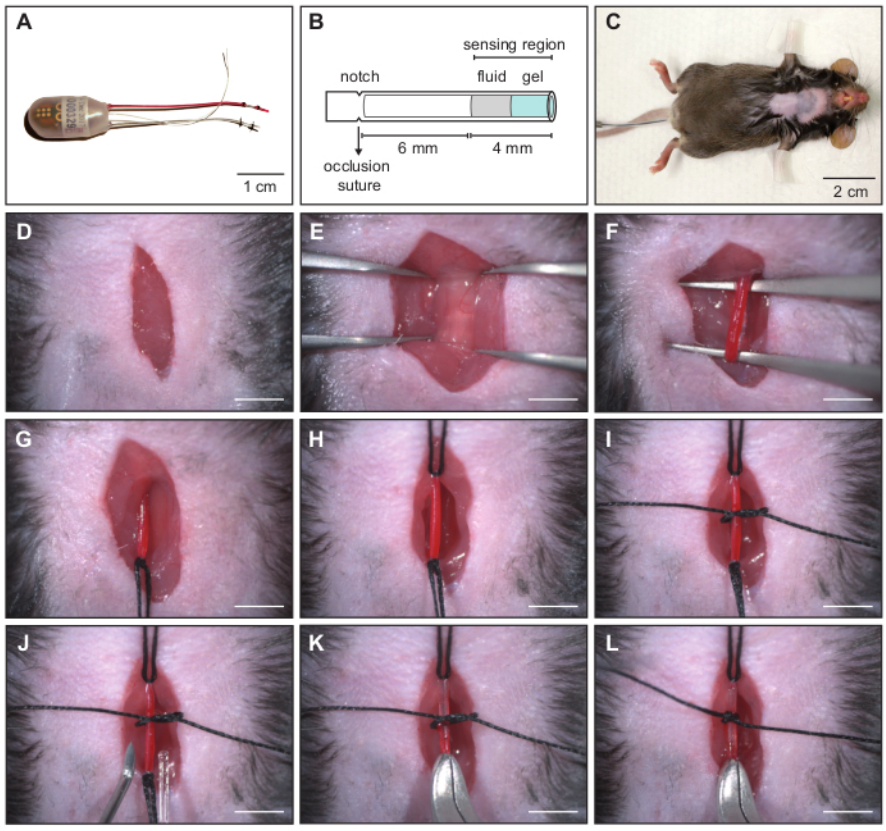

Figure 2: Implantation of a combined ECG and blood pressure transmitter - cannulation of the left carotid artery. (**A**) The telemetry transmitter is composed of a pressure catheter, two biopotential electrodes and the device body. (**B**) Schematic representation of the pressure catheter. The sensor area consists of a non-compressible fluid and a biocompatible gel. The catheter must be inserted into the carotid artery until the notch is at the level of the cranial occlusion suture to ensure proper position in the blood vessel. (**C**) Anesthetized C57BL/6J mouse prepared for surgical transmitter implantation. (**D-L**) Image sequence showing surgical procedure for cannulation of the left carotid artery. (**D**) Cervical skin incision. (**E**) Exposed trachea to identify the left carotid artery located laterally to the trachea. (**F**) Blunt dissection to isolate the artery from adjacent tissue and the vagus nerve. (**G**) Permanent ligation of the left carotid artery with cranial occlusion suture. (**H**) Tension applied to caudal occlusion suture to temporarily stop blood flow. (**I**) Secure suture to keep the catheter in place during cannulation. (**J**) Cannula with curved tip for insertion of the catheter into the blood vessel. (**K**) Pressure catheter is inserted into the carotid artery. (**L**) The catheter tip is positioned in the aortic arch and the catheter secured with the middle suture. Scale bar in D - L shows 4 mm. Reprinted from[16]. Please click here to view a larger version of this figure.

3. Placement of the telemetry device body in a subcutaneous pocket on the left flank of the mouse (**Figure 3**).
    1. Form a subcutaneous tunnel from the neck directed towards the left flank of the animal and form a small pouch using small, blunt dissecting scissors (**Figure 3B**).
    2. Irrigate the tunnel with a 1 mL syringe filled with warm, sterile 0.9% NaCl solution and introduce ~300 µL of the solution into the pouch (**Figure 3C**).
    3. Carefully lift the skin with blunt forceps and introduce the transmitter device body into the pouch (**Figure 3D**). During this step, be very careful not to pull the blood pressure catheter out of the carotid artery.
4. Placement of the ECG leads in Einthoven II configuration.
    1. Form a thin tunnel to the right pectoral muscle with blunt dissecting scissors and place the negative (colorless) lead into the tunnel using blunt forceps. Fix the terminal end of the lead with a stitch to the pectoral muscle using 6-0 absorbable suture material (**Figure 3E**).
    2. Form a loop in the positive (red) lead, position its tip at the left caudal rib region and secure its position with a suture using 6-0 absorbable suture material.
    NOTE: It is important that both leads lie flat against the body for their whole length to avoid tissue irritation (**Figure 3F**).
    3. Close the skin with single knots using 5-0 non-absorbable suture material (**Figure 3H**). Additionally, apply a small amount of tissue adhesive on every knot to keep the animal from biting the suture and prevent dehiscence.
    4. Apply povidone-iodine hydrogel 10% to the wound to prevent wound infection during the recovery phase.
    5. For preemptive pain relief inject 5 mg/kg carprofen in 0.9 % NaCl subcutaneously while the mouse is still under anesthesia.
    6. Set a heating platform to 39 ± 1 °C and place the mouse in a separate housing cage. Position one half of the cage on the platform for 12 h after surgery and transfer the mouse in the warm area. When the animal awakens from anesthesia, it has the option of staying in the warm area or moving to the cooler part of the cage.

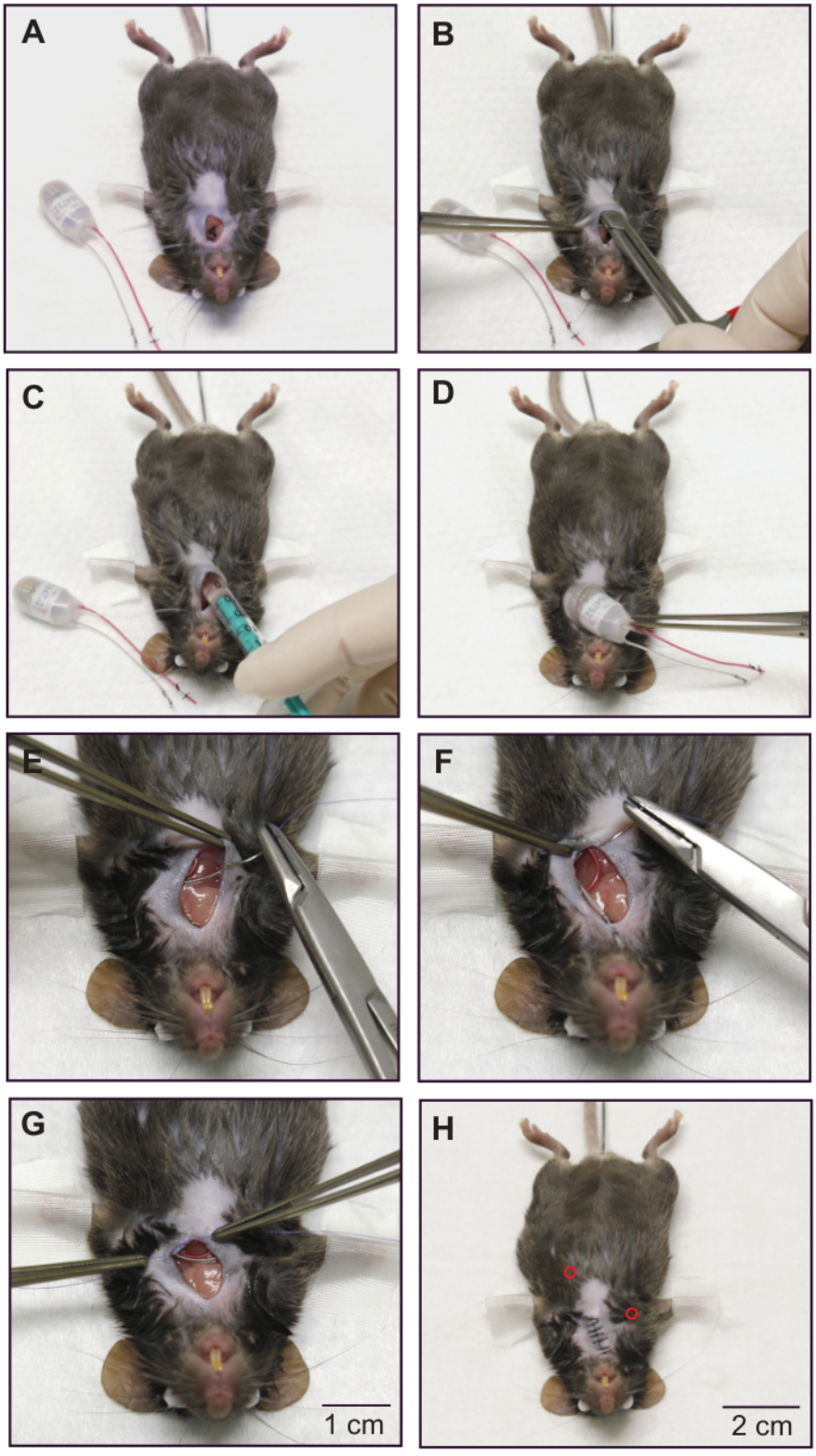

Figure 3: Implantation of a combined ECG and blood pressure transmitter - subcutaneous placement of the ECG electrodes and device body. (**A**) Mouse after insertion of the blood pressure catheter. Catheter position is secured by the occlusion sutures. (**B**) Forming a subcutaneous pocket on the left flank of the animal with blunt scissors. (**C**) The pouch is irrigated with ~300 µL of warm sterile saline. (**D**) The device body is placed in the subcutaneous pocket. (**E**) The terminal end of the negative electrode (colorless) is fixed to the right pectoral muscle with absorbable suture material. (**F**) Fixation of the positive electrode (red) to the left intercostal muscles. (**G**) Placement of a permanent suture on the chest muscle to secure the position of the ECG electrodes. (**H**) Mouse after skin closure. The subcutaneous positions of the ECG electrode tips are indicated by red circles. Reprinted from[16]. Please click here to view a larger version of this figure.

5. Post-operative care
    1. For post-operative pain relief inject 5 mg/kg carprofen in 0.9% NaCl subcutaneously every 12 h for 3-5 days until the wound has healed.
    2. Inject 10 µL/g of warm ringer-lactate solution intraperitoneally to protect the animal from dehydration.
    3. Let the mouse recover for 2-3 weeks before running the first telemetric measurements. Carefully monitor general health conditions, wound healing, body weight, and food and water intake during the recovery period.
    4. At the end of the experiment, euthanize the mouse by carbon dioxide (CO_2) inhalation.

       NOTE: Cervical dislocation or decapitation is not recommended as euthanasia method since this could damage parts of the ECG and BP transmitter device.
6. Data acquisition.
    1. Take measures to avoid acoustic and electronic noise during data recording. Additionally, limit access of personnel during data recording and complete all husbandry procedures prior to the experiment.
    2. Place the animal´s cage on the telemetry receiver plate and turn on the telemetric transmitter by bringing a magnet close to the animal.
    3. Acquire continuous ECG, blood pressure and activity recordings over 72 h (12-h dark/light cycle) with data acquisition software (**Figure 4**).
7. Analysis of the circadian rhythm of heart rate, blood pressure and activity.
    1. Check the presence of a regular circadian rhythm of HR, BP and activity using data acquisition software[12] (**Figure 5**).
8. Data analysis including determination of baroreceptor sensitivity using the sequence method with ECG and BP analysis software.
    1. Export BP and HR data from data acquisition software into ECG and BP analysis software (**Supplemental File 2**). Use the following sequence of commands: **Open ECG and BP analysis software > File > Raw data from converter > Convert non-IOX raw data**. In the new window click **File > Load Dataquest ART4 data**. Again, a new window will open, select **data file for export > New window opens**, select animal from "subjects" list and select ECG and BP from "waveforms list" and

press **OK**. Choose animals from which data should be converted by clicking **Convert data > Create IOX binary site file**.

2. Open IOX binary site file in ECG and BP analysis software by using the following sequence of commands: **File > Load IOX data > Select BP and ECG trace >** press the **green checkmark**.

   NOTE: The following data processing parameters are optimized for data acquired from wildtype mice and should in principle fit all mouse models used in preclinical field. However, adaption of these parameters might be necessary when working with specific experimental models, e.g., mice with extremely high or low HR and/or BP values, or different rodent species. In any case, data processing parameters need to be carefully reviewed to assure that they fit the specific model under study.

3. For settings for ECG, BP and BRS analysis see **Supplemental File 3,4**. For BRS analysis in mice, adjust the BRS parameters to detect only sequences of three (or more) beats exhibiting a delay between SBP and RR of one beat, and set the threshold for SBP and RR change to 0.5 mmHg and 2 ms. Ensure that the correlation coefficient of the slope of the regression line from RR/SBP plots is larger than 0.75 and analyze only sections exhibiting stable sinus rhythm. Set parameters for ECG, BP and BRS analysis accordingly by using the following sequence of commands: **Tune > analysis settings** > new window opens

   1. ECG settings (right-click in the "**ECG mode and signal filtering**" window (**Supplemental File 3**)). Set the parameters as detailed here. Mode: ECG, RR-only, Filter mode: auto, according to set HR, Expected heart rate: bpm > 300, Baseline removal filter width (ms): 100.00, Noise removal filter width: 1.00 ms, Notch filter: 50.0 Hz, Spike removal filter: off, Drop-out detection mode: off, Max RR lengths (ms): 900.00, RR from adjusted R peaks: off, RR_only settings mode: Xsmall: mouse, R peak width (ms): 10.00, PR width (ms): 20.00, RT width (ms): 50.00, Max inter beat artefact (%): 50.00, R to other amplitude ratio: 3.00, R peak sign: positive, and Compute extra parameter: off

   2. For the blood pressure settings (BP, Pressure settings) right-click at the "**BP analyzer**" window (**Supplemental File 4**). Set the parameters as detailed here. Noise removal filter width (ms): 10.00, Derivative filter width (ms): 6.00, Notch filter: 50.0 Hz, Spike removal filter: off, Validation threshold (cal. unit): 12.00, Rejection threshold (cal. unit): 8.00, Derivative at begin upstroke (cal U/s): 10.00, Rejection limits: off, Delay from reference ecg: user defined window, Min delay from ecg Rpeak (ms): 10.00, Max delay from ecg Rpeak (ms): 250.00, Conduct_time_1 from mark: not computed, Conduct_time_2 from mark: not computed, BR (breathing rate): off, BRS (Baroreflex sensitivity): on, Minimum consecutive beat number: 3, Latency beat number: 1, Pressure value: SBP, Mark to compute pulse interval: R, Minimum pressure variation (calU): 0.50, Minimum interval variation (ms): 2.00, Minimum correlation: 0.75

4. Screen the activity signal for a 3-h sequence with low activity. Perform the BRS analysis in this time window since high activity of the animals interferes with BP and RR correlation.

5. Perform a BP and RR analysis during this 3-h time window while subdividing the 3-h analysis into 10 min steps.

6. Perform BRS analysis by using the following sequence of commands: Open **BRS analysis window > View > BRS analysis**. This opens the BRS analysis panel. Manually inspect every sequence displayed in the BRS analysis panel and exclude ectopic beats, sinus pauses, arrhythmic events or noisy data. Make sure to invalidate every single beat of such sequences to successfully exclude them from the analysis.

7. Export the results of the BRS analysis into a spreadsheet file (Results File). Modify the parameters that are exported to the spreadsheet file by using the following sequence of commands (**Supplemental Files 5-7**):

    1. **Tune > Parameters in list/to file > sections > txt** (**Supplemental File 5**). Select the " beats" section and any other section containing information of interest except the invalidated beats section.

    2. **Tune > Parameters in list/to file > steps > txt** (**Supplemental File 6**). Choose step values to be exported.

    3. **Tune > Parameters in list/to file > beats -> txt** (**Supplemental File 7**).

    4. Make sure that the beats section of the file contains at least the following data for every single beat. ECG_RR, ECG_HR, BP_SBP, BP_BRS_deltaP, BP_BRS_# (=consecutive beat intervals of the sequence), BP_BRS_slope, BP_BRS_correl, BP_BRS_shiftI (=RR of the subsequent beat)

    5. Then click **File > Save results file**.

8. Sort the exported data for up and down sequences using the filter function of Excel (**Supplemental File 8**). Calculate the number of sequences, mean BRS slope, standard deviation and standard error of BRS slope for up and down sequences separately. Also calculate the total amount of sequences per 1000 beats.

    NOTE: A spreadsheet template (TemplateBRS) for automated sorting and analysis of up and down sequences is provided in the Supplement (**Supplemental File 8**) and facilitates the analysis. By adjusting the filter function, you can sort sequences by different beat numbers (e.g., three- or four-beat sequences). For further details see Supplemental files 9-13.

    1. Open the Results File and the TemplateBRS Excel file (**Supplemental File 8**). Copy the data of the following columns from the Results File: (Pressure)_BRS_deltaP, (Pressure)_BRS_# and (Pressure)_BRS_slope (**Supplemental File 9**). Paste the data into the respective columns of the "Up sequences" and "Down sequences" spreadsheets in the TemplateBRS file (**Supplemental File 10**). Additionally, copy the data of the column

(Pressure)_BRS_SBP from the Results File (**Supplemental File 11**) and paste it into the "All sequences" spreadsheet in the TemplateBRS file (**Supplemental File 12**).

NOTE: The number in the (Pressure)_BRS_# column is listed only at the last beat of a sequence and depicts the sequence length. Up and down sequences can be distinguished by the sign of the (Pressure)_deltaP value. Negative values for the second and third beat of a three-beat sequence indicate a down sequence. Positive values indicate an up sequence, respectively.

2. Filter the copied data with the default filter settings. Click on the filter icon of the (Pressure)_BRS_# column and press "**ok**" (**Supplemental File 13**). Apply this step to the "Up sequences" and "Down sequences" spreadsheets.

   NOTE: The spreadsheet filters for three-beat sequences. If other sequence lengths are requested the setting of this column has to be changed in the drop-down menu. Calculations for number of sequences, mean BRS slope, standard deviation and standard error of BRS slope are displayed in the green boxes of the "Up sequences" and "Down sequences" spreadsheets. Calculations for the total number of sequences per 1000 beats appear in the green box of the "All sequences" spreadsheet.

Representative Results

Positive results for ECG and BP raw data

Using this protocol high-quality ECG and BP data can be acquired (**Figure 4** and **Supplemental File 14**), allowing not only for precise BRS analysis but also for analysis of a broad range of ECG or BP-derived parameters, e.g. ECG intervals (**Figure 4B**, upper panel), blood pressure parameters (**Figure 4B**, lower panel), heart rate and blood pressure variability, arrhythmia detection etc[12,13,14,15].

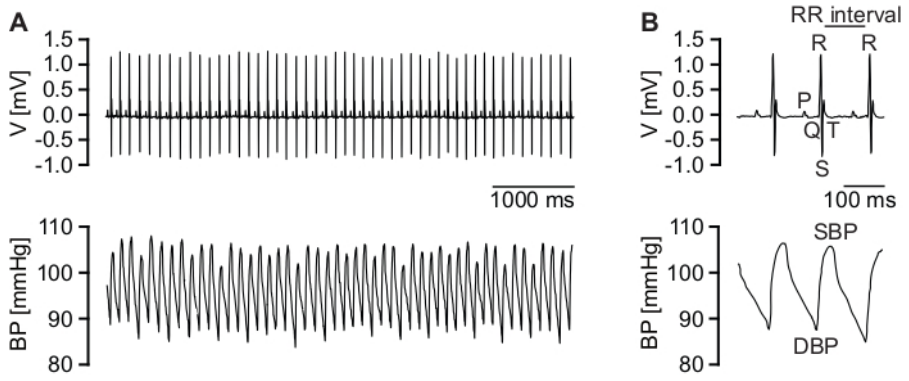

Figure 4: Telemetric ECG and BP recordings. (**A**) Representative, high-quality ECG trace (upper panel) and corresponding high-quality raw BP recordings (lower panel). (**B**) Magnification of ECG traces (upper panel). P wave, QRS complex, T wave and RR interval are indicated. Magnification of corresponding BP data (lower panel). Diastolic BP (DBP) and systolic BP (SBP) are indicated. Please click here to view a larger version of this figure.

Positive results for circadian rhythm

A healthy mouse that has sufficiently recovered from surgery shows a physiological increase of activity, HR and BP during the activity (dark) phase (**Figure 5**). Many different factors can disturb this regular circadian rhythm. These include psychological stress, acoustic or electric noise and pain. For example, an acute pain condition immediately after surgery would result in an increase in heart rate with a simultaneous decrease in activity. Therefore, the circadian rhythm is an important indicator for animal health and well-being and should be routinely checked before BRS analysis.

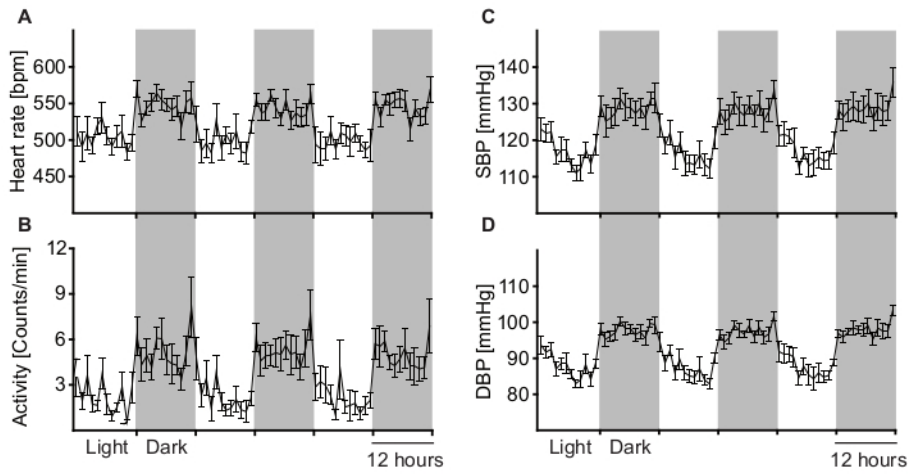

Figure 5: Analysis of long-term telemetry measurements to determine circadian rhythm variations. Circadian rhythm of heart rate (**A**), activity (**B**), systolic blood pressure (**C**) and diastolic blood pressure (**D**) averaged from 9 male wild-type C57BL/6J mice during 12 h light and dark cycles. Grey areas depict the activity (dark) phase and white areas depict the resting (light) phase of the animals. All parameters are physiologically elevated during the animal´s activity (dark) phase. Data are represented as mean +/- SEM. Please click here to view a larger version of this figure.

Positive results for BRS analysis

After performing the analysis as described in the protocol section 2.8 the software will detect up and down sequences, respectively. The method used is called sequence method since changes in SBP and RR intervals are examined on a beat-to-beat basis during short sequences of three or more beats with a spontaneous rise or fall in SBP (**Figure 6**). A continuous elevation in SBP over three heartbeats causes a reflex increase in parasympathetic activity and in consequence slows down HR, which is equivalent to longer RR intervals. The latency for the reflex HR adaption is one beat. Such a sequence is shown in **Figure 6A** and is defined as an up sequence. In contrast, a continuous decrease in SBP over three beats with parallel rise in HR (decrease in RR interval) is defined as a down sequence (**Figure 6B**). To evaluate the correlation between RR and SBP, both parameters are plotted against each other and the slope (ms/mmHg) of the linear regression line is calculated for each sequence (**Figure 6A,B**, lower panels). After sorting by up and down sequences the average number of sequences per 1000 beats (**Figure 6C**) and average gain of spontaneous BRS can be calculated for up and down sequences, respectively (**Figure 6D,E**). The gain of spontaneous BRS is reflected by the slope of the linear regression line calculated from the RR/SBP relation. The deviation from normal BRS values can have various causes. These include changes in ANS input or changes in the responsiveness of the sinoatrial node to autonomic nervous system input. In **Figure 6** increased BRS in a mouse model for sick sinus syndrome (SSS) with exaggerated responsiveness of the sinoatrial node to vagal input is shown[11].

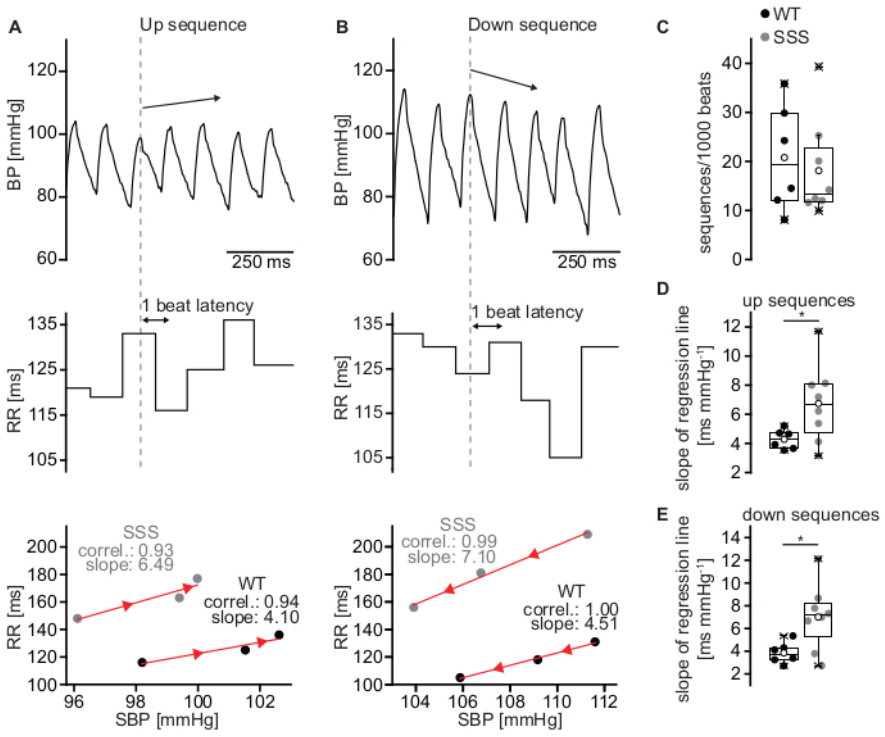

Figure 6: Estimation of BRS using the sequence method. (**A**) Representative BP trace of a wild-type C57BL/6J mouse during an up sequence of three consecutive beats (upper panel) associated with a parallel increase in RR interval (middle panel) which is equivalent to a decrease in HR. The RR intervals were plotted against the SBP (lower panel). The slope of the regression line (red line) for the up sequence depicted in the upper and middle panel (WT, black circles) was 4.10 ms/mmHg. A representative RR/SBP relationship of the sick sinus syndrome mouse model yielded an increased slope of 6.49 ms/mmHg indicating elevated BRS (SSS, grey circles). (**B**) Representative down sequence of a wild-type mouse with a drop in SBP (upper panel) and a subsequent decrease in RR interval (middle panel) which results in a BRS slope of 4.51 ms/mmHg (lower panel; WT, black circles). A representative RR/SBP relationship of the sick sinus syndrome mouse model (SSS, grey circles) with a slope of 7.10 ms/mmHg. The orientation of the red arrowheads indicates the direction of the sequences (up or down sequence). (**C**) Total amount of sequences per 1000 beats for WT and SSS mice. (**D**) Mean slope of the RR/SBP relationship for up sequences for WT and SSS mice. (**E**) Mean slope of the RR/SBP relationship for down sequences for WT and SSS mice. Statistics in (**C-E**) were performed from results of six male WT animals and eight male animals of the sick sinus syndrome mouse model. Boxplots show the median line, perc 25/75, and min/max value; open symbols represent the mean value. Please click here to view a larger version of this figure.

Negative result for raw data quality

Especially during phases of higher activity signal quality might decrease (**Figure 7** and **Supplemental Files 15,16**). This can

be caused by temporary displacement or incorrect position of either the BP catheter or ECG leads or both due to motion of the animal. Also, skeletal muscle activity might be detected from the ECG leads and induce noise (**Figure 7B**, upper panel). With the software settings described above, these low quality beats are not detected and are therefore excluded from analysis. Nevertheless, manual inspection of the analysed raw data is mandatory.

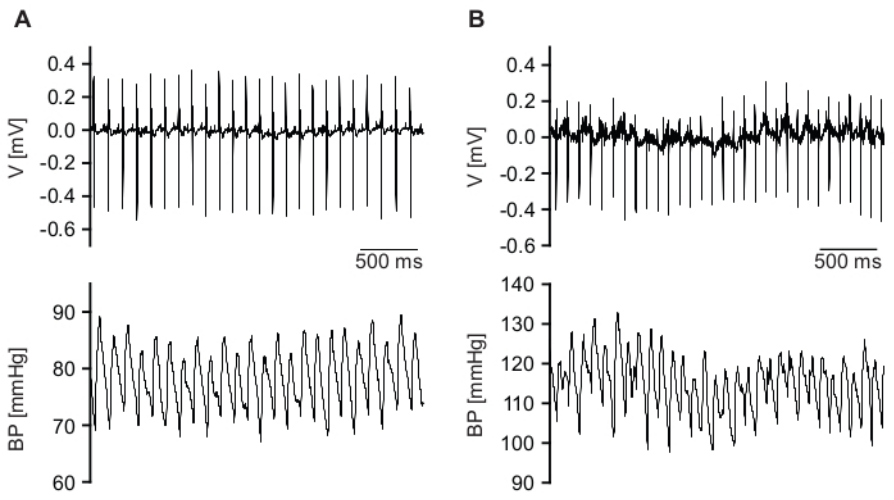

Figure 7: Examples of low-quality raw signals. (**A**) ECG signal (upper panel) is detected with good quality, but BP signal (lower panel) quality is low. (**B**) Qualities of ECG (upper panel) and BP (lower panel) signal are not sufficient. Please click here to view a larger version of this figure.

Negative results for BRS analysis

The BRS analysis settings listed in protocol section 2.8.3 are in general essential for fast and correct detection of up and down sequences. The minimum correlation coefficient for the regression line is set to 0.75. Setting too low values for the minimum correlation coefficient results in false detections of sequences that do not reflect baroreflex activity but rather result from arrhythmic beats (**Figure 8**). For BRS analysis only episodes with stable sinus rhythm must be analysed. Ectopic beats or other arrhythmic events, e.g., sinus pauses, can be found with the HRV option of ECG and BP analysis software and must be invalidated.

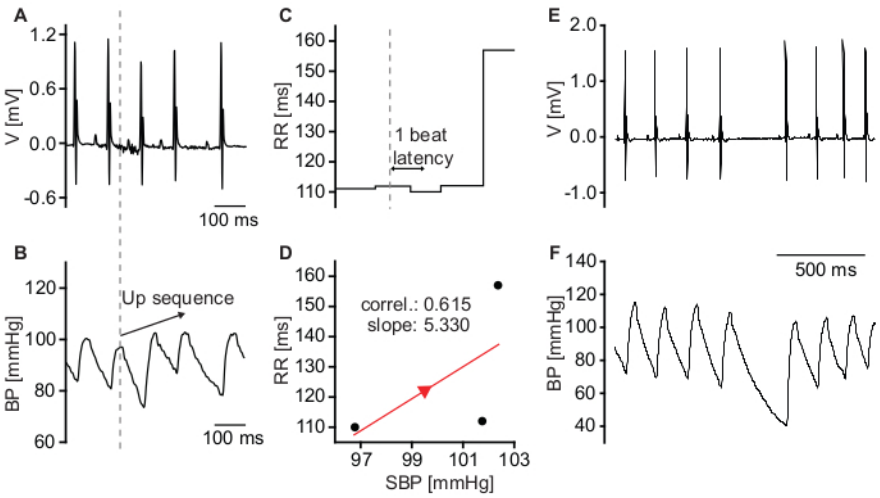

Figure 8: Sequences that do not reflect baroreflex activity. (**A**) ECG trace of a mouse with mild sinus dysrhythmia. (**B**) BP recording depicting a spontaneous increase in SBP. (**C**) Corresponding RR intervals indicate a decrease of HR upon the increase of BP. (**D**) Plot of SBP and corresponding RR intervals. The low correlation coefficient of the regression line indicates that HR reduction was not caused by activity of the baroreflex but rather by sinus dysrhythmia. (**E**) Raw ECG trace depicting a sinus pause. (**F**) Corresponding raw BP signal. The sinus pause causes a drop in diastolic blood pressure. Systolic blood pressure of the subsequent beat is almost unaffected. Please click here to view a larger version of this figure.

Supplemental File 1: Surgery protocol. Template for documentation of the surgical procedure and post-operative care. Please click here to download this File.

Supplemental File 2: Converting Dataquest A.R.T data into IOX data for analysis in ecgAUTO software. Select animals in the subjects list (left) and Pressure and ECG in the waveforms list (right). Press OK to convert data. Please click here to download this File.

Supplemental File 3: ECG settings for BRS analysis. Set parameters as listed, press ok and apply the configuration. Please click here to download this File.

Supplemental File 4: BP settings for BRS analysis. Set parameters as listed, press ok and apply the configuration. Save the configuration as a configuration file to be able to load the settings easily. Please click here to download this File.

Supplemental File 5: Parameters in list/to file window for "sections". Choose sections to be exported under the **sections** > **txt header** (selected) and press **Apply!**. Please click here to download this File.

Supplemental file 6: Parameters in list/to file window for "steps". Choose step data to be exported under the **steps** > **txt header** (selected) and press **Apply!**. Please click here to download this File.

Supplemental File 7: Parameters in list/to file window for "beats". Choose values to be exported under the **beats** > **txt header** (selected) and press **Apply!**. For BRS analysis the

ticked parameters are necessary. Note the order of selection indicated by the numbers. Please click here to download this File.

Supplemental File 8: TemplateBRS spreadsheet file. Spreadsheet template for automated sorting and analysis of up and down sequences. Please click here to download this File.

Supplemental File 9: Copying relevant data from the Results File I. Copy the columns (Pressure)_BRS_deltaP, (Pressure)_BRS_# and (Pressure)_BRS_slope from the Results File. Please click here to download this File.

Supplemental File 10: Spreadsheet template file (TemplateBRS) for data sorting and analysis I. Paste the copied data into the respective columns of the "Up sequences" and "Down sequences" spreadsheet in the TemplateBRS spreadsheet file. Please click here to download this File.

Supplemental File 11: Copying relevant data from the Results File II. Copy the column (Pressure)_BRS_SBP from the Results File. Please click here to download this File.

Supplemental File 12: A spreadsheet template file (TemplateBRS) for data sorting and analysis II. Paste the copied SBP data into the "All sequences" spreadsheet in the TemplateBRS spreadsheet file to calculate the total number of sequences. Please click here to download this File.

Supplemental File 13: Filtering and analyzing the sequences. In the "Up sequences" spreadsheet of the TemplateBRS spreadsheet file, open the drop-down menu of the (Pressure)_BRS_# column filter and press **OK** without changing any parameters. This will automatically sort the data and update the calculations for sequences with 3 beats. Repeat this for the "Down sequences" spreadsheet. Please click here to download this File.

Supplemental File 14: Screenshot of a high-quality recording detected with ECG and BP analysis software. The upper trace (ECG) shows detection of each R-peak and the lower trace (BP) shows detection of each diastolic pressure (DP) and systolic pressure (SP) peak. Areas under successfully detected peaks are marked in red. Please click here to download this File.

Supplemental File 15: Screenshot of a low-quality BP recording where BP parameters are only partially detected. The upper trace (ECG) shows detection of each R-peak but the lower trace (BP) shows gaps between detected BP peaks. Detected peaks of diastolic pressure (DP) and systolic pressure (SP) are marked with red areas. Please click here to download this File.

Supplemental File 16: Screenshot of a low-quality ECG and BP recording where ECG and BP parameters could not be detected. The upper trace (ECG) shows a region (purple background) where ECG parameters could not be detected. BP detection (lower trace) also failed due to low signal quality. Please click here to download this File.

Discussion

Significance of the method with respect to alternative methods

In the present work, we present a detailed protocol to quantify spontaneous BRS using the sequence method. This approach utilizes spontaneous BP and reflex HR changes measured by ECG and BP telemetry. The advantage of this method is that both parameters can be recorded in conscious, freely moving, unrestrained animals without disturbing animals by walking into the room where the measurements are performed or even by physical interaction required for injection of drugs. This point is very important since it has been clearly shown that such disturbances severely interfere with HR and BP recordings. For example, the injection of drugs requires fixation of the mice, which causes a maximum stress response that increases HR up to 650-700 bpm. To circumvent these stress responses, BRS has been previously determined in anesthetized mice. However, standard anesthetics used in veterinary medicine such as ketamine/xylazine or isoflurane induce bradycardia and influence autonomic reflex responses, limiting the validity of these approaches and the interpretation of the results. To partially overcome these limitations implantable drug delivery devices, i.e., osmotic pumps, which can release drugs into the peritoneal cavity were used. However, with osmotic pumps it is not possible to apply a bolus of a defined dose of drug limiting the application of such devices. Alternatively, complex infusion catheters[17] can be implanted into mice in order to administer drugs. However, these catheters are difficult to handle and require surgical skills comparable to those required for the implantation of telemetric devices, while producing less scientific outcome as compared to measurements of spontaneous BRS. Beside the technical issues associated with measuring BRS using injection of drugs, there are some limitations related to the drug action per se. Traditional approaches for determining BRS include bolus injections of vasoactive drugs. However, bolus injection of vasoconstrictors (e.g., phenylephrine) or vasodilators (e.g., sodium nitroprusside) have been considered an excessive and non-physiological stimulus for reflex HR adaption to changes in BP[18]. Spontaneous activity of the baroreceptor reflex can also be quantified using spectral methods. One of these methods assesses BRS in the frequency domain by calculation of the ratio between changes in HR and changes in blood pressure in a specific frequency band[18,19]. Other spectral methods involve the determination of the transfer function of BP and HR or the quantification of the coherence between BP and HR[20,21]. These methods also require telemetric acquisition of spontaneous BP and HR parameters and while they are appropriate for the determination of spontaneous BRS, they require intensive computational tools and are challenging to apply. Furthermore, all spectral methods suffer from the limitation that non-stationary signals preclude the application of spectral methods. In particular, spectral peaks induced by respiration rhythms can be reduced in human patients by asking the patient to stop breathing, while this is obviously not possible in mice. Therefore, the signal-to-noise ratio is frequently quite low in mice. Given the limitations of the methods discussed above, we favor the sequence method for determining BRS in mice. A considerable advantage of this method is the fact that it is a noninvasive technique that provides data on spontaneous BRS under real life conditions[22]. One further important point is that the duration of sequences analyzed using the sequence method are quite short, involving 3-5 beats. Reflex regulation of HR by the vagal nerve is very fast and well within the timeframe of these sequences. Therefore, the sequence method is well suited to evaluate the contribution of the vagal nerve to BRS. By contrast regulation by the sympathetic nervous system is much slower. In fact, during these short sequences activity of the sympathetic nervous system can be assumed to be almost constant. Therefore, the method

is customized to selectively detect reflex changes of the HR driven by vagus nerve activity.

Interpretation of BRS data

For the interpretation of BRS dysfunction or BRS data per se it is important to consider the individual functional levels which are involved in the baroreceptor reflex. On the neuronal level, afferent, central or efferent components of the reflex might be affected[23]. On the cardiovascular level, reduced or exaggerated responsiveness of the sinoatrial node to ANS input might be present[11,24]. A change on each level could lead to changes in the BRS. In order to dissect whether neuronal and/or cardiac mechanisms are responsible for observed changes in BRS, cardiac or neuron specific gene deletion, knock down or gene editing approaches could be used.

Critical steps in the protocol

The most sophisticated and critical step in this protocol is the preparation and cannulation of the left carotid artery (Step 2.3). The tension of the caudal occlusion suture has to be sufficiently high to completely stop the blood flow before cannulation. Otherwise, even a small leakage of blood during cannulation can severely restrict visibility or even cause the mouse to bleed to death. Cannulation should be successful at the first attempt. However, upon failure of the first attempt, it is still possible to carefully retry cannulation.

The midline incision and subcutaneous tunnel from the neck to the left flank (Step 2.3) must be large enough to easily introduce the transmitter without force but must also be as small as possible to keep the transmitter in place. Otherwise, one will need to lock it into position with suture material or tissue adhesive. Since mice have a very delicate skin, necrosis of the skin can occur if the tunnel for the transmitter is too small.

If the ECG electrodes are too long to fit into the subcutaneous tunnel (Step 2.4), it is necessary to form a new tip by shortening the electrode to a proper length. The electrode must lie flat against the body over the entire length of the lead. Too long electrodes will disturb the animals and they will try to open the wound to remove the transmitter, resulting in risk of tissue irritation and wound dehiscence. Leads that are too short can of course not be extended and it may be that in this case the electrodes cannot be positioned in such a way that they correspond to Einthoven II configuration. We therefore recommend to determine the optimal length of the ECG leads on a dead mouse of the same sex, weight, and genetic background.

Mice should be given a longer recovery time after transmitter implantation if they do not have a normal circadian rhythm and this is not the phenotype of the mouse line under study (step 2.7). Another reason for disturbed circadian rhythms could be inadequate acoustic isolation of the animal facility or personnel entering the room during measurement.

ECG, BP and BRS data analysis is straight forward (Step 2.8). The most critical step is to exclude ectopic beats, sinus pauses, arrhythmic episodes or sections with low-quality signals from data analysis.

Disclosures

None

Acknowledgments

This work was supported by the German Research Foundation [FE 1929/1-1 and WA 2597/3-1]. We thank

Sandra Dirschl for excellent technical assistance and Julia Rilling for veterinary advice.

References

1. Landgren, S. On the excitation mechanism of the carotid baroceptors. *Acta Physiologica Scandinavica.* **26** (1), 1-34 (1952).
2. Heyman, C. N., E. Reflexogenic areas of the cardiovascular system. By C. Heymans, M.D., Professor of Pharmacology, University of Ghent; and E. Neil, M.D., D.Sc. John Astor Professor of Physiology, University of London, Middlesex Hospital Medical School. 9¾ × 7 in. Pp. 271 + viii, with 89 illustrations. 1958. London: J., & A. Churchill Ltd. 56s. *British Journal of Surgery.* **46** (195), 92-92 (1958).
3. Lu, Y. et al. The ion channel ASIC2 is required for baroreceptor and autonomic control of the circulation. *Neuron.* **64** (6), 885-897 (2009).
4. Fadel, P. J., Raven, P. B. Human investigations into the arterial and cardiopulmonary baroreflexes during exercise. *Experimental Physiology.* **97** (1), 39-50 (2012).
5. Nagura, S., Sakagami, T., Kakiichi, A., Yoshimoto, M., Miki, K. Acute shifts in baroreflex control of renal sympathetic nerve activity induced by REM sleep and grooming in rats. *The Journal of Physiology.* **558** (Pt 3), 975-983 (2004).
6. Crandall, C. G., Cui, J., Wilson, T. E. Effects of heat stress on baroreflex function in humans. *Acta Physiologica Scandinavica.* **177** (3), 321-328 (2003).
7. Crandall, M. E., Heesch, C. M. Baroreflex control of sympathetic outflow in pregnant rats: effects of captopril. *The American Journal of Physiology.* **258** (6 Pt 2), R1417-1423 (1990).
8. Mortara, A. et al. Arterial baroreflex modulation of heart rate in chronic heart failure: clinical and hemodynamic correlates and prognostic implications. *Circulation.* **96** (10), 3450-3458 (1997).
9. La Rovere, M. T., Bigger, J. T., Jr., Marcus, F. I., Mortara, A., Schwartz, P. J. Baroreflex sensitivity and heart-rate variability in prediction of total cardiac mortality after myocardial infarction. ATRAMI (Autonomic Tone and Reflexes After Myocardial Infarction) Investigators. *Lancet.* **351** (9101), 478-484 (1998).
10. Robinson, T. G., Dawson, S. L., Eames, P. J., Panerai, R. B., Potter, J. F. Cardiac baroreceptor sensitivity predicts long-term outcome after acute ischemic stroke. *Stroke.* **34** (3), 705-712 (2003).
11. Fenske, S. et al. cAMP-dependent regulation of HCN4 controls the tonic entrainment process in sinoatrial node pacemaker cells. *Nature Communications.* **11** (1), 5555 (2020).
12. Fenske, S. et al. Comprehensive multilevel in vivo and in vitro analysis of heart rate fluctuations in mice by ECG telemetry and electrophysiology. *Nature Protocols.* **11** (1), 61-86 (2016).
13. Thireau, J., Zhang, B. L., Poisson, D., Babuty, D. Heart rate variability in mice: a theoretical and practical guide. *Experimental Physiology.* **93** (1), 83-94 (2008).
14. Au - Cesarovic, N., Au - Jirkof, P., Au - Rettich, A., Au - Arras, M. Implantation of radiotelemetry transmitters yielding data on ECG, heart rate, core body temperature and activity in free-moving laboratory Mice. *Journal of Visualized Experiments.* (57), e3260, (2011).
15. Au - Alam, M. A., Au - Parks, C., Au - Mancarella, S. long-term blood pressure measurement in freely moving

mice using telemetry. *Journal of Visualized Experiments.* (111), e53991, (2016).

16. Brox, V. Optical and electrophysiological approaches to examine the role of cAMP-dependent regulation of the sinoatrial pacemaker channel HCN4. *Dissertation, LMU Munich.* .https://edoc.ub.uni-muenchen.de/24431/1/Brox_Verena.pdf, (2019).
17. Just, A., Faulhaber, J., Ehmke, H. Autonomic cardiovascular control in conscious mice. *American Journal of Physiology-Regulatory, Integrative and Comparative Physiology.* **279** (6), R2214-2221 (2000).
18. Parati, G., Di Rienzo, M., Mancia, G. How to measure baroreflex sensitivity: from the cardiovascular laboratory to daily life. *Journal of Hypertension.* **18** (1), 7-19 (2000).
19. Robbe, H. W. et al. Assessment of baroreceptor reflex sensitivity by means of spectral analysis. *Hypertension.* **10** (5), 538-543 (1987).
20. Pinna, G. D., Maestri, R., Raczak, G., La Rovere, M. T. Measuring baroreflex sensitivity from the gain function between arterial pressure and heart period. *Clinical Science.* **103** (1), 81-88 (2002).
21. Pinna, G. D., Maestri, R. New criteria for estimating baroreflex sensitivity using the transfer function method. *Medical and Biological Engineering and Computing.* **40** (1), 79-84 (2002).
22. Laude, D., Baudrie, V., Elghozi, J. L. Applicability of recent methods used to estimate spontaneous baroreflex sensitivity to resting mice. *American Journal of Physiology-Regulatory, Integrative and Comparative Physiology.* **294** (1), R142-150 (2008).
23. Ma, X., Abboud, F. M., Chapleau, M. W. Analysis of afferent, central, and efferent components of the baroreceptor reflex in mice. *American Journal of Physiology-Regulatory, Integrative and Comparative Physiology.* **283** (5), R1033-R1040 (2002).
24. Fleming, S. et al. Impaired Baroreflex Function in Mice Overexpressing Alpha-Synuclein. *Frontiers in Neurology.* **4** (103), (2013).

Supplemental File 1

Chronological sequence

Time point	Action
Test start	Implantation of the telemetric blood pressure- and ECG-transmitter Injection anesthesia: 15 mg/kg xylazine, 100 mg/kg ketamine, 1 mg/kg acepromazine i.p. Medication under anesthesia: Preemptive analgesia (carprofen 5 mg/kg BW s.c.)
From day 1 after surgery	Recovery phase after implantation: approx. 2 weeks Postoperative analgesia: Carprofen 5 mg/kg bw s.c., every 12 hours Day 1 after surgery: Carprofen 5 mg/kg BW s.c. (2 injections) Day 2 after surgery: Carprofen 5 mg/kg BW s.c.(2 injections) Day 3 after surgery: Carprofen 5 mg/kg BW s.c. (2 injections) Day 4 after surgery: Carprofen 5 mg/kg BW s.c. (2 injections) Day 5 after surgery: Carprofen 5 mg/kg BW s.c. (2 injections)
2-3 weeks after surgery	Basal blood pressure and ECG measurement Duration of the measurement: 3 days
The day after the measurement	Euthanasia and transmitter explantation
Total duration of experiments after implantation	**2-3 weeks**

Test report part 1/2

II. Implantation telemetric transmitter			
Title of the animal protocol	Training display		
File number of the animal protocol:		Sex:	
Mouse line/ Genotype:		Weight:	
Mouse ID:		Experimenter:	
Date of birth:		Signature:	
Type of transmitter:	HD-X11	Transmitter-Nr:	
Anesthesia:		Origin of animals:	

Injection anesthesia:	15 mg/kg xylazine, 100 mg/kg ketamine, 1 mg/kg acepromazine i.p.		
Conc. of the injection solution:	µg/µl		
Injection volume:	µL		
Time of injection:	o'clock		
Start of the operation:	o'clock		
Possibly ketamine injection	µL		
Time of injection:	o'clock		
End of surgery:	o'clock		
End of anesthesia:	o'clock		
Reawakening:	☐	Euthanasia: ☐	Euthanasia-reason:
Special remarks:			

Medication under anesthesia:	
Preemptive analgesia:	Carprofen 5 mg/kg BW s.c.
Conc. of the injection solution:	µg/µl
Injection volume:	µl
Dexpanthenol eye ointment/gel:	
0.9% NaCl i.p.:	µL
Miscellaneous:	

Test report part 2/2

Mouse strain / genotype:		Experimenter:	
Mouse identification number:		Signature:	
Observations under anesthesia: see anesthesia protocol			
Other / Remarks:			

Postoperative Analgesia

Mouse strain / genotype:		Experimenter:	
Mouse identification number:		Signature:	
Postoperative Analgesia:			
Postoperative Analgesia:	Carprofen 5 mg/kg BW s.c., every 12 hours		
Conc. of Injection solution:			µg/µl
Day 1 after surgery:			
Injection volume:	µL	Time of injections:	o'clock o'clock
If necessary, further measures:			
Day 2 after surgery:			
Injection volume:	µL	Time of injections:	o'clock o'clock
If necessary, further measures:			
Day 3 after surgery:			
Injection volume:	µL	Time of injections:	o'clock o'clock
If necessary, further measures:			
Day 4 after surgery:			
Injection volume:	µL	Time of injections:	o'clock o'clock
If necessary, further measures:			
Day 5 after surgery:			
Injection volume:	µL	Time of injections:	o'clock o'clock
If necessary, further measures:			

Place, Date

Signature head investigator

Supplemental File 2

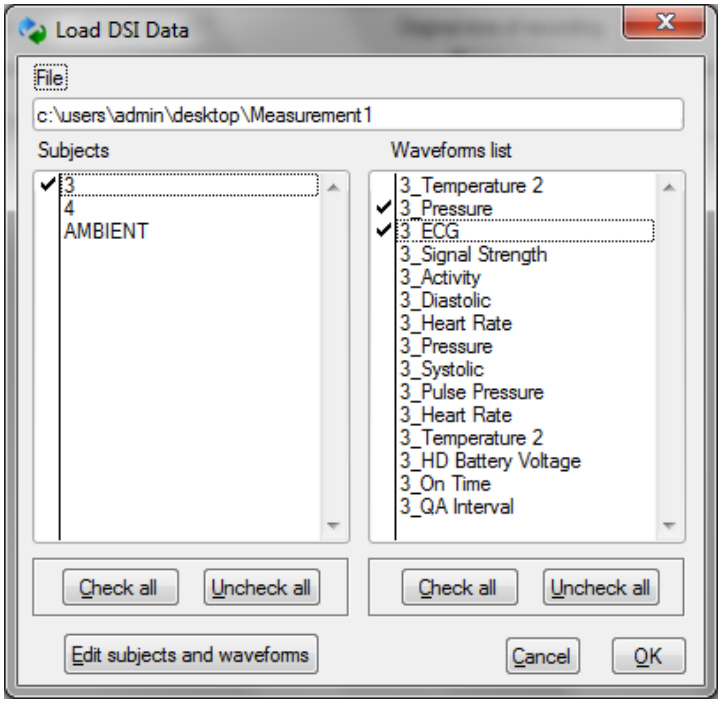

Supplemental File 3

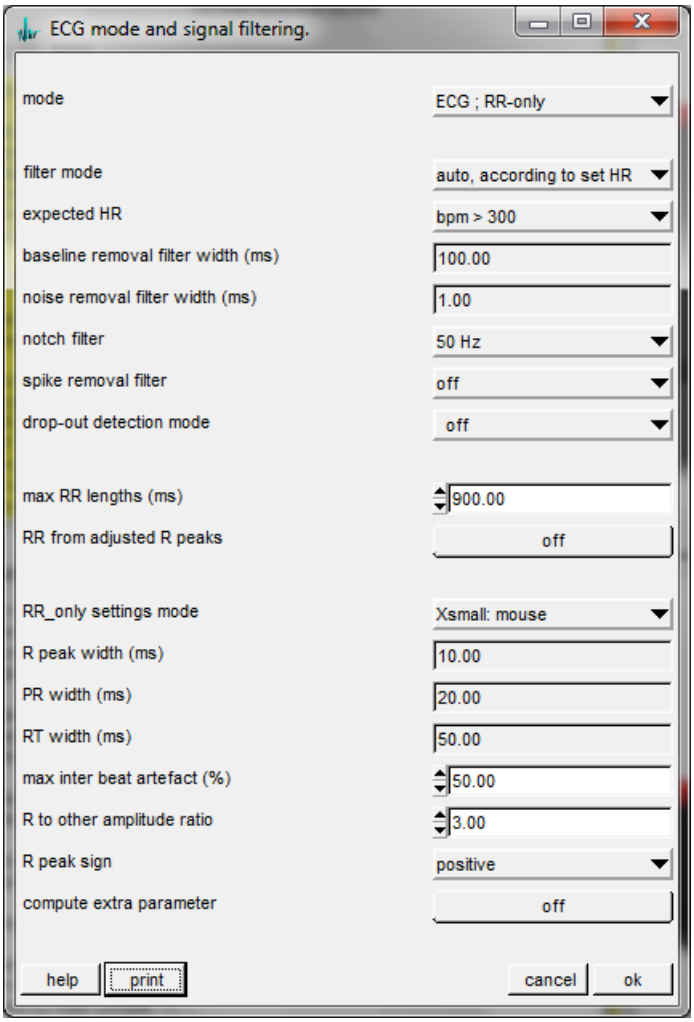

Supplemental File 4

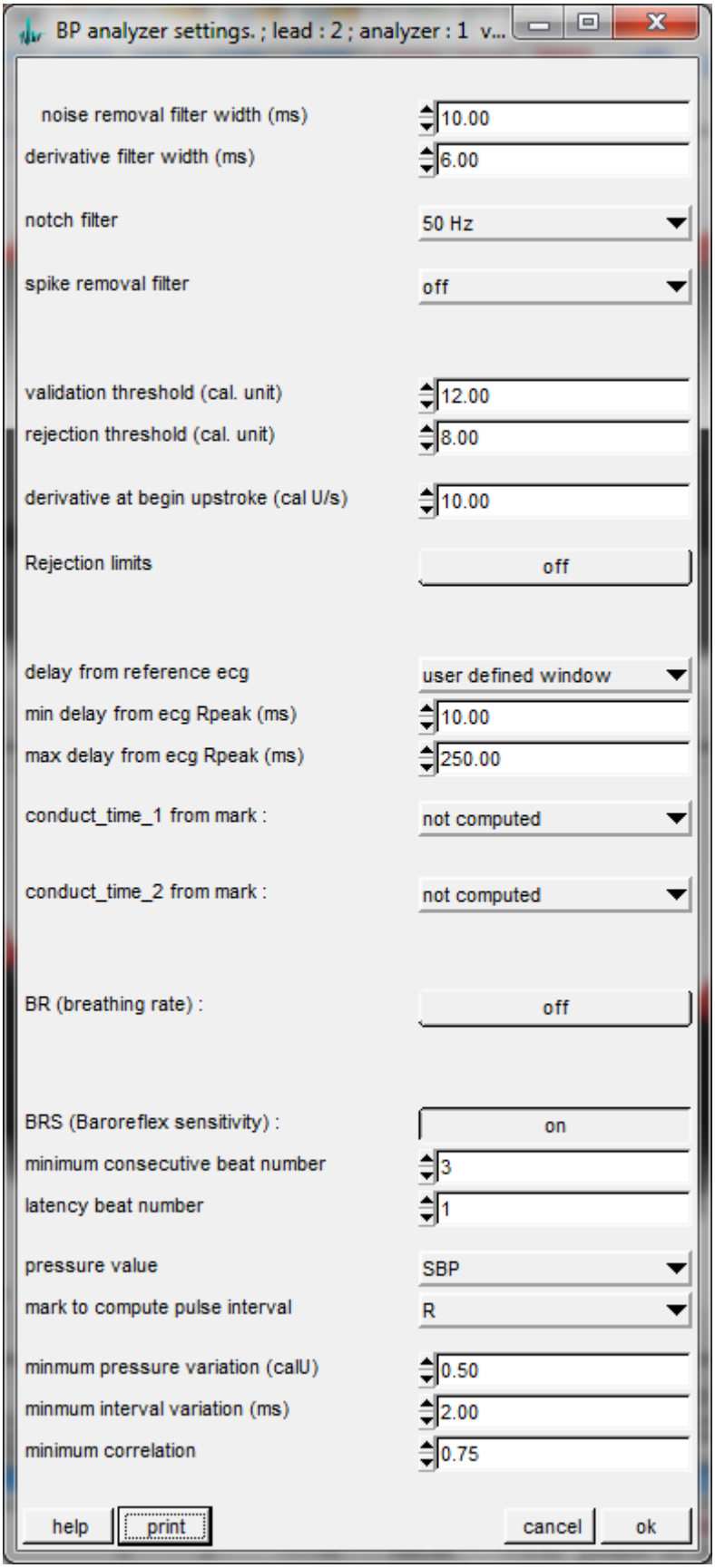

Supplemental File 5

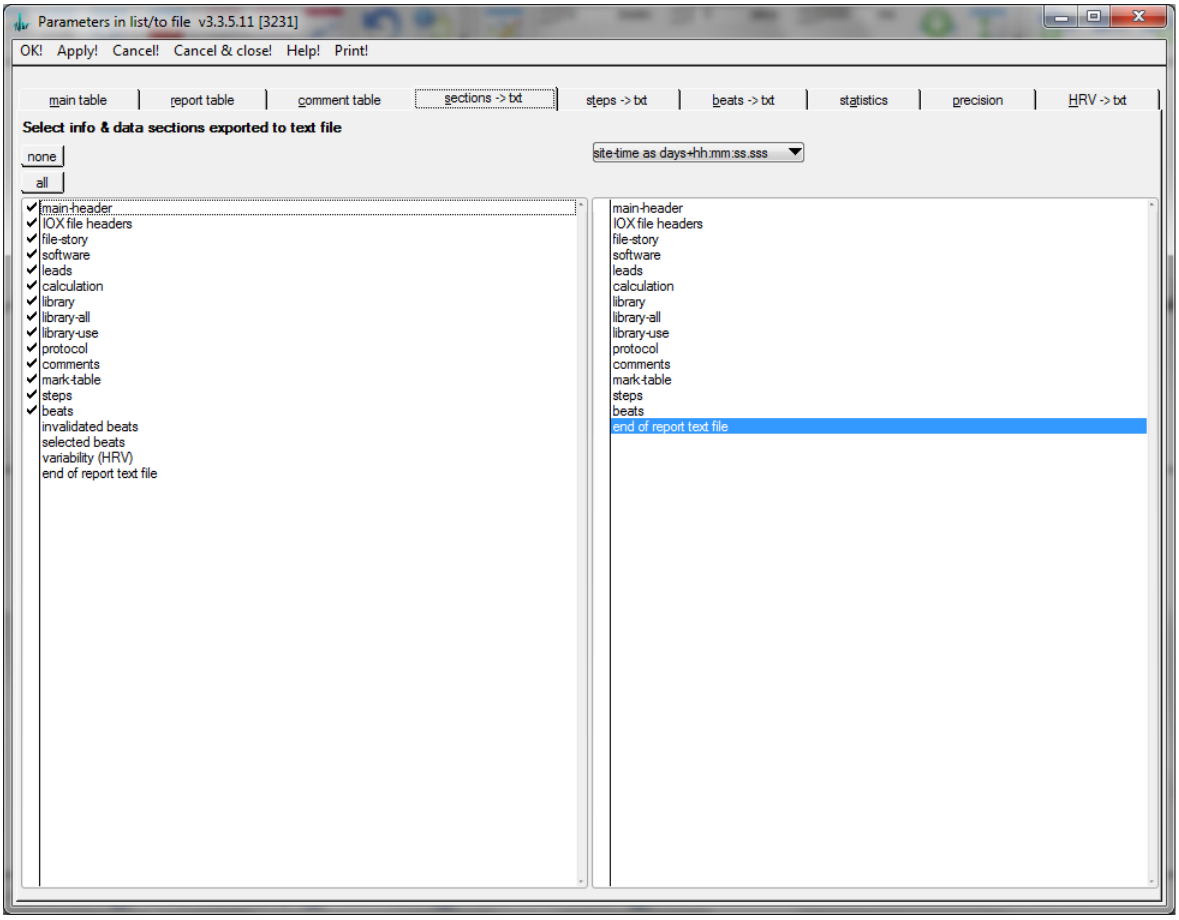

Supplemental File 6

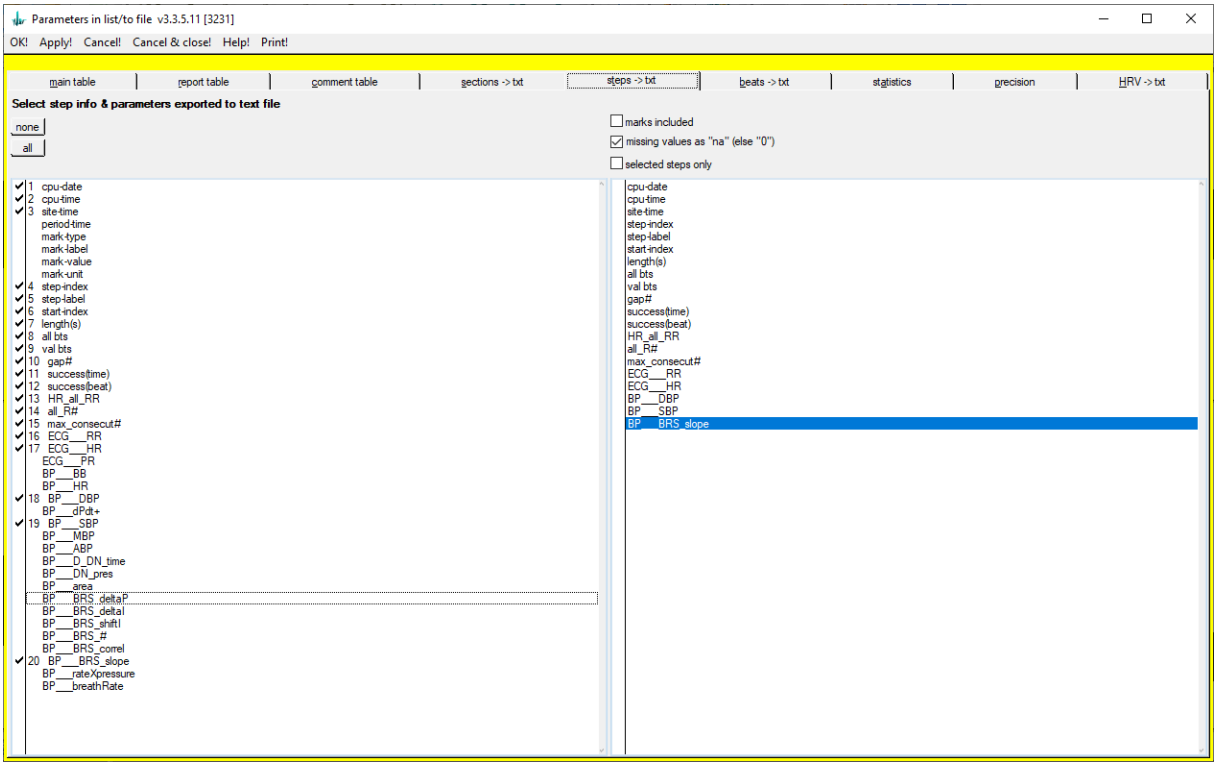

Supplemental File 7

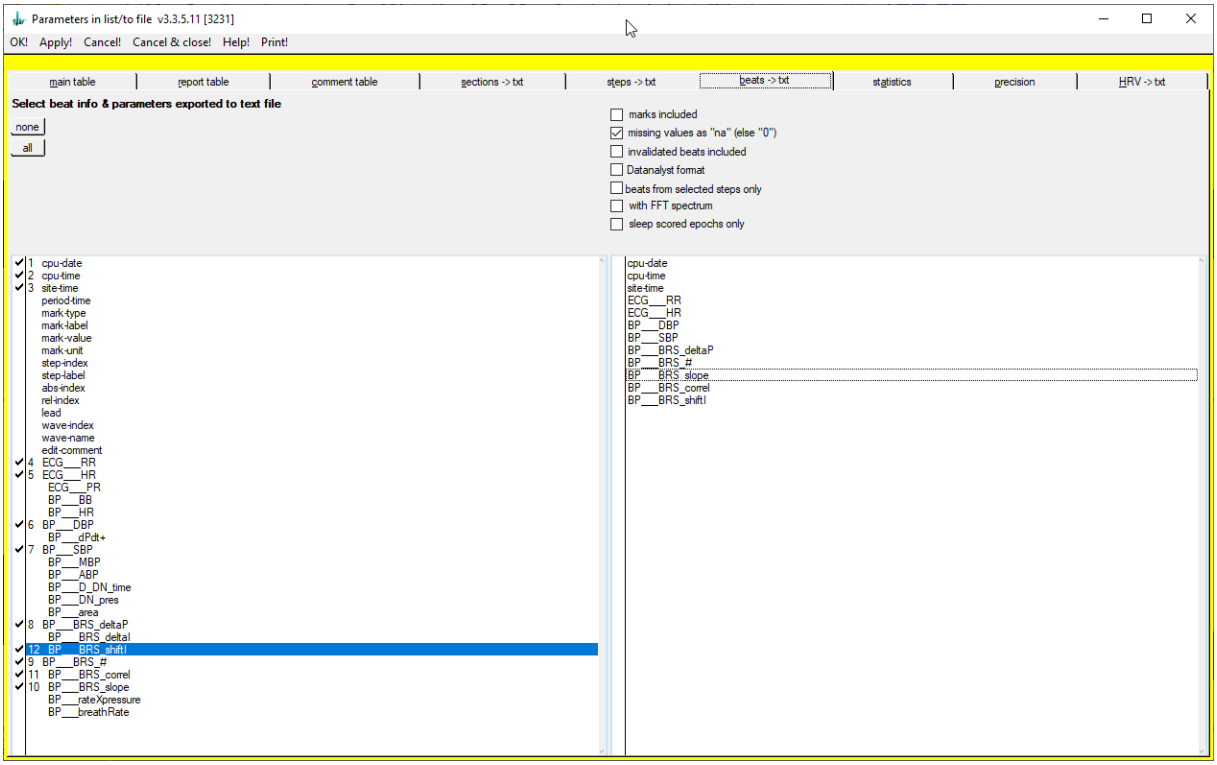

Supplemental File 8

Excel file for calculation not reprinted

Supplemental File 9

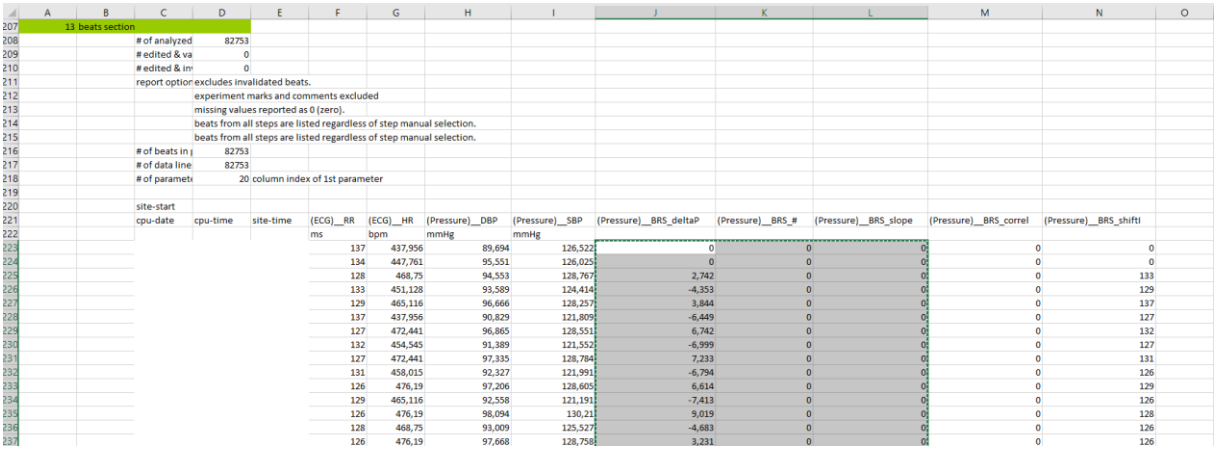

	A	B	C	D	E	F	G	H	I	J	K	L	M	N	O
207	13 beats section														
208			# of analyzed	82753											
209			# edited & va	0											
210			# edited & in	0											
211			report option	excludes invalidated beats.											
212				experiment marks and comments excluded											
213				missing values reported as 0 (zero).											
214				beats from all steps are listed regardless of step manual selection.											
215				beats from all steps are listed regardless of step manual selection.											
216			# of beats in j	82753											
217			# of data line	82753											
218			# of paramete	20	column index of 1st parameter										
219															
220			site-start												
221			cpu-date	cpu-time	site-time	(ECG)__RR	(ECG)__HR	(Pressure)__DBP	(Pressure)__SBP	(Pressure)__BRS_deltaP	(Pressure)__BRS_#	(Pressure)__BRS_slope	(Pressure)__BRS_correl	(Pressure)__BRS_shiftI	
222						ms	bpm	mmHg	mmHg						
223						137	437,956	89,694	126,522	0	0	0	0	0	
224						134	447,761	95,551	126,025	0	0	0	0	0	
225						128	468,75	94,553	128,767	2,742	0	0	0	133	
226						133	451,128	93,589	124,414	-4,353	0	0	0	129	
227						129	465,116	96,666	128,257	3,844	0	0	0	137	
228						137	437,956	90,829	121,809	-6,449	0	0	0	127	
229						127	472,441	96,865	128,551	6,742	0	0	0	132	
230						132	454,545	91,389	121,552	-6,999	0	0	0	127	
231						127	472,441	97,335	128,784	7,233	0	0	0	131	
232						131	458,015	92,327	121,991	-6,794	0	0	0	126	
233						126	476,19	97,206	128,605	6,614	0	0	0	129	
234						129	465,116	92,558	121,191	-7,413	0	0	0	126	
235						126	476,19	98,094	130,21	9,019	0	0	0	128	
236						128	468,75	93,009	125,527	-4,683	0	0	0	126	
237						126	476,19	97,668	128,758	3,231	0	0	0	126	

Supplemental File 10

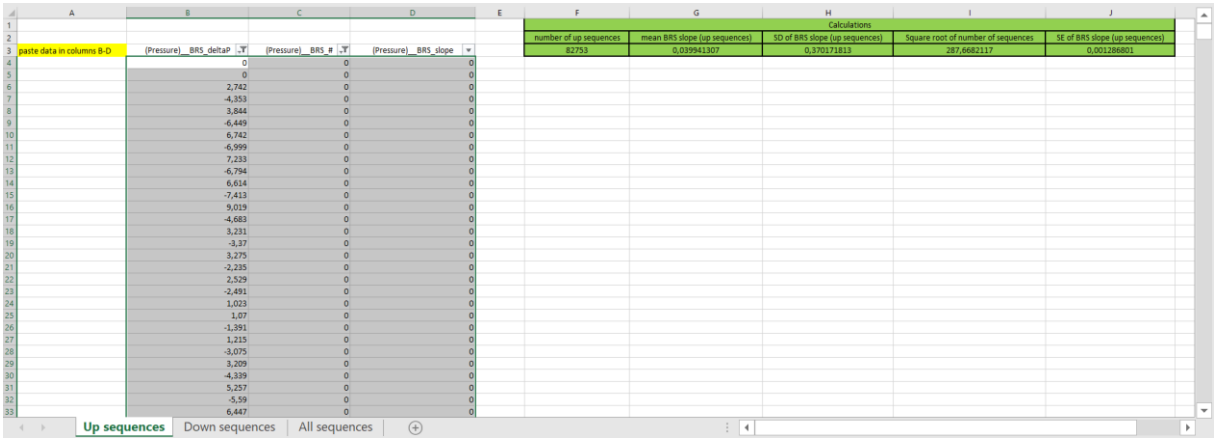

paste data in columns B-D	(Pressure)__BRS_deltaP	(Pressure)__BRS_#	(Pressure)__BRS_slope
	0	0	0
	0	0	0
	2,742	0	0
	-4,353	0	0
	3,844	0	0
	-6,449	0	0
	6,742	0	0
	-6,999	0	0
	7,233	0	0
	-6,794	0	0
	6,614	0	0
	-7,413	0	0
	9,019	0	0
	-4,683	0	0
	3,231	0	0
	-3,37	0	0
	3,275	0	0
	-2,235	0	0
	2,529	0	0
	-2,491	0	0
	1,023	0	0
	1,07	0	0
	-1,391	0	0
	1,215	0	0
	-3,075	0	0
	3,209	0	0
	-4,339	0	0
	5,257	0	0
	-5,59	0	0
	6,447	0	0

Calculations

number of up sequences	mean BRS slope (up sequences)	SD of BRS slope (up sequences)	Square root of number of sequences	SE of BRS slope (up sequences)
82753	0,039941307	0,370171813	287,6682117	0,001286801

Up sequences | Down sequences | All sequences

Supplemental File 11

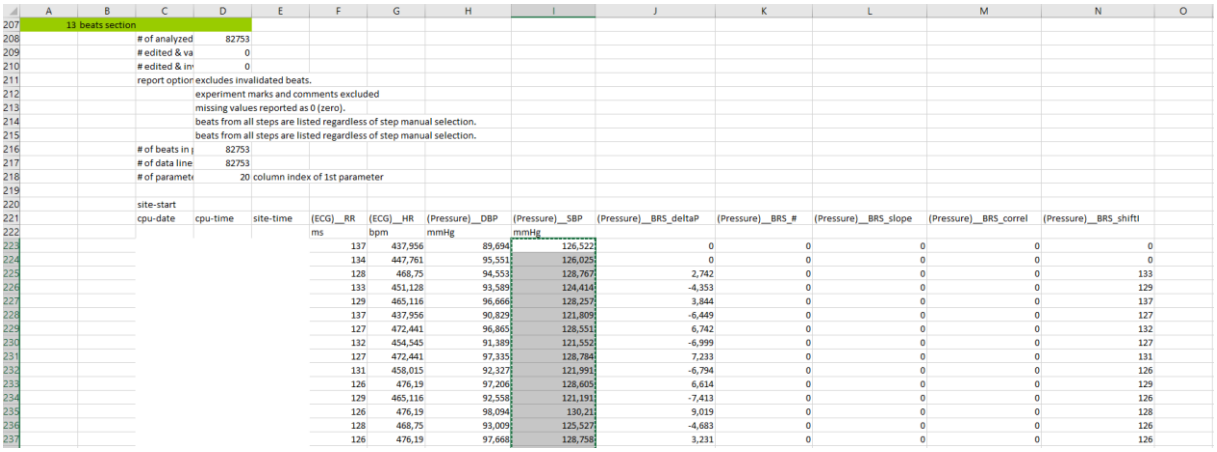

13 beats section

# of analyzed 82753
edited & va 0
edited & in 0
report option excludes invalidated beats.
experiment marks and comments excluded
missing values reported as 0 (zero).
beats from all steps are listed regardless of step manual selection.
beats from all steps are listed regardless of step manual selection.
# of beats in 82753
# of data line 82753
# of paramete 20 column index of 1st parameter

site-start													
cpu-date	cpu-time	site-time	(ECG)__RR	(ECG)__HR	(Pressure)__DBP	(Pressure)__SBP	(Pressure)__BRS_deltaP	(Pressure)__BRS_#	(Pressure)__BRS_slope	(Pressure)__BRS_correl	(Pressure)__BRS_shiftI		
			ms	bpm	mmHg	mmHg							
			137	437,956	89,694	126,522	0	0	0	0	0		
			134	447,761	95,551	126,025	0	0	0	0	0		
			128	468,75	94,553	128,767	2,742	0	0	0	133		
			133	451,128	93,589	124,414	-4,353	0	0	0	129		
			129	465,116	96,666	128,257	3,844	0	0	0	137		
			137	437,956	90,829	121,809	-6,449	0	0	0	127		
			127	472,441	96,865	128,551	6,742	0	0	0	132		
			132	454,545	91,389	121,552	-6,999	0	0	0	127		
			127	472,441	97,335	128,784	7,233	0	0	0	131		
			131	458,015	92,327	121,991	-6,794	0	0	0	126		
			126	476,19	97,206	128,605	6,614	0	0	0	129		
			129	465,116	92,558	121,191	-7,413	0	0	0	126		
			126	476,19	98,094	130,21	9,019	0	0	0	128		
			128	468,75	93,009	125,527	-4,683	0	0	0	126		
			126	476,19	97,668	128,758	3,231	0	0	0	126		

Supplemental File 12

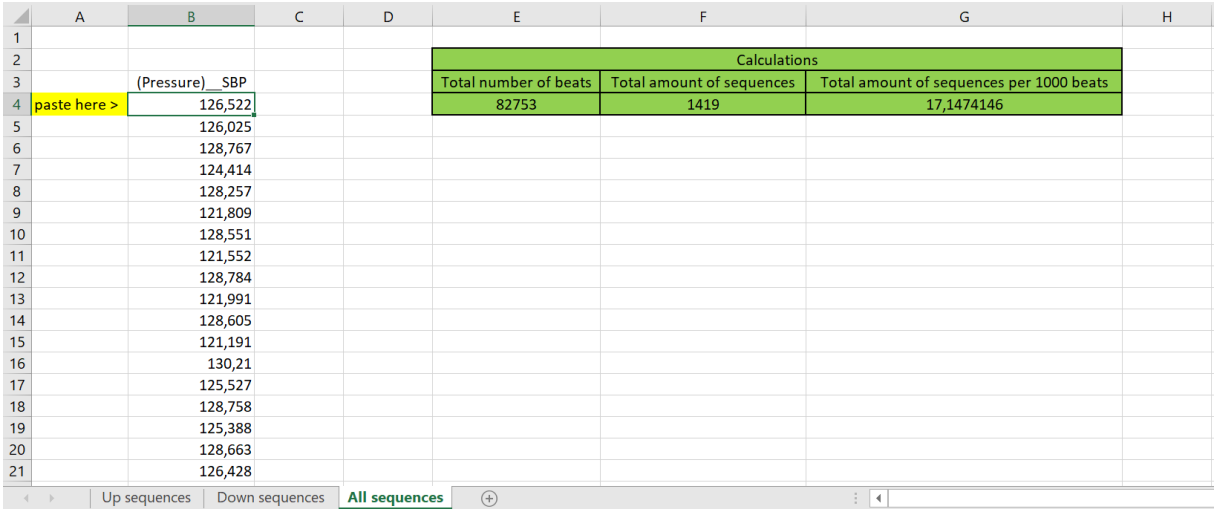

paste here >	(Pressure)__SBP
	126,522
	126,025
	128,767
	124,414
	128,257
	121,809
	128,551
	121,552
	128,784
	121,991
	128,605
	121,191
	130,21
	125,527
	128,758
	125,388
	128,663
	126,428

Calculations

Total number of beats	Total amount of sequences	Total amount of sequences per 1000 beats
82753	1419	17,1474146

Up sequences | Down sequences | All sequences

Supplemental File 13

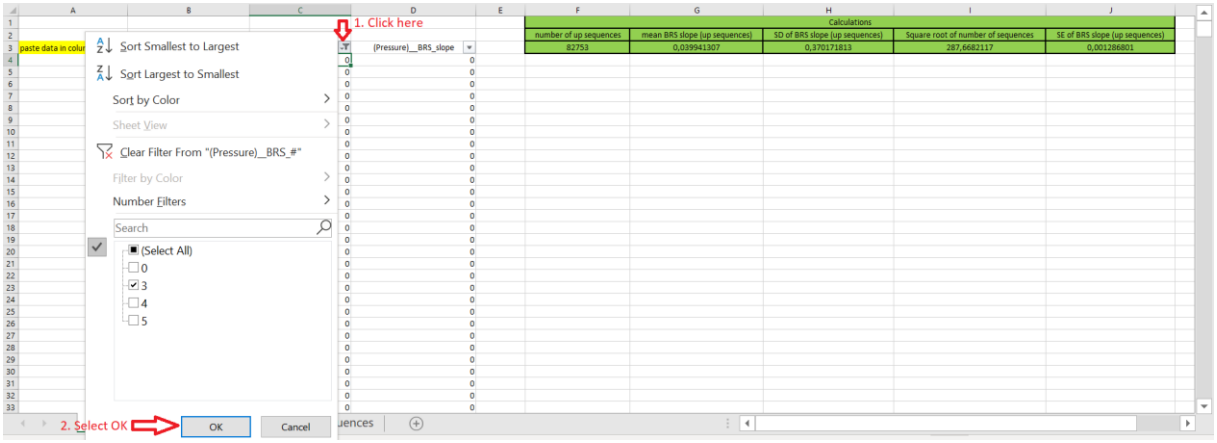

Supplemental File 14

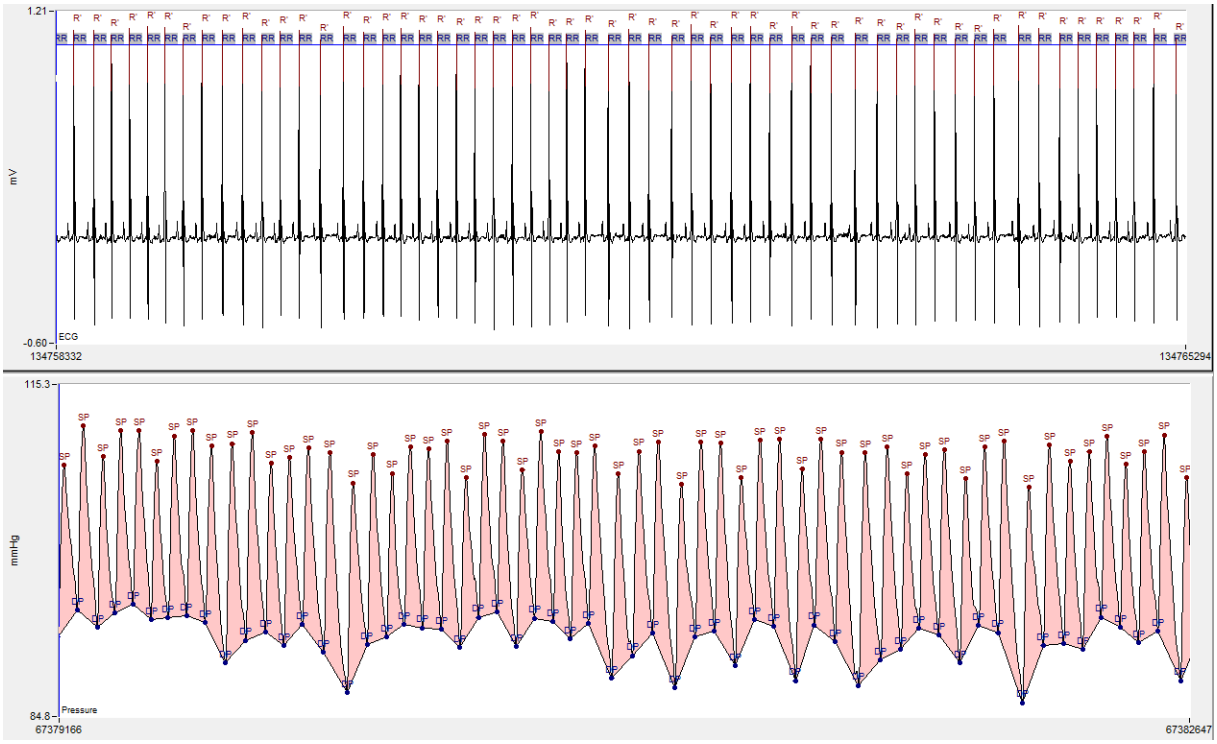

Supplemental File 15

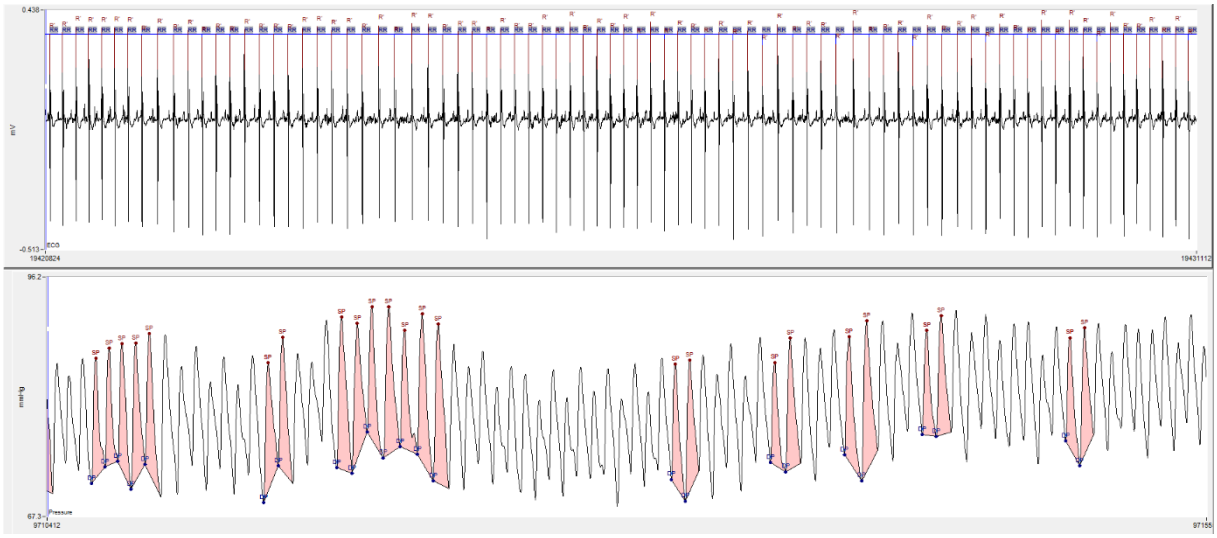

Supplemental File 16